Journal of Science

Volume: 16, Issue: 3, Year: 2020

Contact

Manisa Celal Bayar University

Institute of Natural and Applied Sciences

Campus of Şehit Prof Dr İlhan Varank 45140 Yunus Emre – MANİSA, TURKEY

Tel: (00 90) 236 201 27 05

Fax: (00 90) 236 241 21 49

e-mail: cbujos@gmail.com

Web: http://dergipark.gov.tr/cbayarfbe

"CBU Journal of Science is indexed by ULAKBIM-TUBITAK TR-DIZIN"

ISSN 1305-130X E-ISSN 1305-1385

CBUJOS is published quarterly at Manisa Celal Bayar University Printing House

"CBU Journal of Science is a refereed scientific journal"

Celal Bayar University Journal of Science
Volume 16, Issue 3, 2020, p 1-1

Celal Bayar University Journal of Science

Celal Bayar University Journal of Science
Volume 16, Issue 3, 2020, p 1-1

CBU Journal of Science

Celal Bayar University Journal of Science (CBUJOS) covers scientific studies in the fields of Engineering and Science and publishes accounts of original research articles concerned with all aspects of experimental and theoretical studies. CBU Journal of Science is a refereed scientific journal published four times annually (March, June, September and December) by Institute of Natural and Applied Sciences of Manisa Celal Bayar University. CBU Journal of Science considers the original research articles written in English for evaluation.

CBU Journal of Science is indexed by TUBİTAK ULAKBIM TR-DIZIN, and also is included in DOAJ, Cite Factor, Journal TOCS, Advanced Science Index and OAJI databases. Digital Object Identifier (DOI) number will be assigned for all the articles being published in CBU Journal of Science.

Instructions for Authors and Article Template can be found on the main page of MCBU Institute of Natural and Applied Sciences (http://fbe.cbu.edu.tr)

Celal Bayar University Journal of Science
Volume 16, Issue 3, 2020, p 1-1

Vol: 16, Issue: 3, Year: 2020

Contents

Celal Bayar University Journal of Science
Volume 16, Issue 3, 2020, p 1-1

Celal Bayar University Journal of Science
Volume 16, Issue 3, 2020, p 241-245
Doi: 10.18466/cbayarfbe.729586

Celal Bayar University Journal of Science

Droplet-based Microfluidic Device for the Synthesis of Silica Nanoparticles

Arsalan Nikdoost and E. Yegan Erdem

[1] Mechanical Engineering Department, Bilkent University, Ankara, Turkey
*yeganerdem@bilkent.edu.tr
*Orcid No: 0000-0001-9852-2293

Received: *29 April 2020*
Accepted: *14 September 2020*
DOI: *10.18466/cbayarfbe.729586*

Abstract

Microfluidic reactors are advantageous for nanomaterial synthesis due to their capability to provide controlled reaction environment. In this work, a droplet based microfluidic reactor is designed for the synthesis of silica nanoparticles. The synthesis is carried out in a very controlled environment and a uniform size and shape distribution is achieved. The classical synthesis protocol for silica nanoparticles is modified to use nonpolar solvents in the reaction so that this platform can later be used for coating hydrophobic nanomaterials. Therefore, this study not only presents a new device but also a new synthesis method. The results are compared with conventional batch wise synthesis methods and the obtained nanoparticles showed better size distribution.

Keywords: microreactor, microfluidics, droplet-based flow, nanoparticles, silica nanoparticles, microfluidic synthesis

1. Introduction

Nanoparticles have unique electronic, optic, mechanic and biological properties along with their small size and high surface to volume ratio that make them desirable for applications in many areas such as drug delivery, printable electronics, wearable devices and sensor technologies. Silica nanoparticles are one type of them which attracted attention for their compatibility with other materials such as quantum dots and iron oxide that lead them to be desirable in optics and drug delivery [1-4]. Their properties are highly dependent on their size and morphology; therefore, their functionality increases when they are produced monodispersely.

Synthesis of nanoparticles are mostly done with conventional batch-wise methods where reagents are mixed and heated in large scales; however in these methods it is not always possible to maintain uniform reaction conditions in terms of time and temperature in all parts of the system, which results in polydisperse synthesis inevitably. Microfluidic synthesis methods are used to overcome this limitation as it is possible to control the reaction conditions such as residence time, concentration, temperature, and pH much precisely [5-8].

There are examples in literature that focus on the microfluidic synthesis of silica nanoparticles. For instance, the first sol-gel based microfluidic synthesis was performed by Khan et al. [9] where they used a segmented flow microfluidic device, with gas phase separating the liquid segments, and synthesized particles around 200-700 nm. There were also other examples of microfluidic reactors which followed the well-known Stöber method where TEOS and ammonia solution is mixed [10-16]. In some of these reactors, flow was droplet-based where reagents were carried in the form of separate droplets in the channel [10-14, 17, 18] whereas some of them were continuous flow [15, 16]. In most of these literature examples, though, the obtained particles were micron sized. Only a few of them targeted nanometer scale particles [13, 17].

In almost all these formerly presented work, reactants were prepared inside a polar solvent, mostly ethanol. This works very well if the synthesized particles are going to be used as is. However, for applications that require silica to be synthesized in situ with hydrophobic materials, such as in the case of coating of quantum dots with silica shells, a non-polar solvent is required during the synthesis [19]. Therefore, in this work a new microfluidic device was developed that can work with non-polar solvents in a droplet-based flow and compared to the results obtained by batch-wise synthesis, better size distribution with much reduced residence was achieved.

2. Materials and Methods

2.1. Fabrication of the Microreactor

Microfluidic reactor is designed to have a droplet-based flow inside 200 µm wide and deep channels. Two reagents are delivered into the microreactor by using capillary tubing, as soon as they enter the microchannel, a continuous flow separates them into individual droplets. Due to the circulating flow profile inside droplets, reagents mix rapidly without causing any clogging or contamination on channel walls. Droplet-based flow also maintains same amount of residence time as opposed to continuous flow scheme where the parabolic velocity profile causes an imbalance of total time spent in the channel. A schematic showing the layout of the microreactor is presented in Figure 1.

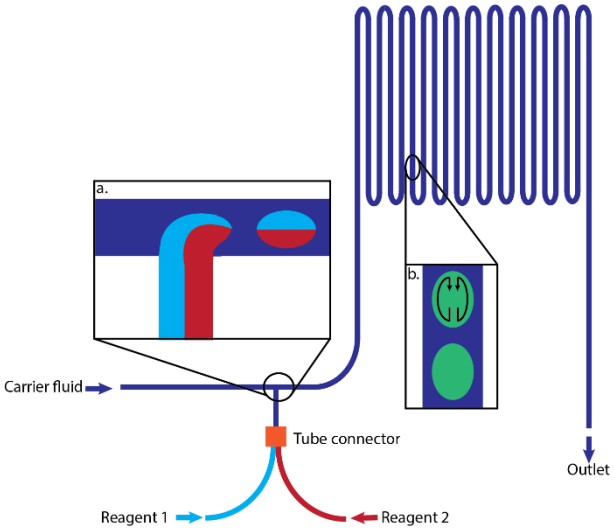

Figure 1. Schematic of the microfluidic device used for silica nanoparticle synthesis. (a) Droplet generation zone. (b) Schematic of the flow profile within droplets.

The fabrication of the microreactor was done in the clean room of National Nanotechnology Research Center (UNAM). The microchannels were etched with deep reactive ion etching in silicon wafer and later bonded to a glass substrate with anodic bonding. Later the capillary tubing is connected to the inlet of the reactor with epoxy. A tube connector is utilized to combine the flow incoming from two separate capillaries that carry two reagents and to deliver them to the microreactor.

2.2. Synthesis Method

The synthesis of silica nanoparticles with a nonpolar solvent was first performed by a batch-wise synthesis method in order to be able to compare the results obtained within the microfluidic reactor.

2.2.1. Batch-wise Synthesis

For the synthesis of silica nanoparticles compatible with hydrophobic coatings, a method proposed by Popovic et al. is adapted and modified [20]. A 1.3 mL IGEPAL CO-520 and 10 mL of anhydrous cyclohexane were mixed. After the through mixing, 80µL of tetraethyl orthosilicate (TEOS) was added to this solution and stirred for 30 mins. Finally, 150 µL of 28 % ammonium hydroxide solution is added and stirred for 48 hours. Reaction was carried out at room temperature. Obtained silica nanoparticles were later centrifuged and dissolved in a 2 M NaOH solution and refrigerated. All solutions were obtained from Sigma Aldrich.

2.2.2. Microfluidic Synthesis

The microfluidic synthesis of silica nanoparticles was performed in a droplet-based flow where the reagents are carried within an immiscible flow as droplets. The selection of the carrier fluid is important as it should provide enough shear stress to form droplets and not mix with them. As the carrier fluid pure N-Methylformamide (NMF) was selected. Droplets were composed of two reagent solutions prepared separately and delivered to the microreactor from two separate capillary tubes. The first reagent solution was prepared with 1.3 ml of IGEPAL CO-520 dissolved in 10ml of anhydrous cyclohexane and 80 µl of TEOS. The second reagent solution was prepared by mixing 150 µl of 28 % aqueous ammonium hydroxide solution with 10 ml of anhydrous cyclohexane. The choice of the carrier fluid was a challenge in here as a nonpolar solvent needed to be chosen for further processing with hydrophobic particles. Even though NMF is immiscible with cyclohexane and TEOS, it is slightly miscible with ammonium hydroxide. This might have resulted in loss of reactants from the droplets to the carrier fluid which would prevent the formation of particles. In order to avoid that, the concentration of the ammonium hydroxide solution in the droplets was determined experimentally.

Two reagent solutions were delivered to the microreactor from two separate capillary tubes, they were merged at a junction connected to the inlet and as soon as they entered the microchannel, the shear stress applied by the carrier fluid divided them into droplets. The two reagents were mixed inside droplets rapidly as they move in the channel.

2.3. Experimental Set-up

Experimental set-up for the microfluidic synthesis is composed of a microscope with camera attachment to monitor flow inside the channels, two syringe pumps for delivering liquids in the channel and a light source for imaging purposes.

3. Results and Discussion

In this work the synthesis was also carried with conventional batch methods to compare results obtained from the microreactor.

3.1. Batch-wise Synthesis Results

Batch-wise synthesis of silica nanoparticles lasted 48 hours as a result of the reverse micelle process explained earlier. The obtained nanoparticles were observed under

Celal Bayar University Journal of Science
Volume 16, Issue 3, 2020, p 241-245
Doi: 10.18466/cbayarfbe.729586

the transmission electron microscope (TEM) and their size distribution is determined by looking at the images and calculating their diameter through direct measurement from these images. Particles were 18.25 ± 2.2 nm in diameter. The TEM images are shown in Figure 2.

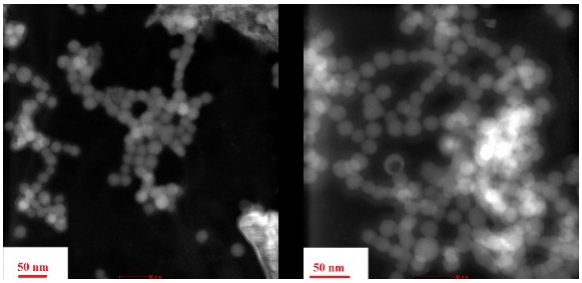

(a) (b)

Figure 2. TEM images of synthesized silica nanoparticles in batch-wise method.

3.2. Microreactor Synthesis Results

For the synthesis of silica nanoparticles inside the microreactor, the flow rate of the continuous carrier fluid (NMF) was selected as 9.2 µl/min and the flow rates of two reagents (TEOS with cyclohexane and ammonium hydroxide with cyclohexane) were set as 1.9 µl/min for a stable droplet generation. Two reagents were delivered from separate capillary tubes as shown in Figure 3a. They merge with a microfluidic tube connector and enter the device, later form droplets (Figure 3b). Total residence time of reagents in the microreactor was 525 seconds and all experiments were carried out at room temperature.

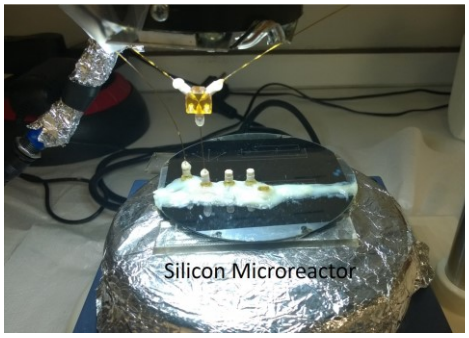

(a)

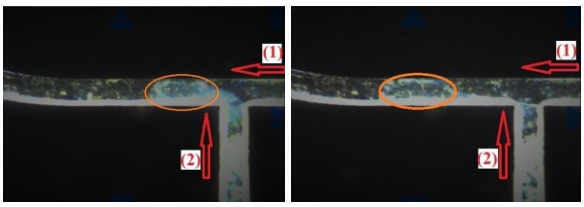

(b)

Figure 3. (a) The microreactor under operation. (b) Droplet formation inside the microchannel. (1) denotes the career fluid whereas (2) denotes the channel where droplet phase is delivered.

In the initial experiments, ammonium hydroxide in cyclohexane was 0.38 M while the TEOS and cyclohexane solution was prepared as described in Section 2.2.2. The flow rate of the carrier fluid was 9.6 µl/min while TEOS solution was 0.8 µl/min and ammonium hydroxide solution with cyclohexane was 1.6 µl/min. With this concentration and flow rates, the obtained silica nanoparticles were less than 4 nm in diameter, their image under the transmission electron microscope is shown in Figure 4.

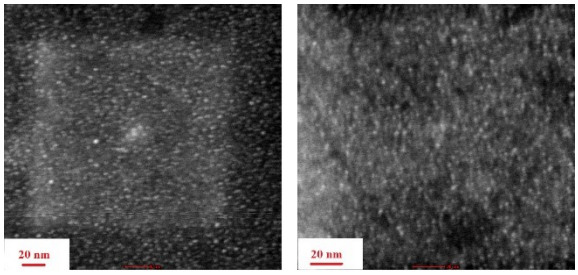

(a) (b)

Figure 4. TEM images of silica nanoparticles synthesized in the microreactor with low ammonium concentration. The average diameter of the nanoparticles was less than 4 nm.

The low ammonium concentration resulted in formation of seed like structures instead of individually distinguished nanoparticles. This may mean that the reagent was not sufficient for growth. In the next set of experiments, the ammonia solution concentration was doubled, and made 0.76 M with a flow rate of 1.9 µl/min. This gave resulted in silica nanoparticles with an average diameter of 25 nm. The TEM images of these particles are shown in Figure 5. Particle sizes were measured by using Adobe Illustrator program with manual measurement of diameter of each particle in the images.

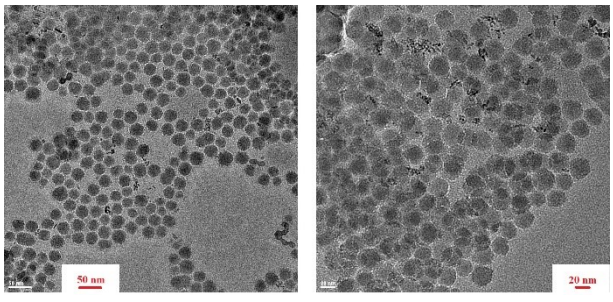

(a) (b)

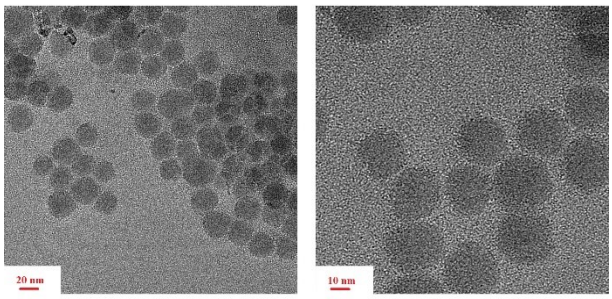

(c) (d)

Figure 5. TEM images of nanoparticles synthesized within the microreactor with high ammonium concentration. Average diameter size is 25 ± 2.7 nm.

In order to confirm the formation of silica nanoparticles, EDX analysis was performed on samples obtained from the microreactor. As a sample holder a TEM grid was used due to the small amount of nanoparticle solution. Figure 6 shows the EDX results. Since the TEM grid was made from Cu, Cu peaks also appeared along with Si and O peaks.

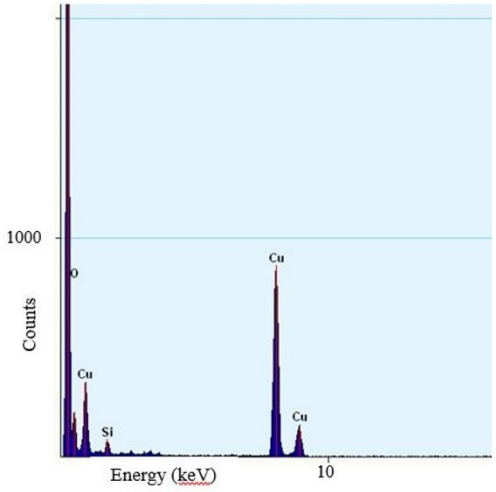

Figure 6. EDX quantification results.

3.3. Comparison of the Results

As a final step the results obtained from batch synthesis and microfluidic synthesis were compared. The major difference is the reaction time and the ammonium hydroxide concentration. In the batch-wise synthesis method, the reaction lasted 48 hours and the ammonium hydroxide concentration was 0.38 M. The resulting nanoparticles were 18.25 ± 2.7 nm in diameter. In the microfluidic synthesis, the ammonium hydroxide concentration was doubled (0.76 M) while the reaction lasted for 8.75 min. The obtained nanoparticles were 25 ± 2.7 nm in diameter. This shows that as the reagent amounts are decreased and reaction is carried out in microenvironments, the residence time decreases while the size distribution is improved. This confirms the advantage of using microfluidic reactors in nanomaterial synthesis.

4. Conclusion

A novel microfluidic device is designed for the synthesis of silica nanoparticles with a nonpolar solvent. A droplet-based flow is utilized to control reagent concentrations precisely and to obtain a uniform mixing. The synthesis was successful and resulted in a narrower size distribution compared to the batch-wise methods. In addition, the synthesis was accomplished in shorter times than available methods in literature. This platform and synthesis method can later be used for coating of quantum dots with silica for increasing their stability.

Acknowledgement

E. Y. Erdem would like to acknowledge the Tübitak 2232 grant that funded this research under the project number 114C092. She also thanks Mr. Alican Özkan for their help in the laboratory studies as well as Dr. Yusuf Keleştemur for assisting with imaging and providing some of the chemicals used in the reaction.

Author Contributions

Arsalan Nikdoost fabricated the microreactor and performed the experimental work.
E. Yegan Erdem designed the microreactor and experimental steps. Both authors contributed in the writing and reviewing of the manuscript.

Ethics

There are no ethical issues after the publication of this manuscript.

References

1. He, Q, Shi, J. 2010. Mesoporous silica nanoparticle based nano drug delivery systems: synthesis, controlled drug release and delivery, pharmacokinetics and biocompatibility. *Journal of Materials Chemistry*; 21: 5845-5855.

2. Zhao, CX, He, L, Qiao, SZ, Middelberg, APJ. 2011. Nanoparticle synthesis in microreactors. *Chemical Engineering Science*; 66(7): 1463-1479.

3. Wu, KCW, Yamauchi, Y. 2012. Controlling physical features of mesoporoussilica nanoparticles (MSNs) for emergingapplications. *Journal of Materials Chemistry*; 22:1251-1256.

4. Mebert, AM, Baglole, CJ, Desimone, MF, Maysinger, Dusica. 2017. Nanoengineered silica: properties, applications and toxicity. *Food and Chemical Toxicology*; 109(1): 753-770.

5. Erdem, EY, Cheng, JC, Doyle, FM, Pisano, AP. 2014. Multitemperature zone, droplet-based microreactor for increased temperature control in nanoparticle synthesis. *Small*; 10(6): 1076-1080.

6. Phillips, TW, Lignos, IG, Maceiczyk, RM, DeMello, AJ, DeMello, A. 2014. Nanocrystal synthesis in microfluidic reactors: where next?. *Lab Chip.*; 14(17): 3172-3180,

7. Chang, CH, Paul, BK, Remcho, VT, Atre, S, Hutchison, JE. 2008. Synthesis and post-processing of nanomaterials using microreaction technology. *Journal of Nanoparticle Research*; 10: 965-980.

8. Nightingale, AM, deMello, JC. 2012. Segmented flow reactors for nanocrystal synthesis. *Advanced Materials*; 25(13): 1813-1821.

9. Khan, SA, Gunther, A, Schmidt, MA, Jensen, KF. 2004. Microfluidic synthesis of colloidal silica. *Langmuir*; 20(20): 8604-8611.

10. Lee, I, Yoo, Y, Cheng, Z, Jeong, HK. 2008. Generation of monodisperse mesoporous silica microspheres with controllable size and surface morphology in a microfluidic device. *Advanced Functional Materials*, 18(24): 4014-4021.

11. Carroll, NJ, Rathod, SB, Derbins, E, Mendez, S, Weitz, DA, Petsev, DN. 2008. Droplet-based microfluidics for emulsion and solvent evaporation synthesis of monodisperse mesoporous silica microspheres. *Langmuir*; 24(3): 658-661.

12. Li, D, Guan, Z, Zhang, W, Zhou, X, Zhang, WY, Zhuang, Z, Wang, X, Yang, CJ. 2010. Synthesis of Uniform-Size Hollow Silica Microspheres through Interfacial Polymerization in Monodisperse Water-in-Oil Droplets. *ACS Appl. Mater. Interfaces*; 2(10): 2711-2714.

13. Su, M, Su, H, Du, B, Li, X, Ren, G, Wang, S. 2014. The properties of silica nanoparticles with high monodispersity synthesized in the microreactor system. *Journal of Sol-Gel Science and Technology*; 72(2): 375-384.

14. Yan, H, Kim, C. 2014. Formation of monodisperse silica microparticles with various shapes and surface morphologies using double emulsion templates. *Colloids and Surfaces A: Physicochemical and Engineering Aspects*; 443(20): 88-95.

15. He, Y, Kim, KJ, Chang, CH. 2017. Continuous, size and shape-control synthesis of hollow silica nanoparticles enabled by a microreactor-assisted rapid mixing process. *Nanotechnology*; 28(23): 235602.

16. Hao, N, Nie, Y. Xu, Z, Closson, AB, Usherwood, T, Zhang, JXJ. 2019. Microfluidic continuous flow synthesis of functional hollow spherical silica with hierarchical sponge-like large porous shell. *Chemical Engineering Journal*; 366: 433–438.

17. He, P, Greenway, G. Haswell, SJ. 2011. Microfluidic synthesis of silica nanoparticles using polyethylenimine polymers. *Chemical Engineering Journal*; 167(2): 694-699.

18. Wacker, JB, Lignos, I, Parashar, VK, Gijs, MAM. 2012. Controlled synthesis of fluorescent silica nanoparticles inside microfluidic droplet. *Lab Chip*; 12: 3111-3116.

19. Kobayashi, Y, Nozawa, T, Nakagawa, T, Gonda, K, Takeda, M, Ohuchi, N, Kasuya, A. 2010. Direct coating of quantum dots with silica shell. *Journal of Sol-Gel Science and Technology*; 55: 79-85.

20. Popović, Z, Liu, W, Chauhan, VP, Lee, J, Wong, C, Greytak, AB, Insin, N, Nocera, DG, Fukumura, D, Jain, RK, Bawendi, MG. 2010. A nanoparticle size series for in vivo fluorescence imaging. *Angewandte Chemie*; 122(46): 8831-8834.

Celal Bayar University Journal of Science
Volume 16, Issue 3, 2020, p 251-255
Doi: 10.18466/cbayarfbe.689482

Celal Bayar University Journal of Science

Chemical Composition of *Taxus baccata* L. Leaves and Male Cones Water: Methanol Extracts

Younes Shirmohammadli[1], Seyyed Khalil Hosseinihashemi[2]*, Abbas Jalaligoldeh[3], Davood Efhamisisi[4], Seyed Hashem Mousavinezhad[5], Amir Lashgari[2]

[1] Department of Civil and Environmental Engineering, Faculty of Engineering, The University of Auckland, New Zealand.
[2] Department of Wood Science and Paper Technology, Karaj Branch, Islamic Azad University, Karaj, Iran
[3] Department of Horticulture Sciences, Karaj Branch, Islamic Azad University, Karaj, Iran
[4] Department of Wood and Paper Science and Technology, Faculty of Natural Resources, University of Tehran, Karaj, Iran
[5] Department of Forestry and Forest Ecology, Gorgan University of Agricultural Sciences and Natural Resources, Gorgan, Iran
*hashemi@kiau.ac.ir
*Orcid No: 0000-0001-6236-0376

Received: *14 February 2020*
Accepted: *14 September 2020*
DOI: *10.18466/cbayarfbe.689482*

Abstract

The yew tree (*Taxus baccata*) is an ancient species in the world that has both toxic and medicinal properties. Identifying the chemical components of different parts of this tree can be useful in the better understanding of the toxicity and medicinal effect of this plant. Therefore, the chemical composition of water: methanol extracts of *T. baccata* L. leaf and male cones obtained from endemic species of Iran were characterized using GC-MS analysis. Twenty two components were identified for leaves including oleic acid (20.87%) and octadeca-9,12-dien-1-ol (17.77%) as the most abundant components, and seventeen components were identified for male cones which were 3-O-methyl-d-glucose (64.00%) and oleic acid (13.32%) as the most abundant components. Furthermore, the potential applications of some of the characterized components are discussed into the depths.

Keywords: *Taxus baccata* leaves and male cones, water: methanol extract, GC-MS, chemical composition, 3-O-methyl-d-glucose.

1. Introduction

Yew (*Taxus baccata*), is a coniferous tree or shrub which reaches a height of 15 meters [1] and widely distributed in western, central and southern Europe, northwest Africa, southwest Asia, and northern Iran [2-4]. Yew has evergreen leaves consist of several short, narrow needles with a length of 1 to 2 cm and a width of 1 to 2 mm [5]. Furthermore, the male cones appear in the axils of the leaves; which are globose with 6-14 peltate scales, each with 4-8 pollen sacs [6].
There have been many observations of poisoning due to the ingestion of yew in animals and humans, and the identification of its constituents can help to a better understanding the toxicity and poisoning of this species [7, 8]. On the other hand, various medical characteristics have been liked to yew and embracing new therapeutic compounds for the treatment of diseases and a tendency to increase the use of natural compounds, the identification of yew compounds can open a new window for human needs [9]. Many studies have been focused on the beneficial component extraction from the bark of the *T. baccata* which dries and destroys this slow-growing and low- population species. One of the means to protect this species is to use the re-growing parts of the plant and also finding and applying the component extraction method is of vital importance [10]. Plant species, habitat environment, and height and the method used to extract the components are effective factors in determining the type and amount of components [11, 12]. This study aimed to extract the leaf and male cones components of yew and identify its constituents to provide a better perspective about the *T. baccata* growing in Iran.

2. Materials and Methods

2.1 Plant Material

Fresh branches containing green needle leaves and male cones of the fallen yew tree due to wind or landslides were collected from Afratakhteh forests in Golestan

province, Iran, in October 2017. The plant material with a voucher specimen number 4657 was deposited to the Herbarium in the college of Agricultural and Natural Resources, Karaj Branch, Islamic Azad University, Karaj, Iran. The plant male cones were isolated from the end of leaves of the plant and they were both washed briefly with distilled water to remove dust and then dried at room temperature. They were kept in the refrigerator at 4 ºC until extraction.

2.2 Extraction

All solvents used for extraction were supplied from Merck Company, Darmstadt, Germany. The water: methanol extracts of leaves and male cones were extracted sequentially in three steps. In the first step, fresh leaves and male cones samples (approximately 10 g of each) were separated and soaked in 150 mL of *n*-hexane in a 250-mL Erlenmeyer flask. The extraction was performed using the shaker technique for 3 h at 4.5 rpm speed. The extracts were filtered and the residue was eluted with 50 mL of *n*-hexane again. In the second step, the residue was processed similarly with the same amount of chloroform for the same period in a dark place at laboratory conditions. The filtered extracts were then evaporated under the laminar flow hood in a dark environment. In the third step, the residue was processed similarly with the same amount of water: methanol (1:1 *v/v*) for the same period and conditions and the extracts were kept dry in sealed Eppendorf tubes with aluminum sheets cover and stored in a refrigerator at 4 ºC prior to chemical analysis. Water: methanol extracts were dried over anhydrous sodium sulfate before the GC-MS analysis.

2.3 GC-MS Analysis

The GC-MS analysis of the resulting extracts was performed using a GC Agilent 7890A and MS Agilent 5975C mass spectrometer detector (Palo Alto, CA, USA) equipped with a HP-5MS cross-linked capillary column (30-m-long and 0.25-mm internal diameter, 0.25 µm film thickness). Helium was used as the carrier gas with a flow rate of 1 mL/min. The run time duration was 48.43 min. The program began at 60 ºC for 2 min and the temperature increased at a rate of 7 ºC/min up to 280 ºC. It remained at this temperature for 15 min. The intrinsic energy that hits the sample in the MS system was 70 eV. The split ratio of the sample was 2:1 with a split flow of 2 mL/min. The individual compounds in the extracts were identified by their retention time relative to known compounds and further identified by comparison of their mass spectra with either the known compounds or published spectral data. Individual components were identified using Wiley 275 L and NIST05 a.L database matching, and by comparing the retention times and mass spectra of constituents with published data [13-15].

3. Results and Discussion

3.1 Leaves and Male Cones Extracts

The number and percentage of the total compounds in the leaves and male cones water: methanol extracts which were identified using GC-MS analysis, were 22 and 97.14% (Table 1), and 17 and 99.29 %, respectively (Table 2).

Table 1. Identified chemical composition of *T. baccata* leaves water: methanol extract.

t_r* (min)	Compound	Class	WM-LE** (%)
6.367	Thymine	Phenolic compound	1.48
7.519	4H-pyran-4-one, 2,3-dihydro-3,5-dihydroxy-6-methyl-	Flavonoid	2.83
9.164	2,3-dihydrobenzofuran	Coumaran	1.93
9.366	2-furancarboxaldehyde, 5-(hydroxymethyl)-	n-Aldehyde	1.29
10.783	Phenol, 4-ethenyl-2-methoxy-	Phenolic compound	0.89
13.294	2-propenoic acid, 3-phenyl-, (E)-	Fatty acid	2.07
13.470	p-Propylguaiacol	Monoterpene	0.50
13.854	3,5-dimethoxyphenol	Taxane	7.65
15.094	Acetic acid, (p-hydroxyphenyl)-	Fatty alcohol	9.67
16.692	3-(2-azidobenzyl)pyridine	Alkaloeid	2.76
17.907	Benzeneacetic acid, 4-hydroxy-3-methoxy-, methyl ester	Fatty acid ester	1.62
18.130	1,7-dimethyl-4,4a,5,6-tetrahydropyrido-1H-[1,2-b]pyridazin-2(3H)-one	Others	2.09
18.955	Pluchidiol	Others	5.05
20.750	1,3-dioxane, 2-(2-bromoethyl)-	Ether	2.96
21.326	Palmitinic acid	Fatty acid	1.80
21.762	2-methyl-1-thia-cyclopentane	n-Alkane	8.87
23.744	Oleic acid	Fatty acid	20.87
23.988	Octadecanoic acid	Fatty acid	1.34
26.328	Fusaric acid	Aromatic carboxylic acid	1.39
29.908	Octadeca-9,12-dien-1-ol	Fatty alcohol	17.77
31.252	3-phenyl-1,4(E)-dodecadiene	Others	0.60
33.929	Cholest-5-en-3-ol (3.beta.)-	Steroid	1.71

*t_r : Retention time; **WM-LE: Water: methanol leaves extract.

Table 2. Identified chemical composition of *T. baccata* male cones water: methanol extract.

t_r* (min)	Compound	Class	WM-MCE** (%)
6.336	Glycerol	Alcoholic sugar	0.48
9.195	2,3-dihydrobenzofuran	Coumaran	1.88
9.895	1,2-Benzenediol, 3-methoxy-	Phenolic compound	1.17
15.131	3-Hydroxyphenylacetic acid	Fatty acid	0.69
16.703	Methyl-(2-hydroxy-3-ethoxy-benzyl)ether	Ether	0.61
18.145	Mome inositol	Sugar	0.66
18.929	2-ethylthiolane	Tioalkaloeid	0.43
19.318	Propyl isopropyl ether	Aromatic ether	0.41
20.044	3,5-Heptadienal, 2-ethylidene-6-methyl-	n-Aldehyde	2.66
22.447	3-O-methyl-d-glucose	Sugar	64.00
23.723	Oleic acid	Fatty acid	13.32
23.982	Stearic acid	Fatty acid	0.77
27.028	Methyl petroselinate	Fatty acid ester	0.75
27.983	Hexadecanoic acid, 2,3-dihydroxypropyl ester	Fatty acid ester	0.64
29.908	9,12-Octadecadien-1-ol	Fatty alcohol	7.70
33.929	Cholest-5-en-3-ol (3.beta.)-	Steroid	1.10
36.259	Stigmasterol, 22,23-dihydro-	Steroid	0.73

* t_r : Retention time; **WM-MCE: Water: methanol male cones extract.

Table 3. Classification of the identified chemical components of the *T. baccata* leaves and male cones water: methanol extract.

No.	Chemical classes	WM-LE* (%)	WM-MCE** (%)	Sum (%)
1	Sugars	0.00	65.14	65.14
2	Acids	37.14	14.78	51.92
3	Alcohols	17.77	7.70	25.47
4	n-Alkanes	8.87	0.00	8.87
5	Taxanes	7.65	0.00	7.65
6	Ethers	2.96	2.19	5.15
7	Flavonoids	2.83	1.29	4.12
8	n-Aldehydes	1.29	2.66	3.95
9	Coumarans	1.93	1.88	3.81
10	Steroids	1.71	1.83	3.54
11	Alkaloids	2.76	0.43	3.19
12	Esters	1.62	1.39	3.01
13	Phenols	2.37	0.00	2.37
14	Terpenes	0.50	0.00	0.50
15	Others	7.74	0.00	7.74
-	Total identified	**97.14**	**99.29**	-

* WM-LE: Water: methanol leaves extract; **WM-MCE: Water: methanol male cones extract.

Through analyzing the qualitative characteristics of flavonoids in yew female cones (seed cones), the researchers showed that there were several flavonoids in methanol extract and the highest concentration of flavonoids (39.37 mg/g) was measured in ethyl acetate extract of seed cones [16]. Compared to the values obtained in leaves extract, seed cones extract had a lower concentration of flavonoids. The results of the data and identified compounds of our studies showed that the compounds 4H-pyran-4-one, 2,3-dihydro-3,5-dihydroxy-6-methyl- (called DDMP) as only flavonoids [17] accounts for only 2.83% in the water: methanol extracts of yew leaves. The identified DDMP is an anti-tumor compound. Moreover, it possesses anti-microbial, anti-oxidant, anti-inflammatory, and anti-mutagenic characteristics [17]. The highest extraction percentage was 3-O-methyl-d-glucose by 64.00% and extracted from the male cones using water: methanol. 3-O-methyl-d-glucose is a nonmetabolizable chemical analog of glucose. Because of its metabolic stability, the early studies investigated the 3-O-methyl-d-glucose as a cellular transport, blood-brain barrier, and tissue apportionment expanse of hexoses [18]. In the more recent researches, 3-O-methyl-d-glucose have been used in cancer identification and track down [19]. Fusaric acid also known as 5-butylpicolinic acid extracted from the leaves using water: methanol as much as 1.39%. Fusaric acid has been known as a wilting agent and also proposed for various therapeutic applications such as quorum sensing inhibitors [20]. Fusaric acid is a

mycotoxin and has negative effects on mammals and also it prevents dopamine beta-hydroxylase enzyme. On the other hand, fusaric acid can prevent cell proliferation and DNA synthesis. However, it is primarily used in research and laboratories.

2-furancarboxaldehyde, 5-(hydroxymethyl)- which is a member of the class of furans, obtained from the leaves by water: methanol at 1.29%. 2-furancarboxaldehyde, 5-(hydroxymethyl)- does not exist in the fresh food, and it is naturally produced (through Millard reaction) from the processing (cooking, drying, or storing) of foods containing sugar. It is used as an index of heat treatment and deterioration in food and products such as tomato paste, honey, and fruit juices [21]. 2-furancarboxaldehyde, 5-(hydroxymethyl)- also has shown hepatoprotective effects on acute alcohol-induced liver oxidative injury in mice [22]. Additionally, 2-furancarboxaldehyde, 5-(hydroxymethyl)- possesses antioxidant properties and prevents the sickling of red blood cells [23-25]. In the yew male cones and leaves, oleic acid was the only fatty acid component which could be extracted using water: methanol (Tables 1 and 2). In this experiment, 2,3-dihydrobenzofuran, also known as coumaran, was identified in both leaves (1.93%) and male cones (1.88%) using water: methanol. 2,3-dihydrobenzofuran has shown effective results against cancer, tuberculosis, malaria, and cataracts [26]. Moreover, some plant species that are reach in 2,3-dihydrobenzofuran possess antioxidant and/or cytoprotective characteristics and insecticidal features [27, 28]. Some of the common uses of oleic acid are in the food, pharmaceutical, cosmetic, and biodiesel industries [29]. Recently, oleic acid has attracted attention due to its positive effect on human disease such as blood pressure [30].

4. Conclusion

In this study, the chemical composition of leaves and male cones extracts of *Taxus baccata* L. were sequentially extracted by water: methanol and then analyzed using the GC-MS technique. In total, identified components are classified as sugars, acids, alcohols, n-alkanes, taxanes, ethers, flavonoids, n-aldehydes, coumarans, steroids, alkaloids, esters, phenolic compounds, terpenes, *etc*. There were many valuable phytocomponents that are potential bioresources for phytopharmaceutics such as 3-O-methyl-d-glucose, 4H-pyran-4-one, 2,3-dihydro-3,5-dihydroxy-6-methyl-, thymine, 2,3-dihydrobenzofuran, oleic acid, and glycerol. Alcohols were identified with almost high percentages in this experiment, the total extraction of alcohols from leaves was 17.77% and from male cones was 7.70%. The other compounds with high extraction percentage were acids, their total extraction using water: methanol solvent from leaves and male cones extracts were 37.14% and 14.78%, respectively. Furthermore, taxanes were extracted as much as 7.65% from leaves extract, while their extraction from male cones extract was 0.00%. Also, the sugar component there was not in the leaves extract by water: methanol extract, while total sugar identification from male cones reached at 65.14%.

Acknowledgement

The authors are grateful for the support of the Department of Wood Science and Paper Technology, Karaj Branch, Islamic Azad University, Karaj, Iran.

Author's Contributions

Younes Shirmohammadli: Developed and performed the experiments and drafted the manuscript.
Seyyed Khalil Hosseinihashemi: Conceived of the presented experiment and supervised the findings of this work.
Abbas Jalaligoldeh: Verified the analytical methods.
Davood Efhamisisi: Aided in interpretation of the results and consulted in technical details.
Seyed Hashem Mousavinezhad: Assisted with laboratory experiments.
Amir Lashgari: Assisted in sourcing materials and planning of the laboratory experiments.

Ethics

There are no ethical issues after the publication of this manuscript.

References

1. Jovanović, B. Taxus L. In: Josifović M (ed) Flora of Serbia 1, SASA, Belgrade, 1970, pp 164-166.

2. Efhamisisi, D.; Topa, A. The effect of xylem extractives on natural durability of yew wood against different rotting fungi. *Journal of Forest and Wood Products*, 2018, 71(1), 49-59.

3. Afraz, S.; Hosseinihashemi, S. K. Extraction and identification of chemical compounds in acetone extract of *Taxus baccata* L. bark. *Iranian Journal of Wood and Paper Science Research*, 2018, 33(1), 88-99.

4. Vencurik, J.; Bosela, M.; Sedmáková, D.; Pittner, J.; Kucbel, S.; Jaloviar, P.; Saniga, M. Tree species diversity facilitates conservation efforts of European yew. *Biodiversity and Conservation*, 2019, 28(4), 791-810.

5. Todorov, T.; Stamberov, P.; Nikolov, B.; Manova, G.; Manov, V. Fatal European yew (*Taxus baccata*) poisoning in two horses. *Tradition Mod Veterinary Medicine*, 2019, 4(2(7)), 34-39.

6. Osuna-Torres, L.; García-Martí, X.; Ventura-Zapata, E.; López-Upton, J.; Zamilpa-Alvarez, A.; González-Cortázar, M.; Tapia-Barrera, N. *Taxus globosa Schltdl.* (Mexican yew) and *Taxus baccata* L. (European yew): intra and interspecies analysis of taxol content and biological activity according to different sources. *Forest Systems*, 2015, 24(3), 045.

7. Dziadosz, M.; Lessig, R.; Bartels, H. A way of handling *Taxus baccata* intoxications in forensic laboratories. *Egyptian Journal of Forestry Sciences*, 2014, 4(2), 50-53.

8. Perju-Dumbravă1, D.; Morar, S.; Chiroban, O.; Lechintan, E.; Cioca, A. Suicidal poisoning by ingestion of *Taxus Baccata* leaves. Case report and literature review. *Romanian Journal of Legal Medicine,* 2013, 21, 115-118.

9. Sarli, S.; Ghasemi, N. Optimization of biosynthesized Zn nanoparticles by poisonous *Taxus baccata* leaves extract and evaluation of their effect on the bacterias and MCF-7 cancer cells. *Eurasian Chemical Communication*, 2020, 2(3), 302-318.

10. Sadeghi-Aliabadi, H.; Asghari, G.; Mostafavi, S. A.; Esmaeili, A. Solvent optimization on Taxol extraction from *Taxus baccata* L., using HPLC and LC-MS. *DARU Journal of Pharmaceutical Science*, 2015, 17(3), 192-198.

11. Yasar, S. Volatile constituents of *Taxus baccata* L. leaves from western and southern Turkey. *Asian Journal of Chemistry*, 2013, 25(16), 9123-9125.

12. Glowniak, K.; Mroczek, T.; Zobel, A. M. Seasonal changes in the concentrations of four taxoids in *Taxus baccata* L. during the autumn-spring period. *Phytomedicine*, 1999, 6(2),135-140.

13. Julain, D.; König, W. A. The Atlas of Spectral Data of Sesquiterpene Hydrocarbons; E. B. Verlag, Hamburg univ. Press: E. B. Verlag, Hamburg, Germany, 1988; pp 661.

14. Adams, R. P. Identification of Essential oil Components by Gas Chromatography/Mass Spectrometry; 1st edn. Allured Publishing Corp., Carol Stream, IL, 60188, USA, 1995; pp 469.

15. Adams, R. P. Identification of Essential Oil Components by Gas Chromatography/Quadrupole Mass Spectroscopy; 3rd edn. Allured Publishing Corp., Carol Stream, IL, 60188, USA, 2001; pp 469.

16. Milutinović, M. G.; Stanković, M. S.; Cvetković, D. M.; Topuzović, M. D.; Mihailović, V. B.; Marković, S. D. Antioxidant and anticancer properties of leaves and seed cones from European yew (*Taxus baccata* L.). *Archives of Biologicsl Sciences*, 2015, 67(2), 525-534.

17. Teoh, Y. P.; Mashitah, M. D. Screening of antifungal activities from genera Trametes against growth of selected wood-degrading fungi from Malaysia. *Australian Journal of Basic & Applied Sciences*, 2012, 6(1), 79-85.

18. Jay, T. M.; Dienel, G. A.; Cruz, N. F.; Mori, K.; Nelson, T.; Sokoloff, L. Metabolic stability of 3-O-methyl-d-glucose in brain and other tissues. *Journal of Neurochemistry*, 1990, 55(3), 989-1000.

19. Sehgal, A. A.; Li, Y.; Lal, B.; Yadav, N. N.; Xu, X.; Xu, J.; Laterra, J.; van Zijl, P. C. M. CEST MRI of 3-O-methyl-glucose uptake and accumulation in brain tumors. *Magnetic Resonance in Medicine*, 2018, 81(3), 1993-2000.

20. Tung, T. T.; Jakobsen, T. H.; Dao, T. T.; Fuglsang, A. T.; Givskov, M.; Christensen, S. B.; Nielsen, J. Fusaric acid and analogues as gram-negative bacterial quorum sensing inhibitors. *European Journal of Medicinal Chemistry*, 2017, 126, 1011-1020.

21. Arena, E.; Fallico, B.; Maccarone, E. Thermal damage in blood orange juice: kinetics of 5-hydroxymethyl-2-furancarboxaldehyde formation. *International Journal of Food Science and Technology*, 2001, 36(2), 145-151.

22. Li, W.; Qu, X.-N.; Han, Y.; Zheng, S.-W.; Wang, J.; Wang, Y.-P. Ameliorative effects of 5-hydroxymethyl-2-furfural (5-HMF) from schisandrachinensis on alcoholic liver oxidative injury in mice. *International Journal of Molecular Sciences*, 2015, 16(2), 2446-2457.

23. Janzowski, C.; Glaab, V.; Samimi, E.; Schlatter, J.; Eisenbrand, G. 5-hydroxymethylfurfural: Assessment of mutagenicity, DNA-damaging potential and reactivity towards cellular glutathione. *Food and Chemical Toxicology*, 2000, 38(9), 801-809.

24. Li, M. M.; Wu, L. Y.; Zhao, T.; Xiong, L.; Huang, X.; Liu, Z. H.; Fan, X. L.; Xiao, C. R.; Gao, Y.; Ma, Y. B.; Chen, J.; Zhu, L. L. The protective role of 5-HMF against hypoxic injury. *Cell Stress and Chaperones*, 2011, 16(3), 267-273.

25. Zhao, L.; Chen, J.; Su, J.; Li, L.; Hu, S.; Li, B.; Zhang, X.; Xu, Z.; Chen, T. In vitro antioxidant and antiproliferative activities of 5-hydroxymethylfurfural. *Journal of Agricultural and Food Chemistry*, 2013, 61(44), 10604-10611.

26. Sheppard, T. D. Strategies for the synthesis of 2, 3-dihydrobenzofurans. *Journal of Chemical Research*, 2011, 35(7), 377-385.

27. Chin, Y. W.; Chai, H. B.; Keller, W. J.; Kinghorn, A. D. Lignans and other constituents of the fruits of Euterpeoleracea (Acai) with antioxidant and cytoprotective activities. *Journal of Agricultural and Food Chemistry,* 2008, 56(17), 7759-7764.

28. Huang, Z.; Cui, Q.; Xiong, L.; Wang, Z.; Wang, K.; Zhao, Q.; Wang, Q. Synthesis and insecticidal activities and SAR studies of novel benzoheterocyclicdiacylhydrazine derivatives. *Journal of Agricultural and Food Chemistry*, 2009, 57(6), 2447-2456.

29. Whelan, L. Oleic acid: Production, Uses and Potential Health Effects, Published by Nova Science Publishers, Inc., UK; 2014, pp 139.

30. Ruiz-Gutierrez, V.; Muriana, F. J.; Guerrero, A.; Cert, A. M.; Villar, J. Plasma lipids, erythrocyte membrane lipids and blood pressure of hypertensive women after ingestion of dietary oleic acid from two different sources. *Journal of Hypertension*, 1996, 14(12), 1483-1490.

Celal Bayar University Journal of Science

Effect of emulsion formulation on characteristics of pea protein-stabilized oil-in-water emulsions

Aslı Can Karaça[1]*

[1] Department of Food Engineering, Istanbul Technical University, 34469, Istanbul, Turkey
*cankaraca@itu.edu.tr
*Orcid No: 0000-0002-4137-0644

Received:*14 June 2020*
Accepted: *14 September 2020*
DOI: *18466/cbayarfbe.752703*

Abstract

The goal of this study was to investigate the effect of emulsion formulation on characteristics of oil-in-water emulsions. Varying concentrations of biopolymers including maltodextrin, gum arabic and pea protein were used in the formulation of emulsions created according to an extreme vertices design. Mean droplet size of oil-in-water emulsions changed between 0.9-2.5 µm and decreased with increasing pea protein concentration. Creaming stability ranged between 9-100% and increased as the concentration of pea protein increased. The results of this research suggest that pea protein can be utilized as an emulsifier for oil-in-water emulsions with low oil concentration as it has the ability to decrease the mean droplet size and increase creaming stability of the emulsions.

Keywords: Creaming stability, droplet size, emulsion, pea protein.

1. Introduction

Oil-in-water emulsions are defined as homogeneous dispersions of oil droplets in water stabilized by emulsifiers [1]. Stability of an emulsion is defined as the ability of an emulsion to conserve its characteristics such as size distribution, state of aggregation, or spatial arrangement of droplets over time and plays an important role on quality and shelf life of numerous food products [2]. The changes in emulsion characteristics result in an alteration in the distribution or organization of molecules or the nature of molecules [3]. The dominant physicochemical mechanisms which lead to destabilization of food emulsions include creaming, flocculation, coalescence, Ostwald ripening, and phase inversion [4]. Creaming takes place due to density difference between the two phases. Oil droplets move upward because they have a lower density than the aqueous phase. Homogenization technique, processing parameters, emulsion formulation, and storage conditions are the key factors in emulsion stability [3].

Amphiphilic nature of proteins allows them to be commonly used in emulsion systems [5, 6]. Proteins have the ability to adsorb at oil-water interfaces and form films around newly formed oil droplets [2]. Emulsifying properties of proteins mainly depend on their structure and interfacial behaviour. There has been a recent trend not only in the academia but also in the food industry towards the use of plant-based ingredients in product formulations. In addition to soy, wheat and corn proteins, pea protein is one of the most commonly investigated plant-based protein for its physicochemical and functional properties such as solubility, water/oil holding, emulsification, foaming and gelling [7]. Emulsifying properties of pea protein have been in the scope of several recent studies. Lam et al. [8] investigated emulsifying properties of pea proteins obtained from various different cultivars. The authors reported that pea proteins showed high emulsion stability (~96%) and no significant difference was observed among cultivars. Effects of homogenization method [9] and several treatments including pH [10, 11], heat [9, 12, 13] and high pressure [14] on emulsifying properties of pea protein were reported.

Maltodextrin and gum arabic are commonly used wall materials in encapsulation of food ingredients. Maltodextrin is produced by hydrolysis of starch and contains linear amylose and branched amylopectin degradation products [15]. It is mainly used as a drying aid in encapsulation and has many advantages including high solubility, neutral taste and low cost. However, maltodextrin has very poor emulsifying properties and therefore it is used in combination with other surface-active materials such as proteins and gum arabic [16]. Gum arabic is a natural hetero polysaccharide obtained

from acacia trees and contains L-arabinose, L-rhamnose, and D-glucuronic acid and 1,3-linked β-D-galactopyranosyl units. Due to its surface active properties, it is widely used as an emulsifier and stabilizer in food and pharmaceutical formulations [17]. Both gum arabic and pea protein are reported to have good emulsifying properties, however they show high viscosity at relatively low concentrations. Therefore, a mixture of maltodextrin, gum arabic and pea protein were used in the formulation of emulsions in this study. Maltodextrin was used as a bulking agent and texture modifier whereas gum arabic and pea protein were used as co-surfactants. The main goal of this research was to examine the effect of emulsion formulation on some characteristics of pea protein-stabilized oil-in-water emulsions and to investigate whether pea protein can be used as an effective emulsifier.

2. Materials and Methods

2.1. Materials

Bioploymer materials used (maltodextrin, gum arabic, and pea protein with 83% protein content) were supplied from Tate & Lyle PLC (London, UK), Alland & Robert (Paris, France), and Roquette (Lestrem, France), respectively. Sunflower seed oil was purchased from a local supplier.

2.2. Emulsions Preparation

Varying amounts of biopolymer materials were dissolved in 52 g of distilled water based on the formulations presented in Table1. For preparation of emulsions, 8 g of sunflower seed oil was added to these solutions and the mixture was homogenized with T18 Ultra-Turrax (IKA®-Werke GmbH & Co. KG, Staufen, Germany) homogenizer at 12,000 rpm for 7 min.

Table 1. Emulsion formulations created according to extreme vertices design.

Run	Maltodextrin (%)	Gum arabic (%)	Pea protein (%)
1	38.25	1.25	0.50
2	35.00	5.00	0.00
3	34.75	3.75	1.50
4	40.00	0.00	0.00
5	36.50	2.50	1.00
6	37.25	1.25	1.50
7	33.00	5.00	2.00
8	38.00	0.00	2.00
9	35.75	3.75	0.50

2.3. Droplet Size

A laser diffraction particle size analyzer was employed to characterize the droplet size distribution of oil-in-water emulsions (Mastersizer 3000, Malvern Instruments Ltd., Worcestershire, U.K.) and reported as volume-surface mean diameters [18].

2.4. Creaming Stability

Creaming stability of emulsions were determined by monitoring the cream layer separation after 1 h of storage [19].

2.5. Experimental Design

An extreme vertices mixture design with 9 experiments (Table 1) was used to investigate the effect of emulsion formulation on characteristics of oil-in-water emulsions. Mixture design was used in the study for designing experimental settings since the main goal of the research was to investigate the effect of formulation which was a mixture of three ingredients (maltodextrin, gum arabic and pea protein). The ranges of concentrations were selected as: 33-40% for maltodextrin, 0-5% for gum arabic, and 0-2% for pea protein. Measurements were performed in triplicate and reported as the mean ± one standard deviation. Minitab® software (Minitab, LLC, Pennsylvania, US) was used for designing experiments, analyzing data and creating contour plots.

3. Results and Discussion

3.1. Droplet Size

Droplet size of oil-in-water emulsions play an important role on the physicochemical stability of emulsions and is affected by not only the formulation of the emulsion but also the processing parameters [20]. In the present study, all emulsions were prepared under the same homogenization conditions and constant oil content in order to investigate the effect of emulsion formulation on emulsion characteristics. Maltodextrin was used as a bulking agent and texture modifier whereas gum arabic and pea protein were used as co-surfactants in the oil-in-water emulsions.

The mean droplet size of oil-in-water emulsions changed between 0.9-2.5 µm under the experimental conditions used. Droplet size distributions were found to be bimodal as indicated in Figure 1. Concentration of maltodextrin, gum arabic, and pea protein were identified as the significant factors for predicting mean droplet size of oil-in-water emulsions (p<0.05; Table 2). This predictive model was able to explain 89% of the variability in the data.

Maltodextrin contains linear amylose and branched amylopectin degradation products and shows no surface-active properties. On the other hand, presence of maltodextrin in the emulsion formulation has been reported to result in both stabilization and destabilization of the emulsion based on the homogenization conditions, emulsion formulation, and maltodextrin type [15]. Gum arabic contains different units and shows good emulsifying properties due to the amphiphilic protein unit in its structure [21]. Similarly, pea protein shows good emulsifying properties due to its amphiphilic

structure and ability to decrease the interfacial tension at the oil-water interphase.

Figure 2 shows the effect of emulsion formulation on mean droplet size of oil-in-water emulsions. The mixture contour plot indicated that mean droplet size decreased from ~2 µm to ~1 µm as the concentration of pea protein increased from 0 to 2%.

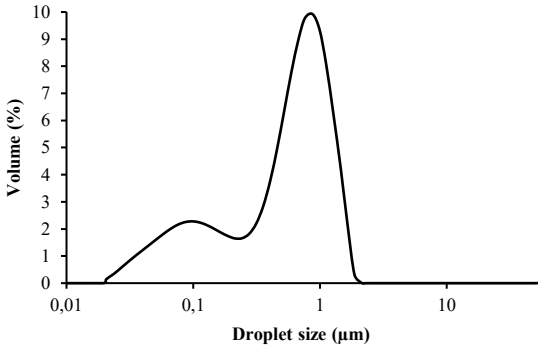

Figure 1. Droplet size distribution of oil-in-water emulsion # Run 8.

It was observed that the emulsions containing 2% pea protein had the lowest droplet size. Peng et al [12] also reported that mean droplet size of pea protein-stabilized oil-in-water emulsions decreased (from ~9.9 to ~1.3 µm) as the protein concentration increased from 0.1% to 0.5%. In another recent study by Aziz et al. [22], mean droplet size of oil-in water emulsions stabilized by acorn protein was reported to decrease as the protein concentration increased from 0.1% to 1%.

An increase in protein concentration results in an effective reduction of interfacial tension, increased surface area and subsequent decrease in droplet size [23, 24]. It has been indicated that an optimum concentration of protein is required to sufficiently cover the newly formed oil droplets during homogenization and provide stability by preventing aggregation in emulsions stabilized by proteins.

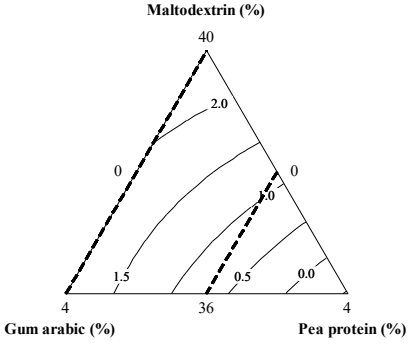

Figure 2. Mixture contour plot of mean droplet size of oil-in-water emulsions.

Table 2. Predictive models for mean droplet size and creaming stability of oil-in-water emulsions.

Dependent variable	Independent variable	Coefficient	*p* value	Model fit
Droplet size	Maltodextrin	0.0612	$p<0.05$	$R^2 = 0.8939$
	Gum arabic	2.2352	$p<0.05$	$R^2(adj) = 0.7878$
	Pea protein	-2.3987	$p<0.05$	$F = 8.43$
	Maltodextrin*Gum arabic	-0.0641	NS	$p<0.05$
	Maltodextrin*Pea protein	0.0476	NS	
Creaming stability	Maltodextrin	0.2674	$p<0.05$	$R^2 = 0.9007$
	Gum arabic	-207.282	$p<0.05$	$R^2(adj) = 0.8013$
	Pea protein	261.079	$p<0.05$	$F = 9.07$
	Maltodextrin*Gum arabic	5.9884	NS	$p<0.05$
	Maltodextrin*Pea protein	-5.8237	NS	

* NS: not significant ($p>0.05$).

3.2. Creaming Stability

Creaming is a common instability mechanism that occurs in emulsions which results in phase separation. Creaming stability of oil-in-water emulsions changed between 9% and 100%. Concentration of biopolymer materials were identified as the significant factors for predicting creaming stability ($p<0.05$; Table 2). This predictive model was able to explain 90% of data variation.
Mixture contour plot in Figure 3 presents the effect of emulsion formulation on creaming stability of oil-in-water emulsions. Creaming stability increased from ~40% to ~100% as the concentration of pea protein increased from 0 to 2%. Emulsions produced with 2% pea protein showed the highest creaming stability. Increase in creaming stability with increased pea protein concentration was found to be in accordance with the results observed for mean droplet size. Ye [25] also reported increased creaming stability with increasing protein concentration up to 2%. However, creaming stability was reported to decrease when the protein concentration was increased further. On the other hand, Hu et al [26] reported that optimum interfacial protein concentration and stability was achieved at 3% protein

concentration in soy protein-stabilized emulsions. Increased emulsion stability with increasing protein concentration observed at relatively low protein concentrations is attributed to increased concentration of interfacial adsorbed proteins, reduction of droplet size and increased viscosity which slow down phase separation [13, 23]. Interfacial protein concentration and droplet size are indicated to be the main factors affecting emulsion stability [25].

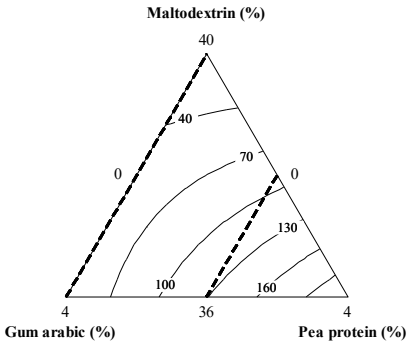

Figure 3. Mixture contour plot of creaming stability of oil-in-water emulsions.

4. Conclusion

Emulsion formulation had a significant effect on mean droplet size and creaming stability of oil-in-water emulsions stabilized by pea protein. Droplet size decreased and creaming stability increased with increasing pea protein concentration. The findings of this study indicate that pea protein can be utilized as an effective emulsifier for oil-in-water emulsions at low oil concentration. Further research is required to elucidate the effect of other formulation parameters such as oil concentration and type on characteristics of pea protein-stabilized oil-in-water emulsions.

Acknowledgement

The author would like to thank Aromsa A.S. for financial support of the study.

Author's Contributions

Aslı Can Karaça: Drafted and wrote the manuscript, performed the experiment and result analysis.

Ethics

There are no ethical issues after the publication of this manuscript.

References

1. Karayıldırım, ÇK. 2017. Characterization and *in vitro* evolution of antibacterial efficacy of novel hesperidin microemulsion. *Celal Bayar University Journal of Science;* 13: 943-947.
2. Dickinson, E. 2003. Hydrocolloids at interfaces and the influence on properties of dispersed systems. *Food Hydrocolloids;* 17: 25-39.
3. McClements, DJ. Emulsion stability. In: Clydesdale FM (ed) Food emulsions: principles, practices, and techniques, 2nd edn. CRC Press, Boca Raton, 2005, pp 269-339.
4. McClements. DJ. 2007. Critical review of techniques and methodologies for characterization of emulsion stability. *Critical Reviews in Food Science and Nutrition;* 47: 611-649.
5. McClements, DJ. Emulsion ingredients. In: Clydesdale FM (ed) Food emulsions: principles, practices, and techniques, 2nd edn. CRC Press, Boca Raton, 2005, pp 95-174.
6. Coşkun, AEİ, Ocak, ÖÖ, Ocak, B, Ötleş, S. 2020. pH-dependent behavior and stability of protein-based particles in aqueous media. *Celal Bayar University Journal of Science;* 16: 95-102.
7. Wang, Y, Guldiken, B, Tulbek, M, House, JD, Nickerson, M. 2020. Impact of alcohol washing on the flavour profiles, functionality and protein quality of air classified pea protein enriched flour. *Food Research International;* 132: 109085.
8. Lam, ACY, Warkentin, TD, Tyler, RT, Nickerson, MT. 2017. Physicochemical and functional properties of protein isolates obtained from several pea cultivars. *Cereal Chemistry;* 94: 89-97.
9. Qamar, S, Bhandari, B, Prakash, S. 2019. Effect of different homogenisation methods and UHT processing on the stability of pea protein emulsion. *Food Research International;* 116: 1374-1385.
10. Gharsallaoui, A, Cases, E, Chambin, O, Saurel, R. 2009. Interfacial and emulsifying characteristics of acid-treated pea protein. *Food Biophysics;* 4: 273-280.
11. Liang, HN, Tang, CH. 2013. pH-dependent emulsifying properties of pea [*Pisum sativum* (L.)] proteins. *Food Hydrocolloids;* 33: 309-319.
12. Peng, W, Kong, X, Chen, Y, Zhang, C, Yang, Y, Hua, Y. 2016. Effects of heat treatment on the emulsifying properties of pea proteins. *Food Hydrocolloids;* 52: 301-310.
13. Chen, M, Lu, J, Liu, F, Nsor-Atindana, J, Xu, F, Goff, HD, Ma, J, Zhong, F. 2019. Study on the emulsifying stability and interfacial adsorption of pea proteins. *Food Hydrocolloids;* 88: 247-255.
14. Chao, D, Jung, S, Aluko, RE. 2018. Physicochemical and functional properties of high pressure-treated isolated pea protein. *Innovative Food Science and Emerging Technologies;* 45: 179-185.
15. Dokic-Baucal L, Dokic P, Jakovljevic J. 2004. Influence of different maltodextrins on properties of O/W emulsions. *Food Hydrocolloids;* 18: 233-239.
16. Reineccius GA. 2004. The spray drying of food flavors. *Drying Technology;* 22: 1289-1324.
17. Dave, NP, Gor, A. Natural polysaccharide-based hydrogels and nanomaterials: Recent trends and their applications. In Hussain CM (ed) Handbook of nanomaterials for industrial applications. Elsevier, Amsterdam, Netherlands, 2018, pp 36-66.
18. Can Karaca, A, Nickerson, MT, Low, NH. 2011. Lentil and chickpea protein-stabilized emulsions: Optimization of emulsion

formulation. *Journal of Agricultural and Food Chemistry;* 59: 13203-13211.

19. Stone, AK, Nickerson, MT. 2012. Formation and functionality of whey protein isolate – (Kappa-, iota-, and lambda-type) carrageenan electrostatic complexes. *Food Hydrocolloids*; 27: 271-277.

20. Ozbek, ZA, Ergönül, PG. 2017. A review on encapsulation of oils. *Celal Bayar University Journal of Science;* 13: 293-309.

21. Randall RC, Phillips GO and Williams PA. 1988. The role of the proteinaceous component on the emulsifying properties of gum arabic. *Food Hydrocolloids;* 2: 131-140.

22. Aziz, A, Khan, NM, Ali, F, Khan, ZU, Ahmad, S, Jan, AK, Rehman, N, Muhammad, N. 2020. Effect of protein and oil volume concentrations on emulsifying properties of acorn protein isolate. *Food Chemistry;* 324: 126894.

23. Boostani, S, Hosseini, SMH, Golmakani, MT, Marefati, A, Hadi, NBA, Rayner, M. The influence of emulsion parameters on physical stability and rheological properties of Pickering emulsions stabilized by hordein nanoparticles. *Food Hydrocolloids;* 101: 105520.

24. Sun, LH, Lv, SW, Chen, CH, Wang, C. 2019. Preparation and characterization of rice bran protein-stabilized emulsion by using ultrasound homogenization. *Cereal Chemistry;* 96: 478-486.

25. Ye, A. 2008. Interfacial composition and stability of emulsions made with mixtures of commercial sodium caseinate and whey protein concentrate. *Food Chemistry;* 110: 946-952.

26. Hu, M, Xie, F, Zhang, S, Li, Y, Qi, B. 2020. Homogenization pressure and soybean protein concentration impact the stability of perilla oil nanoemulsions. *Food Hydrocolloids;* 101: 105575.

Celal Bayar University Journal of Science

Predicting Mixing and Compaction Temperatures of Polymer Modified Bitumen

Ali Almusawi[1]*, Burak Şengöz[2], Derya Kaya Özdemir[2], Ali Topal[2]

[1] Dokuz Eylul University, The Graduate School of Natural and Applied Sciences, İzmir, Turkey
[2] Dokuz Eylul University, Department of Civil Engineering, İzmir, Turkey
*ali89.engin@yahoo.com
*Orcid No: 0000-0002-4507-2492

Received: *20 March 2020*
Accepted: *14 September 2020*
DOI: *10.18466/cbayarfbe.706537*

Abstract

Despite many advantages of using polymer additives in bitumen, there are several challenges bordering on standards and specifications with regards to their utilization. One of these challenges is related with specifying the required heating or mixing and compaction temperatures of the polymer modified bitumen. The standard method (ASTM D 2493) aims to determine mixing and compaction temperatures of the base or unmodified bitumen. Nevertheless, the application of this method in the case of polymer modified bitumen led to very high temperatures which may not be appropriate for PMB. In this paper, some alternative methods named as the high shear rate and steady shear flow method suggested in the literature have been examined and tested for 50/70 and 160/220 penetration grade bitumen samples involving an elastomeric type of additive. A suggested method has also been proposed to overcome the complexities in the implementation of the alternative methods.

Keywords: Mixing, Compaction, Polymer Modified bitumen, High Shear Rate, Steady Shear Flow.

1. Introduction

Over the years, base bitumen has been used in the construction of the asphalt pavement. The rapid growth rate in the traffic volumes showed a limitation in the performance of the conventional bitumen which may be clearly noticed in the earlier failures of the pavement than what is expected. This led to a decrease in service life and an increase in maintenance costs [1]. To overcome such problems and to enhance the performance of the asphalt pavement, in the last few decades modified bitumen with polymers has been adopted [2]. Polymer additives that will provide the desired properties for asphalt materials are applied in the wearing layers in many parts of the world. The polymer additive belonging to the elastomer class called Styrene-Butadiene-Styrene (SBS) was started to be used in the wear layers to produce the polymer modified bitumen PMB. However, selecting suitable temperatures to handle this modified bitumen has become an issue since a suitable method has not been regulated. The traditional method (ASTM D 3493), which has been described and used for the calculation of mixing and compaction temperatures of the base bitumen, yields high temperature when it is applied for the polymer modified bitumen. This is because the ASTM D 2493 method is established for the base bitumen (unmodified) which exhibits Newtonian behavior at high temperatures. In such behavior, viscosity is the shear rate dependent. while modified bitumen exhibits a Non-Newtonian behavior where the viscosity values dependent on shear rate [3-4]. Such high temperatures, especially due to oxidation, cause hardening in bitumen. In most oxidation reactions, the hardening of the bitumen doubles as the temperature increases by 10 ºC. High temperatures also cause emission and odor problems [3-10]. In the absence of a reliable method for the selection of mixing and compaction temperatures for polymer modified bitumen, many agencies have designed their own standards to estimates the appropriate temperatures of each modified bitumen. Obviously, there is a need for a formal method to determine the mixing and compaction temperatures of the modified bitumen and must consider its behavior [3-15].

In this study, two alternative methods named as High Shear Rate Method (HSR) and Steady Shear Flow (SSF) have been applied on using two penetration bitumen grades (50/70 and 160/220) samples involving elastomeric polymer called Styrene-Butadiene-Styrene (SBS) to determine mixing and compaction temperatures. Also, the alternative methods have been

Celal Bayar University Journal of Science
Volume 16, Issue 3, 2020, p 263-268
Doi: 10.18466/cbayarfbe.706537

correlated with the ASTM D 3493 method to find more simple approach to determine the required mixing and compaction temperatures of PMB.

2. Materials and Methods

In this study 50/70 and 160/220 penetration grades base bitumen supplied by DERE Group were used.

Some of the conventional tests have been conducted on the base bitumen such as penetration test, softening point test, and rolling thin film oven test to measure the bitumen characteristics. Table 1 shows the test results according to the ASTM specification.

Table 1. Properties of the base bitumen.

Test	Specification	Results		Specification limits	
		50/70	160/220	50/70	160/220
Penetration (25 ºC; 0.1 mm)	ASTM D5 EN 1426	65	190	50-70	160-220
Softening point (ºC)	ASTM D36 EN 1427	51	41	46-54	35-43
Penetration index (PI)	-	0.35	0.123	-	-
Rolling thin film oven test (RTFOT)	ASTM D2872-12				
Change of mass (%)	-	0.160	0.94	0.5 (max.)	0.5 (max.)
Penetration (25 ºC; 0.1 mm)	ASTM D5 EN 1426	53	97	50 (min.)	50 (min.)
Retained penetration (%)	ASTM D36 EN 1427	82	51	50 (min.)	50 (min.)
Softening point after RTFOT (ºC)	ASTM D36 EN 1427	58	50	48 (min.)	48 (min.)

2.1. Preparation of Polymer Modified Bitumen

The SBS polymer used was Kraton D-1101 supplied by the Shell Chemicals Company. The SBS concentration was selected as 5% as an optimum content based on the past researches [16-18]. High shear laboratory mixer was used to prepare the polymer modified bitumen as shown in Fig. 1. The bitumen was heated to (180-185 ° C) and poured into glass beaker. The SBS in powder form was added gradually to the base bitumen and the rotating speed was maintained at 2000 rpm for 1 hour.

Figure 1. High shear laboratory mixer.

The utilization of the shear mixer rate is made based on past researches. The mixing speed of 2000 rpm has seen to be suitable compare to the higher shear rate since the viscosity of the polymer modified bitumen sample remains almost the same regardless of the duration used compared to the higher shear rates [18,19].

2.2. Determination of Mixing and Compaction Temperatures

Mixing and compaction temperatures are determined through the standard method (ASTM D2493). Several alternative methods have been suggested in the literatures to implement for the polymer modified bitumen such as high shear rate, steady shear flow. The summarized procedure for each method is presented below

2.2.1. ASTM D 2493 Method

The device used for this method is the Brookfield viscometer. Based on ASTM D 2493, the viscosity of bitumen sample at two different temperatures (135 ° C and 165 ° C) is determined at a constant shear rate of 6.8 1 / s.

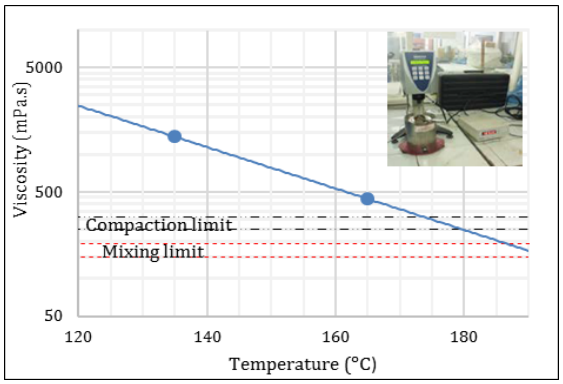

Figure 2. Determination of mixing and compaction temperatures.

Celal Bayar University Journal of Science
Volume 16, Issue 3, 2020, p 263-268
Doi: 10.18466/cbayarfbe.706537

The obtained viscosity values are plotted on a semi-logarithmic graph as shown in Figure 2. Mixing and compaction temperatures are corresponding to 170 ± 20 mPa. s and 280 ± 30 mPa. s, respectively [20].

2.2.2. High Shear Rate method (HSR)

Solaimanian et al. found the shear rate during the Superpave compactor is higher than the one used in ASTM D2493 method (6.8 1/s). They found the shear rate value is around 500 1/s. The viscosity at this shear rate must be calculated and used for mixing and compaction temperatures determination. In this method, Brookfield viscometer is used to determine the viscosity of the bitumen at different shear rates and then drawn and extrapolated to 500 1/s shear rate as shown in Fig. 3. Mixing and compaction temperatures are found by using the same viscosity limits used in the traditional method 0.17±0.02 Pa. s and 0.28±0.03 Pa. s, respectively (High Shear Rate original (HSR-O)). In attempt trying to get lower temperatures in 2006 , the authors suggested a higher viscosity range to be used which are 0.275±0.03 Pa. s and 0.550±0.06 Pa.s. (High Shear Rate Evolution (HSR-E)) [21-22].

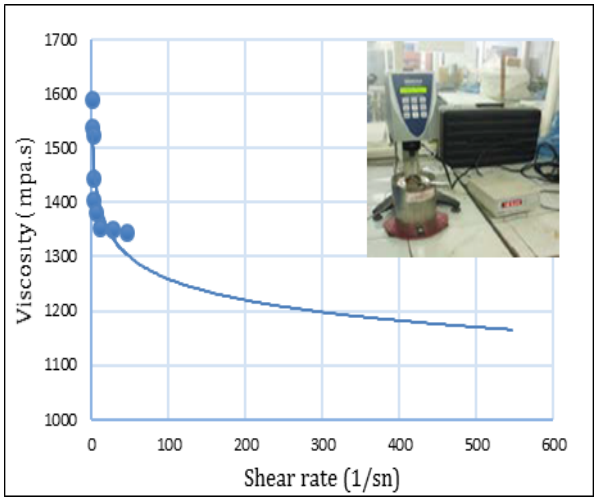

Figure 3. High shear rate method.

2.2.3. Steady Shear Flow Method (SSF)

This method is based on the shear dependency behavior of the polymer modified bitumen. Using Dynamic Shear Rheometer (DSR) and the procedure recommended by Reink, the mixing and compaction temperatures of the bitumen can be determined. It is proposed that the viscosity values are measured at different shear stresses and the suggested stress levels are from 0.3 to 500 Pa at different temperatures 76 ºC, 82 ºC and 88 ºC as shown in Fig. 4. The measured viscosity values at 500 Pa or 1000 Pa are then plotted using a log viscosity versus log temperature chart and extrapolated to obtain the mixing and compaction temperatures through using the suggested viscosity limits 0.17 ± 0.02 Pa s and 0.35 ± 0.03 Pa s, respectively [23].

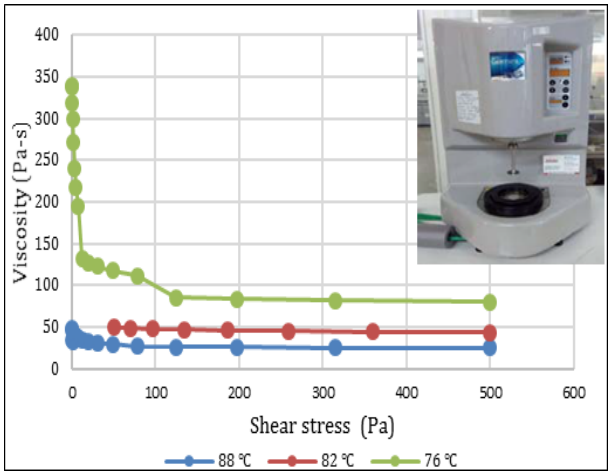

Figure 4. Steady shear flow method.

3. Results and Discussion

3.1. Mixing and compaction determination results

The determined mixing and compaction temperatures for each of the alternative methods are presented in Fig. 5. As depicted in Figure 5, the mixing and compaction temperatures obtained from the ASTM method were the highest compared to the other alternative methods for both bitumen grades. Also, 50/70 PMB samples yielded higher mixing and compaction temperatures than 160/220 PMB samples regardless of the implemented approach. This is attributed to the higher consistency of the 50/70 penetration grade compared to the 160/220 penetration grade which is less viscous. So, the required handling temperature for 50/70 would be higher to reach the desired workability during construction of the asphalt mixtures.

For the mixing and compaction temperatures determined by the High shear rate method, the results for bitumen polymers modified samples involving SBS have shown a noticeable reduction in mixing and compaction temperatures compared to the ASTM method for both bitumen grade types. The reduction in the obtained mixing and compaction temperatures is attributed to the lower viscosity value used in this method compared to the ASTM method. The HSR method proposes the utilization of viscosity value for PMB at a high shear rate (around 500 1/s). The reason behind obtaining a lower viscosity value at a high shear rate is associated with the behavior of the polymer modified bitumen. The PMB generally tends to exhibit a non-Newtonian behavior in which the viscosity is sensitive to the change in the shear rate and any increase in the shear rate will result in a decrease in the viscosity value. Also, mixing and compaction temperatures results for 50/70 PMB samples are higher than the 160/220 samples. As expected, as the penetration value of the bitumen increases the more fluid it becomes, and this explains the variation in the mixing and compaction temperatures between 50/70 PMB and 160/20 PMB.

For a steady shear flow method, the determined mixing and compaction temperature results demonstrated a discernible reduction in mixing and compaction temperatures compared to the ASTM method. Also, it can be noticed that the obtained mixing and compaction temperatures through this method is lesser than the temperatures determined through the HSR method. The substantial reduction in the obtained mixing and compaction temperatures for PMB samples by implementing the SSF method is associated with the sensitivity of the PMB samples while being tested at Dynamic Shear Rheometer (DSR). PMB samples are more susceptible to the variation in both temperature and the applied stress and this attributed to the Non-Newtonian behavior of the PMB. Also, in this method, the proposed limits to determine the required mixing and compaction temperatures for PMB are different from both ASTM and HSR methods and this is generating lower temperatures. As mentioned earlier, the variation in mixing and compaction temperatures for 50/70 PMB and 160/220 PMB is due to the difference in the bitumen stiffness.

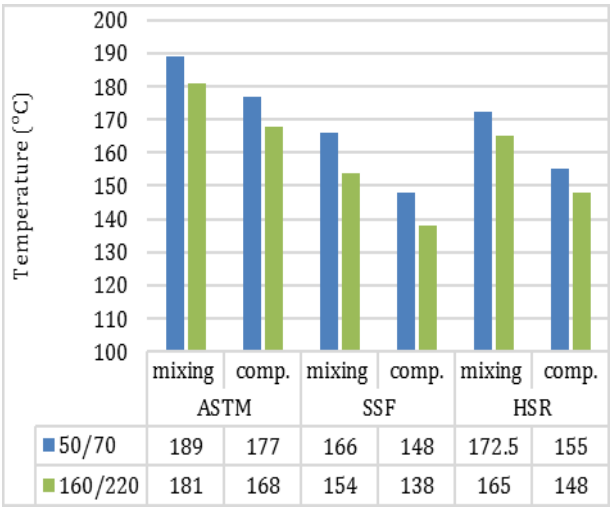

Figure 5. Mixing and compaction temperatures.

3.2. Simplification of the HSR and SSF approaches

The above-mentioned methods are relatively difficult to apply and they have not standardized yet. The HSR method requires the use of the rotational viscometer at the maximum range of shear rates at which data can be collected (0.1 1/s to 100 1/s). While the SSF method requires the utilization of the Dynamic Shear Rheometer (DSR) and the test duration is higher compared to the ASTM method. In order to overcome these complexities, an empirical equation has been developed to determine the mixing and compaction temperatures of the PMB samples.

Based on the obtained mixing and compaction temperatures, it has been noticed that the reduction amount in the temperatures for both PMB samples, when compared to the ASTM method, is almost constant. The mixing temperatures using the SSF method is almost less by 25 ºC compared to the ASTM results. Also, the compaction temperatures have a constant reduction amount which is about 29.5 ºC. The same conclusion applies to the HSR method and the reduction in mixing and compaction temperatures is 16.25 ºC and 21 ºC, respectively.
Thus, the following eq. (3.1) and eq. (3.2) can be proposed to simplify the determination of mixing and compaction temperatures of SBS polymer modified bitumen for SSF method.

$$T_{mix.\ SSF} = T_{mix.\ ASTM} - 25 \quad (3.1)$$

$$T_{comp.\ SSF} = T_{comp.\ ASTM} - 29.5 \quad (3.2)$$

The same approach has also been made for the high shear rate method as explained in eq. (3.3) eq. (3.4).

$$T_{mix.\ HSR} = T_{mix.\ ASTM} - 16.25 \quad (3.3)$$

$$T_{comp.\ HSR} = T_{comp.\ ASTM} - 21 \quad (3.4)$$

The results of the application of the above mentioned equations are presented in Table 2. The determined temperatures by the alternative methods (SSF and HSR) are almost similar to the temperatures obtained by the application of the proposed equations. Also, it should be noted that the equations above are valid for the PMB used in this study.

Table 2. Comparison of temperatures results with the new proposed equations.

	Method	50/70	160/220
Mixing (ºC)	SSF	166	154
	Proposed SSF	164	156
	HSR	172.5	165
	Proposed HSR	172.75	164.75
Compaction (ºC)	SSF	148	138
	Proposed SSF	147.5	138.5
	HSR	155	148
	Proposed HSR	156	147

4. Conclusion

The selection of the mixing and compaction temperatures of PMB has no specific standards and the application of the ASTM method is not practical. In this study, two penetration grade bitumen 50/70 and 160/220 samples involving styrene butadiene styrene (SBS) at 5% have been used. The proposed methods, HSR and SSF, have been implemented and the results were compared with the ASTM method. Also, an empirical equation has been developed to simplify the determination of the mixing and compaction temperatures for PMB. The obtained results showed the following

1. The implementation of the ASTM method resulted in high mixing and compaction temperatures for both PMB grades. The ASTM method is designed based on the base (unmodified) bitumen behavior by considering the viscosity value at a constant shear rate (6.8 1/s). The viscosity of the PMB at a low shear rate is generally high and the utilization of such high viscosity value would generate an excessive temperature for PMB.
2. 50/70 modified bitumen samples depicted the highest mixing and compaction temperatures for all methods compared with 160/220 penetration grade bitumen. This is because 50/70 is harder and more viscous than the 160/220 penetration grade. Moreover, adding the SBS polymer to the 50/70 bitumen grade considerably increases its stiffness compared to the 160/220 bitumen grade, and this results in a higher required handling temperature for 50/70 PMB.
3. The application of the SSF method resulted in the lowest mixing and compaction temperatures for both bitumen grades compared to other methods.
4. Based on the output of this study, the empirical equations that proposed to simplify the determination of the mixing and compaction temperatures for PMB resulted in very close mixing and compaction temperatures results compared to the alternative methods (HSR and SSF). This is may exclusively valid for bitumen samples with 5% SBS polymer utilized in this study.

The conclusion of this study covers the utilization of two SBS polymer additive. More research should be carried out by using different penetration grade bitumen involving different kinds of polymers and WMA additives in order to perform more validation.

Acknowledgement

This research was sponsored by the Department of Scientific Research projects, Dokuz Eylul University under the project number 2019.KB.FEN.021 for which the authors are greatly indebted. The authors are also thankful to the Graduate School of Natural and Applied Sciences of Dokuz Eylul University for its support.

Author's Contributions

Ali Almusawi: Drafted and wrote the manuscript, performed the experiment and result analysis.
Burak Şengöz, Derya Kaya Özdemir, Ali Topal: Assisted in analytical analysis on the structure, supervised the experiment's progress, result interpretation and helped in manuscript preparation.

Ethics

There are no ethical issues after the publication of this manuscript.

References

1. Hunter, R. N., Self, A., & Read, J. The shell bitumen handbook. 6th edn, ICE Publishing, 2015.

2. Sengoz, B., & Isikyakar, G. 2008. Evaluation of the properties and microstructure of SBS and EVA polymer modified bitumen. *Construction and Building Materials;* 22(9): 1897-1905.

3. Şirin Micaelo, R., A. Santos, and C. Duarte.: Mixing and compaction temperatures of asphalt mixtures with modified bitumen, 5th Eurasphalt & Eurobitume Congress, Istanbul, Turkey, 2012, pp. 7.

4. West, R. C., Watson, D. E., Turner, P. A., & Casola, J. R. 2010. Mixing and compaction temperatures of asphalt binders in hot-mix asphalt (No. Project 9-39).

5. Terrel, R.L., and J.A. Epps. 1989.Using Additives and Modifiers in Hot Mix Asphalt," *Quality Improvement Series 114,* National Asphalt Pavement Association,

6. Shenoy, A. 2001. Determination of the temperature for mixing aggregates with polymer-modified asphalts. *International Journal of Pavement Engineering;* 2(1): 33-47.

7. Shuler, T., D. Hanson, and R. McKeen. 1992. Design and Construction of Asphalt Concrete Using Polymer Modified Asphalt Binders, ASTM STP 1108.

8. Clark, R. C. 1958. Practical results of asphalt hardening on pavement life. *Journal of the Association of Asphalt Paving Technologists;* 27: 196-208.

9. Bahia, H.U., D.I. Hanson, M. Zeng, H. Zhai, M.A. Khatri, and R.M Anderson. 2001. NCHRP Report 459: Characterization of Modified Asphalt Binders in Superpave Mix Design, Transportation Research Board, National Research Council, Washington, D.C.

10. Stroup-Gardiner, M., Lange, C. R., & Carter, A. 2005. Quantification of emission potential from asphalt binders using mass loss and opacity measurements. *International Journal of Pavement Engineering;* 6(3): 191-200.

11. Khatri, A., H.U. Bahia, and D. Hanson. 2001. Mixing and Compaction Temperatures for Modified Binders using the Superpave Gyratory Compactor, Journal of the Association of Asphalt Paving Technologists, Vol. 70.

12. Stuart, K.D. 2002. Methodology for Determining Compaction Temperatures for Modified Asphalt Binders, FHWA-RD-02-016, Federal Highway Administration.

13. Anjan Kumar, S., Sarvanan, U., Murali Krishnan, J., & Veeraragavan, A. 2014. Rheological characterisation of modified binders at mixing and compaction temperature. *International Journal of Pavement Engineering;* 15(9): 767-785.

14. Grover, R. 2002. "Determining Mixing and Compaction Temperatures of Asphalt Binders Using Zero Shear Viscosity," RMAUPG Binder Subcommittee Meeting.

15. Lange, C. R., & Stroup-Gardiner, M. 2005. Quantification of potentially odorous volatile organic compounds from asphalt binders using head-space gas chromatography. *Journal of Testing and Evaluation;* 33(2): 101-109.

16. Sengoz, B., & Isikyakar, G. 2008. Analysis of styrene-butadiene-styrene polymer modified bitumen using fluorescent microscopy and conventional test methods. *Journal of Hazardous Materials;* 150(2): 424-432.

17. Kaya, D., Topal, A., & McNally, T. 2019. Relationship between processing parameters and aging with the rheological behaviour of

SBS modified bitumen. *Construction and Building Materials*; 221, 345-350.

18. Uncu, D, Topal, A, Seydibeyoglu, M O, & Sengoz, B. Investigation of Phase Separation and Storage Stability Behaviour of SBS Polymer Modified Bitumens Containing Sepiolite Nanoclay, 13th International Congress on Advances in Civil Engineering, Izmir, TURKEY, 2018, pp 1-8.

19. Munera, J. C., & Ossa, E. A. 2014. Polymer modified bitumen: Optimization and selection. *Materials & Design* (1980-2015), 62, 91-97.

20. ASTM D2493 "Standard Viscosity-Temperature Chart for Asphalts." American Society for Testing and Materials; West Conshohocken, PA, 2010.

21. Yildirim, Y., Solaimanian, M. and Kennedy. 2000. Mixing and compaction temperatures for hot mix asphalt concrete", Center for Transportation Research, Austin, USA, Rep. 1250-5.

22. Yildirim, Y., Ideker, J., & Hazlett, D. 2006. Evaluation of viscosity values for mixing and compaction temperatures. *Journal of materials in civil engineering;* 18(4): 545-553.

23. Reinke, G. "Determination of Mixing and Compaction Temperature of PG Binders Using a Steady Shear Flow Test," presentation made to the Superpave Binder Expert Task Group,https://engineering.purdue.edu/~spave/old/Technical%20Info/Meetings/Binder%20ETG%20Sept%2003%20Las%20Vegas,%20NV/Reinke_MIX%20AND%20COMPACTINO%20INFO%20FOR%20ETG%209-15-03.pdf.September 2003

Celal Bayar University Journal of Science
Volume 16, Issue 3, 2020, p 269-279
Doi: 10.18466/cbayarfbe.750565

Celal Bayar University Journal of Science

Artificial Intelligence in Building Information Modeling Research: Country and Document-based Citation and Bibliographic Coupling Analysis

Gozde Basak Ozturk[1*] and Mert Tunca[2]

[1,2]Aydın Adnan Menderes University, Civil Engineering Department, Aydın, Turkey
*gbozturk@adu.edu.tr
*Orcid No: 0000-0003-4617-6936

Received: *16 July 2020*
Accepted:*14 September 2020*
DOI: *10.18466/cbayarfbe.750565*

Abstract

The intense association of the architecture, engineering, construction, operation, and facility management (AECO/FM) industry with cognitive and behavioral technologies leads to the increase in productivity of industry activities. In light of these thoughts, the building information modeling (BIM) platform is included in the AECO/FM industry to further increase efficiency and deliver construction projects economically, timely, and safely. While the BIM platform can work integrated with many programs and systems, concepts that offer innovative and fast solutions such as artificial intelligence (AI) benefit the AECO/FM industry. The main aim of this study is to establish an understanding of the tendency of AI in BIM research carried out in different countries and by various scholars. This study adopts a bibliometric search, and a scientometric analysis and mapping approach with applying document-based citation analysis, country-based citation analysis, and country-based bibliographic coupling analysis of scientific research of AI and BIM integration. Data about AI in BIM research has been collected by reviewing and screening articles selected from the Scopus database. The results reveal that information management, decision support systems, genetic algorithms, neural networks, knowledge-based systems, machine learning, and deep learning effect AI in BIM research. This article contributes to the AECO/FM literature by analyzing and visualizing the current status and relationship between AI and BIM. Therefore, the findings highlight the gaps and trends in AI and BIM studies and provide new recommendations for future studies.

Keywords: Artificial Intelligence (AI), Building Information Modelling (BIM), Scientometric Analysis, Scientometric Mapping

1. Introduction

Construction projects face many obstacles such as accidents in construction sites, unreliable complex schedule and cost planning, errors caused by inadequate planning, and lack of collaboration. Building information modeling (BIM) has been utilized in the architecture, engineering, construction, operation, and facility management (AECO/FM) industry to overcome these obstacles. BIM is a platform that adopts a very different design understanding and approach with the use of computer-aided technologies used in the AECO/FM industry. The construction project activities inevitably require BIM to be implemented or greater efficiency improvements and less cost and time lost throughout the project life cycle. A project lifecycle consists of a series of processes that a project goes through from its beginning to its closure. BIM has become more and more widely adopted day by day in the AECO/FM industry. As a result of this, it has begun to change the way the construction project delivered and the facility managed [1]. Thereby, the BIM platform provides fast solutions with the support of interoperability and management. Interoperability enables products, systems, or business processes to work together to carry out a common process [2]. However, to achieve accurate results, BIM requires a good work plan and regulations [3]. Therefore, the BIM platform must be integrated with new technologies such as artificial intelligence (AI), machine learning, the internet of things, and immersive technologies to provide more automated and faster solutions.

AI is a computer science that aims to adopt and apply like human thoughts, learning and perception

capacities, and information storage abilities. AI is an important technology area that helps daily social life and activities and is directed towards the development of information communication technology (ICT) and robot technology (RT). AI creates rational agents that can perceive its environment and act to achieve goals. It develops in a predictable order and achieves its goals by performing analytical and intuitive movements. The tendency in AI research has increased since the mid-20th century, as it provided solutions and applied to a wide range of engineering and science problems. The performance of AI systems in deep learning stages can be used in the classification of big databases, visualization, explanation, and interpretation of their models. Probabilistic scientific data analysis, machine learning, and cognitive science, information theory which explains and interprets how to change the problems between these models, provide access to this area, and with this access, probabilistic programming, optimization, data compression, and automatic modeling occur.

Scientific data analysis is the process of analyzing, cleaning, transforming and modelling data with the aim of finding useful information, informing the results and supporting decision making. Machine learning is a science that deals with the design and development processes of algorithms that enable learning based on data types such as computer sensor data or databases. Cognitive science is an interdisciplinary approach that addresses the functioning of mind and intelligence and explores the dynamics and structures of intelligent systems. Probabilistic programming is a programming paradigm where probability models are specified, and inference is performed automatically for these models. Maximizing or minimizing some functions relative to a set represents a number of options available in a particular situation. Data compression is the process of changing, encoding or converting the bit structure of the data to take up less space. Automated model generation framework is used to identify three nonlinear dynamic benchmark processes. When big data is interpreted with the correct analysis methods, it can enable the strategic decisions to be taken correctly, to manage risk better, and to innovate. Data mining is the study of accessing useful information from large-scale data and mining information. Digital storage is a technology that consists of computer components and the recording medium is used to protect digital data. Data science is a multidisciplinary area that uses scientific methods, processes, algorithms, and systems to obtain information and insights from structured and unstructured data. Knowledge-based Engineering (KBE) can be defined as a program used to develop or query a knowledge base. Fuzzy Logic (FL) is a method of reasoning that is similar to human reasoning. Artificial neural networks (ANN) are an information technology developed by inspiring the information processing technique of the human brain. Genetic algorithms (GE) are search and optimization methods that work in a similar way to the evolutionary process observed in nature and seek the best holistic solution according to the principle of survival of the best in complex multi-dimensional search space. A learning algorithm is a method used to process data to extract patterns appropriate for application in a new situation. In particular, the goal is to adopt a system to a specific input-output transformation task. Semantics is a linguistic and philosophical analysis of the meaning in language, programming languages, formal logic, and semiotics. Indicators relate to what they actually represent, such as words, phrases, signs, and symbols, and the relationship between their expressions.

Artificial intelligence use in the AECO/FM industry has been focused on increasing efficiency. Developing the construction process for decreasing project resources spent through effective planning via autonomous equipment that is aware of their surroundings is used for surveying, gathering site information to create maps, blueprints, and plans. AI also is used for monitoring and controlling tasks, choosing best alternatives, optimizing the processes and results, automation of systems and equipment [4, 5, 10]. AI and machine learning enhanced robots can also be used in dangerous and risky situations. IoT integrated systems offer a safer and efficient processes in both construction and operation of the facility.

The AECO/FM industry, which has experienced a radical revision with BIM adoption, has had the opportunity to integrate the above-mentioned new innovative solutions with utilizing AI. The digital data in a modeled project can be solved for AECO/FM industry by using computational research areas such as big data, data mining, digital storage, and data science. AI is available in AECO/FM industry in project planning tools, building design analysis. It also includes tools of AI methods such as knowledge-based engineering (KBE), fuzzy logic (FL), neural networks, genetic algorithms, learning algorithms, and semantics. AI can provide fast results in many different designs and project submissions and can contain many alternative solutions. As a result of these alternatives, the processes of planning, construction, maintenance, and operation can be improved. The adaption of the AECO/FM industry to the digitalization era is late. However, can provide very effective solutions for the industry. The implementation of AI methods integration to

the BIM platform for construction applications can provide benefits. In the light of the current literature, this article presents important research routes of AI in BIM research for the AECO/FM industry, discussion of the latest trends, and suggestions for future studies. The integration of AI on the BIM platform has already been implementation areas in practical AECO/FM industry activities such as Internet of Things (IoT) integration [6], Historical Building Information Modeling (HBIM) [7], smart energy systems [8], safety, decision support systems [9] and so many others [10].

2. Methodology

In this article, the tendency of AI use in BIM research that was carried out in different countries and by various scholars in the AECO/FM industry was investigated to put forth an overview and understanding by using bibliometric search, scientometric analysis and mapping. The selection of bibliometric search and scientometric analysis and mapping method was made in order to scientifically prove the results based on natural language processing of data from articles gathered by the bibliometric search to be utilized in scientometric analysis and mapping which allowed to empirically analyze the related literature data. The scientometric analysis was done via the document-based citation analysis, country-based citation analysis, and country-based bibliographic coupling analysis. The bibliometric search should be done in one database since there is no any tool to robustly combine the data that is retrieved from more than one database. Therefore, bibliometric search of publications of AI and BIM was performed in Scopus, one of the main search engines for academic research outputs. There are also other established, comprehensive, inclusive, and well-accepted databases. However, the Scopus database covers more journals and more publications than other sources [11]. Scopus uses an API search system that combines keywords with operators to refine the search for getting consolidated and relevant results by using Boolean Syntax. Scientometric mapping is a part of a scientometric analysis that evaluates research policies and processes by using bibliometric data [12]. Scientometric mapping is used to display a research domain's dynamic and structural aspects by defining the relationships among disciplines, fields, and papers [13]. VOSviewer is a tool that is used for visualizing large networks via natural language processing algorithms and text mining techniques and is a commonly used tool in scientometric analysis [14]. This research involves a scientometric mapping and analysis based on bibliometric data obtained by clustering and sequencing combinations of items such as documents and countries. It visualizes, computes, analyzes and explores the AI in BIM research area in the context of the AECO/FM industry. Bibliometric search was applied using the Boolean Syntax with combining words mentioned in Figure 1 via the Scopus database. As a result of this research, 199 results have been reached. Further limitations such as English language and scientific research field restrictions were applied, and the number of files decreased to 195.

```
{artificial intelligence} OR {AI} AND {building information modelling} OR {building information modeling} OR {BIM} OR {building information model} (LIMIT-TO (LANGUAGE, "English")) AND (LIMIT-TO (SUBJAREA, "ENGI") OR LIMIT-TO (SUBJAREA, "COMP") OR LIMIT-TO (SUBJAREA, "SOCI") OR LIMIT-TO (SUBJAREA, "BUSI") OR LIMIT-TO (SUBJAREA, "ENER") OR LIMIT-TO (SUBJAREA, "ENVI") OR LIMIT-TO (SUBJAREA, "DECI") OR LIMIT-TO (SUBJAREA, "MATE" ) OR LIMIT-TO (SUBJAREA, "ARTS") OR LIMIT-TO (SUBJAREA, "MULT"))
```

Figure 1. Bibliometric search input

The VOSviewer software was developed to generate and display scientific measurement results and maps by utilizing natural language processing algorithms based on keyword, journal, author, and document data. In this research, the VOSviewer software was used to analyze and calculate Scopus data using for AI in BIM research. Country-based citation analysis was done to reveal the links of the countries in which the articles were prepared. The minimum number of documents of a country was set to 5, and the minimum number of citations of a country was set to 1. The threshold was reached by 13 countries out of 41. Country-based bibliographic coupling analysis was performed to indicate common references in articles of countries. The minimum number of documents of a country was determined as 5, and the minimum number of citations of a country was set to 1. The threshold was reached by 13 countries out of 41. Document-based citation analysis was done for published

articles and trends of the articles and their belonged cluster was determined. The minimum number of citations of a document was determined as 19 The threshold met by 12 documents out of 185.
A network of items was established in VOSviewer by natural language processing algorithms to explore the relationship between them and to organize the knowledge by using clustering methods [15]. The items were clustered by VOS clustering technique and color-coded in Figures 2, 3, and 4. The color of an item symbolizes the cluster to which it belongs. The clusters are presented in Tables alongside their constituent items (country, document). There can only be one link between two items. The strength of a link is denoted by a positive value. The lower the strength, the weaker the link; the higher the strength, the stronger the link. The strength of a link represents the number of papers in which two items occur together. The meanings of the column headings in Tables are explained below.

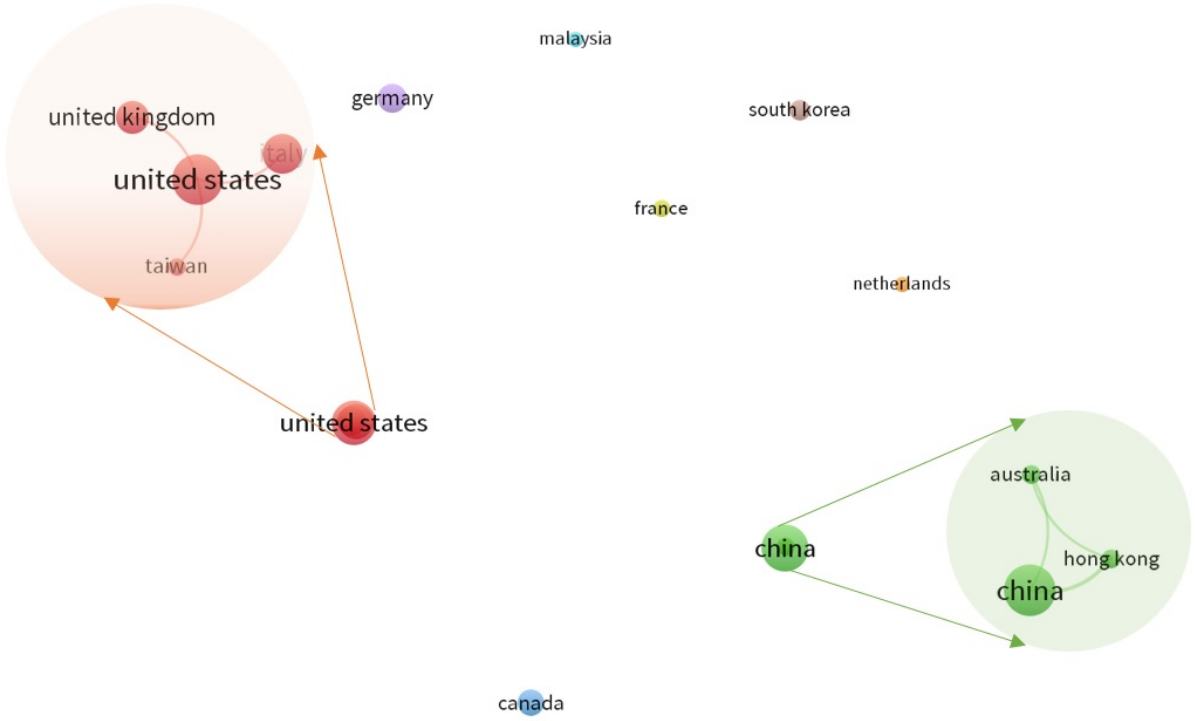

Figure 2. Network visualization map of the country-based citation analysis of AI in BIM research (detailed visual representation of linked countries was zoomed in).

• The number of links between a keyword and other keywords represents the relatedness between the keywords.

• Total link strength demonstrates the strength of the relationship between keywords.

• Average publication year of the papers in which a keyword occurs displays the chronology of a keyword's appearance in the related literature. The more recent the average year published, the newer the keyword is and so is the research subject.

• Average citation represents the total number of citations received by all the papers in which a keyword occurs, divided by the number of papers in which this keyword occurs.

• Average normalized citation indicates the average of the normalized citation for all documents in the set. Normalized citation is calculated by dividing the total number of citations of a paper by the number of citations of papers of the same type. The higher the average normalized citation, the higher the impact on the literature.

3. Findings

3.1. Results of The Country-Based Citation Analysis

The use of AI and BIM together is an approach that is constantly developing with research in different countries. The citation analysis has been made to show the country-based effect on the literature that presents in Figure 2 via VOSviewer, and the scientometric map achieved as a result of the

scientometric analysis. As a result of the analysis, 8 clusters have occurred. Each of the clusters has been shown in a different color. The links among circles, colors, and distance represent the relationship between the country pairs. From these clusters, it is seen that red and green are connected within themselves, while other clusters are separate and distant from each other. The data obtained as a result of the analysis are listed in Table 1. The three countries that publish the most on 'AI in BIM research' are China, the United States, and Italy. Total link strength shows the strength of a country-based research link with other countries. The three highest total link strength valued countries are respectively, the United States, China, and Hong Kong. When the researches of the three countries are examined, it can be seen that modern technology tools are utilized such as computers and sensors, learning systems, information management, automation, and semantic.

Table 1. The country-based citation analysis of AI in BIM research.

Cluster	*Link*	*Total Link Strength*	*Document Numbers*	*Average Publication Year*	*Average Citations*	*Average Normalized Citations*
Research Region 1						
Italy	1	1	19	2017.68	5.16	1.26
Taiwan	1	1	5	2018.20	0.20	0.11
United Kingdom	1	1	14	2016.86	5.29	1.17
United States	3	3	28	2015.68	11.68	1.41
Research Region 2						
Australia	2	2	6	2017.00	6.67	5.61
China	2	3	30	2016.53	7.93	1.17
Hong Kong	2	3	6	2014.50	32.00	2.61
Research Region 3						
Canada	0	0	12	2016.42	4.75	0.73
Research Region 4						
France	0	0	7	2015.71	3.43	0.54
Research Region 5						
Germany	0	0	15	2015.47	8.47	1.86
Research Region 6						
Malaysia	0	0	5	2014.40	9.00	1.49
Research Region 7						
Netherlands	0	0	5	2015.60	1.20	0.20
Research Region 8						
South Korea	0	0	8	2014.88	5.62	0.58

3.2. Results of the country-based bibliographic coupling analysis

The bibliographic coupling demonstrates the conflict in the reference lists. If there is a common citation in both articles, these two articles are bibliographically related. The common reference number of the two articles reflects the strength of the bibliographic match relationship between articles. In this section, bibliographic matching analysis of the countries was applied to see the bibliographic matching relations of the countries. As a result of the analysis, the network visualization map was produced (Figure 3). As seen in the analysis the 3 different colors shown on the map represent the 3 clusters formed. The links and distance between circles represent publishing relations between country couples. The data obtained as a result of country-based bibliographic coupling analysis are listed in Table 2. The total link strength value indicates the strength of the publication relationship between the two countries. The three countries with the highest total link strength value are the China, Germany, and the United Kingdom. Looking at the three most publishing countries are China, United States and Italy, respectively.

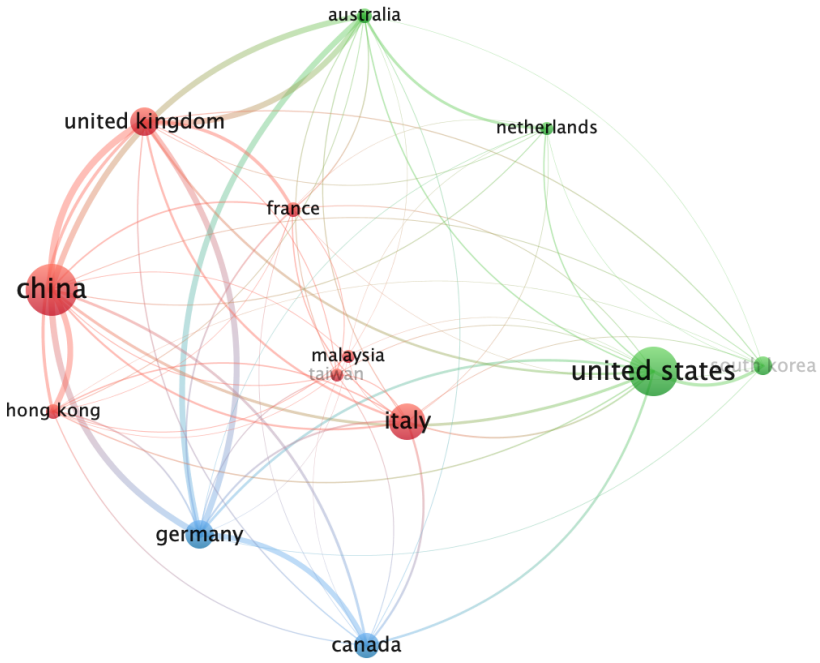

Figure 3. Network visualization map of the country-based bibliographic coupling analysis of AI in BIM research.

Table 2. The country-based bibliographic coupling analysis of AI in BIM research.

Cluster	*Link*	*Total Link Strength*	*Document Numbers*	*Average Publication Year*	*Average Citations*	*Average Normalized Citations*
Research Region 1						
China	12	903	30	2016.53	7.93	1.17
France	11	114	7	2015.71	3.43	0.54
Hong Kong	11	272	6	2014.50	32.00	2.61
Italy	12	139	19	2017.68	5.16	1.26
Malaysia	9	17	5	2014.40	9.00	1.49
Taiwan	10	44	5	2018.20	0.20	0.11
United Kingdom	11	764	14	2016.86	5.29	1.17
Research Region 2						
Australia	12	589	6	2017.00	6.67	5.61
Netherlands	9	61	5	2015.60	1.20	0.20
South Korea	9	73	8	2014.88	5.62	0.58
United States	12	229	28	2015.68	11.68	1.41
Research Region 3						
Canada	10	257	12	2016.42	4.75	0.73
Germany	12	786	15	2015.47	8.47	1.86

3.3. Results of the documents-based citation analysis

The network visualization map was obtained from document-based citation analysis of AI in BIM research, Figure 4 presents the image from the VOSviewer. The lines, colors, and distance between circles show the relationship between the documents' mutual quotes and document pairs. The size of the circle and the fonts show additive of the document to the research area. The large circle reflects that the document contributes more to the research topic. The link, citation, normalized citation and publication year data obtained as a result of the document-based citation analysis are shown in Table 3. The link values represent interconnected articles. The number of citations explains results of the number of times the article was cited as a source in documents to be published by an author. In Table 3, the 12 documents revealed in the analysis are interconnected. The three most cited documents are "Golparvar-Fard et al., 2015" [21], “Chen et al., 2015” [20], and “Teizer, 2015” [27] (Fig. 3 and Table 3).

Golparvar-Fard et al. [21] investigates automated progress monitoring using unordered daily construction photographs and Industry Foundation

Classes-based (IFC-based) building information models. This study shows a new automated understanding of the recognition of physical progress according to the two main sources of information that have emerged. The first is unordered daily construction photo data, collected almost free of charge at all available construction sites. The second is the BIM designs, which are increasingly becoming the binding components of architectural, engineering and construction contracts.

Chen et al. [20] investigates the relation between bridging BIM and building and provides a conceptual structure for bridging the BIM and the building, which emphasizes the importance of real-life information synchronization. The prepared structure is presented in more detail with the prefabricated residential construction in Hong Kong.

Teizer [27] studies the status quo and open challenges in vision-based sensing and tracking of temporary resources on infrastructure construction sites. This study provides an overview of the vision-based sensing technology available for resource monitoring in infrastructure construction sites. Second, it provides research applications by highlighting the case study. Third, it opens a discussion about the current advantages and limitations of visual perception and monitoring.

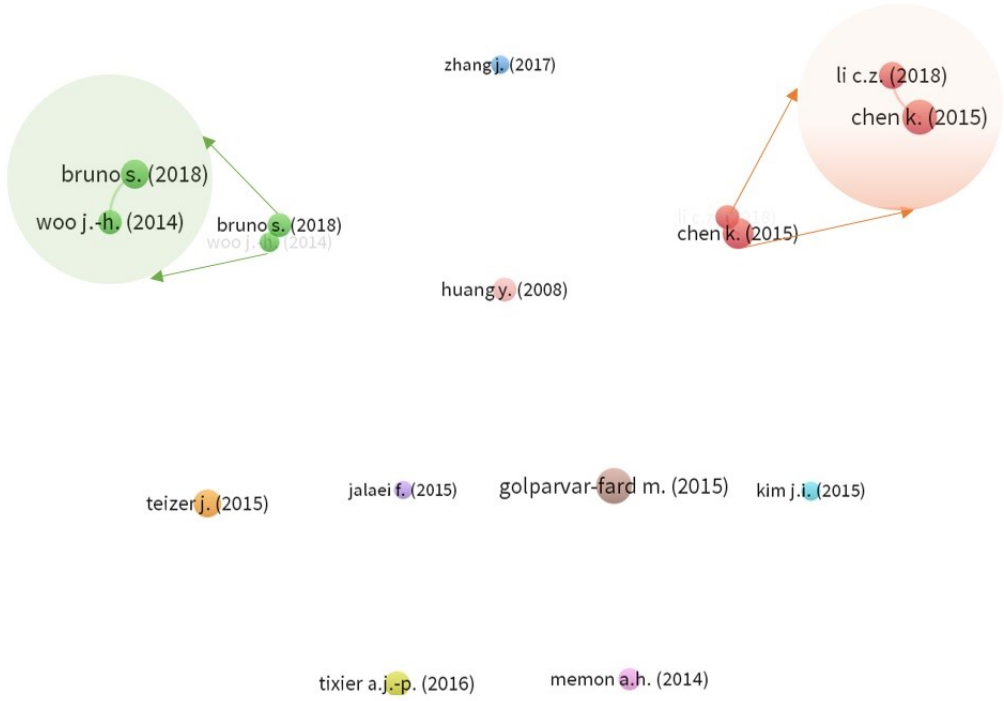

Figure 4. Network visualization map of the document-based citation analysis of AI in BIM research.

Table 3. The document-based citation analysis of AI in BIM research.

Documents	*Link*	*Citation*	*Normalized Citation*	*Publication Year*
Bruno et al., 2018 [31]	1	41	7.88	2018
Chen et al., 2015 [32]	1	81	3.03	2015
Golparvar-Fard et al., 2015 [33]	0	117	4.37	2015
Huang et al., 2008 [34]	0	40	1.67	2008
Jalaei et al., 2015 [35]	0	21	0.78	2015
Kim et al., 2015 [36]	0	24	0.90	2015
Li et al., 2018 [37]	1	42	8.07	2018
Memon et al., 2014 [38]	0	33	4.12	2014
Teizer, 2015 [39]	0	59	2.20	2015
Tixier et al., 2016 [40]	0	47	7.66	2016
Woo et al., 2014 [41]	1	26	3.25	2014
Zhang et al., 2017 [42]	0	21	6.52	2017

4. Discussions

BIM model development and intervention require multiple software use and integration. Considered as a platform, the BIM model requires enhanced systems integration for the AECO/FM industry. Research study on AI in BIM research attracts many researchers as it will be seen as an important factor in the faster adoption of BIM in the AECO/FM industry. As the use of BIM in the AECO/FM industry becomes more common, advances in BIM model technology have increased rapidly due to the needs of stakeholders and consequently, concepts such as AI are included.
BIM research focuses mostly on computer-aided design today. It is extremely important in the AECO/FM industry that the BIM model now moves from a 3D information database to an nD multi-information platform. With this importance, it is thought to produce solutions in management-based studies in the AECO/FM industry since construction management has recently used cognitive technologies in construction project processes. The integration of the BIM model and AI solutions becomes particularly interesting in project management. BIM model integration with real-world instantaneous building data increases the use of model information throughout the life cycle of projects. That is why the BIM model and building information integration can be realized through the AI integration such as using Internet of Things (IoT) sensors.

Information processing and information technology studies on AI integration via interoperability are prioritized in BIM research [11]. In order to integrate the BIM model with metadata that can be interpreted by machine learning, semantic web technology development studies are carried out for use in information management and facility management. As a result of these integrability developments, GIS integration has been provided

and widely used in the BIM model together with deep learning systems. With the developed models, information was used with electronic data exchange tools and the use of information for decision-making systems was at the focal point of recent researches. In addition, thanks to the building automation provided by the AI integrated systems of the BIM model, efforts are made to increase energy efficiency and sustainable that smart building designs that streamline energy use have been frequently encountered in the literature recently [16]..

4.1. Discussions of the country-based citation analysis

Many countries attach importance to studies on AI adaptation and increase their study day by day. The AECO/FM industry is also affected by this increasing trend in recent years. The two countries with the most research were China and the United States. These countries are followed by Italy, Germany, United Kingdom and Canada respectively. South Korea, France, Australia, Hong Kong, Taiwan, Malaysia, and Netherlands follow countries with less research studies than other countries. Especially, the use of information management and decision-making and implementation systems show that countries have begun to develop sustainable methods. New methods, such as semantics and automation, can be a potential to remain permanently for AI utilization in the AECO/FM industry. Countries' study on AI in BIM research contributes to both economic development and sustainable building cycles. It is thought that new methods of using and developing technology so closely can create new conveniences and opportunities in the AECO/FM industry [17, 18]. Since BIM and AI integration is a new and hot topic, the scarcity of studies on their use together is remarkable. The papers within this research's sample were examined in detail and it was seen that new technological methods are used in only a few studies in some countries. The topics that are beginning to be the new trend in the countries are data mining and digital storage. In these studies, methods such as learning systems were used as technological tools. The lack of studies in these areas causes an important gap in the literature. AI and multiple technologies together can be integrated into the BIM platform to achieve sustainability in the AECO/FM industry.

4.2. Discussions of the country-based bibliographic coupling analysis

Countries have started to study various subjects in this area for many different purposes. It is discovered that AI can provide potential benefits in different disciplines within the industry in order to make the project and construction management processes more efficient [4]. For example, there may be many more advantages such as direct prevention of cost overruns, better-designed buildings, and minimizing risk. Countries often introduce new studies by benefiting from each other's work and by making use of joint studies in bibliographic matching. The fact that most countries have little research on AI in BIM research which, shows how hot and promising the topic is in the literature. The leading countries in this regard are China and the United States. The countries that

follow these two countries with their artificial intelligence studies and are in the development stages are Italy, Germany, United Kingdom and Canada. South Korea, France, Australia, Hong Kong, Taiwan, Malaysia, and the Netherlands are the countries that have fewer research studies in this field compared to other countries. When the studies are examined in detail, it can be seen from the links that countries proceed with by publishing together or citing each other's articles. There are not many publications yet about approaches to BIM and AI integration. New job opportunities can be created because there is little implementation on this subject. In this sense, the use of highly critical technologies such as AI within the AECO/FM industry demonstrates the fact that it may enable sustainability in construction in the future by influencing the change in the processes, techniques, equipment, and work routines.

4.3. Discussions of the document-based citation analysis

The fact that technology is a constantly and rapidly improving scientific research branch, it has led to the emergence of many specialties and disciplines in the AECO/FM industry. AI individually contributed to the research in construction [4, 5, 6, 7, 8, 9, 10, 16, 17, 18]. The papers within this research's sample were in detail, the influential articles contain subjects such as information management, information technologies, and semantics. Since there are a lot of complex information and data, it becomes obvious that AI should be on the focus of researchers for the improvements in the industry. Studies focus on big data, digital storage and IFC as a result of the need for data flow and storage needs. In addition, there are many application areas that are practiced and preferred in the industry namely; preventing cost exceed, minimizing risk, operations and facility management, and energy performance estimation [5, 6, 7, 8, 9, 10, 16, 17, 18]. The study of the different specialties and disciplines is accepted to be independent of each other in groups. Integration into the BIM platform is a new phenomenon, as AI is a broad area. Therefore, it makes it difficult for AI to be examined as a whole in the AECO/FM industry as part of the BIM technology.

4.4. Gaps and trends

Integrated use of BIM and AI is still a very new and hot topic. Information management and decision support systems are the subjects where BIM and AI studied intensively. In this process, data are collected by obtaining different opinions from many specialties such as architecture, engineering, and computer science. Studies resulting from the collection of data generate complex information and independent from each other. These complexities and problems can be avoided and can be collected and processed in a single environment by using AI. Providing a common space with BIM to work together can help to resolve information clutter. The information obtained can be modeled at the nD level using the BIM platform. AI can prevent time loss and ensure complete storage of information. Computer science, which offers great potential for integrated solutions, is used in some countries very effectively such as in the USA and China. These two countries are followed by Italy, Germany, England and Canada with their constantly developing works. Also, although South Korea, France, Australia, Hong Kong, Taiwan, Malaysia and the Netherlands have fewer research studies than other countries, their future work is expected to increase. The study contributes to the AECO/FM industry literature by analyzing and visualizing the current situation of AI in BIM research.

5. Conclusion

In this study, it is aimed to reveal the scientific tendency related to the AI in BIM research and to explain the research orientation in different countries. Combining and developing AI and BIM research areas reduces cost, time, and increases productivity [16]. Therefore, a scientometric analysis and mapping of bibliometric data have been done by country-based citation analysis, document-based citation analysis, and country-based bibliographic coupling analysis thanks to VOSviewer software. As seen in the analysis of the countries, 8 regions were revealed. There are 12 documents found as the result of document-based citation analysis. The analysis revealed that interconnected documents study in similar areas and 8 independent documents contain publications from different specialties. The idea of the integrated operation of BIM and AI is the idea of creating intelligent systems that can help learn and solve problems quickly. In the AECO/FM industry, AI provides advantages to deal with complex engineering, management, and implementation issues, unlike solutions based on traditional computing and design methods [4, 5, 6, 7, 8, 9, 10, 16, 17, 18]. As a result of these advantages, it aims to solve many problems faster by integrating into the BIM platform throughout the design, construction, operation, and facility management processes throughout the project life cycle. In many countries, mainly China, the USA, and Italy actively use BIM and AI with a processable structure. It has been observed that it increases productivity and efficiency, especially in information management and decision-making

system organization. As seen in the document-based citation analysis independent examination of the research fields makes it difficult to examine the studies with a holistic view. Apart from being a new and hot topic, the complexity of the wide range of research areas and scarcity of studies in the field can create difficulties. However, in the future, the use of technology platforms for integration in BIM and AI processes can ensure the interoperable information management systems used for different areas of expertise and benefit from the study of different perspectives can yield efficiency. Although the high contribution of this study to figure out the research tendency in different countries, it has limitations such as the time period of the data acquisition causes a static output, further analysis need, the Scopus' coverage of all publications, and so on. The findings of this research provide a broad understanding of the current research approach, research gaps, and future research trends of AI in BIM research for the AECO/FM industry.

Author's Contributions

Gozde Basak Ozturk: Drafted and wrote the manuscript, performed the analyses, and result interpretation.
Mert Tunca: Drafted and wrote the manuscript, performed the analyses, and result interpretation.

Ethics

There are no ethical issues after the publication of this manuscript.

References

1. Liu Z, Lu Y, Peh L C (2019) A review and scientometric analysis of Global Building Information Modeling (BIM) Research in the Architecture, Engineering and Construction (AEC) industry. Buildings, 9, 10 DOI: 10.3390/buildings9100210.

2. Ganzha M, Paprzycki M, Pawłowski W, Szmeja P, Wasielewska K (2017) Semantic interoperability in the Internet of Things: An overview from the INTER-IoT perspective. *Journal of Network and Computer Applications*, 81, 111-124 DOI: 10.1016/j.jnca.2016.08.007.

3. Aljobaly O, Banawi A (2020) Evaluation of the Saudi Construction Industry for Adoption of Building Information Modelling. *Advances in Artificial Intelligence, Software and Systems Engineering*. 488-498 DOI: 10.1007/978-3-030-20454-9_49.

4. Parveen, R. (2018). Artificial intelligence in construction industry: Legal issues and regulatory challenges. International *Journal of Civil Engineering and Technology*, 9(13), 957-962.

5. Guzmán, J.I. And Malcolm, A.A. (2002) "Autonomous vehicles in the construction process", *Construction Innovation*, Vol. 2 Issue: 3, pp.211- 224, https://doi.org/10.1108/14714170210814775.

6. Li, C. Z., Xue, F., Li, X., Hong, J., and Shen, G. Q. (2018). An internet of things-enabled BIM platform for on-site assembly services in prefabricated construction. *Automation in Construction*, 89, 146-161. doi:10.1016/j.autcon.2018.01.001.

7. Bruno, S., De Fino, M., and Fatiguso, F. (2018). Historic building information modelling: Performance assessment for diagnosis-aided information modelling and management. *Automation in Construction*, 86, 256-276. doi:10.1016/j.autcon.2017.11.009.

8. O'Dwyer, E., Pan, I., Acha, S., and Shah, N. (2019). Smart energy systems for sustainable smart cities: Current developments, trends and future directions. *Applied Energy*, 237, 581-597. doi:10.1016/j.apenergy.2019.01.024.

9. Hwang, B., Shan, M., and Looi, K. (2018). Knowledge-based decision support system for prefabricated prefinished volumetric construction. *Automation in Construction*, 94, 168-178. doi:10.1016/j.autcon.2018.06.016.

10. Sacks, R., Girolami, M., Brilakis, I. (2020). Building Information Modelling, Artificial Intelligence and Construction Tech, Developments in the Built Environment, 100011, ISSN 2666-1659, https://doi.org/10.1016/j.dibe.2020.100011.

11. Ozturk, G.B. Interoperability in building information modeling for AECO/FM industry. *Automation in Construction*, 2020, 113, 103122. https://doi.org/10.1016/j.autcon.2020.103122.

12. Xu, Y.; Zeng, J.; Chen, W.; Jin, R.; Li, B.; and Pan, Z. (2018). "A holistic review of cement composites reinforced with graphene oxide", *Construction Building Materials,* Vol. 171, pp.291–302. https:// doi.org/10.1016/j.conbuildmat.2018.03.147.

13. Cobo, M.J.; López-Herrera, A.G.; Herrera-Viedma, E.; and Herrera, F. (2011). "An approach for detecting, quantifying, and visualizing the evolution of a research field: a practical application to the fuzzy sets theory field", *Journal of Informetrics*, Vol. 5 No. 1, pp.146-166. https:// doi.org/10.1016/j.joi.2010.10.002.

14. Hosseini, M.R.; Martek, I.; Zavadskas, E.K.; Aibinu, A.A.; Arashpour, M.; and Chileshe, N. (2018). "Critical evaluation of off-site construction research: a scientometric analysis", *Automation in Construction*, Vol. 87, pp.235–247. https://doi.org/10.1016/j.autcon.2017.12. 002.

15. Van Eck, N.J. and Waltman, L. (2014). "Visualizing bibliometric networks", in: Y. Ding, R. Rousseau, & D. Wolfram (Eds.), Measuring Scholarly Impact: Methods and Practice, Springer, Cham, pp. 285–320. http://dx.doi.org/10.1007/978-3-319-10377-8_13.

16. Natephra, W., Yabuki, N., and Fukuda, T. (2018). Optimizing the evaluation of building envelope design for thermal performance using a BIM-based overall thermal transfer value calculation. *Building and Environment*, 136, 128-145. doi:10.1016/j.buildenv.2018.03.032.

17. Parra, J., Pérez-Pons, M., and González, J. (2021). Technology as a lever for the evolution and recovery of the financial and construction sectors in Spain doi:10.1007/978-3-030-53829-3_17.

18. Khairulzaman, H. A., and Usman, F. (2018). Automation in civil engineering design in assessing building energy

efficiency. International *Journal of Engineering and Technology*, 7(4), 722-727. doi:10.14419/ijet.v7i4.35.2309.

19. Bruno S, Fino M D, Fatiguso F (2018) Automation in Construction Historic Building Information Modelling: performance assessment for diagnosis-aided information modelling and management. *Automation in Construction*. 86, December 2017, 256-276 DOI: 10.1016/j.autcon.2017.11.009.

20. Chen K, Lu W, Peng Y, Rowlinson S, Huang G Q (2015) Bridging BIM and building: From a literature review to an integrated conceptual framework. *International Journal of Project Management.* 33, 6, 1405-1416 DOI: 10.1016/j.ijproman.2015.03.006.

21. Golparvar-Fard M, Peña-Mora F, Savarese S (2015) Automated Progress Monitoring Using Unordered Daily Construction Photographs and IFC-Based Building Information Models. *Journal of Computing in Civil Engineering*. 29, 1 DOI: 10.1061/(ASCE)CP.1943-5487.0000205.

22. Huang Y, Huang K, Wang L, Tao D, Tan T, Li X (2008) Enhanced biologically inspired model. IEEE Conference on Computer Vision and Pattern Recognition. DOI: 10.1109/CVPR.2008.4587599.

23. Jalaei F, Canada C, Jrade A (2015) Integrating decision support system (DSS) and building information modeling (BIM) to optimize the selection of sustainable building components *Journal of Information Technology in Construction,* 20, 399-420 DOI: itcon.org/2015/25.

24. In J, Kim J, Fischer M, Orr R (2015) Automation in Construction BIM-based decision-support method for master planning of sustainable large-scale developments. *Automation in Construction*, 58, 95-108 DOI: 10.1016/j.autcon.2015.07.003.

25. Liu R, Yang B, Zio E, Chen X (2018) Artificial intelligence for fault diagnosis of rotating machinery: A review. *Mechanical Systems and Signal Processing*, 108, 33-47 DOI: 10.1016/j.ymssp.2018.02.016.

26. Memon A H, Rahman I A, Memon I, Azman N I A (2014) BIM in Malaysian Construction Industry: Status, Advantages, Barriers and Strategies to Enhance the Implementation Level. Research *Journal of Applied Sciences, Engineering and Technology*, 606-614 DOI: airitilibrary.com/Publication/alDetailedMesh?docid=20407467-201408-201502170022-201502170022-606-614.

27. Teizer J (2015) Status quo and open challenges in vision-based sensing and tracking of temporary resources on infrastructure construction sites. *Advanced Engineering Informatics,* 29, 2, 225-238 DOI: 10.1016/j.aei.2015.03.006.

28. Tixier A J, Hallowell M R, Rajagopalan B, Bowman D (2016) Automation in Construction Application of machine learning to construction injury prediction. *Automation in Construction*, 69, 102-114 DOI: 10.1016/j.autcon.2016.05.016.

29. Woo J, Menassa C (2014) Virtual Retrofit Model for aging commercial buildings in a smart grid environment. *Energy and Buildings*, 80, 424-435 DOI: 10.1016/j.enbuild.2014.05.004.

30. Zhang J, El-gohary, N M (2017) Automation in Construction Integrating semantic NLP and logic reasoning into a unified system for fully-automated code checking. *Automation in Construction*, 73, 45-57 DOI: 10.1016/j.autcon.2016.08.027.

Celal Bayar University Journal of Science

Investigation of The Effect of Aggregate Type on Concrete Cost: Example of Adıyaman

Kadir Güçlüer[1*], Osman Günaydın[2], Samet Göymen[3]

[1]Vocational School of Technical Science, Department of Construction, Adıyaman University, Adıyaman, Turkey
[2]Faculty of Engineering, Department of Civil Engineering, Adıyaman University, Adıyaman, Turkey
[3]Graduate School of Natural and Applied Science, Department of Civil Engineering, Adıyaman University, Adıyaman, Turkey
*kgucluer@adiyaman.edu.tr
*Orcid No: 0000-0001-7617-198X

Received: *29 April 2020*
Accepted: *14 September 2020*
DOI: *10.18466/cbayarfbe.729086*

Abstract

Concrete is a building material that is considered as a granular composite. The factor in its acceptance as granular is the aggregate in its content. In addition to forming the vast majority of aggregate concrete volume, it is also extremely important in the development of strength and durability factors. Although cement is the most costly input of concrete, it can affect the cost of concrete in changes in aggregate type. For this purpose, in this study, concrete samples were produced with different types of aggregates from different quarries operating in Adıyaman province. Only the type of aggregate was changed, and cost calculations were made, provided that the cement type and amount and other components in the mixture remained constant. In addition, cost and strength comparisons were made by measuring compressive strength values for 7 and 28 days. It has been determined that with the change of aggregate type, cost and compressive strength value change.

Keywords: Concrete, Aggregate, Cost, Adıyaman.

1. Introduction

Concrete is the most used building material in the world. An average of 10 billion tons of concrete is produced annually in the world. This value is estimated to reach 18 billion tons annually by 2050 [1-6].

Aggregates are the main component that covers the volume of concrete at about 70-80%. Therefore, aggregates are expected to have a significant impact on concrete properties. At the same time, choosing the appropriate aggregate for the type of structure to be produced changes the cost of concrete and structure. The choice of aggregate type in concrete production is a determining factor for concrete quality. Concretes produced with the use of aggregates with the same type and quality cement as well as aggregates with different textural properties and mineralogy may differ, especially the compressive strength [7-12].

There are studies in the literature examining how aggregate variability affects the properties of concrete. Güçlüer [13] determined that the textural properties of aggregate in concrete produced with 3 different types of aggregates, and especially the surface roughness factor, varies in the compressive strength values, and higher compressive strength value are obtained in concretes produced with aggregates with high surface roughness.
Beshr et al. [14] conducted mechanical measurements on concretes produced with aggregates in 4 different mineralogies in their study. They found that aggregate quality was directly related to concrete compressive strength. Özturan and Çeçen [15] stated that the compressive strength value of the concrete test samples produced with different types of aggregates vary depending on the textural and mechanical properties of the aggregate. Yılmaz and Tuğrul [16] found that the strength of concrete produced with different types of coarse aggregate is affected by aggregate mineralogy and surface roughness.
Ahmed and Alghamdi [17] state that in the concrete they produce with basalt and limestone aggregates, the

Celal Bayar University Journal of Science
Volume 16, Issue 3, 2020, p 281-284
Doi: 10.18466/cbayarfbe.729086

compressive strength values of concrete with limestone aggregates are higher than those with basalt aggregates.

For this purpose, in this study, natural (NS) and crushed (CS) stone aggregates obtained from two different aggregate quarries in Adıyaman province and concrete experiment samples were produced. Besides the effects of aggregates on cost, their effects on compressive strength were also investigated.

2. Materials and Methods

CEM I 42.5 R type Portland cement compliant with TS EN 197-1 [18] was used as binder in the study. Physical properties and chemical components of cement are given in Tables 1 and 2.

Table 1. Chemical component of cement.

Oxide	CaO	SiO_2	Fe_2O_3	Al_2O_3	MgO	SO_3	K_2O	LOI
Cement	62,63	19,29	4,25	3,88	3,42	2,58	0,34	2,86

Table 2. Physical properties of cement.

Properties		Results
Specific gravity (g/cm^3)		3.09
Setting time	Firstly (min)	125
	Finish (min)	190
Blaine fineness (cm^2/g)		3420

One of the aggregates obtained from the aggregate quarry is natural stone aggregate and the other is crushed stone aggregate. Physical properties of these two types of aggregates are given in Table 3.

Table 3. Physical properties of aggregate.

Aggregate	Specific Gravity (g/cm^3)	Water Absorption (%)
Natural Stone Aggregate	2.42	2.48
Crushed Stone Aggregate	2.44	3.00

The aggregates to enter the concrete mixture are prepared according to the method of saturation of dry water. The same consistency value was taken as the basis for both aggregate types and the amount of water was arranged according to this value. In addition, it is aimed that the concrete produced from both aggregates will show resistance in accordance with the C30/37 class. Naphthalene sulfonate-based superplasticizer chemical additive was used to facilitate workability in concrete mixtures. Concrete mixing ratios are made according to TS EN 206-1[19] and slump value of 15cm is targeted for both mixtures (Table 4). Compressive strength tests were carried out on concrete samples that were kept in the cure pool for 7 and 28 days in accordance with the TS EN 12390-3 [20] standard on cube samples with 15 cm edges.

Table 4. Concrete mix ratio for $1m^3$.

Aggregate Type	Cement (kg)	0-5mm Aggregate (kg)	5-15 mm Aggregate (kg)	15-22 mm Aggregate (kg)	Water (kg)	SP (kg)
NS Aggregate	308	944	366	626	169	4.6
CS Aggregate	318	988	338	595	175	4.1

The cost calculations of the materials used as concrete components were made according to the unit price method. The unit prices are based on the values used in the enterprises operating in the Adıyaman region.

3. Results

3.1 Compressive Strength Results

7 and 28 days compressive strength findings of concrete experimental samples produced using natural and crushed stone aggregates are given in Figure 1.

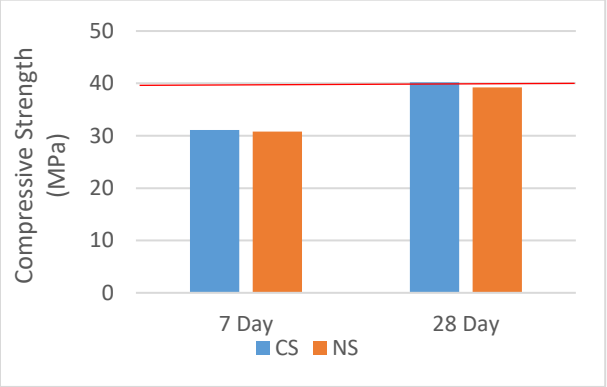

Figure 1. Measured value of compressive strength of concrete samples.

Higher values were determined in the compressive strength data of concrete produced with crushed stone aggregates compared to concrete produced with natural aggregate.

Although there is no effective increase in 7-day curing period, after 28 days curing period, 2.5% increase in the compressive strength value of concrete produced with crushed stone aggregate was found compared to concrete produced with natural stone aggregate. The fact that crushed stone aggregates have higher surface roughness and strengthened adhesion in the cement-aggregate interface area may have been effective in this situation. Aspect ratio and roundness in aggregates are important textural features and are thought to be effective in strength. As the roundness value of the aggregates approaches 1, a perfect roundness is mentioned. The aspect ratio briefly describes the elongation of aggregates (Figure 2).

Celal Bayar University Journal of Science
Volume 16, Issue 3, 2020, p 281-284
Doi: 10.18466/cbayarfbe.729086

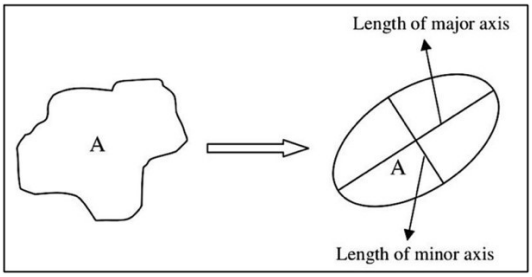

Figure 2. Schematic representation of the aspect ratio [21].

In Figure 3, images of samples taken from natural and crushed stone aggregate pile are given. The roundness of natural aggregates is seen better than crushed stone aggregates. In the study conducted by Güçlüer [7], it was determined that the aspect ratio values of crushed stone aggregates are higher than the natural aggregate and the compressive strength values of the samples produced with crushed stone aggregate are higher. This information supports the higher compressive strength of concrete samples produced with crushed stone aggregates compared to concrete samples produced with natural aggregates.

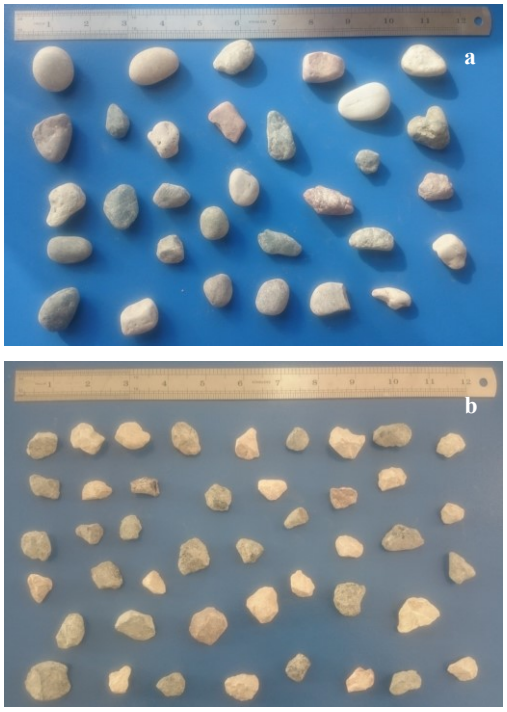

Figure 3. Natural stone aggregate (a), crushed stone aggregate (b).

3.2 Cost Results

Mix ratios and cost calculations of the mixture together with unit prices for C30/37 class concretes produced with natural and crushed stone aggregates are given in Tables 5 and 6.

Cost advantage for C30/37 class concrete produced with natural and crushed stone aggregates has been determined in concretes produced with natural aggregate. When the cost values are examined, the cost of concrete produced with natural aggregate is 10.99% lower than the cost of concrete produced with crushed stone aggregate.

Table 5. Cost rates for natural stone aggregate.

Concrete Class C30/37	Amount (kg)	Unit Price (TL/ton)	Price (TL)
Natural sand 0-5mm	944	₺16,68	₺ 15,75
Natural stone aggregate 15-22,4mm	626	₺16,68	₺ 10,44
Natural stone aggregate. 5-15mm	366	₺16,68	₺ 6,11
Water	169	₺7,20	₺ 1,22
CEM I 42.5 R	308	₺200,00	₺ 61,60
SP	4,6	₺2.000,00	₺ 9,20
Total			**104,31**

*SP= Superplasticizer

However, this situation is inversely proportional to the compressive strength values. Although the cost of concrete produced with crushed stone aggregate is high, compressive strength values are determined higher.

Table 6. Cost rates for crushed stone aggregate.

Concrete Class C30/37	**Amount (kg)**	**Unit Price (TL/ton)**	**Price (TL)**
Crushed sand 0-5mm	988	₺ 22,24	₺ 21,97
Crushed stone aggregate 15-22,4mm	595	₺ 22,24	₺ 13,23
Crushed stone aggregate 5-15mm	338	₺ 22,24	₺ 7,52
Water	175	₺ 7,20	₺ 1,26
CEM I 42.5 R	318	₺ 200,00	₺ 63,60
SP	4,1	₺ 2.000,00	₺ 8,20
Total			**115,78**

Table 7. Aggregate cost ratios in concrete.

Concrete Class C30/37	Aggregate Price (TL)	Percentage of aggregate cost(%)	Concrete Price (TL)
NS aggregate	₺32,30	30,96	₺ 104,31
CS aggregate	₺42,72	36,89	₺ 115,78

Aggregate based cost percentages are given in Table 7. The cost of aggregate in concrete produces with CS aggregate is higher than the cost of aggregate in concrete produced with NS aggregate

4. Conclusion

In the scope of Adıyaman province, the following conclusions have been reached with the research in which the cost analysis of the concrete produced with natural and crushed stone aggregates is made;

•The cost of concrete produced with natural stone aggregate is cheaper than concrete produced with crushed stone aggregate.

•The compressive strength values of concrete produced with crushed stone aggregates are higher than those produced with natural stone aggregate.

• When these data are limited to Adıyaman province, it can be said that concrete production with natural aggregate may be less costly. However, the use of crushed stone aggregates can be recommended at points where strength and durability axis expectations are taken into consideration.

Parameters such as raw material supply, distances of the quarry and concrete batching plant to each other can directly affect the cost of concrete. In this sense, it may be beneficial for the literature and concrete industry to carry out similar studies on different regions.

Author's Contributions

Kadir Güçlüer: Drafted and wrote the manuscript, performed the experiment and result analysis.
Osman Günaydın: Assisted in analytical analysis on the structure, supervised the experiment's progress, result interpretation and helped in manuscript preparation.
Samet Göymen: Assisted in analytical analysis on the structure, result interpretation and helped in manuscript preparation.

Ethics

There are no ethical issues after the publication of this manuscript.

References

1. Meyer, C, 2009. The greening of the concrete industry, *Cement& Concrete Composite*. 31: 601–605.

2. Mehta, P.K, Monteiro, P. Concrete: Microstructure, Properties, and Materials*;* McGraw-Hill Publishing: New York, NJ, USA, 2006, pp 21-47.

3. Ghorbani, S, Sharifi, S, Ghorbani, S, Tam, V, Brito, J.D, Kurda, R, 2019. Effect of crushed concrete waste's maximum size as partial replacement of T natural coarse aggregate on the mechanical and durability properties of concrete, *Resources, Conservation & Recycling*, 149: 664–673.

4. Neville, A.M. Properties of concrete: 5th edition, Pearson: England, 2011, pp 17-267.

5. Alexander, M., Mindess, S. Aggregates in concrete: Taylor and Francis: England, 2010, pp 16-65.

6. Thomas M.D.A, Folliard, K.J, Concrete aggregates and the durability of concrete: Page C.L, and Page M.M (ed) Durability of concrete and cement composites, CRC Press, England, 2007, pp 247-277

7. Petrounias, P, Giannakopoulou, P.P, Rogkala, A, Stamatis, P.M, Tsikouras, B, Papoulis, D, Lampropoulou, P, Hatzipanagiotou, K, 2018. The influence of alteration of aggregates on the quality of the concrete: A case study from serpentinites and andesites from central Macedonia (North Greece), *Geosciences*, 8:115.

8. Yilmaz, M, Turul, A, 2012. The effects of different sandstone aggregates on concrete strength, *Construction and Building. Mater*ials, 35: 294–303.

9. Mays G. Durability of concrete structures: Taylor and Francis, England, 2003, pp 3-9.

10. Khatib M.J. Sustainability of construction materials: CRC Press, England, 2009, pp 2-20.

11. Shetty M.S. Concrete technology theory and practice: S. Chand Company Ltd., India, 2005, pp 66-118.

12. Erdoğan T. Beton: ODTÜ Yayıncılık, Türkiye, 2015, pp 66-115.

13. Güçlüer, K, 2020. Investigation of the effects of aggregate textural properties on compressive strength (CS) and ultrasonic pulse velocity (UPV) of concrete, *Journal of Building Engineering* , 27: 100949.

14. Beshr, H, Almusallam, A, Maslehuddin, M, 2003. Effect of coarse aggregate quality on the mechanical properties of high-strength concrete, *Construction and Building Materials*, 17:97–103.

15. Ozturan, T, Cecen, C, 1997. Effect of coarse aggregate type on mechanical properties of concretes with different strengths, *Cement and Concrete Research,* 27:165–170.

16. Yilmaz, M, Turul, A, 2012. The effects of different sandstone aggregates on concrete strength, *Construction and building Materials*, 35:294–303.

17. Ahmad, S, Alghamdi, S.A, 2012. A study on effect of coarse aggregate type on concrete performance. *Arabian Journal of Science and Engineering*, 37:1777–1786.

18. TS EN 197–1, Çimentoların Bileşim, özellikler ve uygunluk Kriterleri, Türk Standartları Enstitüsü, Ankara, 2002.

19. TS EN 206-1, Beton-Bölüm 1: Özellik, performans, imalat ve uygunluk, Türk Standartlar Enstitüsü, Ankara, 2002.

20. TS EN 12390–3, Beton-Sertleşmiş beton deneyleri-Deney numunelerinde basınç dayanımı tayini, Türk Standartlar Enstitüsü, Ankara, 2003.

21. Kahraman, S, Alber M, Fener, M, Gunaydın, O, 2008. Evaluating the geomechanical properties of Misis fault breccia (Turkey), *International Journal Rock Mechanics and Mining Sciences,* 45: 1469–1479.

Celal Bayar University Journal of Science

Copper Nanoparticles Supported on a Schiff base-Fullerene as Catalyst for Reduction of Nitrophenols and Organic Dyes

Serkan Dayan*

Drug Application and Research Center, Erciyes University, 38039 Kayseri, Turkey
*serkandayan@erciyes.edu.tr
*Orcid No: 0000-0003-4171-7297

Received: *26 May 2020*
Accepted: *14 September 2020*
DOI: *10.18466/cbayarfbe.742711*

Abstract

The *N*-(3-((2-hydroxybenzylidene)amino)phenyl)benzamide Schiff base ligand (L) was synthesized and characterized. The ligand was immobilized on the fullerene material with a reduction copper material. The resulting nanocomposite Cu/Ligand@Fullerene (**M$_1$**) was characterized by FE-SEM EDX, EDX mapping, FT-IR, and XRD techniques and tested as a catalyst for reduction of nitrophenols (2-nitrophenol (2-NP), 4-nitrophenol (4-NP)) and organic dyes (methylene blue (M.B.), Rhodamine B (Rh B)) under ambient temperature in water. The catalytic conversions and the reaction rate constant per total weight of the **M$_1$** catalyst were recorded as 89.9% at 300 s for 2-nitrophenol, 97.9% at 300 s for 4-nitrophenol, 90.6% at 360 s for Rhodamine B, and 98.3% at 60 s for methylene blue. For 4-NP, the reusability study was carried out as five cycles between 97.9% - 87.3% conversions, respectively. The fabricated Cu/Ligand@Fullerene (**M$_1$**) nanocomposite has good catalytic efficiency and reusability, low cost, and easy to produce.

Keywords: Copper nanoparticle, Schiff base, Reduction, Nitrophenol, Organic Dyes.

1. Introduction

Nitro compounds and organic dyes are currently used in many industries and pose a serious threat to environmental pollutants and the phenomenon of disposal of these wastes stands out as a serious situation. Also, amino compounds formed by the reduction of these compounds can be used as starting or intermediate chemicals in many application areas [1-3]. These application areas can be listed as chelating agents in pharmaceuticals, polymers, pesticides, explosives, fibers, dyes, and cosmetics, etc. [4-10]. The reduction reactions are among the frequently used reactions as in the past. To provide better catalytic conditions in the reduction reactions, both the efficiency of the catalyst must be good, and it can be easily produced. In this context, many metals (copper [11], cobalt [12], palladium [13], ruthenium [3], silver [14], nickel [15], etc.) have been used as catalysts in nanoparticle reduction reactions. Copper nanoparticles can be seen as preferred materials in many aspects especially in recent years [16, 17]. Copper nanomaterials, which are also frequently used in immobilization processes, are also widely used as catalysts [18, 19]. The catalysts obtained from the immobilization of copper nanoparticles with Schiff base ligands have also been used in reduction reactions and the successful results have been obtained [20, 21]. Both Schiff base compounds and the copper nanoparticles are often preferred because they are easy to manufacture, synthesize with high yields, and are readily available. In this work, the Cu/Ligand@Fullerene (**M$_1$**) nanocomposite was fabricated with immobilization methodology as a catalyst by fullerene support material, Schiff base ligand, and copper nanoparticles. The nanocomposite **M$_1$** was used in the reduction of nitrophenols and some organic dyes under ambient temperature with $NaBH_4$ as a hydrogen source in water. The catalytic results were quite promising for this type of nanocomposite in the reduction reactions.

2. Materials and Methods

All the chemicals and solvents were purchase from chemical manufacturers. In the FT-IR analysis was used a Perkin Elmer 400 FT-IR/FT-FIR Spectrometer Spotlight 400 Imaging System to confirm the molecular interaction between Fullerene and ligand and reduced copper nanoparticles. For NMR analyses was used a Bruker 400. The FE-SEM, EDX, and mapping employed a Zeiss GeminiSEM 500 for surface morphological characterization and mapping analysis.

X-ray diffraction (Malvern panalytical XRD) was used to confirm for immobilization and reduction methodology. The UV-vis spectrophotometer (Shimadzu UV-2700) measurements were used for monitoring the reduction of nitrophenols and dyes.

2.1. Experimental

2.1.1. Synthesis of Schiff base ligand (L)

In a typical reaction, the 1,3-diaminobenzene (0.25 mmol) and benzoyl chloride (0.25 mmol) compounds were reacted in THF (10 ml). After the reaction, the mixture was filtered-dried and added to 2-hydroxy-benzaldehyde (0.25 mmol in methyl alcohol (15 ml) was stirred for Schiff base ligand formation overnight. After the process, the solvent was removed by a vacuum system. The residue was dissolved in ethyl alcohol (5 ml) and the microcrystalline product in the refrigerator was filtered off and dried in the vacuum system (Figure-1).

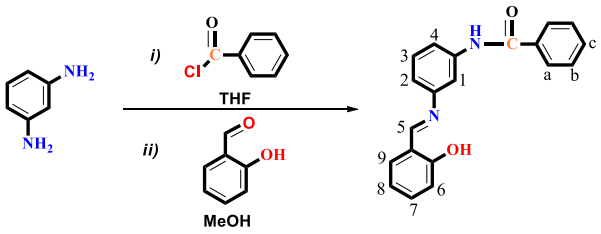

Figure-1. The numbering synthesis scheme for Schiff base ligand (L).

2.1.2. Founded Data for the ligand

For Schiff base ligand (L)

N-(3-((2-hydroxybenzylidene)amino)phenyl)benzamide: **Color**: Yellow. **Yield**: 73 %. **^{1}H-NMR ($CDCl_3$, δ ppm):** 6.94-7.50 (6H, -H_c, -H_7, -H_6, -H_4, -H_3, -H_2), 7.53 (d, 2H, J=8 Hz, -H_a), 7.58 (d, 2H, J=8 Hz, -$H_{8,9}$), 7.80 (s, 1H, -H_1), 7.90 (d, 2H, J=8 Hz, -H_b), 8.68 (s, 1H, -H_5), 13.19 (1H, -O*H*). **^{13}C-NMR ($CDCl_3$, ppm):** 112.5, 117.3, 117.9, 118.3, 119.2, 119.9, 127.0 (-C_a), 128.9 (-C_b), 129.9, 132.1, 132.5, 133.4, 134.7, 139.0, 149.3, 161.2, 163.2 (-N=*C*H), 165.8 (-*C*=O). **FT-IR (cm^{-1}):** 3308, 3127, 3106, 3083, 3057, 3038, 3010, 2986, 2938, 2881, 1647, 1620, 1596, 1574, 1525, 1490, 1479, 1456, 1447, 1430, 1403, 1359, 1315, 1303, 1294, 1277, 1259, 1215, 1201, 1180, 1155, 1150, 1113, 1087, 1074, 1026, 1002, 983, 963, 924, 909, 886, 861, 852, 837, 800, 793, 756, 711, 690, 678, 655, 608, 582, 572, 551, 541, 510, 485, 472. **ESI–MS (-) (m/z):** 316.200 (calc: 316.121).

2.1.3. Fabrication of Cu/Ligand@Fullerene nanocomposite (M_1)

The synthesis process of Cu/Ligand@Fullerene nanocomposite (**M_1**) materials followed the route: 20 % (w/w) of ligand and 80 % (w/w) of Fullerene (C60) as adsorbent material was added to a schlenk tube (25 ml) as separately with organic solvent media (2-propanol / diethyl ether, 5 / 1) and sonicated for 3 hours to form a stable suspension. Then, the organic solvents were removed by the vacuum system, and the residue was dissolved again with methyl alcohol (10 ml) and added to $CuCl_2.2H_2O$ (20 mg) and $NaBH_4$ as a reducing agent [22]. The mixture was stirred and sonicated for 3 hours to a stable form. Also, the precipitated materials were subjected to the following operations in sequence: filtering, washing with methanol and water and drying process at ambient temperature (Figure-2). After that, the nanocomposite was characterized by FT-IR, XRD, and FE-SEM-EDX and mapping.

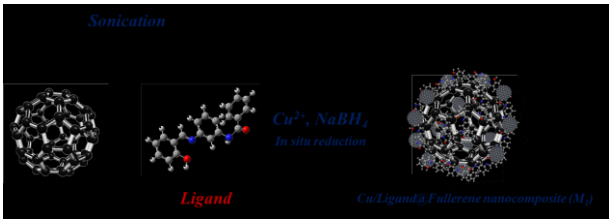

Figure-2. Fabrication of Cu/Ligand@Fullerene nanocomposite (**M_1**).

2.1.4. Catalytic Reduction of Nitrophenols and Organic Dyes

The catalytic efficiency of **M_1** was examined for the reduction of 2-nitrophenol, 4-nitrophenol, methylene blue, rhodamine B in the presence of BH_4^- ion as a hydrogen source in the aqueous solution at ambient temperature. In a typical reaction, 2.5 mg of the **M_1** catalyst was added to nitrophenols and dyes and $NaBH_4$ (0.03 M, freshly, optimum concentration [12, 23]) in water (10 ml) at ambient temperature and stirred for a period of the desired time. Importantly, the catalytic reaction started instantly after the addition of the catalyst. At the end of the catalytic period followed, the reaction samples are taken from the reaction and filtered through the micro-column with cotton. The catalytic efficiency of the **M_1** catalyst was seen by comparing the bands which appeared and disappeared after reduction on the UV-vis spectrum.

3. Results and Discussion

3.1. Characterizations

The fabrication process of *N*-(3-((2-hydroxybenzylidene)amino)phenyl)benzamide (**L**) and Cu/Ligand@Fullerene (**M_1**) compounds were explained in the Figure-1 and experimental section.

In the FT-IR spectra of the bare fullerene were observed the specific 1427, 1180, 960, 738, 574, 524 cm^{-1} peaks. For the ligand, the *O-H*, the aromatic *C-H*, the aliphatic -*C-H* stretching, the -*C=O* bond, and the -*CH=N*- bond vibrations were aligned at 3308, 3127 – 3106, 3010 – 2881, 1647, and 1620, respectively. Also, the peaks of the FT-IR spectrum belonging to Cu/Ligand@Fullerene (**M_1**) was founded as 3662, 2987, 2971, 2901, 1644,

Celal Bayar University Journal of Science
Volume 16, Issue 3, 2020, p 285-291
Doi: 10.18466/cbayarfbe.742711

1601, 1518, 1472, 1449, 1406, 1394, 1382, 1323, 1250, 1242, 1230, 1181, 1075-1066-1057 (Cu-OH-), 1028, 897 (CuO), 892, 793, 710, 693 (CuO), 575, 525, 502, 493, 471, 459 cm^{-1}. When the spectrum of nanocomposite was examined, the presence of peaks originating from both ligand and fullerene structure was determined and the comparative spectrums are given in Figure-3.

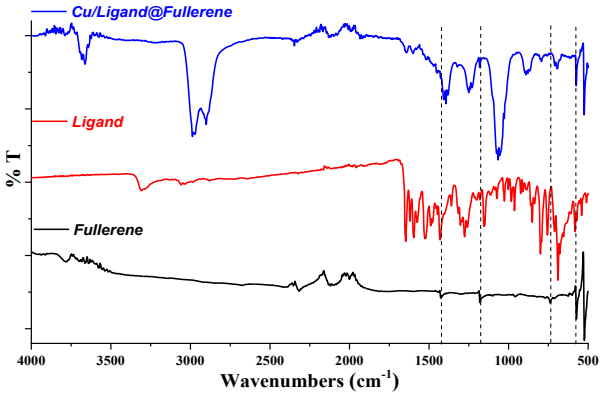

Figure-3. FT-IR comparative spectra of Fullerene, Ligand, and Cu/Ligand@Fullerene nanocomposite (**M1**).

The XRD peaks and (hkl) of bare fullerene (C60) were observed as 10.79° (111), 17.67° (220), 20.74° (311), 21.69° (222), 27.38° (331), 28.12° (420), 30.85° (422), 32.79° (511). For Cu/Ligand@Fullerene nanocomposite (**M1**), the XRD peaks were founded as 6.61°, 9.00°, 10.76° (Fullerene-111), 12.21°, 13.81°, 14.70°, 17.67° (Fullerene-220), 19.56°, 20.74° (Fullerene-311), 21.69° (Fullerene-222), 23.37°, 25.13°, 25.49°, 27.41° (Fullerene-331), 28.12° (Fullerene-420), 30.82° (Fullerene-422), 32.77° (Fullerene-511), 35.63°, 37.05°, 41.64°, 42.30°, 45.74°.

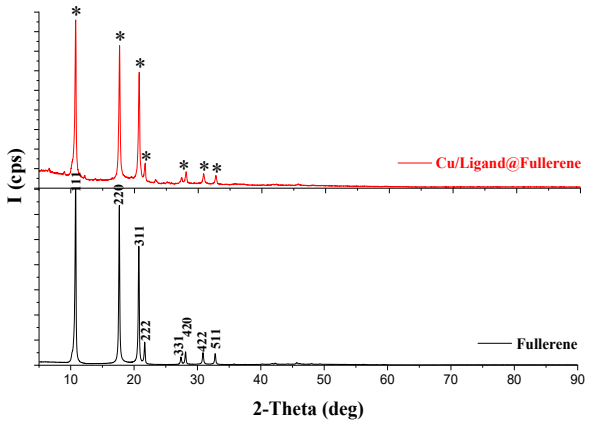

Figure-4. XRD comparative patterns of Fullerene, Cu/Ligand@Fullerene nanocomposite (**M1**).

According to the obtained XRD pattern data, the fabricated nanocomposite contains characteristic peaks originating from fullerene as well as peaks originating from ligand and metal was founded (Figure-4).

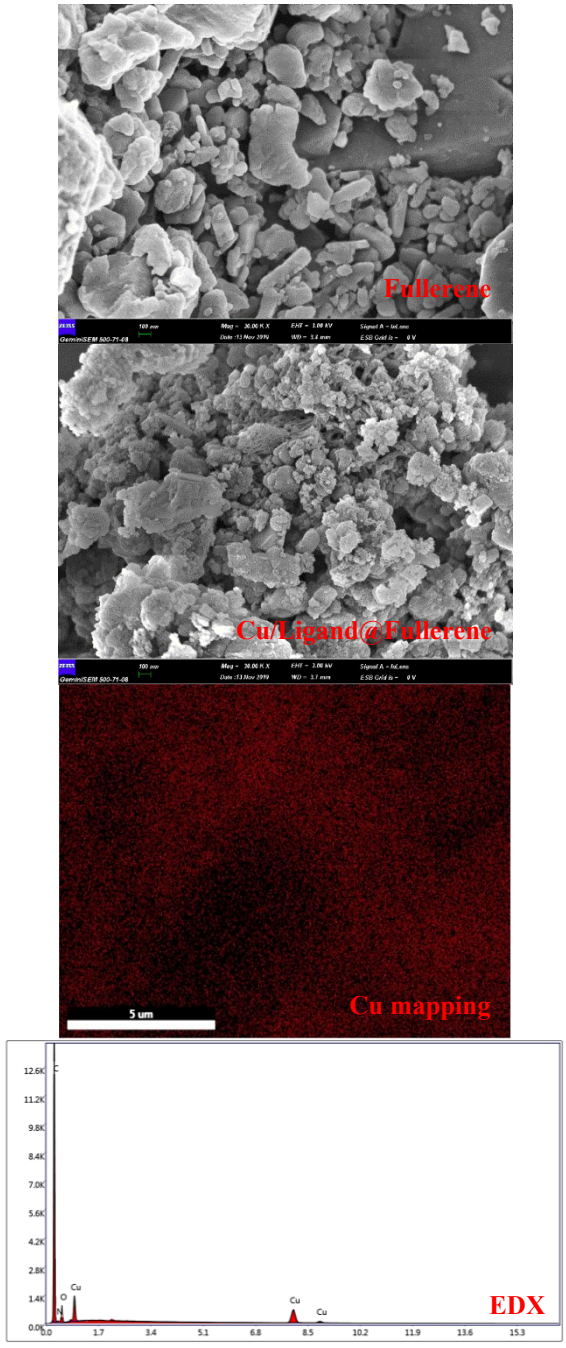

Figure-5. SEM-EDX (30.00 KX) analysis and copper mapping images of Cu/Ligand@Fullerene nanocomposite (**M1**).

The FE-SEM, EDX, and Cu mapping analysis of Cu/Ligand@Fullerene nanocomposite (**M1**) was achieved, and the surface morphologies and elemental images are given in Figure-5. The surface structures of the bare fullerene and **M1** nanocomposite (30.00 KX zoom) are similar, but the material deposits from ligand and copper on the fullerene layers were observed. The presence of copper metal (Cu weight: ≈7.00% with EDX analysis) dispersed Cu/Ligand@Fullerene nanocomposite (**M1**) was approved by the EDX and copper mapping methods. Each sheet was shown to

Celal Bayar University Journal of Science
Volume 16, Issue 3, 2020, p 285-291
Doi: 10.18466/cbayarfbe.742711

have a length of 20 – 500 nm. The surface analyses show that the immobilization and metal reduction process was successfully performed (Figure-5).

3.2. Catalytic Studies

We investigated the catalytic efficiency of **M1** nanocomposite by using the reduction of 2-nitrophenol (2-NP), 4-nitrophenol (4-NP) as nitrobenzenes, methylene blue, and rhodamine B as organic dyes in the presence of $NaBH_4$ in the water at ambient temperature. The catalytic reaction was monitored spectrophotometrically due to the 2-nitrophenol (2-NP) reactant and product having different absorption bands such as λ_{max}= 414 nm (-NO_2 group of 2-NP). Firstly, the 2-nitrophenol ($5x10^{-4}$ M) mixture has a yellow colour which is the colour of the adsorption band belonging to the 2-nitrophenolate, this colour gradually vanished because of the formation of the 2-aminophenol and the catalytic conversions were seen at different times between 30 s to 300 s. The catalytic activity of **M1** nanocomposite was achieved as 34.2%, 73.1%, and 89.9% at the end of 30, 90, and 300 s, respectively (Figure-6).

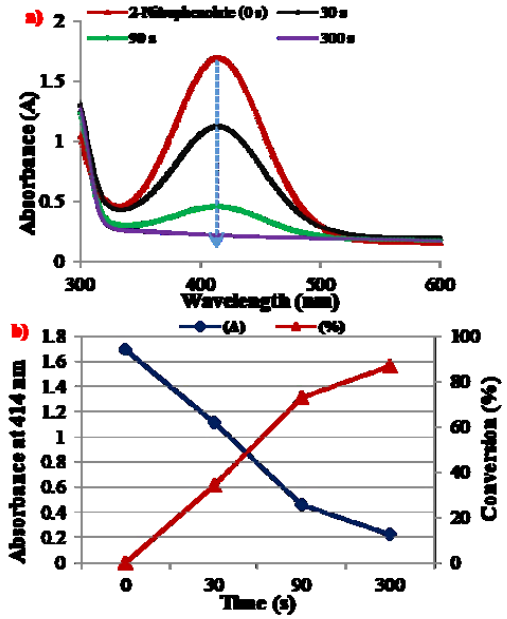

Figure-6. Time-dependent UV–vis absorption spectra of the 2-nitrophenol ($5.0x10^{-4}$ M) reduced by $NaBH_4$ catalyzed by the **M1** nanocomposite (a) UV-vis spectra, b) Absorbance-Conversion curve).

We have also worked the reduction of 4-nitrophenol ($2.5x10^{-4}$ M, 4-NP) by **M1** nanocomposite under likewise reaction conditions. The absorption band of the 4-nitrophenolate arises at 398 nm from the –NO_2 (nitro) group to -NH_2 (amine) group. The catalytic conversion results were obtained to be 51.2% (30 s), 59.1% (90 s), 97.9% (300 s) for **M1** nanocomposite (Figure-7).

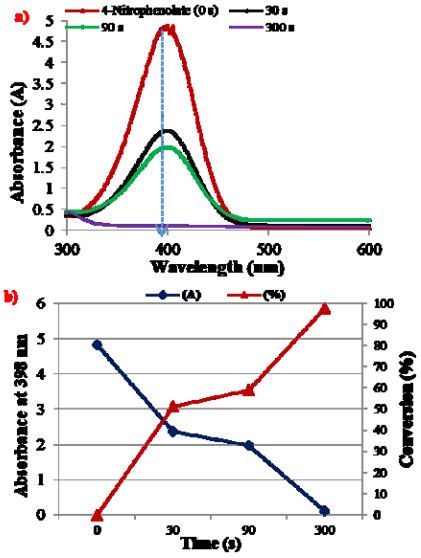

Figure-7. Time-dependent UV–vis absorption spectra of the 4-nitrophenol ($2.5x10^{-4}$ M) reduced by $NaBH_4$ catalyzed by the **M1** nanocomposite (a) UV-vis spectra, b) Absorbance-Conversion curve).

Moreover, the Cu/Ligand@Fullerene **M1** nanocomposite was used as catalysts for the reduction of some dyes (methylene blue (MB) and rhodamine B) under the optimized conditions. The adsorption band disappeared after reduction at 664 nm for MB, 550 nm for Rhodamine B. The catalytic conversions were founded as 91.6% (30 s), 98.3% (60 s) for MB dye, 67.3% (120 s), 83.5% (240 s), 90.6% (360 s) for Rhodamine B (Figure-8,9).

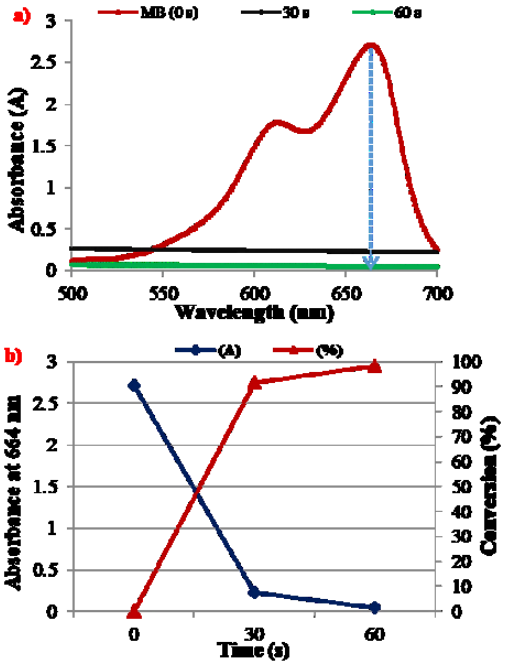

Figure-8. Time-dependent UV–vis absorption spectra of the methylene blue ($5.0x10^{-5}$ M) reduced by $NaBH_4$ catalyzed by the **M1** nanocomposite (a) UV-vis spectra, b) Absorbance-Conversion curve).

Celal Bayar University Journal of Science
Volume 16, Issue 3, 2020, p 285-291
Doi: 10.18466/cbayarfbe.742711

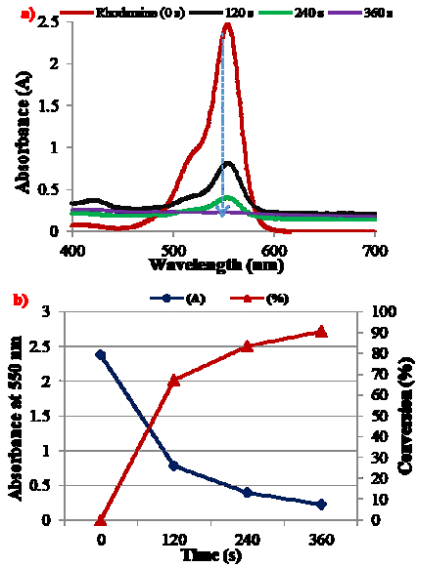

Figure-9. Time-dependent UV–vis absorption spectra of the Rhodamine B (10 ppm) reduced by $NaBH_4$ catalyzed by the **M_1** nanocomposite (a) UV-vis spectra, b) Absorbance-Conversion curve).

Summarize, the kinetic equation for the reduction of nitrophenols and dyes can be represented as $\ln(C_t/C_0) = -kt$, where t is time for the catalytic reaction and, k is the apparent first-order rate constant (s^{-1}) in Table-1. Moreover, the k' = k/M parameter (M: the amount of the catalyst) is introduced for quantitative comparison and the parameter is defined as the ratio of the rate constant k to the weight of the catalyst added [24]. In Table-1, the catalytic activity rate constant parameters were compared for the nanocomposite (**M_1**).

The reaction rates of nitrophenols with catalyst M_1 at 300 s were recorded as 6.78E-03 s^{-1} (2-NP) and 1.28E-02 s^{-1} (4-NP) and for dyes, the rates were founded as 6.80E-02 s^{-1} at 60 s (M. Blue) and 6.58E-03 s^{-1} at 360 s (Rhodamine B).

A mixture of 4-nitrophenol, rhodamine B, and methylene blue substrates was prepared to better demonstrate the effectiveness of the catalyst, and their reduction with the **M_1** catalyst was observed. In the results, after 300 seconds, the **M_1** catalyst was able to reduce all three substrates >90%, simultaneously (Figure10).

Table 1. The catalytic efficiency rate constant of **M_1** catalysts.

Substrate	k (s^{-1})[a]			k/M (s^{-1} g^{-1})[b]		
2-NP	*30 s*	*90 s*	*300 s*	*30 s*	*90 s*	*300 s*
	1.39E-02	**1.46E-02**	**6.78E-03**	**5.57E+00**	**5.83E+00**	**2.71E+00**
4-NP	*30 s*	*90 s*	*300 s*	*30 s*	*90 s*	*300 s*
	2.39E-02	**9.95E-03**	**1.28E-02**	**9.58E+00**	**3.98E+00**	**5.12E+00**
M. Blue	*30 s*		*60 s*	*30 s*		*60 s*
	8.26E-02		**6.80E-02**	**3.30E+01**		**2.72E+01**
Rhodamine B	*120 s*	*240 s*	*360 s*	*120 s*	*240 s*	*360 s*
	9.31E-03	**7.52E-03**	**6.58E-03**	**3.72E+00**	**3.01E+00**	**2.63E+00**

[a] The reaction rate constant. [b] The reaction rate constant per total weight of tested catalyst (2.5 mg).

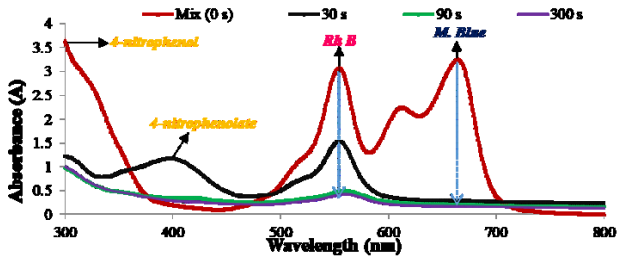

Figure-10. Time-dependent UV–vis absorption spectra of 4-NP, Rh B, and M. Blue reduced by $NaBH_4$ catalyzed by the **M_1** nanocomposite.

To determine the efficiency of the catalyst, a reusability study was carried out. The 4-nitrophenol was chosen as the model substrate and the Cu/Ligand@Fullerene (**M_1**) catalyst was used 5 times in the same reaction (Figure-11). The reusability results (I – V) were recorded as 97.9%, 97.7%, 97.7%, 97.3%, and 87.3%, respectively. According to the reusability results, the efficiency of the catalyst was determined to be good and suitable for economic purposes.

The production costs are as important as the catalytic activities of the catalysts produced. As is known, the copper nanoparticles can be manufactured in many easy routes. At the same time, their catalytic activities can be increased by creating hybrids with many materials.

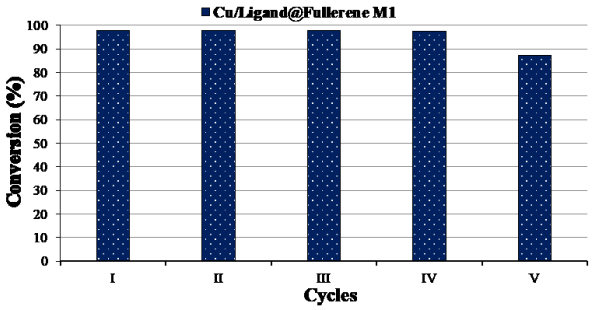

Figure-11. Catalytic activities of Cu/Ligand@Fullerene (**M_1**) nanocomposite in 5 cycles.

It can be said that the catalytic activity results in this study are at a good level compared to their peers in the literature (Table-2).

Considering the substrate concentrations in the solution, it can be said that the **M1** nanocomposite shows the highest activity with 2-nitrophenol. However, the good catalytic results with **M1** nanocomposite were obtained for other substrates and it is well known that dyes such as nitrophenols and methylene blue, especially Rhodamine B, are serious environmental pollutants. The removal of these compounds is very important, and, in this study, it was determined that a material that can be easily produced reduces these harmful compounds with high activity.

Table 2. The comparative data of the reduction reactions.

Catalyst	Substrate	Time (s)	Catalytic rate constant "k" (s^{-1})	References
AG-CuO hydrogel	2-Nitrophenol	*420*	5.11E-03	[25]
Cu^0-NPANI-$ZrSiO_4$	2-Nitrophenol	*120*	9.73E-03	[26]
Cu/Ligand@Fullerene	2-Nitrophenol	*300*	6.78E-03	*Present study*
CuO NPs	4-Nitrophenol	*360*	8.80E-02	[11]
Cu@Pd NPs	4-Nitrophenol	*720*	5.80E-03	[27]
Cu/Ligand@Fullerene	4-Nitrophenol	*300*	1.28E-02	*Present study*
CuVOS-3	M. Blue	*480*	1.21E-02	[28]
C@Cu	M. Blue	60	8.90E-2	[29]
Cu/Ligand@Fullerene	M. Blue	*60*	6.80E-02	*Present study*
CuVOS-3	Rhodamine B	*480*	1.55E-02	[28]
TEA1.5-G150°C-CuO150°C	Rhodamine B	210	4.70E-02	[30]
Cu/Ligand@Fullerene	Rhodamine B	*360*	6.58E-03	*Present study*

4. Conclusion

Herein, we have reported the fabrication of *N*-(3-((2-hydroxybenzylidene)amino)phenyl)benzamide (**L**) ligand and Cu/Ligand@Fullerene nanocomposite (**M1**) nanocomposite, and the **M1** nanocomposite was tested as a catalyst in the reduction of nitrophenols (2-NP, 4-NP) and organic dyes (M. Blue, Rhodamine B). The fabricated nanocomposite **M1** is highly efficient in the reduction of nitrophenols (2-NP, 4NP) (>90% catalytic conversion in 5 min.), M. blue (>90% catalytic conversion in 0.5 min.), and Rhodamine B (> 90% catalytic conversion in 6 min.) at ambient temperature. In this study, the advantages such as the ease of synthesis, high activity results, and easy workability of the produced material came to the fore.

Author's Contributions

Serkan Dayan: Drafted and wrote the manuscript, performed the experiment and result analysis.

Ethics

There are no ethical issues after the publication of this manuscript.

References

1. Xu, YL, Shi, XF, Hua, R, Zhang, R, Yao YJ, Zhao, B, Liu, T, Zheng, JZ, Lu, G. 2020. Remarkably catalytic activity in reduction of 4-nitrophenol and methylene blue by Fe_3O_4@COF supported noble metal nanoparticles. *Applied Catalysis B: Environmental*; 260.

2. Yang, YT, Wang, TA, Jing, XF, Zhu, GS. 2019. Phosphine-based porous aromatic frameworks for gold nanoparticle immobilization with superior catalytic activities. *Journal of Materials Chemistry A*; 7(16): 10004-10009.

3. Dayan, S, Arslan, F, Ozpozan, NK. 2015. Ru(II) impregnated Al_2O_3, Fe_3O_4, SiO_2 and N-ecoordinate ruthenium(II) arene complexes: Multifunctional catalysts in the hydrogenation of nitroarenes and the transfer hydrogenation of aryl ketones. *Applied Catalysis B: Environmental*; 164: 305-315.

4. Dell'Anna, MM, Intini S, Romanazzi, G, Rizzuti, A, Leonelli, C, Piccinni, F, Mastrorilli, P. 2014. Polymer supported palladium nanocrystals as efficient and recyclable catalyst for the reduction of nitroarenes to anilines under mild conditions in water. *Journal of Molecular Catalysis A*; 395: 307-314.

5. Hu, XW, Long, Y, Fan, MY, Yuan, M, Zhao, H, Ma, JT, Dong, ZP. 2019. Two-dimensional covalent organic frameworks as self-template derived nitrogen-doped carbon nanosheets for eco-friendly metal-free catalysis. *Applied Catalysis B: Environmental*; 244: 25-35.

6. Shokouhimehr, M, Kim, T, Jun, SW, Shin, K, Jang, Y, Kim, BH, Kim, J, Hyeon, T. 2014. Magnetically separable carbon nanocomposite catalysts for efficient nitroarene reduction and Suzuki reactions. *Applied Catalysis A: General*; 476: 133-139.

7. Das, P, Ghosh, S, Baskey, M. 2019. Heterogeneous catalytic reduction of 4-nitroaniline by RGO-Ni nanocomposite for water resource management. *Journal of Materials Science: Materials in Electronics*; 30: 19731-19737.

8. Qu, YM, Chen, T. 2020. Fullerene derivative supported Ni for hydrogenation of nitrobenzene: Effect of functional group of fullerene derivative. *Chemical Engineering Journal*; 382: 122911.

9. Liu, Q, Tadrent, S, Proust, C, Gomez, F, Khelfa, A, Luart, D, Len, C. 2020. Theoretical analysis of the "green" synthesis of

aniline by reduction of nitrobenzene. *Chemical Engineering Science*; 211: 115275.

10. Du, JT, Shi, J, Sun, Q, Wang, D, Wu, H, Wang, JX, Chen, JF. 2020. High-gravity-assisted preparation of aqueous dispersions of monodisperse palladium nanocrystals as pseudohomogeneous catalyst for highly efficient nitrobenzene reduction. *Chemical Engineering Journal*; 382: 122883.

11. Baloch, GNL, Mahesar, SA, Khan, S, Niisar, J, Sherazi, STH. 2020. Ranolazine-functionalized CuO NPs: efficient homogeneous and heterogeneous catalysts for reduction of 4-nitrophenol, Turkish Journal of Chemistry; 44 (1): 168-179.

12. Dayan, S, Altinkaynak, C, Kayaci, N, Dogan, SD, Özdemir, N, Ozpozan, NK. 2020. Hybrid nanoflowers bearing tetraphenylporphyrin assembled on copper(II) or cobalt(II) inorganic material: A green efficient catalyst for hydrogenation of nitrobenzenes in water. *Applied Organometallic Chemistry*; 34 (3): e5381.

13. Hira, SA, Nallal, M, Park, KH. 2019. Fabrication of PdAg nanoparticle infused metal-organic framework for electrochemical and solution-chemical reduction and detection of toxic 4-nitrophenol. *Sensors and Actuators B: Chemical*; 298: 126861.

14. Shahini, P, Ashkarran, AA. 2018. Immobilization of plasmonic Ag-Au NPs on the TiO_2 nanofibers as an efficient visible-light photocatalyst. *Colloids and Surfaces A*; 537: 155-162.

15. Mahnaz, F, Mostafa-Al-Momin, M, Rubel, M, Ferdous, M, Azam, MS. 2019. Mussel-inspired immobilization of Au on bare and graphene-wrapped Ni nanoparticles toward highly efficient and easily recyclable catalysts. *RSC Advances*; 9 (52): 30358-30369.

16. Li, CX, Wang, JK, Jiang, ZH, Hu, PG. 2015. Co/Cu_2O assisted growth of graphene oxide on carbon nanotubes and its water splitting activities. *New Journal of Chemistry*; 39 (6): 4562-4567.

17. Jiang, JW, Lim, YS, Park, S, Kim, SH, Yoon, S, Piao, L. 2017. Hollow porous Cu particles from silica-encapsulated Cu_2O nanoparticle aggregates effectively catalyze 4-nitrophenol reduction. *Nanoscale*; 9 (11): 3873-3880.

18. Taherinia, Z, Ghorbani-Choghamarani, A. 2019. Cu(I)-PNF, an organic-based nanocatalyst, catalyzed C-O and C-S cross-coupling reactions. *Canadian Journal of Chemistry*; 97 (1): 46-52.

19. Singh, G, Rani, S, Arora, A, Sanchita, Duggal, H, Mehta, D. 2017. Organic-inorganic nano-hybrid decorated by copper (II) incarceration: A versatile catalytic assembly for the swift reduction of aromatic nitro and dye compounds. *Molecular Catalysis*; 431: 15-26.

20. Ahmadi, A, Sedaghat, T, Motamedi, H, Azadi. R. 2020. Anchoring of Cu (II)-Schiff base complex on magnetic mesoporous silica nanoparticles: catalytic efficacy in one-pot synthesis of 5-substituted-1H-tetrazoles, antibacterial activity evaluation and immobilization of alpha-amylase. Applied Organometallic Chemistry; 34 (5) e5572.

21. Tahmasbi, L, Sedaghat, T, Motamedi, H, Kooti, M. 2018. Mesoporous silica nanoparticles supported copper(II) and nickel(II) Schiff base complexes: Synthesis, characterization, antibacterial activity and enzyme immobilization. *Journal of Solid State Chemistry*; 258: 517-525.

22. Ramu, VG, Bordoloi, A, Nagaiah, TC, Schuhmann, W, Muhler, M, Cabrele, C. 2012. Copper nanoparticles stabilized on nitrogen-doped carbon nanotubes as efficient and recyclable catalysts for alkyne/aldehyde/cyclic amine A(3)-type coupling reactions. *Applied Catalysis A: General*; 431: 88-94.

23. Dayan, S, Kayaci, N, Dayan, O, Ozdemir, N, Ozpozan, NK. 2020. Nickel (II) complex $[NiCl_2(DMF)_2L_2]$ bearing diaminobenzene and sulfonamide: Crystal structure and catalytic application in the reduction of nitrobenzenes. *Polyhedron*; 175: 114181.

24. Baghbamidi, SE, Hassankhani, A, Sanchooli, E, Sadeghzadeh, SM. 2018. The reduction of 4-nitrophenol and 2-nitroaniline by palladium catalyst based on a KCC-1/IL in aqueous solution. *Applied Organometallic Chemistry*; 32 (4): e4251.

25. Kamal, T. 2019. Aminophenols formation from nitrophenols using agar biopolymer hydrogel supported CuO nanoparticles catalyst. *Polymer Testing*; 77: 105896.

26. Mahmoud, ME, Amira, MF, Abouelanwar, ME, Seleim, SM. 2020. Catalytic reduction of nitrophenols by a novel assembled nanocatalyst based on zerovalent copper-nanopolyaniline-nanozirconium silicate. *Journal of Molecular Liquids*; 299: 112192.

27. Li, ML, Chen, GF. 2013. Revisiting catalytic model reaction p-nitrophenol/NaBH4 using metallic nanoparticles coated on polymeric spheres, *Nanoscale*; 5 (23):11919-11927.

28. Sun, HZ, Zelekew, OA, Chen, XY, Guo, YB, Kuo DH, Lu, QX, Lin, JG. 2019. A noble bimetal oxysulfide CuVOS catalyst for highly efficient catalytic reduction of 4-nitrophenol and organic dyes. *RSC Advances*; 9 (55): 31828-31839.

29. Ahsan, MA, Jabbari, V, El-Gendy, AA, Curry, ML, Noveron, JC. 2019. Ultrafast catalytic reduction of environmental pollutants in water via MOF-derived magnetic Ni and Cu nanoparticles encapsulated in porous carbon. *Applied Surface Science*; 497: 143608.

30. Liang, X, Chen, XW, Xiang, ZL, Yan, R, Xi, H, Bian, T, Zhang, JJ, Zhao, JX, Cai, QH, Wang, HX. 2018. Design and synthesis of surface-controlled CuO_x/rGO nanocomposites with unusually high efficiency in catalytic conversion of organic reactants in the presence of $NaBH_4$. *Applied Surface Science*; 459: 716-722.

Celal Bayar University Journal of Science

Synthesis and Characterization of Barium Titanate Nanopowders by Pechini Process

Pelin Sözen Aktaş*

*Manisa Celal Bayar University, Faculty of Arts and Sciences, Department of Chemistry, 45140 Muradiye-Manisa, Turkey
*pelin.sozen@cbu.edu.tr
*Orcid No: 0000-0003-2140-2650

Received: *8 May 2020*
Accepted: *14 September 2020*
DOI: *10.18466/cbayarfbe.734061*

Abstract

Barium titanate ($BaTiO_3$) is the first known ferroelectric ceramics and a suitable candidate for various applications due to its unique dielectric, ferroelectric and piezoelectric properties. It is well known that $BaTiO_3$ powder features strongly depend on the synthesis route and heat-treatment conditions. In the present study, $BaTiO_3$ nanoparticles have been synthesized via the Pechini method, using barium acetate and an aqueous solution of titanium(IV) (triethanolaminato) isopropoxide. The starting materials are stable in an aqueous environment, and $BaTiO_3$ can be efficiently prepared at an industrial scale. The structural properties of $BaTiO_3$ were characterized by X-ray diffraction (XRD), Rietveld refinement, scanning electron microscopy (SEM), energy dispersive X-ray spectrometry (EDX), thermogravimetric analysis (TGA) and Fourier-transform infrared spectroscopy (FT-IR). XRD and Rietveld refinement studies revealed that $BaTiO_3$ has a cubic structure with a space group of *Pm-3m* (#221). As estimated by the Scherrer formula, the average crystallite size was accurately determined to be 51.9 nm for the calcined temperature at 800ºC. The SEM micrographs of powder showed that the $BaTiO_3$ grains are round-shaped, and the average grain size is observed about 40-90 nm.

Keywords: Barium titanate, Pechini, Rietveld, XRD

1. Introduction

In the early 1940s, after the discovery of barium titanate, which is the first oxide compound in perovskite structure with ferroelectric behavior, has been used for an extensive range of scientific and industrial applications, like piezoelectric infrared sensors, capacitors (electrical storage circuit element), ultrasonic transducers (the electrical device that converts electrical energy into mechanical motion). Because of its versatility, barium titanate has enhanced one of the most relevant electro-ceramic elements among ferroelectric materials. Its ferroelectric characteristics are connected with three structural phase transitions. Three-phase transitions are potential in the $BaTiO_3$, endowing with to temperature: from orthorhombic to tetragonal (-90ºC to 5ºC), tetragonal ferroelectric (5ºC to 120ºC) to cubic paraelectric (T>120ºC) structure. The dielectric features of the $BaTiO_3$ are significant in microelectronic devices production. $BaTiO_3$ nano and microstructures with high purity are essential for the production of these microelectronics [1].

There are many methods for the synthesis of barium titanate system in the literature. The solid-state method, co-precipitation, sol-gel process and hydrothermal synthesis can be used to synthesize Barium titanate perovskite structures [2-6]. Considering these methods in general, there are disadvantages such as high temperature when using metal oxides and derivatives in the solid-state method, the use of expensive and air-sensitive starting materials in some other techniques (use of air-sensitive $TiCl_4$, etc.), inhomogeneous distribution, porous structure. Recently, researchers have focused on new methods of synthesis (sonochemical, flame spray pyrolysis) at low temperatures in various sizes and morphology. However, these new methods are generally costly compared to existing powder production techniques [7-9].

To address the above problems, wet chemical methods have been systematically studied to synthesize high-quality ceramic materials. In particular, the Pechini method (Polymeric precursor technique) has advantages over other chemical processes such as controlling stoichiometry, lower reaction temperature, higher

chemical homogeneity, and distribution equation, obtaining nanoscale particles and smaller grain size [6, 10, 11].

In the Pechini process, metals form a complex with citric acid in the aqueous solution. Ethylene glycol, which is a polyalcohol-like, is added to this solution and heated at high temperatures. The gel is obtained as a result of the polyesterification of metal chelates. It is possible to obtain nano-sized crystallites by thermal decomposition of the gel. A large number of mixed oxide compositions can be prepared using this method [12, 13].

In the present study, the Pechini synthesis procedure was utilized to sufficiently prepare $BaTiO_3$ nanostructures. The obtained results pointed out that this technique is a promising option for good chemical homogeneity and precise control of the stoichiometry. The study also aims to produce high-quality materials at an industrial scale and economy by consuming commercially available organic titanate.

2. Materials and Methods

Barium acetate ($Ba(CH_3COO)_2$, 99% purity, Sigma-Aldrich), titanium(triethanolaminato) isopropoxide solution (80%wt. in isopropanol, Sigma Aldrich), citric acid ($C_6H_8O_7$,≥ 99.5%, Sigma-Aldrich) and ethylene glycol ($C_2H_6O_2$, 99.8%, Sigma-Aldrich) were used as starting materials. FTIR spectra of the samples were recorded on Spectrum BX Perkin Elmer FT-IR System spectrometer using KBr pellets. Thermogravimetric analysis was performed with an SII 7300 Perkin Elmer thermal analyzer using flowing N_2 at 2.5 mL/min from 25 to 1200°C at a heating rate of 10°C/min. The powders were characterized by using X-ray diffraction (XRD) on a PANalytical Empyrean diffractometer with Cu K_α radiation (λ= 1.5406Å). Match! Version 3 Crystal impact was used for phase identification [14]. The X-ray pattern of the corresponding compound was analyzed by Rietveld refinement program FULLPROF [15]. The crystallite size estimation calculation for the corresponding phase was done by using the Scherrer formula:

$$L \text{ (average in Å)} = K\lambda / (FWHM{*}cos\theta)$$

where L refers to crystallite size, K is the Scherrer constant, λ is the wavelength of the radiation, θ is the diffraction angle of the peak, and $FWHM$ is the full width at half maximum of (110) peak. Scanning electron microscopy (SEM) was used to analyze the morphology of the $BaTiO_3$ structure. SEM images were taken by a Zeiss Gemini 500 microscope. The average particle diameters were measured from each SEM image. Energy-dispersive X-ray spectroscope (EDX) was used to ascertain the chemical composition of the material.

2.1. Preparation of $BaTiO_3$ nanoparticles

The $BaTiO_3$ nanoparticles were prepared by the Pechini technique. The flow chart of the method is given in Figure 1. The metal-citrate solutions were prepared using barium acetate, titanium(IV) (triethanolaminato) isopropoxide, citric acid and ethylene glycol. Considering the molar amounts of starting precursors, molar ratio can be expressed as $Ba(CH_3COO)_2$: organic titanate: citric acid: ethylene glycol = 1: 1: 4.5: 20.
The preparation steps are given below.

Preparation of Barium Citrate Solution
2.02 g (7.90 mmol) of barium acetate was dissolved in ~2.7 mL ethylene glycol, and 1.51 g citric acid was then added to this solution.

Preparation of Titanium Citrate Solution
Titanium citrate solution was prepared by mixing 2.5 g (7.90 mmol) titanium (triethanolaminato)isopropoxide (80% wt. in isopropanol) and 5.31 g citric acid in 6.2 mL ethylene glycol.

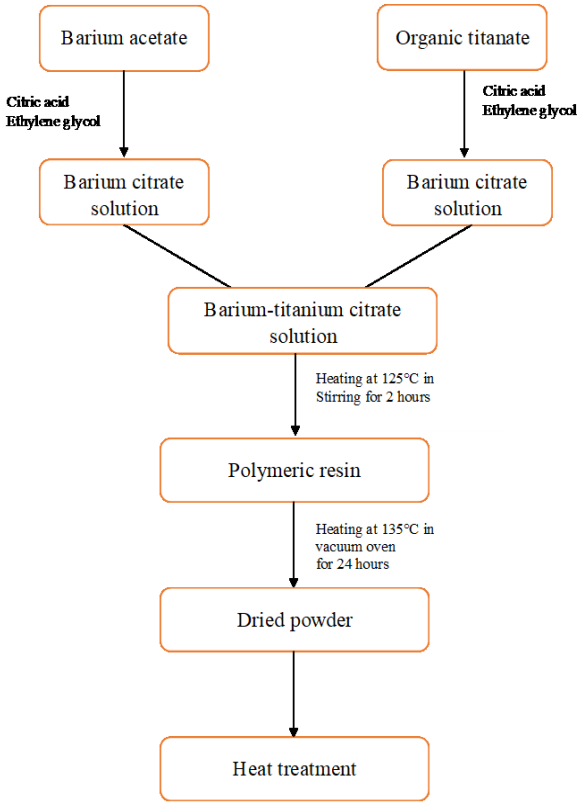

Figure 1. Flow chart of the synthesis of $BaTiO_3$ using the Pechini method.

Finally, two solutions (barium citrate and titanium citrate) were mixed, and a clear yellow solution was achieved. After stirring at 125°C for 2 hours, the yellow gel was obtained. The polymeric gel was heated in a vacuum oven at 135°C for 24 hours to obtain a dry powder. The dried powder was heated up in two steps:

Celal Bayar University Journal of Science
Volume 16, Issue 3, 2020 p 293-300
Doi: 10.18466/cbayarfbe.734061

firstly, at 400°C for 4 hours, then treated at 800ºC for 4 hours with a heating rate of 10ºC/min and then slowly cooled at room temperature.

The minor amount of $BaCO_3$ was typically observed, which result in regards to the open-air system. Powder samples were washed with acetic to remove the undesired $BaCO_3$ phase.

3. Results and Discussion

3.1. X-ray diffraction and Rietveld Refinement

The XRD pattern of the heat-treated at 800°C $BaTiO_3$ powder synthesized via the Pechini method is presented in Figure 2. The XRD and Rietveld refinement results obtained from in this study positively confirmed the $BaTiO_3$ phase maintains a cubic crystal system. The refinements of the crystal structure were performed by the Rietveld method. Rietveld refinement results of XRD profiles are given in Figure 3. All the peaks are indexed (identified using JCPDS:79-2263) for cubic phase formation, and lattice powders indicate the formation of the cubic phase, which belongs to space group *Pm-3m* (#221). The lattice parameters obtained from Rietveld refinement were a=4.0047Å, V=64.22 Å^{3,} and the calculated density is found 6.03 g/cm^3. The parameters of refinement are R_F= 2.89 and χ^2= 3.56. The reliability factors and refined structural parameters of $BaTiO_3$ are summarized in Table 1. In table 1, R factors present a good agreement between refined and experimental XRD profile for barium titanate. The average crystallite sizes, as estimated by Scherrer formula was 51.9 nm for calcined temperature 800ºC using (110) major diffraction peak.

Table 1. Structure refinement parameters and crystal data for $BaTiO_3$.

Formula	$BaTiO_3$
Formula weight	233.13 g/mol
Temperature (K)	298
λ (Å)	1.54060
Crystal system	cubic
space group	*Pm-3m* (#221)
Unit cell dimensions	a=4.0047Å,
V (Å^3)	64.22
Calc. Density (g/cm^3)	6.03
2θ range	10.0078-79.9922
(step)(°)	0.0131
$\chi 2$	3.56
R_F ,R_{Bragg}(%)	2.89, 4.48
R_p, R_{wp}, R_{exp} (%)	13.3, 11.4, 6.02

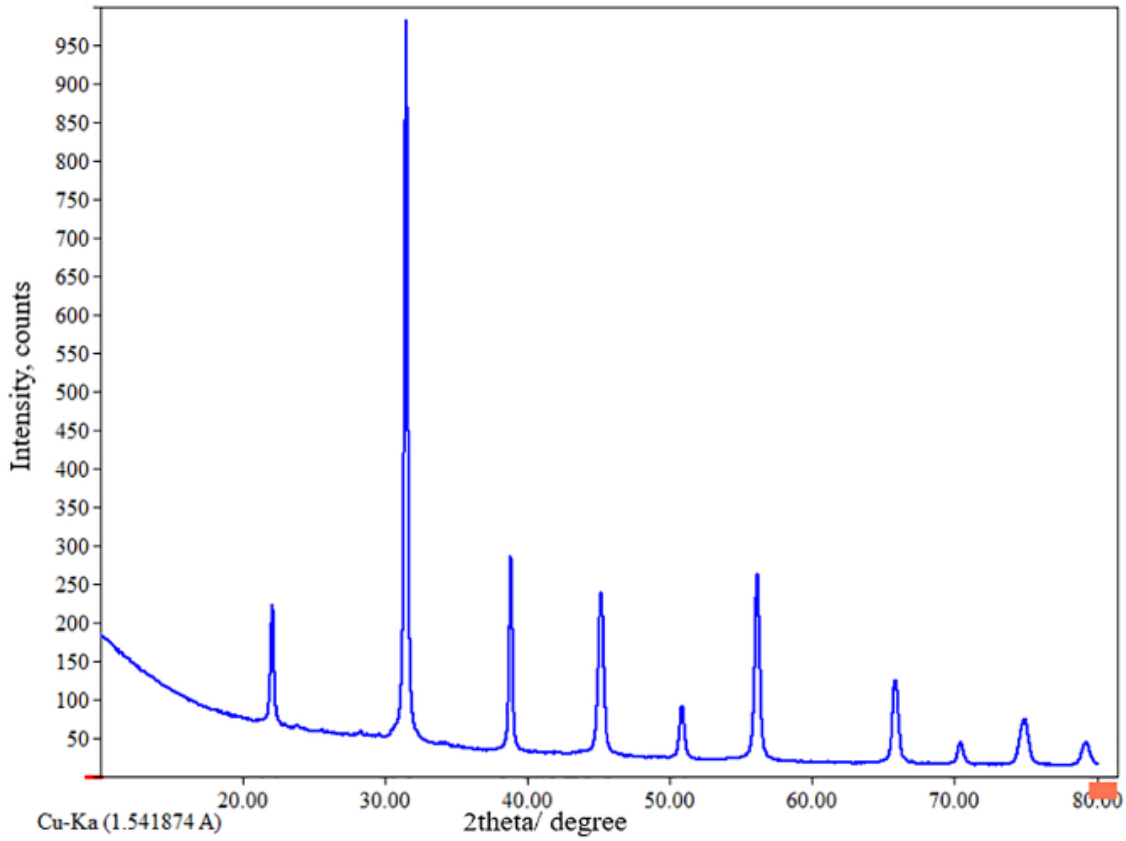

Figure 2. XRD pattern of $BaTiO_3$ nanopowders calcined for 4 hours at 800 ºC.

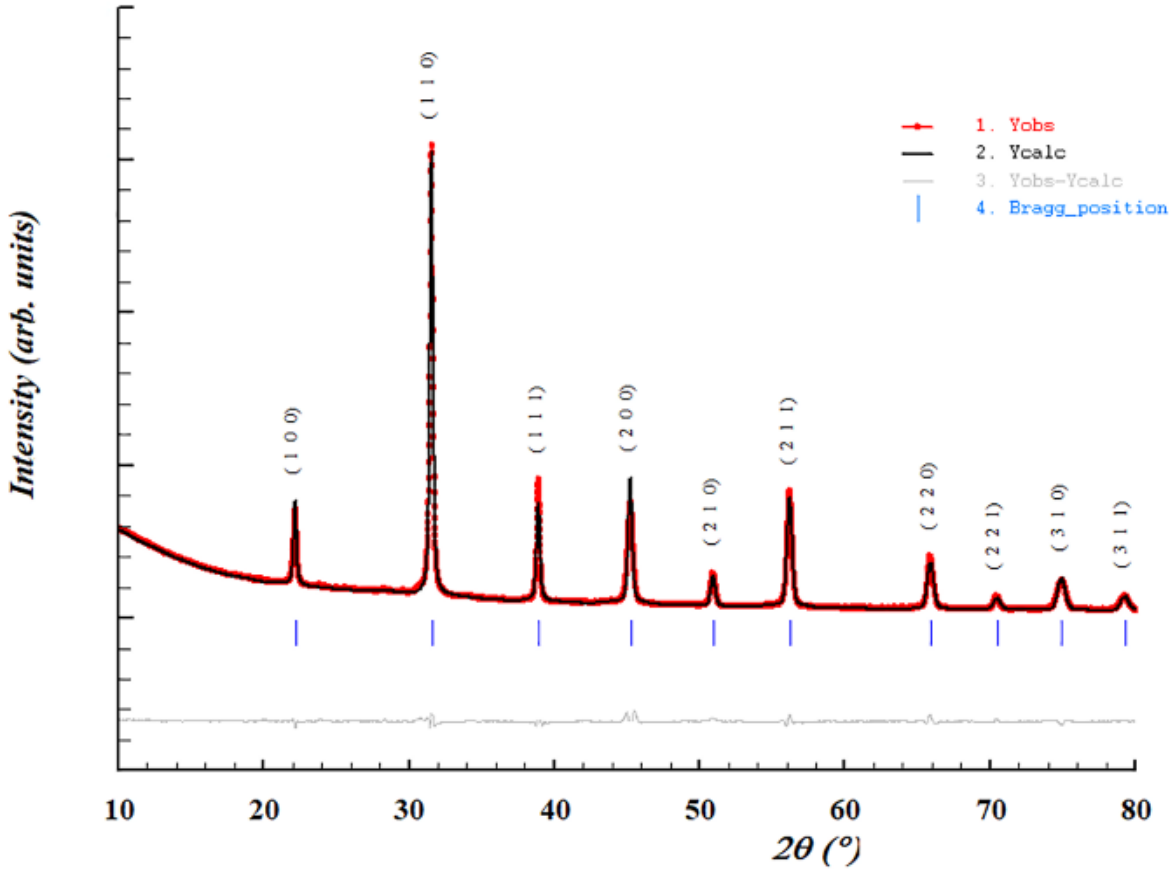

Figure 3. Rietveld refinement of $BaTiO_3$ calcined at 800 ºC for 4 hours. Experimental (1) and calculated (2) diffraction patterns of $BaTiO_3$ after Rietveld refinement. Difference (3), Bragg Positions (4).

The crystal structure of $BaTiO_3$ is shown in Figure 4. Ba^{2+} traditionally builds a cuboid box, and TiO_6 octahedron falls within the box. Ti^{4+} is ideally placed around the center of the oxygen octahedron. It can be recognized that Barium atom has 12-fold coordination for Ti atom is 6. The crystal structure was pictured by the VESTA program [16].

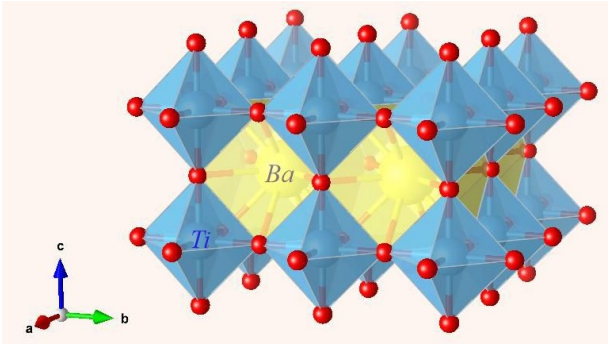

Figure 4. Schematic illustration of the refined crystal structure of the Barium titanate. Ba: yellow, Ti: blue, O: red colored.

3.2. Thermal Analysis

The thermal analysis of the $BaTiO_3$ synthesized through the Pechini method was carried out using DTG, DTA, and TGA up to 1200 °C at a heating rate of 10°C/min. Figure 5. indicated the TGA, DTA, and DTG plots of the as-prepared powders of $BaTiO_3$. The thermal analysis of Barium titanate shows two degradations. The first weight loss for a temperature range between 25°C and 200°C in the TGA curve is 5% and which corresponds to the adsorbed moisture and volatiles present in the sample. This weight loss indicated a maximum at 160°C in the DTG curve. The second weight loss between 200-600°C is due to dehydration and destruction of organic molecules, which are also observed at the FT-IR spectrum of dried powder at 135°C. Finally, between 630 and 850°C, the powder weight remains almost stable, with a total reduction of 1% may be due to the evolution of CO_2 and CO. After the calcination process at 800°C, 25% of powder was obtained, as seen in the TGA profile.

Celal Bayar University Journal of Science
Volume 16, Issue 3, 2020 p 293-300
Doi: 10.18466/cbayarfbe.734061

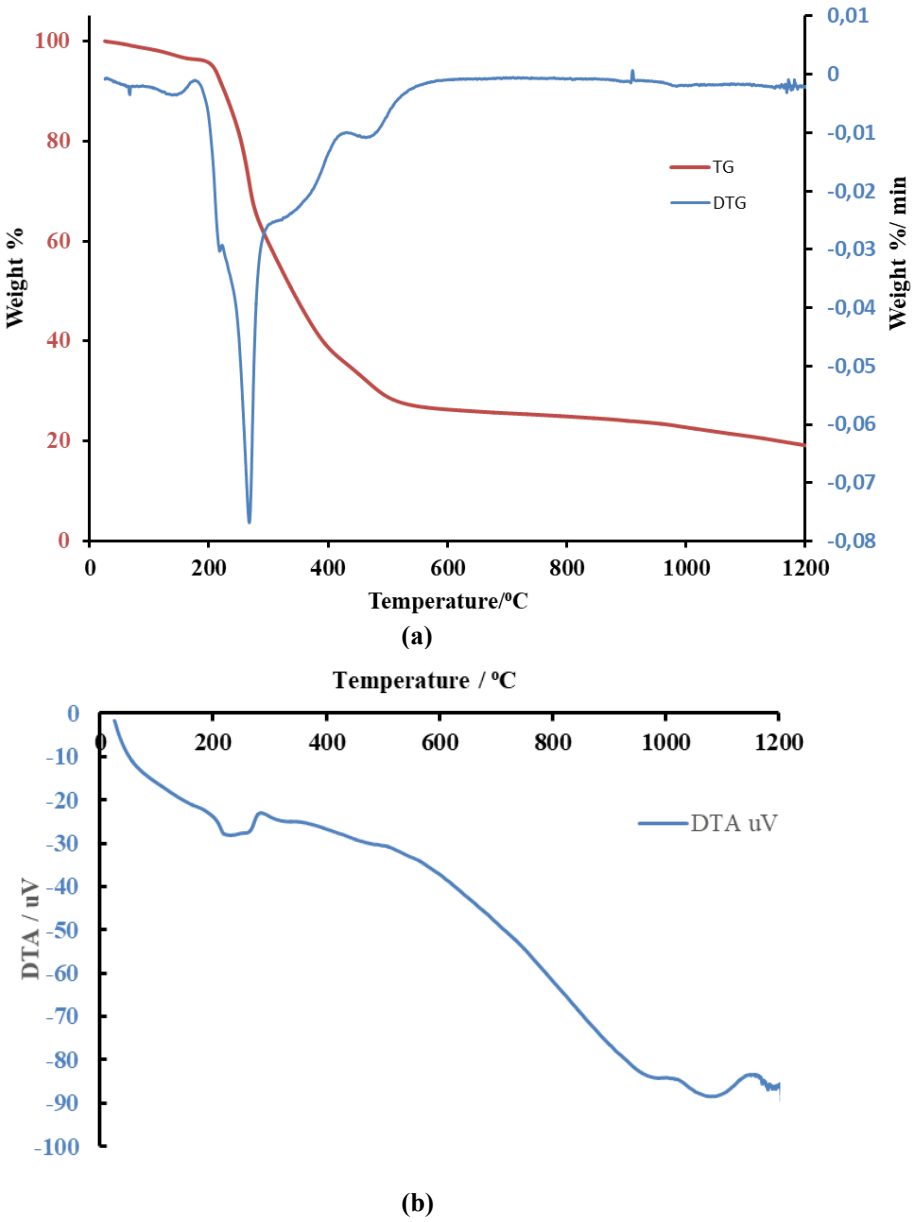

Figure 5. TGA, DTG (a) and DTA (b) plots of as-prepared $BaTiO_3$ powder.

3.3. FT-IR Analysis

In order to understand the thermal decomposition of the organic components in the reaction medium, FT-IR analysis was achieved. The spectrum of the gel powder (at 135°C) shows bands at 3319, 2958, 1739, 1591, 1181, 1076, 647, and 543 cm^{-1}. The absorption bands at 3319, 2958 cm^{-1} are assigned to O-H and C-H stretching vibrations, respectively, as well as confirm absorbed moisture and presence of $–CH_2$ and $–CH_3$ organic groups. Two peaks at 1739 and 1591 cm^{-1} indicate the existence of acetate groups also supports the symmetric and asymmetric stretching vibrations of carboxylate [17]. When the temperature reaches 400°C, a significant change is observed in the IR spectrum. The bands of organic groups have disappeared. Two new peaks in 1441 and 858 cm^{-1} indicate the presence of $BaCO_3$. After calcination at 800°C, these peaks are disappeared. The new bands below 800 cm^{-1} indicate the formation of the $BaTiO_3$ structure. The FTIR spectrum of $BaTiO_3$ has characteristic absorption peaks between 800–400 cm^{-1}, related to used to identify the phase formation [18]. A new broad absorption peak at 576 cm^{-1} is due to the stretching vibration of Ti-O. These FT-IR analysis results confirm the formation of the $BaTiO_3$ structure.

Celal Bayar University Journal of Science
Volume 16, Issue 3, 2020 p 293-300
Doi: 10.18466/cbayarfbe.734061

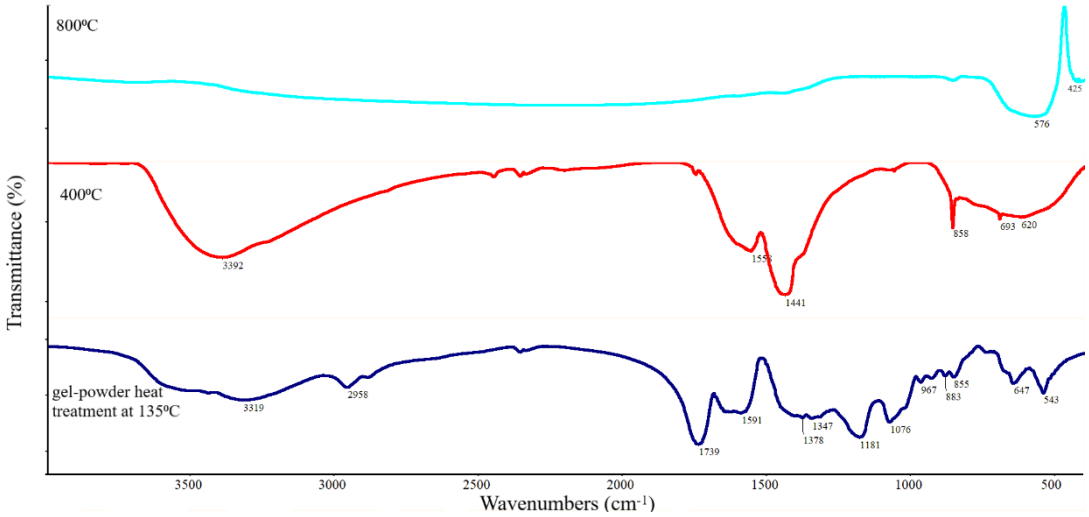

Figure 6. FT-IR spectra of $BaTiO_3$ samples at different temperatures.

3.4. SEM and EDX Analysis

The surface morphology of the calcined sample of $BaTiO_3$ was investigated by scanning electron microscopy, which is presented in Figure 7. Figure 7(a1) shows particles and their agglomerates. The powders have been agglomerated because of various operations during the heat treatment of the gel precursor. There are small and spherical particles coalesced in each cluster. As shown in Figure (a2 and a3), round-shaped grains were observed with an approximate diameter of 40-90 nm.
EDX analysis of particles calcined at 800°C is given in Figure 8 and confirmed the accuracy of elemental composition. The particles are composed of Ba, Ti, and O elements.

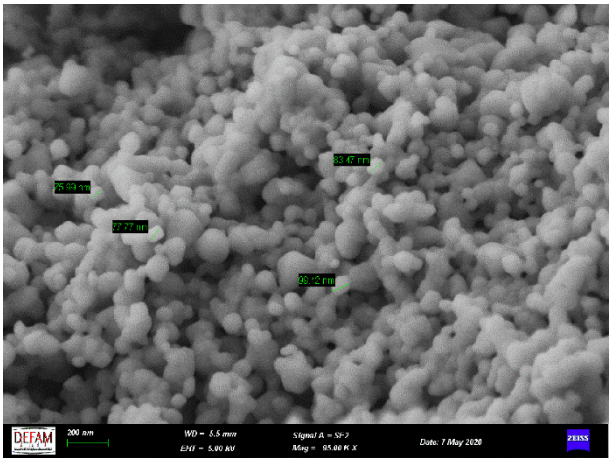

(a2)

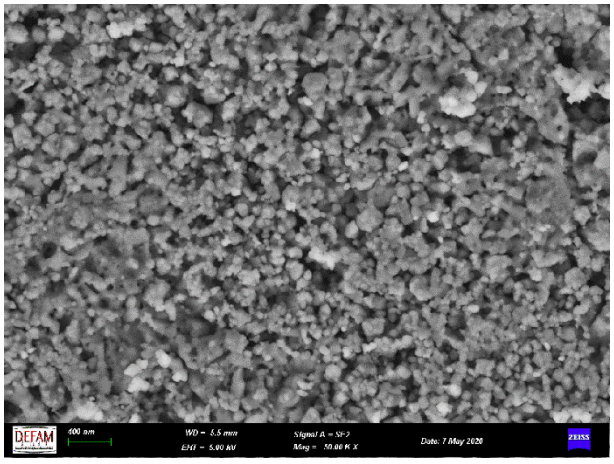

(a1)

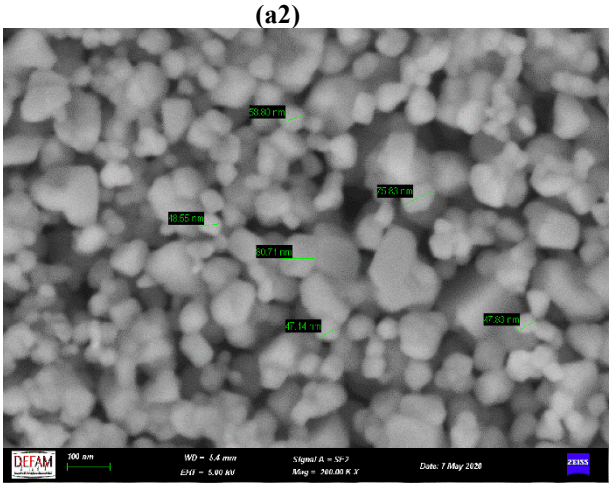

(a3)

Figure 7. SEM images of $BaTiO_3$ samples synthesized at 800ºC by Pechini process (a1) 50.000 zoom, (a2) 95.000 zoom, (a3) 200.000 zoom. Detected grain sizes from selected points (a2: 75.99, 77.77, 99.12, 83.47 nm; a3: 47.14, 47.83, 48.55, 58.80, 75.83, 80.71 nm).

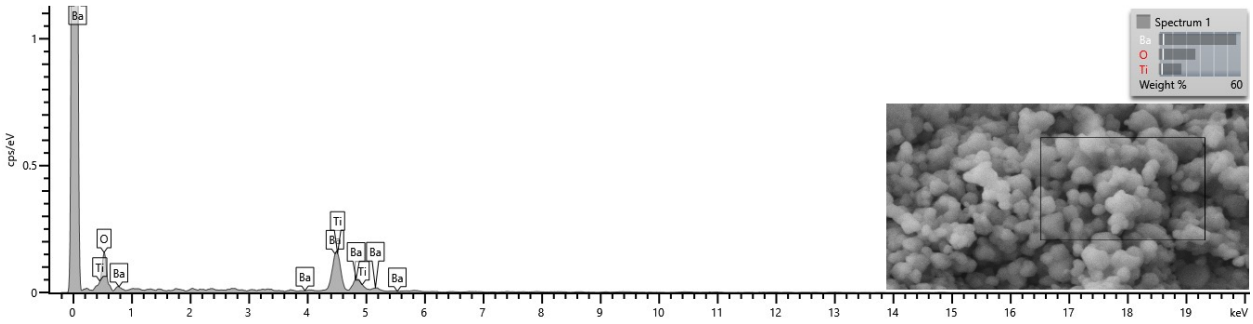

Figure 8. EDX analysis of particles calcined at 800ºC.

Table 1. Experimental conditions for $BaTiO_3$ by Pechini and Sol-precipitation method.

Method	Precursors	Conditions	Phase	Morphologies (Grain size)	Reference
Pechini	$Ba(CH_3COO)_2$ organic titanate	4h, 800°C	Cubic	40-90 nm	In the present study
Pechini	$Ba(CH_3COO)_2$ Ti-isopropoxide	5h, 600°C	Cubic	44±15 nm	[5]
Pechini	$Ba(CH_3COO)_2$ Ti-isopropoxide	3 h, 700ºC	Pseudo-cubic	40-80 nm	[19]
Pechini	$Ba(CH_3COO)_2$ Tetra butyl titanate	6h, 720°C	Cubic	20-130 nm	[20]
Sol-precipitation	$Ba(OH)_2$ organic titanate	12h, 400°C	Cubic	23-31 nm	[4]

*organic titanate: titanium(IV)(triethanolaminato)isopropoxide

3.5. Comparison of results with literature data

The synthesis processes of $BaTiO_3$ are summarized in Table I (also include the corresponding literature for comparison). In the present study, $BaTiO_3$ was synthesized from $Ba(CH_3COO)_2$ and organic titanate precursor with 40-90 nm grain size. When compared with the reactions performed with the Pechini method using Barium acetate, it is seen that the obtained barium titanate is in the cubic phase and has similar morphological properties. In these methods, an expensive and easily hydrolyzable titanium precursor is used. The Pechini method is more advantageous than the conditions realized using organic titanate with the sol-precipitation [4] method. The smaller grain size was obtained by stirring at high speed, precipitated with the centrifuge, and sintering for 12 hours. The industrial application of the method is not beneficial. In the present study, the synthesis process was demonstrated favorable properties, such as lack of a minor second phase, using economically inexpensive non-air sensitive precursors, simply applicability in the industry.

4. Conclusion

In this paper, nanoscale barium titanate powders have been synthesized from gel precursors by the Pechini process. In the process, it is advantageous to use titanium (triethanolaminato)isopropoxide, which is not sensitive to air and cheap as a starting material. The XRD results of the $BaTiO_3$ sample indicated that the material is in pure phase with a cubic structure. TGA-DTG and FT-IR analyses confirm that the nanopowders were obtained at a calcination temperature of 800°C. The average crystallite size was 51.8 nm, as determined by XRD. SEM analyses were showed that the grains were agglomerated, and the grain size determined between 40-90 nm.

Acknowledgment

This work was supported by the Scientific Research Project Office of Manisa Celal Bayar University project no: 2019-056. The experiments in this paper were partially performed at Manisa Celal Bayar University (Turkey)- Applied Science and Research Center (DEFAM).

Author's Contributions

Pelin Sözen Aktaş: Performed the experiments, analyzed the results and wrote the manuscript.

Ethics

There are no ethical issues after the publication of this manuscript.

References

1. Jiang, B, Iocozzia, J, Zhao, L, Zhang, H, Harn, Y, Lin, Z. 2019. Barium titanate at the nanoscale: controlled synthesis and dielectric and ferroelectric properties. *Chemical Society Reviews;* 48: 1194-1228.

2. Buscaglia, MT, Bassoli, M, Buscaglia, V, Alessio, R. 2005. Solid-state synthesis of ultrafine $BaTiO_3$ powders from nanocrystalline $BaCO_3$ and TiO_2. *Journal of American Chemical Society*; 88: 2374-2379.

3. Prasadarao, AV, Suresh, M, Komarneni, S. 1999. pH dependent coprecipitated oxalate precursors–a thermal study of barium titanate. *Materials Letters*; 36(6): 359-363.

4. Upadhyay, RH, Argekar AP, Deshmukh RR. 2014. Characterization, dielectric and electrical behavior of BaTiO3 nanoparticles prepared via titanium(IV) triethanolaminato isopropoxide and hydrated barium hydroxide. *Bulletine of Material Science;* 37(3): 481-489.

5. Prado, LR, de Resende, NS, Silva, RS, Egues, SMS,Salazar-Banda, GR. 2016. Influence of the synthesis method on the preparation of barium titanate nanoparticles. *Chemical Engineering and Processing: Process Intensification*; 103: 12–20.

6. Vinothini, V, Paramanand, S, Balasubramanian, M. 2006. Synthesis of barium titanate nanopowder using polymeric precursor method. *Ceramics International;* 32: 99-103.

7. Xu, M, Lu, Y-N, Liu, Y-F, Shi, S-Z, Qian, T-S, Lu, D-Y. 2006. Sonochemical synthesis of monosized spherical $BaTiO_3$ particles. *Powder Technology;* 161(3): 185-189.

8. Jung, DS, Hong, SK, Cho, JS, Kang, YC. 2008. Nano-sized barium titanate powders with tetragonal crystal structure prepared by flame spray pyrolysis. *Journal of the European Ceramic Society;* 28(1): 109-115.

9. Terashi, Y, Purwanto, A, Wang, WN, Iskandar, F, Okuyama, K. 2008. Role of urea addition in the preparation of tetragonal $BaTiO_3$ nanoparticles using flame-assisted spray pyrolysis. Journal of European Ceramic Society; 28:2573-2580.

10. Kumar, S, Messing, GL, White, WB. 1993. Metal Organic Resin Derived Barium Titanate: I, Formation of Barium Titanium Oxycarbonate Intermediate. *Journal of American Ceramic Society*; 76: 617.

11. Cho, WS. 1998. Structural evolution and characterization of $BaTiO_3$ nanoparticles synthesized from polymeric precursor. *Journal of Physics and Chemical Solids*; 59(5): 659-666.

12. Ring, TA. Fundamentals of Ceramic Powder Processing and Synthesis; Academic Press: California, USA, 1996; pp 346.

13. Assirey, EAR. 2019. Perovskite synthesis, properties and their related biochemical and industrial application. *Saudi Pharmaceutical Journal*; 27: 817-829.

14. Match! - Phase Identification from Powder Diffraction, Crystal Impact - Dr. H. Putz & Dr. K. Brandenburg GbR, Kreuzherrenstr. 102, 53227 Bonn, Germany, http://www.crystalimpact.com/match

15. Rodríguez-Carvajal, J. 1993. Recent advances in magnetic structure determination by neutron powder diffraction. *Physica B: Condensed Matter;* 192: 55–69.

16. K. Momma, K, Izumi, F. 2008. *VESTA*: a three-dimensional visualization system for electronic and structural analysis. *Applied Crystallography;* 41: 653–658.

17. Ashiri, R, Nemati, A, Ghamsari, MS, Sanjabi, S, Aalipour, M. 2011. A Modified method for Barium Titanate nanoparticles synthesis. *Materials Research Bulletine*; 46: 2291-2295.

18. Ashiri, R. 2013. Detailed FT-IR spectroscopy characterization and thermal analysis of synthesis of barium titanate nanoscale particles through a newly developed process. *Vibrational Spectroscopy*; 66: 24-29.

19. Lazarevi´c, Z, Vijatovi´c, M, Doh˘cevi´c-Mitrovi´c, Z, Rom˘cevi´c, NZ, Rom˘cevi´c, MJ, Paunovi´c, N, Stojanovi´c, BD. 2010. The characterization of the barium titanate ceramic powders prepared by the Pechini type reaction route and mechanically assisted synthesis. *Journal of the European Ceramic Society;*30: 623-628.

20. Wu, YT, Wang, XF, Yu, CL, Li, EY. 2012. Preparation and Characterization of Barium Titanate (batio$_3$) Nanopowders by Pechini Sol-gel Method. *Materials and Manufacturing Processes*; 27: 1329-1333.

Celal Bayar University Journal of Science

The Expressions of Small Ubiquitin-like Modifier (SUMO) Related Genes Under Metal (Cu, Zn and Fe) Toxicity in *Arabidopsis thaliana*

Baris Uzilday[1]*

[1] Department of Biology, Faculty of Science, Ege University, Bornova, Izmir, 35100, Turkey
*baris.uzilday@ege.edu.tr
*Orcid No: 0000-0001-8168-056X

Received: *8 April 2020*
Accepted: *14 September 2020*
DOI: *10.18466/cbayarfbe.716691*

Abstract

Aim of this work was to investigate effects of toxic levels of Cu, Zn and Fe treatments on small ubiquitin-like modifier (SUMO) machinery of *Arabidopsis thaliana*. SUMO is a 100-115 amino acid post-translational modifier that can regulate stability, activity or sub-cellular localization of target proteins. *A. thaliana* plants were treated with 50 µM Cu, 700 µM Zn and 400 µM Fe for 7 d and then expressions of genes related to SUMOylation and deSUMOylation of target proteins were measured with qRT-PCR. Only Cu treatment was able to induce genes related to SUMOylation (*SUM3, SAE2, SIZ1*) of target proteins, while all of the three metals used in this study was effective in inducing a deSUMOylation related gene. Results of this study indicate that deSUMOylation of proteins might be a part of plant response to metal toxicity.

Keywords: *Arabidopsis thaliana*, deSUMOylation, metal toxicity, small ubiquitin-like modifier (SUMO), SUMOylation

1. Introduction

As sessile organisms, plants should rapidly respond to changes in environmental conditions to survive. These responses can be at different levels such as transcriptional, post-transcriptional, translational or post-translational [1]. Among these, post-translational modifications are rapid since there is no need for transcription of a gene and synthesis of a new protein and are involved in stress perception, signaling and acclimation [2]. Post-translational modifications are defined as addition or removal of small molecules to target proteins [3]. In eukaryotic cells activity, stability or sub-cellular localization of proteins can be controlled via modifications such as phosphorylation, acetylation, methylation, glycosylation, disulfide bond formation or ubiquitination [4]. Another lesser known post-translation modification that is involved in regulation of cellular functions is small ubiquitin-like modifier (SUMO) [5]. SUMO is a polypeptide that contains 100-115 amino acids and is encoded by four genes in model plant *Arabidopsis thaliana* (*SUM1, 2, 3* and *5*) [6]. During SUMOylation SUMO covalently binds to a lysine residue of a protein and this is reversible. In *A. thaliana* SUMOylation occurs with involvement of E1, E2 and E3 enzymes, which are SUMO activation, conjugation and ligation enzymes, respectively [7].

SUMO is activated by E1 SUMO activation enzyme, which is comprised of two small (SAE1a and SAE1b) and one large sub-unit (SAE2) [8]. Following activation, SUMO polypeptide is transferred to E3 ligases by the E2 SUMO conjugation enzyme (SCE1). E3 ligases that transfer SUMO to target proteins are encoded by *HIGHPLOIDY2* (*HPY2*) and *SAP & MIZ1* (*SIZ1*) in Arabidopsis [9]. On the other hand, removal of SUMO modification from target proteins is done by deSUMOylation enzymes such as *OVERLY TOLERANT TO SALT 1* (*OTS1*), *OTS2, EARLY IN SHORT DAYS 4* (*ESD4*), *ESD4 like SUMO PROTEASE* (*ELS1*), *ULP1b*, *ULP2a* and *ULP2b* [10].

SUMOylation and deSUMOylation can affect protein activity and cell metabolism in two different ways. The first of these is the regulation of protein-protein interactions and therefore signaling pathways and circuits in the cell. The second effect of SUMOylation on protein activity is that it protects proteins against ubiquitin-mediated protein breakdown [11]. Since ubiquitin and SUMO bind to the same lysine residues on target proteins, binding of SUMO to a protein prevents ubiquitin from binding to the protein of interest. It is well documented that ubiquitination of a protein creates a signal for the degradation of that protein by 26S proteasome [12]. The accumulation of

SUMOylated proteins in response to environmental stresses such as heat shock, cold, drought, salinity is vital for the plant. With the increase in amount of SUMOylated proteins, the levels of the free SUMO levels decrease. Following this with the relief of stress amount of free SUMO levels increases rapidly [13]. Moreover, mutants missing the SIZ1 allele were susceptible to abiotic stresses. For example, SUMOylation of ICE1 mediated by SIZ1 in Arabidopsis controls CBF3/DREB1A expression and affects freezing tolerance [14].

Metals such as Cu, Zn, Mn, Fe, Ni, and Co are essential for plant growth and development; however, accumulation of excess levels of these metal ions in plant cells can cause various detrimental toxic effects [15]. For example, direct or indirect production of reactive oxygen species and oxidative stress is a common effect caused by most of the metals, especially that of redox active metals such as Fe and Cu. On the other hand, some metals such as As, Cd, Cr, Pb, Hg might affect protein function by replacing other metals in active site of the proteins or by interfering with function of functional groups [16]. Metal toxicity is a wide-spread phenomenon observed in arable lands that can be caused by natural or anthropogenic activities such as mining, excessive use of fertilizers and irrigation with groundwater [17]. Therefore, it is vital to understand plant response to metal toxicity for sustainable plant productivity in metal contaminated soils. There are numerous studies that investigate uptake, translocation, sequestration of metals in plants and plant response to heavy metals at biochemical and molecular level such as antioxidant response, regulation of metalloenzymes and accumulation of phytochelatins [18, 19]. However, transcriptional response of SUMO metabolism to essential metals such as Cu, Zn and Fe has not been elucidated before.

Therefore, aim of this work was to elucidate how metal toxicity affects SUMO machinery of *A. thaliana* at transcriptional level. For this *A. thaliana* plants were treated with toxic concentrations of Cu, Zn and Fe and expressions of genes related to SUMOylation and deSUMOylation were measured with qRT-PCR.

2. Materials and Methods

2.1. Materials

Arabidopsis thaliana Col-0 ecotype was used in this work as plant material.

2.2. Methods

2.2.1. Growth Conditions and Treatments

Sterilized seeds were sown on ½ Murashige-Skoog (MS) medium with Gambrog's vitamins [20] and 1% sucrose in petri dishes and then were grown in a growth chamber in 22/20 °C, 12/12 dark/light and 60% relative humidity conditions. After 2 days of germination period, 5 days old seedlings were treated with 50 µM Cu, 700 µM Zn and 400 µM Fe for 7 days. Metal concentrations were selected according to previous studies [21-23]. At the end of experiments whole seedlings were harvested, then flash frozen in liquid nitrogen and were stored at -80 °C until further analysis.

2.2.2. Quantitative Real-Time PCR Analysis

Measurement of gene expressions was done according to Ozgur *et al.* [24]. 0.1 g fresh samples were used for RNA isolation which was determined with NucleoSpin RNA Plant Kit (Macherey-Nagel) according to directions. DNAse I was used for DNA digestion to prevent any genomic DNA contamination. High-Capacity cDNA Reverse Transcription Kit (Applied Biosystems) was used to perform reverse transcription (1µg of RNA). SYBR green Master mix (Applied Biosystems) were used to perform qRT-PCR. PCR amplification protocol was as follows, 95 °C for 5 minutes, 95 °C (15 s), 60 °C (15 s) and at 72 °C (30 s) for 40 cycles. StepOne Plus software was used to analyze the resulting data. Control group was designated as the reference and the value of the control groups was set to 1 when calculating the expression levels of the genes. *ACTIN8* gene was used as house-keeping gene and expressions of other genes were normalized according to it. Primers used in this study can be found in Table 1.

Table 1. List of qRT-PCR primers used in the study.

SUMO	*SUM1*	F	GACCGGCAATCTGTGGACAT
		R	CCATGTCAAGCTCATCGGGA
	SUM2	F	AGGGACAGGCATTTTTCGTTG
		R	TCCACAGACTGACGGTCACA
	SUM3	F	CAAGAGCCAGGATGGAGACG
		R	TCTCCAGGCCACCTATACGA
	SUM5	F	TGGTGAGTTCCACAGACACAA
		R	ATCCTCTGCTCCCTGTTGGT
E1	*SAE1a*	F	TCCTCGGAGAACAGCAAAGC
		R	TCTGGCAAGATCGAGTAGCG
	SAE1b	F	CACAAAGAAAAAGCTTGATGAAACA
		R	TCCACGGTACTGAAACTGCC
	SAE2	F	ACGGAAGCATTCTCACAGTCG
		R	GAGTTTAGGGAAAGTCGATGGT
E2	*SCE1*	F	GATGGAGACCAGCCATCACC
		R	AACCATCTGTCTGTGCAGGG
E3	*HPY2*	F	TGTCTCCGATAACAGTTCCACG
		R	TCAAGGTCCTTAACCTTGTCCG
	SIZ1	F	TTTTGGGTTACAGTGGCACA
		R	ACACTCTGCATTGTGCTTGC
deSUMOylation	*ELS1*	F	TTGGAGACAAGATGAAGAACCA
		R	TTGAGATGGTAGCCCAACCT
	OTS1	F	TGCGAGCGAGTACAGCCTCA
		R	AATCTTGGCAGCGACCGCCA
	OTS2	F	GGGAAAGCTGAGCACAGTGCA
		R	TCCCAAGACCACTCCCTAGGAGT
	ACT8	F	TCAGCACTTTCCAGCAGATG
		R	ATGCCTGGACCTGCTTCAT

Celal Bayar University Journal of Science
Volume 16, Issue 3, 2020, p 301-305
Doi: 10.18466/cbayarfbe.716691

2.2.6. Statistical Analysis

Experiments were repeated twice with 3 replicates (n = 6). The results were expressed as mean and error bars were used to indicate the standard error of the mean. (± SEM). Treatment groups were compared to controls using students-t test. Significant differences ($p < 0.05$) were marked with an asterisk (*).

3. Results and Discussion

3.1. The Expressions of SUMO Encoding *SUM1*, *SUM2*, *SUM3* and *SUM5* Genes

Cu, Zn and Fe treatments did not have statistically significant effects on the expressions of *SUM1*, *SUM2* and *SUM5* genes (Figure 1). However, the expression of *SUM3* changed with Cu treatment. Cu toxicity enhanced the expression of *SUM3* gene by 3.2 folds as compared to controls. SUMO3 is responsible for mono-SUMOylation of proteins while SUMO1 and 2 can form poly-SUMO chains on proteins. These results indicate that mono-SUMOylation might be required for plant response to Cu as it was shown in drought stress previously [25]. Although there is no information in literature related to transcriptional response of different *SUM* genes to metal stress, it has been demonstrated that oxidative stress and heat shock can induce accumulation of SUMO conjugates in Arabidopsis [26].

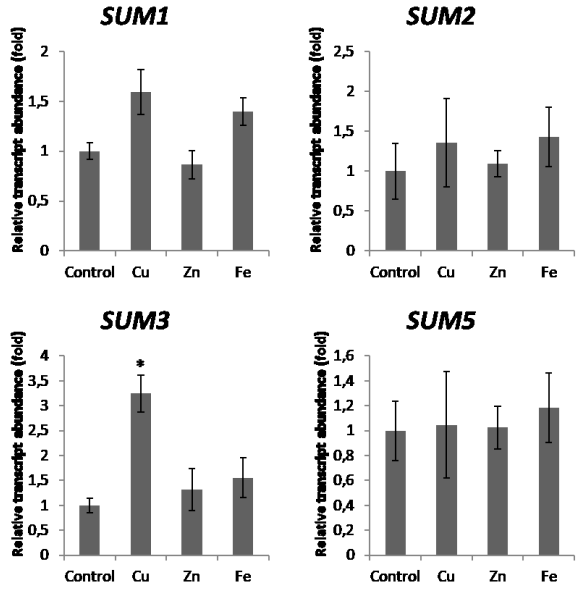

Figure 1. qRT-PCR analysis of *SUM1*, *SUM2*, *SUM3* and *SUM5* genes under Cu,Zn and Fe toxicity.

3.2. The Expressions of Genes Encoding SUMO E1 Activating Enzymes (*SAE1* and *SAE2*) and SUMO E2 Conjugating Enzyme (*SCE1*)

The expressions of *SAE1A* and *SAE1B* did not change under toxic levels of Cu, Zn and Fe treatments (Figure 2). However, Cu treatment enhanced *SAE2* expressions 2.3 folds as compared to controls while Zn treatment decreased it by 2 folds as compared to controls. On the other hand, metal treatments did not have any effect on the expression of *SCE1* expression. Previous studies demonstrated that *SCE1* expression was induced with high temperature stress in rice [27]. Moreover, *SCE1* was also induced in tomato species that is tolerant to bacterial pathogens [28]. E1 complex is comprised of SAE1A, SAE1B and SAE2, but results of this study indicates that SAE1 subunits does not respond to metal toxicity, while SAE2 can be induced by Cu toxicity. How this changes stoichiometry and activity of this protein deserves further scrutiny.

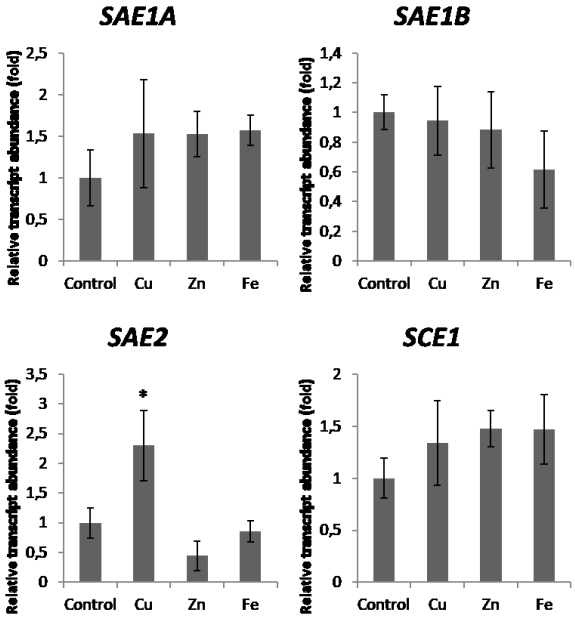

Figure 2. qRT-PCR analysis of *SAE1A*, *SAE1B*, *SAE2* and *SCE1* genes under Cu,Zn and Fe toxicity.

3.3. The Expressions of SUMO E3 Ligase Encoding Genes *HPY2* and *SIZ1*

The expression of *HPY2* gene decreased by 2 folds as compared to control under Cu toxicity, while Zn and Fe treatments did not change the expressions of *HPY2* (Figure 3). Moreover, Cu toxicity increased the expression of *SIZ1* by 2.3 folds as compared to controls, whereas Zn and Fe treatments did not have any effects on the *SIZ1* expressions. SIZ1 and HPY2 are thought to have different roles in plant stress response since heat-stress induced SUMOylated protein patterns in *siz1* and *hpy2* mutant plants are different [29]. It has been demonstrated that *siz1* mutation causes Cu stress sensitivity [30]. Chen et al. [30] demonstrated that SUMOylation controls mRNA levels of YSL1 and YSL3 (*Yellow Stripe-Like1* and *Yellow Stripe-Like3*), which encode Cu transporters, either through regulation of transcription or affecting mRNA stability under excess Cu conditions. Moreover, they showed that that SIZ1 activity is required for maintenance of basal transcription levels of YSL1 and YSL3 under non-stress conditions Another role of SIZ1 is related to low

temperatures, where SIZ1 mediated SUMOylation of ICE1 is required for freezing stress tolerance in *Arabidopsis thaliana* [14]. Moreover, overexpression of SIZ1 leads to increased tolerance to cold and salt stresses and attenuates response to abscisic acid in *Arabidopsis thaliana* [13]. Results of current study supports the idea that HPY2 and SIZ1 have different functions in plants, which is evident from induced expression of *SIZ1* under Cu toxicity, while *HPY2* did not change.

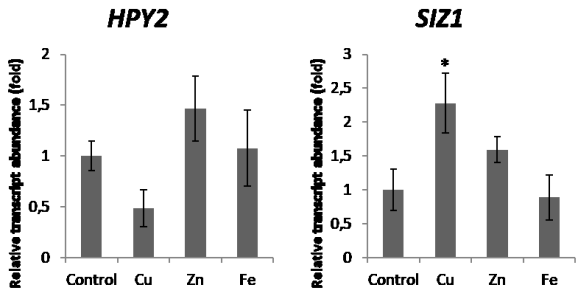

Figure 3. qRT-PCR analysis of *HPY2* and *SIZ1* genes under Cu, Zn and Fe toxicity.

3.4. The Expressions of Genes Encoding DeSUMOylation Enzymes ELS1, OTS1 and OTS2

Cu and Zn treatments enhanced the expressions of *ELS1* by 3.7 and 8 folds respectively as compared to controls while Fe toxicity showed no significant effect on the expression of *ELS1* (Figure 4). The expression of *OTS1* under Cu and Fe treatments also showed no differences, but Zn treatment enhanced the expression of *OTS1* by 2 folds as compared to control.

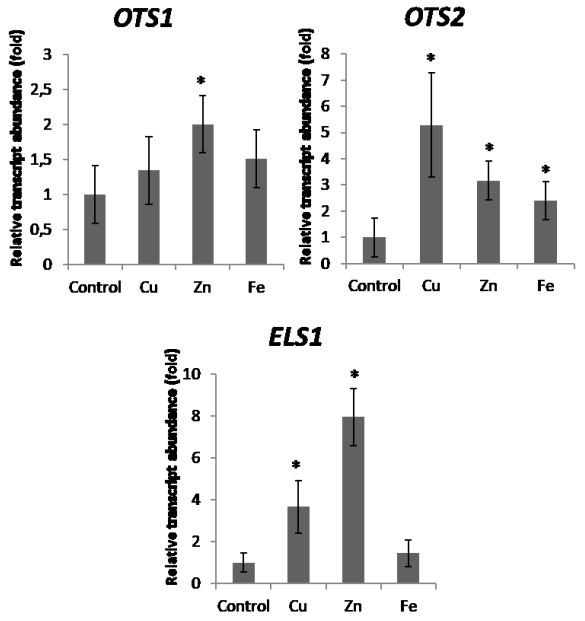

Figure 4. qRT-PCR analysis of *ELS1, OTS1* and *OTS2* genes under Cu, Zn and Fe toxicity.

The expression of *OTS2* was enhanced with all three metal treatments. Cu treatments enhanced it by 5 folds, while Zn treatments induced it 3 folds as compared to control. Moreover, Fe toxicity also enhanced the expression of *OTS2* by 2 folds as compared to controls. deSUMOylation enzymes are vital to control accumulation of SUMO substrate and can provide specificity since they are encoded by a higher number of genes [11]. Moreover, deSUMOylation enzymes are important components of plant stress tolerance. For example, *ots1 ots2* double mutant is sensitive to salt stress and accumulates higher levels of SUMO1/2 conjugated proteins [10]. On the other hand, over-expression of *OTS1* can confer plants tolerant to salt stress by reducing SUMO1/2 conjugates [10]. Results obtained in this study are consistent with the literature since all of the three deSUMOylation genes investigated are induced with metal treatments, indicating that protein deSUMOylation might be more critical than SUMOylation during metal toxicity.

4. Conclusion

Overall, this study demonstrates that among the metals tested only Cu induces genes related to SUMO polypeptides or SUMOylation enzymes (*SUM3, SAE2, SIZ1*) and Zn and Fe toxicity does not have such effect. On the other hand, all three metals, Cu, Zn and Fe, induced expressions of deSUMOylation related genes, especially that of *ELS1,* indicating that deSUMOylation of proteins might be a part of plant response to metal toxicity. Since *ELS1* can also play a role in maturation of SUMO peptides [11] further roles of ELS1 in metal toxicity tolerance should be evaluated by investigating SUMO conjugate levels in wild-type and ELS1 mutants under metal toxicity.

Author's Contributions

Baris UZILDAY: Designed and performed the experiments and evaluated the results. He prepared figures, drafted and wrote the manuscript.

Ethics

There are no ethical issues after the publication of this manuscript.

References

1. Osakabe Y, Osakabe K, Shinozaki K, Tran LSP. 2014. Response of plants to water stress. *Frontiers in Plant Science*; 5: 86.

2. Filichkin S, Priest HD, Megraw M, Mockler TC. 2015. Alternative splicing in plants: directing traffic at the crossroads of adaptation and environmental stress. *Current Opinion in Plant Biology*; 24: 125-135.

3. Waszczak C, Akter S, Jacques S, Huang J, Messens J, Van Breusegem F. 2015. Oxidative post-translational modifications

of cysteine residues in plant signal transduction. *Journal of Experimental Botany*; 66(10): 2923-2934.

4. Mann M, Jensen ON. 2003. Proteomic analysis of post-translational modifications. *Nature Biotechnology*; 21(3): 255.

5. Park HJ, Kim WY, Park HC, Lee SY, Bohnert HJ, Yun DJ 2011. SUMO and SUMOylation in plants, *Molecules and Cells*; 32(4):305.

6. Hanania U, Furman-Matarasso N, Ron M, Avni A. 1999. Isolation of a novel SUMO protein from tomato that suppresses EIX-induced cell death. *The Plant Journal*; 19(5): 533-541.

7. Castaño-Miquel L, Mas A, Teixeira I, Seguí J, Perearnau A, Thampi BN, Coca M. 2017. SUMOylation inhibition mediated by disruption of SUMO E1-E2 interactions confers plant susceptibility to necrotrophic fungal pathogens. *Molecular Plant*; 10(5): 709-720.

8. Castro PH, Couto D, Freitas S, Verde N, Macho AP, Huguet S, Azevedo H. 2016. SUMO proteases ULP1c and ULP1d are required for development and osmotic stress responses in *Arabidopsis thaliana. Plant Molecular Biology*; 92(1-2): 143-159.

9. Miura K, Hasegawa PM. 2010. SUMOylation and other ubiquitin-like post-translational modifications in plants. *Trends in Cell Biology*; 20(4): 223-232.

10. Yates G, Srivastava AK, Sadanandom A. 2016. SUMO proteases: uncovering the roles of deSUMOylation in plants. *Journal of Experimental Botany*; 67(9): 2541-2548.

11. Castro PH, Bachmair A, Bejarano ER, Coupland G, Lois L M, Sadanandom A, Azevedo H. 2018. Revised nomenclature and functional overview of the ULP gene family of plant deSUMOylating proteases. *Journal of Experimental Botany*; 69(19): 4505-4509.

12. Vierstra, R. D. (2003). The ubiquitin/26S proteasome pathway, the complex last chapter in the life of many plant proteins. Trends in plant science, 8(3): 135-142.

13. Li Y, Wang G, Xu Z, Li J, Sun M, Guo J, Ji W. 2017. Organization and regulation of soybean SUMOylation system under abiotic stress conditions. *Frontiers in Plant Science*; 8: 1458.

14. Miura K, Jin JB, Lee J, Yoo CY, Stirm V, Miura T, Hasegawa PM. 2007. SIZ1-mediated sumoylation of ICE1 controls CBF3/DREB1A expression and freezing tolerance in Arabidopsis. *The Plant Cell*; 19(4): 1403-1414.

15. Hasan M, Cheng Y, Kanwar MK, Chu XY, Ahammed GJ, Qi ZY. 2017. Responses of plant proteins to heavy metal stress—a review. *Frontiers in Plant Science*; 8: 1492.

16. Jalmi SK, Bhagat PK, Verma D, Noryang S, Tayyeba S, Singh K, Sinha AK. 2018. Traversing the links between heavy metal stress and plant signaling. *Frontiers in Plant Science*; 9: 12.

17. Nagajyoti PC, Lee KD, Sreekanth TVM. 2010. Heavy metals, occurrence and toxicity for plants: a review. Environmental Chemistry Letters; 8(3): 199-216.

18. Thakur S, Singh L, Ab Wahid Z, Siddiqui MF, Atnaw SM, Din MFM. 2016. Plant-driven removal of heavy metals from soil: uptake, translocation, tolerance mechanism, challenges, and future perspectives. *Environmental Monitoring and Assessment*; 188(4): 206.

19. Sharma SS, Dietz KJ. 2009. The relationship between metal toxicity and cellular redox imbalance. *Trends in Plant Science*; 14(1): 43-50.

20. Gamborg OL, Murashige T, Thorpe TA, Vasil IK. 1976. Plant tissue culture media. *In vitro*;12(7): 473-478.

21. Kumar V, Vogelsang L, Seidel T, Schmidt R, Weber M, Reichelt M, Dietz KJ. 2019. Interference between arsenic-induced toxicity and hypoxia. Plant, Cell & environment; 42(2): 574-590.

22. Milner MJ, Seamon J, Craft E, Kochian LV. 2013. Transport properties of members of the ZIP family in plants and their role in Zn and Mn homeostasis. *Journal of Experimental Botany*; 64(1): 369-381.

23. Sanz A, Pike S, Khan MA, Carrió-Seguí À, Mendoza-Cózatl DG, Peñarrubia L, Gassmann W. 2019. Copper uptake mechanism of Arabidopsis thaliana high-affinity COPT transporters. *Protoplasma*; 256(1): 161-170.

24. Ozgur R, Uzilday B, Turkan I, Sekmen AH. 2017. The effects of melatonin on transcriptional profile of unfolded protein response genes under endoplasmic reticulum stress in Arabidopsis thaliana. *Plant Molecular Biology Reporter*; 35(2): 188-202.

25. Guo Q, Zhang J, Gao Q, Xing S, Li F, Wang W. 2008. Drought tolerance through overexpression of monoubiquitin in transgenic tobacco. *Journal of Plant Physiology*; 165(16): 1745-1755.

26. Kurepa J, Walker JM, Smalle J, Gosink MM, Davis SJ, Durham TL, Vierstra RD. 2003. The small ubiquitin-like modifier (SUMO) protein modification system in Arabidopsis accumulation of sumo1 and -2 conjugates is increased by stress. *Journal of Biological Chemistry*; 278(9): 6862-6872.

27. Nigam N, Singh A, Sahi C, Chandramouli A, Grover A. 2008. SUMO-conjugating enzyme (Sce) and FK506-binding protein (FKBP) encoding rice (*Oryza sativa* L.) genes: genome-wide analysis, expression studies and evidence for their involvement in abiotic stress response. *Molecular Genetics and Genomics*; 279(4): 371-383.

28. Lara-Ávila JP, Isordia-Jasso MI, Castillo-Collazo R, Simpson J, Alpuche-Solís ÁG. 2012. Gene expression analysis during interaction of tomato and related wild species with *Clavibacter michiganensis* subsp. *michiganensis*. *Plant Molecular Biology Reporter*; 30(2): 498-511.

29. Ishida T, Yoshimura M, Miura K, Sugimoto K. 2012. MMS21/HPY2 and SIZ1, two Arabidopsis SUMO E3 ligases, have distinct functions in development. *PloS One*; 7(10).

30. Chen CC, Chen YY, Tang IC, Liang HM, Lai CC, Chiou J M, Yeh KC. 2011. Arabidopsis SUMO E3 ligase SIZ1 is involved in excess copper tolerance. *Plant Physiology;* 156(4): 2225-2234.

Celal Bayar University Journal of Science
Volume 16, Issue 3, 2020, p 307-321
Doi: 10.18466/cbayarfbe.740343

Celal Bayar University Journal of Science

Real-Time Prediction of Electricity Distribution Network Status Using Artificial Neural Network Model: A Case Study in Salihli (Manisa, Turkey)

Mahmut Sayar[1]*, Hilmi Yüksel[2]

[1,2] Department of Business Administration, Dokuz Eylul University, Izmir, Turkey
*mahmutsayar@hotmail.com
*Orcid No: 0000-0002-1852-6276

Received: *20 May 2020*
Accepted: *14 September 2020*
DOI: *18466/cbayarfbe.740343*

Abstract

Electricity distribution networks are critical to the delivery of energy and the continuity of the economy. The healthy and efficient operation of these networks depends on the prediction of failures, their early detection and the rapid recovery of the resulting failures. The causes of failure are internal and external factors. Many studies in different sectors that use different techniques for failure prediction in the literature. The use of artificial intelligence techniques, which are becoming increasingly important today, in failure estimates; in terms of estimation success and effectiveness, it brings many privileges compared to other techniques. In this study, a status prediction model has been developed by using artificial neural network (ANN) technique for power outages and healthy working conditions of the electricity distribution network installed in Salihli district of Manisa province. In previous studies, using artificial intelligence techniques in the energy sector generally focused on one component of network, lifetime, energy demand estimation, battery life and goods failures. The effect of meteorological factors has not been studied on the distribution network situation using artificial intelligence techniques. In this study we use hourly power outages and hourly meteorological factors that cause failures or healthy conditions. It is aimed to effective risk management and make anticipation of power outage occurring in electricity transmission network, to make preventive maintenance for failures, to make suggestions for early intervention and shortening downtime and maintenance.

Keywords: Production and Service Systems, Operations Management, Artificial Intelligence, Electric Power Distribution Network, Fault Diagnosis, Risk Management, Reliability

1. Introduction

Artificial intelligence (AI) can be defined as the whole of multidisciplinary theories, techniques, concepts and technologies applied to develop machines that can simulate intelligence. AI is a science that has been researched and developed in many fields such as machine learning (ML), image processing, natural language processing and robotics etc. The success of machine learning algorithms is shaped by the experience preferences of the model developer. For this reason, AI's success in industrial applications depends on the developer's capabilities. AI is a discipline that focuses on developing, validating, and implementing learning algorithms for industrial applications. AI will be integrated with cyber physical systems, Internet of Industrial Things (IIoT), big data and cloud computing in the process of expanding Industry 4.0 integration.

Celal Bayar University Journal of Science
Volume 16, Issue 3, 2020, p 307-321
Doi: 10.18466/cbayarfbe.740343

As a result, industry processes will acquire flexible, efficient and sustainable capabilities [1]. Artificial neural networks (ANN) is one of the artificial intelligence techniques. It can be defined as one of the important modeling tools used for modeling complex problems in many disciplines, which are easier to use recently in line with the developments in hardware and software. ANNs are composed of interconnected adaptable processing elements that can perform parallel calculations [2]. The ANN technique uses what is known about the functionality of biological organisms to solve complex problems. The advantages of ANN models are due to the characteristics of biological systems such as nonlinearity, high parallelism, error tolerance, learning and fuzzy computing privileges [3].

In previous studies, using artificial intelligence techniques in the energy sector generally focused on issues such as energy demand estimation, battery life, battery charging time, wind power plants, lifetime and electronic goods failures. Studies on failures in power distribution network are generally on one component of the network. The effect of meteorological factors has not been studied on the distribution network situation using artificial intelligence techniques. Factors causing failure in electricity distribution networks are separated into two groups, internal and external factors. Internal factors include transmission cable length, transformer properties, equipment, brands, etc. external factors include meteorological factors. In this study, it is aimed to create a real-time failure and healthy conditions prediction system of the electric power distribution network in dynamic environment conditions, to increase the security level of the system and to reduce system failure probabilities using ANN. By using historical, real time and predictive meteorology data and healthy/faulty status data; system faults and healthy conditions have been estimated in Salihli district.

2. Artificial Neural Network (ANN)

Artificial neural networks have been developed based on the working principle of the brain's nerve structure. As it is known, the learning event of the brain takes place through experiments. It consists of three main sections: input layer, hidden layer and output layer. The first entries of the input data into the neural network are done through the input layer. The values in this layer are moved to the neural network and neurons transmit information to the other layer as value. The hidden layer is located between the input and output layers. In this layer, the depth and number of neurons are done by experimental studies. The output values of the network are created in the output layer [4].

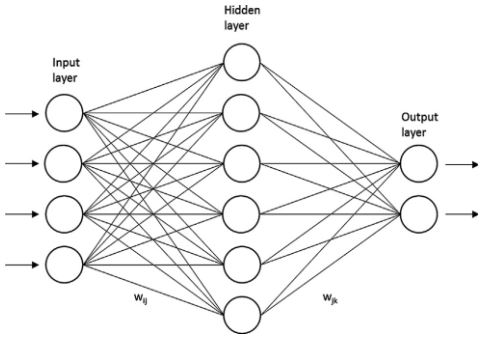

Fig. 1. General Structure of an Artificial Neural Network [5].

ANN is defined as a model consisting of one or more layers formed by neurons and calculating based on the working principle of the human brain. With the selection of the calculation type, it is decided that the ANN model will have feedforward or back propagation architecture. In the ANN learning process, weights of neural network connections are adjusted according to learning rules. Neural networks can be designed according to supervised learning, unsupervised learning and reinforcement learning method. While deciding which of these learning methods to use, it is taken into consideration the problem studied. Activation functions such as hyperbolic tangent, sigmoid, radial basic function and Rectified Linear Unit are commonly used in ANN [6]. The multi-layer perceptron (MLP) consists of the input layer, one-multiple hidden layers and output layers. Each neuron in one layer is connected with every node in the next layer. MLP uses back propagation method in supervised learning situations [7].

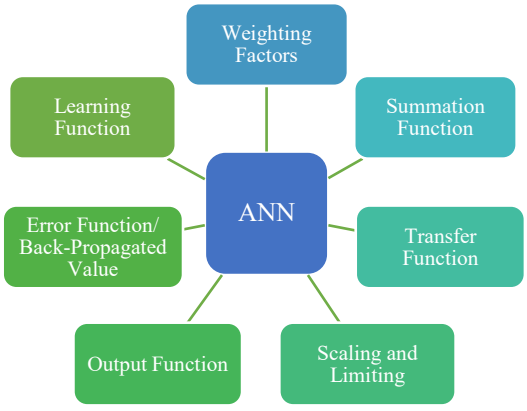

Fig. 2. Major Components of an Artificial Neuron [8].

Celal Bayar University Journal of Science
Volume 16, Issue 3, 2020, p 307-321
Doi: 10.18466/cbayarfbe.740343

ANN, developed by inspiring the brain's nerve structure. The brain performs the basic learning event with the data obtained from the experiences. This bio-inspired method will have an important place in the computer and computing industry. ANN is different from traditional computing and it does not use traditional programming methods. In solving the problems, it generally generates parallel networks and focuses on the training of these networks. ANN includes processes such as behaving, reacting, self-organizing, learning, generalizing, and forgetting [8].

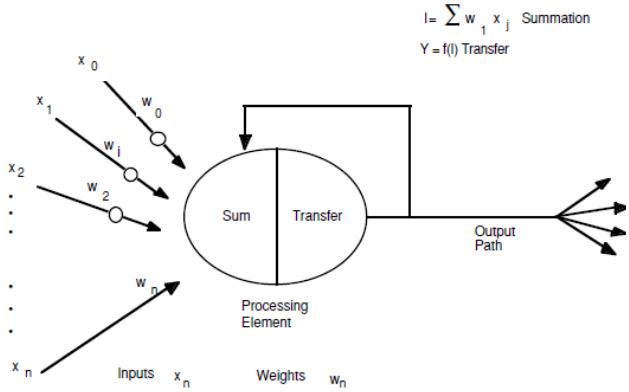

Fig. 3. A Basic Artificial Neuron [8].

In Fig. 3, x(n) shows the various inputs to the network. Each of these input values is multiplied by the link weights indicated mathematically with w(n). The results of the products are summed or subjected to other mathematical calculations. Output is produced after processing with a transfer function to produce results [8].

When calculating the output of the hidden layer, the ω_{ij} connection weight and the bias b_i between the hidden layer and the previous layer are used:

$$H_j = f\left(\sum_{i=1}^{n} \omega_{ij} x_i + b_i\right), j = 1,2,\ldots.l$$

In the formula, l represents the number of hidden layer neurons and f represents the activation function of the hidden layer. The final output of the ANN is calculated as follows:

$$O_k = f\left(\sum_{j=1}^{n} \omega_{ij} H_J + b_j\right), k = 1,2,\ldots.m$$

Where m represents the number of neurons in the output layer, ω_{ij} is connection weight and b_j is bias between the output layer and hidden layer.

The Mean Relative Error Rate (MRER) is determined as the error function of the SOH estimation model. Mean Absolute Error (MAE) was used as an error function in the training process of the RUL estimation model. The formulas of MRER and MAE are as follows:

$$MRER = 1/m \sum_{k=1}^{m} |(Y_k - O_k)/Y_k|, k = 1,2,\ldots.m$$

$$MAE = 1/m \sum_{k=1}^{m} |(Y_k - O_k)|, k = 1,2,\ldots.m$$

In the formula, m indicates the number of observations. Y_k represents the actual value and O_k represents the estimated value of ANN. The formula of the back propagation algorithm used for trainining process as follows:

$$\Delta\omega_{jk} = -\gamma \frac{\partial e_k}{\partial \omega_{jk}}, j = 1,2,\ldots.l;\ k = 1,2,\ldots.m$$

γ indicates the connection weight that takes values in the range of 0-1. It shows the degree of adjustment of the connection weight and bias [9].

ANN is used as alternatives to traditional statistical modeling techniques in different disciplines. Gardner and Dorling provides a general discussion for the final applications of the multilayered perceptron in atmospheric sciences, which is a kind of ANN [10]. Neural networks are used for solving problems related to many areas such as forecasting, optimization, clustering, pattern classification, function approximation, control etc [3], [5].

Celal Bayar University Journal of Science
Volume 16, Issue 3, 2020, p 307-321
Doi: 10.18466/cbayarfbe.740343

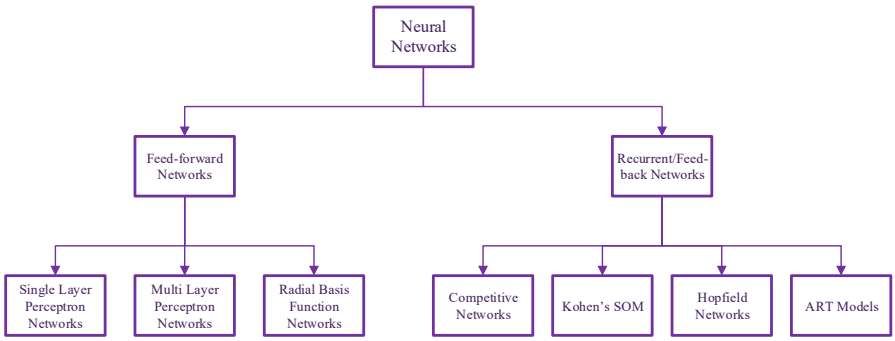

Fig. 4. A Classification of Neural Network Architectures [10].

Learning process and testing process in ANNs are two important steps. After training process in ANN, the success of training process is tested through test data. The success of learning is determined by comparing the predicted values of the training model with the data realized. The working scheme of the ANN is presented in Fig. 5.

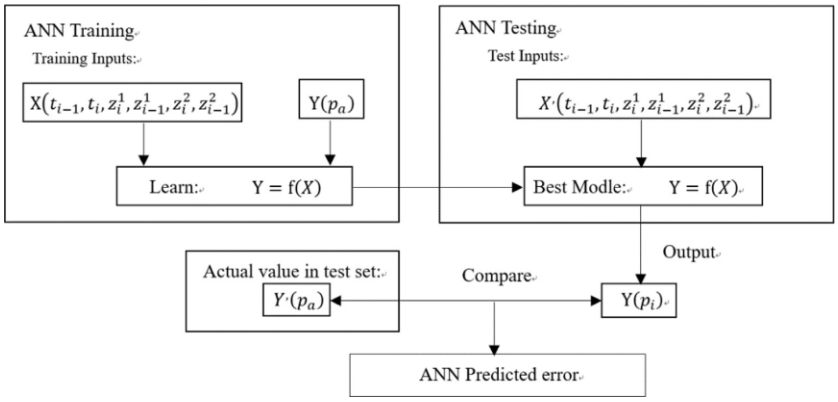

Fig. 5. Artificial neural network scheme used for predictive failure [11].

2.1. The Multilayer Perceptron Application

Models consisting of interconnected neurons that show a nonlinear network between the input and output vectors are defined as multilayer perceptron (MLP). Neurons are connected by definite weights and output values produced. Signals and weights are a function of the sum of the inputs to the neuron replaced by the activation function. It is formed by combining many nonlinear transfer functions that enable the multilayer perceptron to converge to nonlinear functions.

Since the logistic function can be easily derived, it is widely used in transfer functions. The output of a neuron is determined by the connection weight and this output is transmitted to the neuron of the next layer. With this structure, a multilayered sensor is known as feed forward neural network. The structure of a multilayer perceptron varies depending on the situation. When the input layer of neural networks (NN) is examined, no calculation is made in this layer. The task of this layer is to ensure that the input vector is transferred to the neural network. A multilayered perceptron consists of one or more hidden layer. It has only one output layer. MLP are defined as fully connected to each neurons, depending on each node in the previous and next layer [10]. Each layer except the input layer takes the necessary actions using the output from the previous layer and transfers the results to the next layer [12].

Multilayered perceptron gain the ability to learn using training data set consisting of input and relevant outputs. During the training process, the appropriate amount of training data is given to the multilayer perceptron and the weights in the network are adjusted

until the desired input-output level is achieved. MLP are trained by supervised learning method. During training process, the output of the MLP for a given input may differ from the desired output. This error is defined as the difference between the actual and expected value. General error is reduced by using the value of the error signal to determine the values of connection weights in the network during training. The training of a MLP is done through trials where certain connection weights are re-determined to resolve the network modeling relationship. Many algorithms that can be used to train a multi-layered perception. The backpropagation algorithm uses this method to find the general min value of the error surface [10].

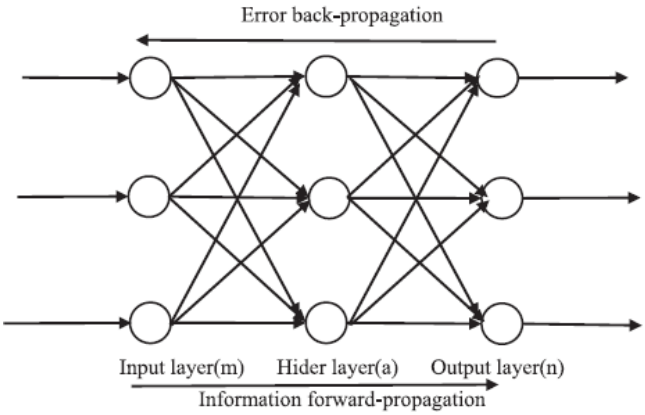

Fig. 6. Structure diagram of a three-layer back propagated neural network (BPNN) [13].

The back propagation algorithm used by Rumelhalt et al is the most suitable method for the training of the MLP. Connection weights in neural network are initially determined as small random values. After the initial calculations, the backpropagation method find out the local gradient of the error surface. It updates the weights in the steepest local gradient direction. It is hoped that the weights will approach the global minimum of the error surface. Training must be finished when the multi-layer perceptron's performance on independent test data is maximized and network error is minimized [10].

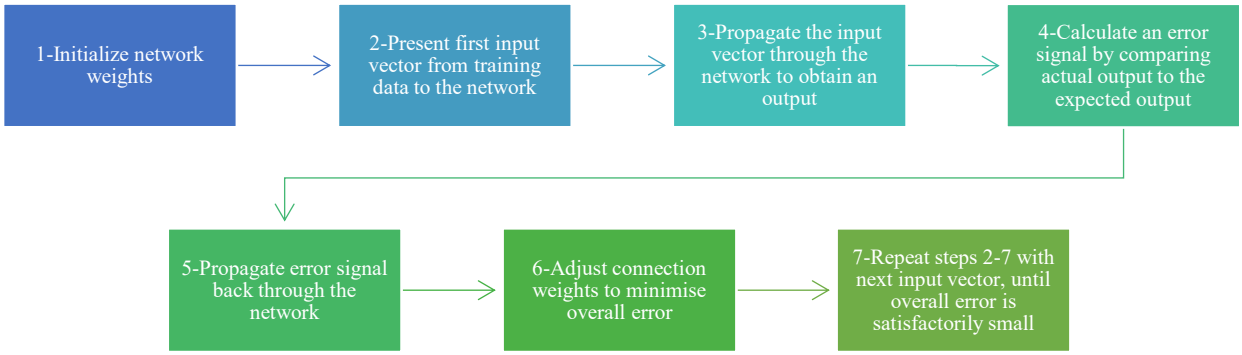

Fig. 7. The back propagation algorithm [10].

2.2. Teaching an Artificial Neural Network

Training an ANN is similar to the learning method of the brain. The brain learns through experiences and experiments. In ANNs, there are three learning rules under reinforcement learning (RL), supervised learning (SL) and unsupervised (USL) learning.

In the SL method, the real output of a NN is compared with the desired output. The randomly assigned connection weights are then set by the network. In this way, the next iteration generates a closer match between actual and desired output. While the learning method is running, it tries to minimize valid errors of all processing items. This global error reduction is

constantly changing the connection weights until an acceptable accuracy value is achieved over time. The training data set provides input and output data to the neural network that occurred in previous times. The corresponding desired output set is also provided for each input set. Actual data is used in most applications. The learning process can take a long time with the hardware that has inadequate processing power. The training of neural networks is completed when it reaches the level of predefined parameters. When training is complete, the current weights are often frozen. For the success of the neural networks calculation, the training data set must be in a large volume containing all the necessary information [8].

Unsupervised learning is an important area where great advances in the future will be made. It paves the way for computers to learn robotically on their own in the future. Such networks are not widely used. These networks do not use any external factors to update their connection weights. Instead, it monitors its performances internally. These networks examine trends or regularity in the input signals and adapt them to the network. The network has some information about how to organize itself. This information is included in learning rules and network architecture. In the training of clusters, weights of only the winning process elements are updated with the learning competition rule [8].

The learning rate is closely related to the learning performance of the network in ANN. The learning rate is the value that indicates how important we consider the error. Given the high rate of learning values errors lead to big changes. Choosing a high learning rate reduces the learning ability of the network. Even with small values, it extend the learning time of the ANN. Therefore, the optimal value should be chosen.

3. Electric Power Distribution

Electrical energy makes our life easier in almost every field. It is also a very important component for the development of the industry. Electricity is generally derived from fossil fuels, nuclear and other non-renewable sources. New power generation systems can easily fail due to random features and effects. For this reason, there are many studies on the reliability and stability problem of the system. System reliability can generally be defined as the probability of reaching certain targets at the desired level under certain internal and external factors. Reliability engineering started to develop after 1940 with the development of statistical methods. This engineering field has started to be used frequently in defense industry. In the 1960s, electrical errors and other system instabilities began to appear in many countries such as Japan and the USA. Power system reliability has been emphasized in the literature since these dates. The power system consists of three main parts. The generation system, transmission system and distribution system are interconnected to each other. The generation system is separated into two classes as renewable and traditional electricity generation system [14].

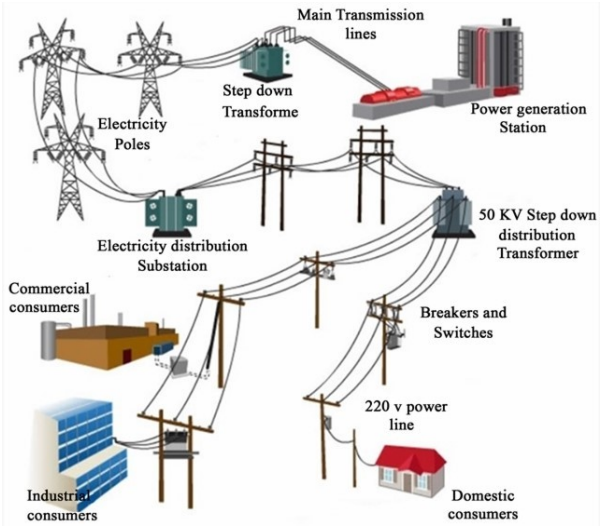

Fig. 8. Electric Power Distribution Network [15].

Transmission lines connect power plants and distribution system. The main objective of the generation and transmission system is to provide sufficient electric power to each main load points within the network. Short circuits or other serious defects often cause the electrical failures in the transmission system. Reliability criteria in the power system are basically the probability of failure, expected reduced load and the expected load reduction time. Indices evaluating the distribution system reliability are used as customer average interrupt frequency index (CAIFI), customer average interrupt duration index (CAIDI), system average interrupt frequency index (SAIFI), system average interrupt duration index (SAIDI). Production, transmission and distribution system will work uninterruptedly in all working situations. Therefore, handling three system reliability simultaneously is an important approach to increase overall electric power system reliability [14].

The success of failure diagnostics plays a crucial role in the reliable and healthy operation of power supplies. The applications of expert systems on failure diagnostics give successful results. Besides, application times take a long time [16].

Yongxing et al. calculated the probability of power network failure considering their some meteorological factors. Calculating the probability of real time failure of electric power transmission lines is significant in terms of online risk assessment and real time reliability of the power system network. In the study, fuzzy member functions of the factors were examined first. The uncertainty theory is combined with the fuzzy evaluation method to designate the weighting coefficient of layers. Actual data was collected for simulating the model. The model was verified with actual weather data and power network fault data. Research results showed that the recommended method was successful. Mechanical faults are caused by metal damage, wire fracture, insulator chain fracture or crack, foundation collapse, etc. Current studies on electric power network failure mainly includes weather and operational risk assessment. In the study, real-time failure probability assessment method is presented for overhead electric power transmission lines using meteorological factors [17].

McElroy detected four single-phase EHV transformer faults at the American public institution caused by transformer winding resonance. In previous researches, only the errors of the transformer components were detected with the help of statistical analysis methods. Detailed root causes related to faults have not been investigated. In McElroy's study, not only defining the fault mode, but also the main causes of failures are investigated [18]. Coughlin emphasized that there is no scientific research of the relationship between the physical effects and quantitative analysis used in climate change and energy planning studies in the literature. The study includes determinations on how to use climate models to define how these risks can change over time, including the sensitivity of the electrical system to physical weather risk and the elimination of uncertainties [19].

3.1. Previous Studies Using Artificial Neural Network

Baqqar uses generalized regression neural network (GRNN), back propagated ANN (BPNN) and adaptive network-based fuzzy inference system (ANFIS) for status monitoring of gearboxes in electric motors [20]. Cristaldi et al. [21] used ANN and statistical approaches to predict the remaining useful lifes of medium and high voltage circuit breakers. Seidgar et al. [22] used a multi-purpose algorithm improved with neural networks for the maintenance schedule and work order to reduce production disruptions [23]. Zhang et al. used methods of ANN and partial incremental capacity to predict the health and remaining useful lifes of the batteries under constant current discharge. Estimations with high reliability and accuracy were made with the proposed methods [9]. Marugán et al. provide a comprehensive review of ANNs used in wind energy systems. Researchers determine the most used methods for applications and shows that ANNs can be an alternative to traditional methods in many cases. According to the literature review in the study, the main difficulties and technological inadequacies regarding the application of ANN to wind turbines are explained [5].

Mousavian et al. proposes a NN based protection method by investigating the risks against cyber-attacks associated with the data of electric power system transmission. The proposed model can monitor the output of power flow calculations and detect data abnormalities in real time. In the study, it was mentioned that cyber attacks can be as dangerous as physical attacks on the power grid due to the great damage and losses [24]. Silva et al. used an incremental learning algorithm based on real data to predict high impedance failures in electrical power distribution system. The efficiency of recommended evolutionary system to detect and classify failures was compared with the multilayered NN, probabilistic NN and support vector machine(SVM) methods. The results of the study state that the recommended system is suitable for changes [25]. Significant progress is being made in the field of electric power systems in all sectors. Renewable energy sources, their increasing influence, increasing the number of customers and appropriate green energy policies trigger the development of the electrical system. In the light of these developments, Saviozzi et al. used ANN to increase the functionality of the load estimation and load modeling processes required by distribution management systems [26].

Đozić et al. analyze it by developing a model of ANNs to predict CO_2 emissions by 2050 based on the EU's current energy policy. With the study, ANN has been effective in predicting the behavior of CO_2 emissions. It

will also change the indicator's value by 2050 to ensure that CO_2 emissions are reduced in a planned manner, ensuring timely improvement of economic and energy strategy [27]. Khwaja et al. use ANN based ensemble ML to improve short term electrical charge estimation. The recommended technique combines both strengthening and bagging to train ANN. A group of multiple ANN models were trained in parallel. To obtain the last estimated load, the estimated loads of these models are averaged [28]. The first researches on wind speed estimation were generally done using numerical and physical mathematical models [29]. Lawan et al. proposed a wind condition-forecasting model using topographic machine learning to study wind energy potential in Sibu. In the study where a land-based ANN was developed, it was found that wind speed values can be successfully estimated in the areas where the model is applied [30].

Condition based maintenance method (CBM) predicts a maintenance plan depends on data obtained in case of failure and non-faulty operating situations. Various sensors and monitoring devices such as acoustic-ultrasonic sensor, accelerometer, current measurements and thermocouples are needed to monitor the status of a system with CBM. In addition, it provides highly useful information from environment condition's data such as pressure, humidity, temperature et.al to increase the effectiveness of the model. In the light of this data, certain KPIs are analyzed to reveal potential tendencies that can lead to a critical failure. The aim is to adopt a suitable CBM system that provides forecasting and monitoring capabilities by simultaneously combining important data to ensure maximum reliability [23]. The purpose of Mohamed and Rao's study is to develop a fault diagnostic system for distribution networks using ANN. In this study, multi-layer feed forward neural network with back propagation algorithm was used. In the study, the determination of the error, identification of the defective parts and the classification of the errors according to the types were carried out [16].

4. Prediction of Electric Power Distribution Condition Using Artificial Neural Network

In this section, a case study of the electricity distribution network of Salihli district is presented. The data of the district were obtained from the electricity distribution company and Turkish State Meteorological Service. ANN model was developed for the status of the electricity distribution network by matching the data obtained from these institutions. Learning for the unplanned power outages and healthy conditions of the distribution network has been made and the predictions of the future system status have been made.

4.1. Data

Salihli, located in Turkey's Aegean province of Manisa is one of the districts. The ancient city of Sardes, where the first money was used in history and now included in the UNESCO World Heritage Temporary List, is located in this district. The surface area of the district is 1359 km² and the altitude is 108m. According to 2019 data, its population is 162787 people. Totally more than 5000 unplanned power cuts occurred in the district in 2017 and 2018. Power outages negatively affects the economic and social life in the district. In our study, the hourly condition (outage or healthy) of the electricity distribution line of Salihli and meteorological data that occurred at that time were used.

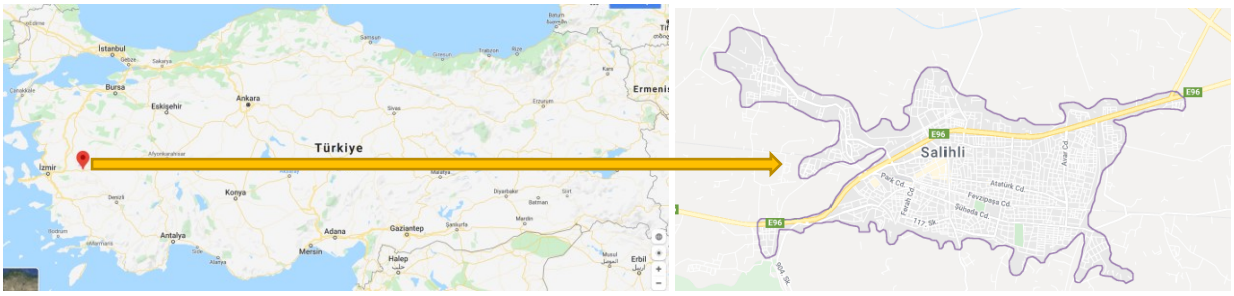

Fig. 9. The location of Salihli in Turkey.

Celal Bayar University Journal of Science
Volume 16, Issue 3, 2020, p 307-321
Doi: 10.18466/cbayarfbe.740343

In this study, we used a total of 11428 hours data set regarding meteorological data and power grid status (1:Outage - 0:Healthy). We randomly divided 80% (9149) of the data set into learning (training) and 20% (2279) as test data. We took atmospheric pressure (hPa), relative humidity (%), wind speed (m / s), wind direction (°), temperature (°C) and amount of precipitation (mm = kg / m²) as inputs of the model. Example of data set prepared for training process is presented in Table 1.

Table 1. Part of The Data Set Ready for The Training Process.

Date & Hour	Power Outage (1-0)	Atmospheric Pressure	Relative Humidity (%)	Wind Speed (m÷sn)	Wind Direction (°)	Temperature (°C)	Amount of Precipitation (mm=kg÷m²)
17-1-2018 13	0	993.3	46	1.6	146	16.5	0
17-1-2018 14	1	992.4	49	2.3	138	15.8	0.2
17-1-2018 15	0	991.6	48	2.7	196	15.4	0
17-1-2018 16	0	990.7	49	4	212	15.5	0.4
17-1-2018 17	1	989.8	55	2.4	138	13.6	0
17-1-2018 18	1	989	57	2.6	267	14.4	0
17-1-2018 19	0	988.7	57	1.9	38	15	0
17-1-2018 20	0	988	57	1.5	299	16	0.2
17-1-2018 21	1	987.4	64	1.8	88	13.9	0
17-1-2018 22	0	986.4	68	1.8	104	13.4	0
…..	…..	…..	…..	…..	…..	…..	…..
…..	…..	…..	…..	…..	…..	…..	…..
Total 11428 hours of data set							

General statistical distribution of input data are presented as Fig. 10, Fig. 11, Fig. 12, Fig. 13, Fig. 14 and Fig. 15.

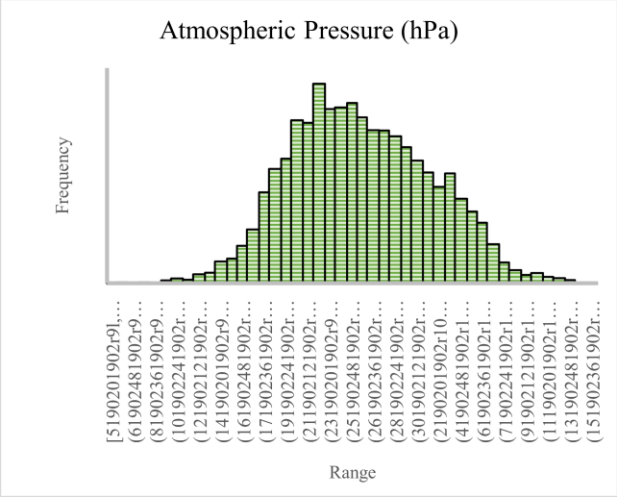

Fig. 10. Atmospheric Pressure Diagram (hPa).

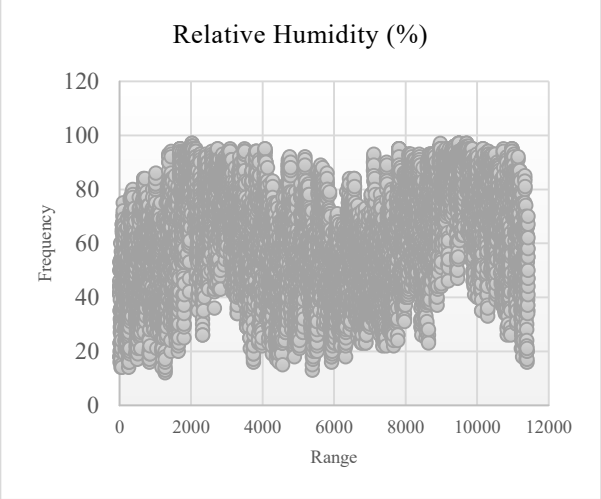

Fig. 11. Relative Humidity Diagram (%).

Celal Bayar University Journal of Science
Volume 16, Issue 3, 2020, p 307-321
Doi: 10.18466/cbayarfbe.740343

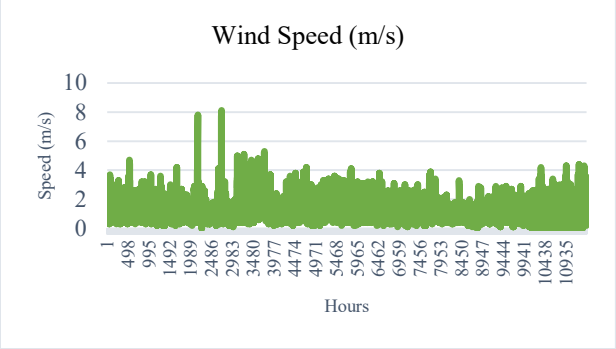

Fig. 12. Wind Speed Diagram.

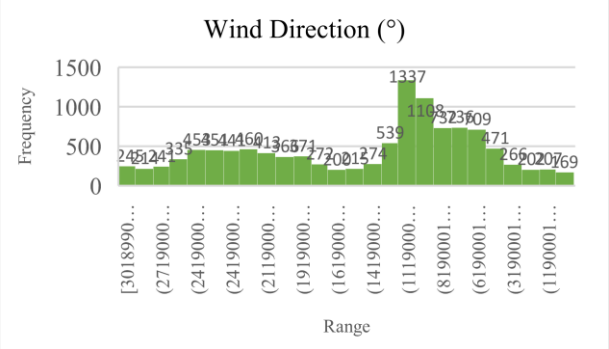

Fig. 13. Wind Direction Diagram.

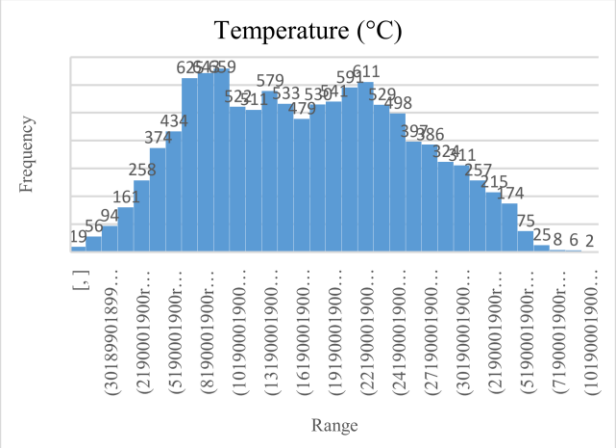

Fig. 14. Temperature Diagram.

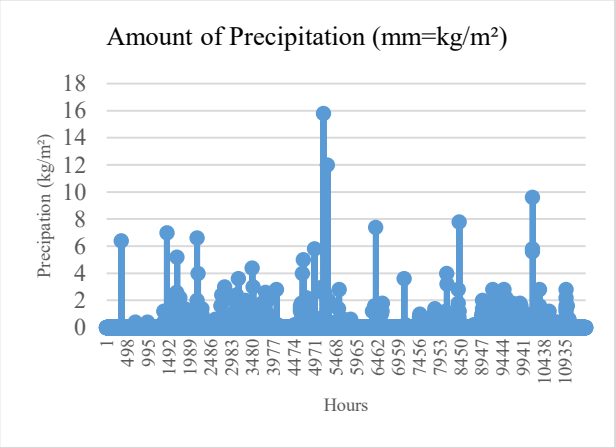

Fig. 15. Amount of Precipitation Diagram.

As the target of the study, we determined the hourly forecast of the healthy status and power outage conditions of the electricity distribution networks.

4.2. ANN Model

In this study, the situation of the network is tried to be estimated with the supervised learning method by using meteorological factors, which are the external factor for distribution networks, in cases where the electricity distribution network is healthy or outage. We established our ANN model after the data cleaning and combining processes. The installation parameters of the model are determined as follows Table 2. The process of cleaning, editing, merging and adapting the data sets from different data sources are very important for the success of the model of ANN. ANN modeling process is shown in Fig. 16 as algorithm steps.

Fig. 16. ANN Design Procedure.

We set the input parameters as temperature, relative humidity, atmospheric pressure, wind speed, wind direction and amount of precipitation and we determined the neural network as multilayer perceptron (MLP). We tried different network structures with the SPSS Modeler in determining the appropriate model. For this, we have repeatedly updated the model's layers and the number of neurons. As a result of these updates, the neural network structure in Fig. 17 gave appropriate results. Our neural network consists of 12 neurons in the first hidden layer and 9 neurons in the second hidden layer. We set the model type as classification and train neural network 750 times with learning data set. During this learning process, the network learned 9149 hours of data set in total 11428 hours of data set.

Table 2. Parameters of ANN Model.

Fields		
	Target	
		Power Grid Status (1:Outage - 0:Healthy)
	Predictors(Inputs)	
		Relative Humidity (%)
		Wind Speed (m/s)
		Amount of Precipitation (mm=kg/m²)
		Atmospheric Pressure (hPa)
		Wind Direction (°)
		Temperature (°C)
Build Options		
	Basics	
		Neural network model: Multilayer Perceptron (MLP)
		Hidden Layer-1: 12
		Hidden Layer-2: 9
	Stopping Rules	
		Use max training time (per component model): True
		Customize number of max training cycles: True
		Maximum number of cycles: 750
		Accuracy (%): 95.0
	Advanced	
		Overfit prevention set(%): 2
		Replicate Results: True
		Random seed: 75987945
		Missing values in predictors: Delete listwise
Training Summary		
	Method	Neural Networks
	Records used in training	9149
	Model type	Classification
	Predictors used in model	
		Amount of Precipitation (mm=kg/m²)
		Atmospheric Pressure (hPa)
		Relative Humidity (%)
		Temperature (°C)
		Wind Direction (°)
		Wind Speed (m/s)

Celal Bayar University Journal of Science
Volume 16, Issue 3, 2020, p 307-321
Doi: 10.18466/cbayarfbe.740343

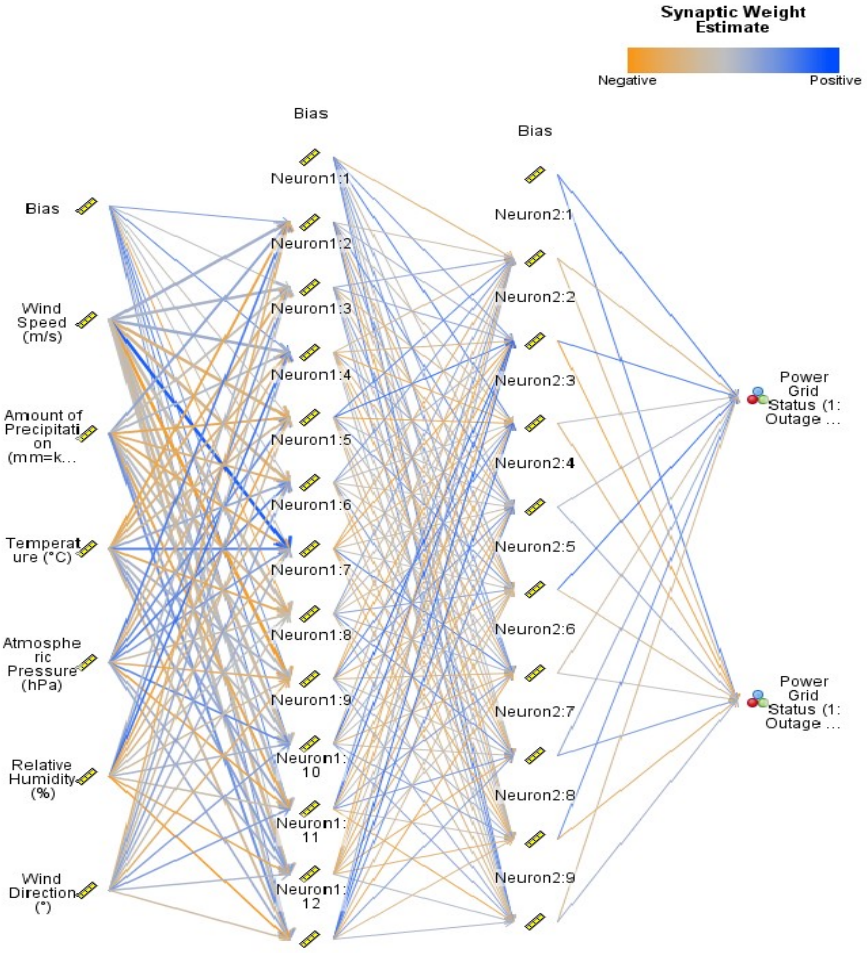

Fig. 17. Artificial Neural Network Model of Salihli Electricity Distribution Network.

Table 3. Actual and Prediction Results of Power Grid Status With Test Data Set (1:Outage - 0:Healthy).

Result No	Power Grid Status (1:Outage - 0:Healthy)	Prediction of Power Grid Status (1:Outage - 0:Healthy)	
1	0	0	True Positive
2	1	0	False Negative
3	0	0	
4	1	0	
5	1	0	
6	0	0	
7	0	0	
8	1	1	True Negative
9	1	1	
10	0	1	False Positive
11	1	0	
12	0	0	
13	1	0	
14	0	0	
15	1	1	
…	…	…	
…	…	…	
2278	0	0	

5. Results and Discussion

The ANN model is runned 750 times using the learning dataset of 9149 (80%) hours and the test dataset of 2278 (20%) hours, which is randomly partitioned into two parts over the data set of Salihli district. The results of the prediction of the model are given in confusion matrix (Table 3 and Table 4).

After the learning process, using the 2278 hour test data set, in the prediction process regarding the status of the network; 1491 healthy conditions (True Positive) and 117 fault conditions (True Negative) were estimated correctly.

Table 4. Classification for Power Grid Status With Test Data Set (1:Outage - 0:Healthy).

	Predicted		
Observed	0	1	Total
0	1491	155	1646
1	515	117	632
Total	2006	272	2278

In 155 cases, there was no real fault, but the result of a failure situation was estimated (False Positive). It has been estimated that the network will operate properly for 515 cases where there are actually a failures (False Negative). Overall predictive accuracy of the model is given Table 5. and Fig. 18.

Table 5. Overall Predictive Accuracy of The Model with Test Data.

	Overall Prediction	%
Correct	1608	70.59%
Wrong	670	29.41%
Total	2278	100.00%

According to the results, when all the estimation scores are combined, our model predicts the hourly status of the electricity distribution network of Salihli district by 70.59% accuracy and 29.41% error.

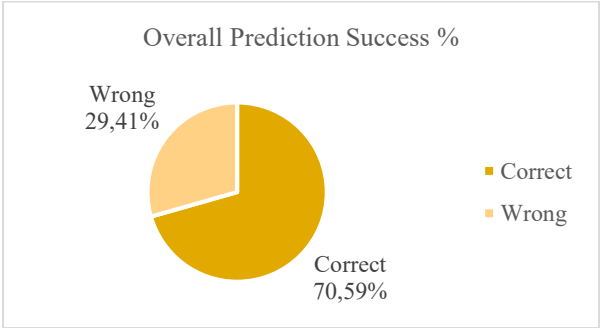

Fig. 18. Overall Prediction Score Chart.

As a result, when all the estimation scores are combined, our model predicts the hourly status of the electricity distribution network of Salihli district by 70.59% accuracy and 29.41% error.

Table 6. Predictor Importance of ANN Model.

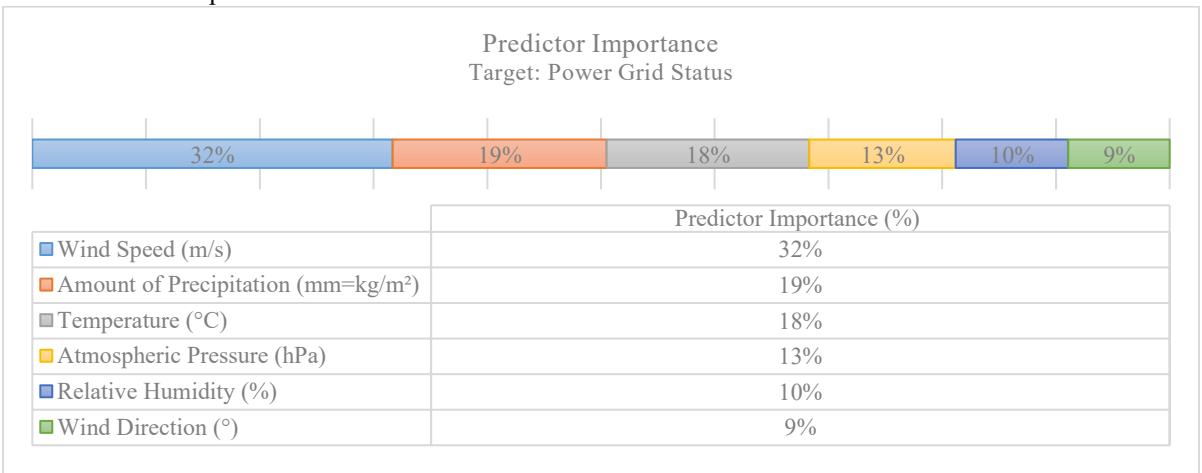

	Predictor Importance (%)
Wind Speed (m/s)	32%
Amount of Precipitation (mm=kg/m²)	19%
Temperature (°C)	18%
Atmospheric Pressure (hPa)	13%
Relative Humidity (%)	10%
Wind Direction (°)	9%

In this article, where we examine the effect of meteorological factors on the status of electricity distribution network in Salihli district, it is analyzed that the importance of each factor in predicting the status of the network is different. Predictors importance are given in Table 6. In our ANN model, it is calculated

that the wind speed is the best predictor for the network status for the district of Salihli (32%). The predictive significance levels of precipitation amount and temperature values are close to each other; The amount of precipitation is 19% and the temperature is 18% predictive. Atmospheric pressure is 13% and relative humidity is 10% predictive; The wind direction has the lowest predictive significance with a value of 9%.

According to the results, the ANN model can make the forecast with a high success rate of the distribution network status by using the future forecast data of meteorological factors. Real-time data sharing between electricity distribution companies and meteorological measurement institutions is of great importance in terms of electricity distribution network security.

6. Conclusion

This study was carried out to draw attention to the need for simultaneous evaluation of internal factors (transformer information, cable lengths, brand ... etc.) and external factors (meteorological) affecting the working status of electricity distribution networks. In our study, ANN model was developed by using only external factors (meteorological) that affect the working status of the electricity distribution network. According to the obtained results, hourly estimation of the healthy and power outage conditions of the network with 70.59% accuracy has been realized successfully. Thanks to our ANN model, the status of the electricity distribution network of Salihli can be estimated with 70.59% accuracy level by using meteorological forecast data of the future. It will be appropriate to take preventive precaution by the relevant institutions to reduce the damage caused by wind speed, air temperature and other factors in order of importance to the transmission lines.
In later studies, with the Industry 4.0 infrastructure to be integrated into the electricity distribution networks, the data on the internal (transmission cable lengths, cable cross section, transformer properties, brands, etc) and external factors of the network will be obtained more accurately and easily. In addition, better prediction results can be obtained with deep learning models that will be created by using different learning algorithms and increasing the number of layers, neurons and epoch values in neural networks.

Author's Contributions

Mahmut Sayar: Drafted and wrote the manuscript, performed the experiment, result analysis and interpretation.
Hilmi Yüksel: Supervised the manuscript's progress, interpretation and helped in manuscript preparation.

Ethics

There are no ethical issues after the publication of this manuscript.

References

1. Lee, J., Davari, H., Singh, J. ve Pandhare, V. (2018). Industrial Artificial Intelligence for industry 4.0-based manufacturing systems. *Manufacturing Letters*, *18*, 20–23. doi:10.1016/j.mfglet.2018.09.002.

2. Hecht-Nielsen, R. (1990). Neurocomputing, Addison. *Wesely Publishing Company. Hornik, K. Stinchcombe, M. White, H.(1989). Multilayer feedforward networks are universal approximators, Neural Networks*, *2*(359366), 3168–3176.

3. Basheer, I. A. ve Hajmeer, M. (2000). Artificial neural networks: fundamentals, computing, design, and application. *Journal of microbiological methods*, *43*(1), 3–31.

4. Shaban, S. E., Hazzaa, M. H. ve El-Tayebany, R. A. (2019). Applying Monte Carlo and artificial intelligence techniques for 235U mass prediction in samples with different enrichments. *Nuclear Instruments and Methods in Physics Research, Section A: Accelerators, Spectrometers, Detectors and Associated Equipment*, *916*, 322–326. doi:10.1016/j.nima.2018.10.008.

5. Marugán, A. P., Márquez, F. P. G., Perez, J. M. P. ve Ruiz-Hernández, D. (2018). A survey of artificial neural network in wind energy systems. *Applied energy*, *228*, 1822–1836.

6. Kruse, R., Borgelt, C., Braune, C., Mostaghim, S. ve Steinbrecher, M. (2016). Multilayer perceptrons. *Computational Intelligence* içinde (ss. 47–92). Springer.

7. Zhang, J. ve Li, J. (2020). Testing and verification of neural-network-based safety-critical control software: A systematic literature review. *Information and Software Technology*, 106296.

8. Anderson, D. ve McNeill, G. (1992). Artificial neural networks technology. *Kaman Sciences Corporation*, *258*(6), 1–83.

9. Zhang, S., Zhai, B., Guo, X., Wang, K., Peng, N. ve Zhang, X. (2019). Synchronous estimation of state of health and remaining useful lifetime for lithium-ion battery using the incremental capacity and artificial neural networks. *Journal of Energy Storage*, *26*, 100951.

10. Gardner, M. W. ve Dorling, S. R. (1998). Artificial neural networks (the multilayer perceptron)—a review of applications in the atmospheric sciences. *Atmospheric environment*, *32*(14–15), 2627–2636.

11. Lu, Y., Sun, L., Zhang, X., Feng, F., Kang, J. ve Fu, G. (2018). Condition based maintenance optimization for offshore wind turbine considering opportunities based on neural network approach. *Applied Ocean Research*, *74*, 69–79.

12. Berecibar, M., Devriendt, F., Dubarry, M., Villarreal, I., Omar, N., Verbeke, W. ve Van Mierlo, J. (2016). Online state of health estimation on NMC cells based on predictive analytics. *Journal of Power Sources*, *320*, 239–250.

13. Sun, W. ve Xu, Y. (2016). Financial security evaluation of the electric power industry in China based on a back propagation neural network optimized by genetic algorithm. *Energy*, *101*, 366–379.

14. Wang, J., Zhao, X., Guo, X. ve Li, B. (2018). Analyzing the research subjects and hot topics of power system reliability through the Web of Science from 1991 to 2015. *Renewable and Sustainable Energy Reviews*, *82*, 700–713. doi:10.1016/j.rser.2017.09.064.

15. Pngio. (2020). Electric Power Distribution. CRC Press. https://pngio.com/images/png-a1356339.html (accessed at 05.17.2020)

16. Mohamed, E. A. ve Rao, N. D. (1995). Artificial neural network based fault diagnostic system for electric power distribution feeders. *Electric Power Systems Research*, *35*(1), 1–10.

17. Yongxing, C., Yufang, Z. ve Hongyu, Z. (2017). Real-time Evaluation Model of Power Line Fault Probability based on Multiple Meteorological factors. *Procedia Computer Science*, *107*, 231–235. doi:10.1016/j.procs.2017.03.084.

18. McElroy, A. J. (1975). On the significance of recent EHV transformer failures involving winding resonance. *IEEE Transactions on Power Apparatus and Systems*, *94*(4), 1301–1316. doi:10.1109/T-PAS.1975.31968.

19. Coughlin, K. ve Goldman, C. (2008). Physical Impacts of Climate Change on the Western US Electricity System: A Scoping Study. *Lawrence Berkeley National Laboratory*, 29. http://escholarship.org/uc/item/8rc6q28 adresinden erişildi.

20. Baqqar, M. (2015). Machine Performance and Condition Monitoring Using Motor Operating Parameters Through Artificial Intelligence Techniques. University of Huddersfield.

21. Cristaldi, L., Leone, G., Ottoboni, R., Subbiah, S. ve Turrin, S. (2016). A comparative study on data-driven prognostic approaches using fleet knowledge. *2016 IEEE International Instrumentation and Measurement Technology Conference Proceedings* içinde (ss. 1–6).IEEE.

22. Seidgar, H., Zandieh, M. ve Mahdavi, I. (2017). An efficient meta-heuristic algorithm for scheduling a two-stage assembly flow shop problem with preventive maintenance activities and reliability approach. *International Journal of Industrial and Systems Engineering*, *26*(1), 16–41.

23. Diez-Olivan, A., Del Ser, J., Galar, D. ve Sierra, B. (2019). Data fusion and machine learning for industrial prognosis: Trends and perspectives towards Industry 4.0. *Information Fusion*, *50*, 92–111. doi:10.1016/j.inffus.2018.10.005.

24. Mousavian, S., Valenzuela, J. ve Wang, J. (2013). Real-time data reassurance in electrical power systems based on artificial neural networks. *Electric Power Systems Research*, *96*, 285–295.

25. Silva, S., Costa, P., Gouvea, M., Lacerda, A., Alves, F. ve Leite, D. (2018). High impedance fault detection in power distribution systems using wavelet transform and evolving neural network. *Electric Power Systems Research*, *154*, 474–483.

26. Saviozzi, M., Massucco, S. ve Silvestro, F. (2019). Implementation of advanced functionalities for Distribution Management Systems: Load forecasting and modeling through Artificial Neural Networks ensembles. *Electric Power Systems Research*, *167*, 230–239. doi:10.1016/j.epsr.2018.10.036.

27. Đozić, D. J. ve Urošević, B. D. G. (2019). Application of artificial neural networks for testing long-term energy policy targets. *Energy*, *174*, 488–496.

28. Khwaja, A. S., Anpalagan, A., Naeem, M. ve Venkatesh, B. (2020). Joint bagged-boosted artificial neural networks: Using ensemble machine learning to improve short-term electricity load forecasting. *Electric Power Systems Research*, *179*, 106080. doi:10.1016/j.epsr.2019.106080.

29. Carta, J. A., Ramirez, P. ve Velazquez, S. (2009). A review of wind speed probability distributions used in wind energy analysis: Case studies in the Canary Islands. *Renewable and sustainable energy reviews*, *13*(5), 933–955.

30. Lawan, S. M., Abidin, W. A. W. Z. ve Masri, T. (2019). Implementation of a topographic artificial neural network wind speed prediction model for assessing onshore wind power potential in Sibu, Sarawak. *Egyptian Journal of Remote Sensing and Space Science*. doi:10.1016/j.ejrs.2019.08.003.

Celal Bayar University Journal of Science

Classification of Haploid and Diploid Maize Seeds based on Pre-Trained Convolutional Neural Networks

Emrah Dönmez[1]*

[1]İnönü University, Central Campus Battalgazi/Malatya, Turkey
*emrah.donmez@inonu.edu.tr
*Orcid No: 0000-0003-3345-8344

Received: *26 May 2020*
Accepted: *14 September 2020*
DOI: *10.18466/cbayarfbe.742889*

Abstract

Analysis of agricultural products is an important area that is widely emphasized today. In this context, with the development of technology, computer-aided analysis systems are also being developed. In this study, a system has been proposed for classifying maize seeds as haploid and diploid using pre-trained convolutional neural networks. For this purpose, AlexNet, GoogLeNet, ResNet-18, ResNet-50, and VGG-16 pre-trained models have been used as feature extractors for the haploid and diploid seed classification process. In the first stage, the deep features of haploid and diploid maize seeds have been obtained in these models. The features have been taken from different layers of network architecture. Instead of softmax classifier in the last layer of the network, classifiers based on decision tree, k-nearest neighbor, and support vector machine have been used. According to the classification results with these features, the achievements in network architectures and classifier methods have been observed. The experiments have been carried out on a publicly available dataset consisting of 3000 haploid and diploid maize seed images. The experimental results revealed that the developed classification systems demonstrate a remarkable performance.

Keywords: Haploid Maize Seed Identification, Deep Features, Artificial Learning, Convolutional Neural Networks, Image Processing

1. Introduction

The researches have focused on computer-aided agriculture systems in terms of providing advantages such as growing healthy products, increasing production efficiency, and reducing costs in recent years. The main contribution of these systems is that they save time and labor. Computer-aided agricultural researches have gradually gained momentum [1, 2]. These systems are utilized extensively in most of the agricultural processes. The agricultural tools supported by these systems as well are commonly developed today. These systems prevent product havoc caused by human errors and ensure maximum efficiency.

In vivo maternal haploid breeding method has become the standard method in modern maize breeding because of its advantages compared to traditional methods [3]. In this maize breeding method, artificial chromosome folding is performed by treating haploid individuals with single chromosomes with colchillin and 100% pure lines can be obtained in 1-2 years [4]. Haploids must be separated from diploids after hybridization in order to increase the effectiveness of the method and to be successful. Depending on the characteristics of the inducer line used, haploid individuals in the range of 2-15% are obtained [5]. Separation of haploid individuals during the seed period is of great importance in terms of reducing greenhouse area, labor, and planting costs [4].

Although different genetic markers have been proposed to differentiate haploid maize seeds from diploids, the most common and successful method is the R1-nj color marker. In this method, which has been first used by Nanda and Chase [6], the inducer line carries the dominant R1-nj gene, which causes red-purple coloration in the embryo and endosperm. Since diploid seeds obtained as a result of crossbreeding carry chromosomes belonging to the inducer line, this coloration occurs in both embryos and endosperms. Haploid seeds, on the other hand, carry the chromosome of the inducer line in their endosperms, their embryos with single n chromosomes consist only of the chromosomes of the donor parent. Therefore, R1-nj coloration is seen in the endosperms of haploid seeds, but R1-nj coloration does not occur in their embryos.

This coloration difference occurring in embryos enables the visual separation of haploid and diploid seeds [7]. This separation is done manually today. In addition to this, it causes separation with high error rates; costs increase and separation takes a long time. Computer-aided classification methods are developed to overcome these problems. Today, with the advances in machine learning methods, deep learning methods based on convolutional neural networks (CNN) are widely used for computer-aided classification studies.

CNN aims to calculate the features of an object in image data based on multiple processing layers of artificial neural networks without using an external method [8]. Image processing techniques are used for the detection of the features (color, shape, texture, pattern, etc.) of the objects, segmenting the related objects properly and/or classification of the objects in the image data. Feature inputs used for traditional machine learning methods are obtained by processing image data. In the CNN method, the image data feeds the network input layer directly. Features are acquired from these layers without using additional image processing methods. More data may be required to train the network comparing to traditional methods. On the other hand, the transfer learning approach can be utilized to retrain classification part of a pre-trained CNN model to speed-up the training phase.

In summary, the CNN approach can provide great flexibility and remarkable achievements in the classification of object images. In this context, different CNN models have been used to classify images of maize seeds as haploid and diploid.

Related studies are given in the second part of the study. In the third section, the dataset and recommended methods are mentioned. The experimental findings obtained on the dataset are given in the fourth section. In the fifth section, the results obtained within the scope of the study are discussed and future studies are mentioned. In the last part, the references for the study are given.

2. Related Studies

There are some prominent studies using computer-aided methods and approaches to facilitate the separation of maize seeds. Some studies have focused to identify seed characteristics by using special imagining equipment or software tools. Recently, a remarkable number of studies have investigated the machine learning (ML) methods to extract features of the maize seeds. Then these features are used to train classification algorithms based on ML. Moreover, electro-mechanical systems have been also developed to classify the maize seeds. Based on all these studies, literature have been deeply investigated and state-of-the-art studies have been analyzed.

Couto and Davide [9] aims to identify haploids by flow cytometry and relate nuclear DNA content to the morphological and morphometric properties of the seeds that reveal them. In the study, molecular markers have been used to confirm the androgenetic nature of haploid. Boote et al. [10] have developed a new fluorescent-based method for inbred haploid discrimination in maize kernels using R1-nj color marker with fluorescence microsproscopy and imaging. In the study, seven inbred lines have been used with the changing R1-nj marker. As a result of the experiments carried out; the fluorescent response of diploid nuclei at the embryonic spot point is shown to have a lower intensity. Yu et al. [11] have proposed a nonlinear feature analytical method to identify haploid maize seeds based on Supervised Virtual Sample Kernel Locality Preservation Projection to take full advantage of class label information. They have said that using near-infrared spectroscopy technology to distinguish haploid seeds from hybrid seeds has the advantages of being non-destructive, fast, and cost-effective. Lin et al. [12] emphasized that maize haploid seeds have been automatically selectable using near-infrared (NIR) spectrum properties, thanks to the diffuse transmission technology of NIR spectroscopy. However, the NIR spectra of maize seeds have also been expressed to contain a lot of unnecessary features and noise that will reduce the identification performance. They have explained that they have overcome this problem by designing a low size and uniform size of the seed spectrum properties to improve the collected spectra. Wang et al. [13] aimed to investigate a fast and accurate method to identify haploid maize kernel using infrared hyperspectral imaging technology. This technology has been utilized to overcome the current automatic haploid identification limitations and provide a more accurate screening of haploid. Fuente et al. [14] focuses on defining the haploid lineage. In the study, six inbred lines have been developed with the maternal haploid inducer 'RWS / RWK-76' and a seed sample has been manually aligned for each line.

Wang et al. [15] have carried out the selection model design of high accuracy maize haploid seeds from diploid ones based on optimum waveband selection of the LSTM-CNN algorithm with deep learning and hyperspectral imaging technology. As a result of the experiments, it has been claimed that the accuracy rate reached 97% in the optimum waveband of 1367.6-1526.4nm. Altuntaş et al. [7] have proposed a method to classify haploid and diploid maize seeds using image processing and classification methods. Firstly, five different features are obtained from each maize seed image. Then the feature vectors are classified using a support vector machine classifier. In the study [16], texture features of maize seed embryos have been used. These features are derived from the gray level co-occurrence matrix. In another of their study [17], it is inspired by the latest achievements of deep transfer

learning, they address this problem as a computer vision task to present a non-destructive, fast, and low-cost model. To achieve this goal, CNN have been used to automatically recognize haploid and diploid maize seeds with a transfer learning approach. Altuntaş and Kocamaz [18] have proposed a computer-based method for the identification of haploid maize seeds. Maize seed embryos have been segmented by the k-means clustering method. In RGB, HSV, and Lab color spaces, the first four-degree color moments have extracted for each color channel. The obtained features then have been classified with SVM.

Song et al. [19] have designed an automatic separation system that can separate the haploid maize seeds from hybrid seeds marked with the R1-nj label, in their study. The system includes seed feeding, image acquisition, sorting, and system control units. The seed feeding unit distributes the maize seeds on a synchronous belt. The image acquisition unit acquires images of maize seeds and separates the heterozygous from the haploid nuclei depending on the color property of the endosperm. Finally, the separation unit performs physical separation with mechanical arms and solenoid valves that can select the heterozygous seeds using air intake.

3. Materials and Methods

3.1. Dataset

The dataset consisting of 3000 maize seed images in total [17] contains 1230 haploid and 1770 diploid maize seed images. The dataset occupies 49.3 MB of disk space. Each image obtained is in RGB color space and format is JPEG. Since the resolutions of the images in the dataset vary between 300x289 pixels and 610x637 pixels depending on seeds size, the images have been resized to the appropriate resolution according to the input layer of each CNN model. In this context, while 227x227 resolution is used for the AlexNet model, 224x224 resolution is used for GoogLeNet, Resnet18, ResNet50, and VGG16 models. Sample maize seeds have been demonstrated in Figure 1.

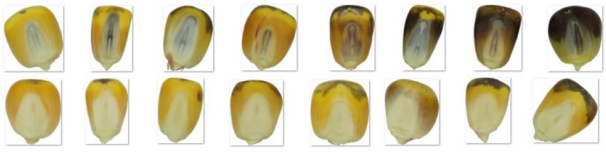

Figure 1. Sample diploid (top) and haploid (bottom) maize seed images from the dataset.

3.2. Deep Feature Extraction

A deep feature in the context of deep learning is that a unit (layer) within a hierarchical model responds consistently to an input, where this response contributes to the model's decision. Deep features are obtained from pre-trained CNN models. In other words, pre-trained CNN models can be used as feature extractors to feed any classifiers. Depending on where the model is located along with its hierarchical structure, one layer can be considered deeper than the other. Each of the network layers has deep features. Deep features are used in the network layers of the CNN model like convolution, pooling, etc. Their values/weights vary depending on the filter and mathematical operations applied in the layers. Deep features are expected to represent the highest level of images of objects intended to be classified.

AlexNet [20] is one of the pioneering deep learning algorithms. It has been introduced for the first time in 2012 as part of the ImageNet Large Scale Visual Recognition Challenge (ILSVRC). In this competition, it has attracted attention to the CNN architecture by providing a remarkable high performance. AlexNet is a CNN architecture with a total of 25 layers: input, convolution, ReLU (Rectified Linear Unit: it simply changes all the negative activations to 0. It is a basic layer for all CNN architectures), normalization, pooling, fully connected layer, drop-out, classification, and output. The AlexNet model has a total of 60 million computational parameters. The architecture takes 227x227 colored images as input.

ResNet [21] is a CNN architecture that uses the residual learning framework module to facilitate network training. The focus of this architectural model is the degradation problem. The novelty of the model is the use of residual blocks and the depth in its architecture. In a conventional convolutional deep learning model, stacked layers fit a desired underlying mapping, while the ResNet model allows these layers to be seated in a residual mapping. In this study, Resnet-18 and ResNet-50 have been used.

GoogLeNet [22] is another deep learning network that has managed to attract attention. Similarly, it has been revealed in the ILSVRC competition held in 2014. The most important difference in this architecture is the inception module added to the layers as a new block. This module consists of branching to more than one depth that works like a shortcut between layers. The most prominent feature of this CNN architecture is that the architecture increases width and depth while keeping the computational cost constant. It makes this possible with the newly added inception module. The module has improved the level of utilization of computing resources within the network architecture. GoogLeNet consists of 22 layers in total and 7 million computational parameters.

VGGNet [23] is a CNN architecture presented for the first time in the ILSVRC competition held in 2014. The most unique property about VGG16 is that instead of having many hyper-parameters, it is focused on having the convolution layers of a step-1 (stride-1) and 3x3 filter, and use always the same fill and maxpool layer of

the 2x2 step-2 (stride-2) filter. The convolution and maximum pool layers have been maintained consistently throughout the entire architecture. VGG16 is a fairly large network, it consists of 41 layers in total and has about 138 million (approximately) parameters.

3.3. Classifier Methods

A classification method uses a learning algorithm to define the model that is optimal to the relationship between the feature set of input data and the class label/tag. Therefore, the primary goal of the learning algorithm is to create a smart model that accurately predicts class tags of previously unknown records. The classifier method is employed to determine the label data of different classes in the utilized data set in this study.

Support Vector Machine (SVM) [24] are supervised learning models used for classification and regression analysis, analyzing data, with associated learning algorithms in machine learning. An SVM is a separator classifier that is formally defined by a separator hyperplane. In other words, when labeled training data is given, the algorithm produces an optimal hyperplane that categorizes new samples. The general SVM function dual version is given below (1). The second-order (quadratic) SVM classifier has been used to avoid the local minimum, in the study.

$$\boldsymbol{f(x) = \sum_{i=1}^{N} a_i \cdot y_i \cdot K(x, x_i) + b} \quad \textbf{(1)}$$

The N value given in the equation indicates the number of support vectors. Parameter $K(x, x_i)$ expresses support vectors. The parameter a refers to weight. The y_i parameter indicates the class to which the observations belong. The b corresponds to the bias rate threshold. The SVM model is the representation of samples as points in space so that samples of individual categories are divided into as wide space as possible. In addition to performing linear classification, SVMs can perform a nonlinear classification by indirectly matching their input to high-dimensional property fields. Given a set of training examples, each marked as one or the other of two classes, an SVM algorithm is used as a non-probable binary linear classifier by assigning new samples to one class or the other.

K-Nearest Neighbor (KNN) [25] is one of the basic classification algorithms in machine learning. Its classification approach is quite simple and can be easily applied to various problems. It is mainly based on feature similarity. KNN checks how similar a data point is to its neighbor and classifies the data point into the class it most closely resembles. In the experiments carried out in this study, Euclidean distance has been used for the KNN classifier. This distance calculation is made with equation (2).

$$\sqrt{\sum_{i=1}^{k} (x_i - y_i)^2} \quad \textbf{(2)}$$

The equation simply calculates the distance between the pairs (x, y) in 2d Cartesian space. Unlike most algorithms, KNN is a non-parametric model, meaning it makes no assumptions about the dataset. This makes the algorithm more effective as it can process realistic data. KNN is a lazy algorithm, which means that it memorizes the training dataset rather than learning a distinctive function from the training data. In this study, weighted KNN will be used as a classifier. Unlike the traditional KNN method, K is weighted with the nearest neighbor $1 / k$ in weighted KNN, while the weight of other data is considered to be 0. For this purpose, the closest neighbor $'i.'$ is weighted for n samples with the following equation (3).

$$\sum_{i=1}^{n} w_{ni} = 1 \quad \textbf{(3)}$$

Decision Tree (DT) [26] is a simple and widely used classification technique. It applies a simple approach to solve the classification problem. The DT classifier performs a series of specially crafted branching about the features of the test data. If a result is reached about the class label of the data as a result of the branching, the algorithm is terminated; otherwise, the next branching continues until a result is reached. Within the scope of the study, the maximum deviation reduction (MDR) has been used as the division criterion. It is also known as the entropy function and found by the following equation (4).

$$I_E(N) = -K \sum f(N, j) \log f(N, j) \quad \textbf{(4)}$$

Here, K is the proportion of observations, function f is the frequency of class j in node N. The purpose of MDR is to reduce uncertainty until a pure leaf node is established. In DT, root and internal nodes contain feature test conditions to separate data with different features. All terminal nodes are assigned a class label 'Yes' or 'No'. Once DT is created, it is quite easy to classify a test record. Starting from the root node, the test condition is applied to the data and the appropriate branch is monitored according to the result of the test. The branching then takes place towards another inner node or a leaf node to which a new test condition is applied.

4. Results

The computer used in the experiments within the scope of the study has an I7 6700HQ CPU, 8GB RAM, 2GB GTX950 GPU, and 240GB SSD HDD. Experiments have been carried out using MATLAB (2019b) environment.

The features of 3000 maize seed images have been obtained on the CNN models within the scope of the study. For this purpose, it is provided to extract features from 9 different layers in total over five different CNN models. Obtained features have been given to the classifier algorithms as input to perform the classification process. SVM, KNN, and DT classifiers have been used for this process. Regarding the classifiers used; in the DT classifier, the maximum split parameter (max split) value has been set to 20. The partition criterion is made according to the MDR technique. In the KNN classifier; a weighted tree structure has been used and the k neighborhood parametric value is set to 20. On the other hand, Euclidean distance has been used to measure neighborhood distance. The squared inverse technique is used as the weighting approach. As support vector classifier; the second-order (quadratic) SVM method has been used. The box constraint level is set to 1. Kernel scaling has been used in auto mode. All these classifier adjustments have been determined empirically with different parametric combinations. The overall structure of the proposed model is shown in Figure 2.

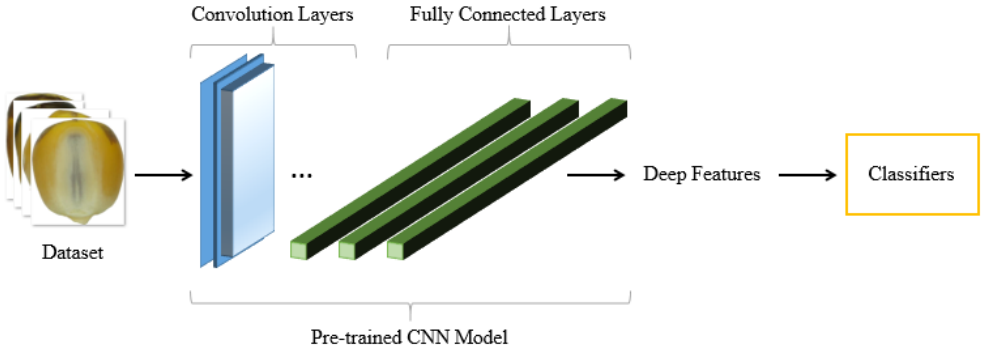

Figure 2. Overall structure of the proposed model.

In the AlexNet model feature extraction has been made from three layers: 'FC6', 'FC7', and 'FC8' layers. In the GoogLeNet model, features have been obtained from the fully connected layer named "Loos-3". In ResNet-18 and ResNet-50 models, the features have been obtained from the "FC1000" fully connected layers. Finally, in the VGG16 model, it has been provided to obtain features from 'FC6', 'FC7', and 'FC8' layers which are fully connected layers similar to the AlexNet model. The number of features obtained and the elapsed times of obtaining the features are given in Table 1. The elapsed time of acquiring the features vary according to the number of layers of the models, processes like the applied mathematical filter, convolution and etc. In a low-complexity CNN model, features can be obtained more quickly.

Table 1. Feature acquiring times.

CNN Model	Feature Number	Feature Acquiring Time
AlexNet FC6	4096	382,86s
AlexNet FC7	4096	422,20s
AlexNet FC8	1000	212,50s
GoogLeNet	1000	332,08s
ResNet18	1000	324,89s
ResNet50	1000	310,17s
VGG16 FC6	4096	1101,48s
VGG16 FC7	4096	1121,74s
VGG16 FC8	1000	958,94s

In the study, 10-fold cross-validation method has been used to divide the dataset into training and test sets for obtain more generalized results. The effects of deep features obtained from fully connected layers on classification performance have been analyzed. Accuracy, precision, sensitivity, F-score, and classification times have been used as performance metrics to evaluate these effects. Accuracy, precision, sensitivity, and F-score performance metrics are calculated based on confusion matrix. The classification times refer to the time elapsing to classify the maize seed types according to the features.

The confusion matrix allows the measurement of model performance by comparing the number of true and false predictions made by classifiers on the test set for the CNN models. Since there are fewer haploid maize seeds compared to diploid maize seeds in this study, the positive class has been determined as haploids and the negative class has been determined as diploids. Among the samples labeled as haploid in the dataset, it is the true positive (TP) data that the proposed methods predict as haploid. What the method predicts as diploid is handled as false negative (FN). Among the samples labeled as diploid in the dataset, they are true negative (TN) data that the method predicts as diploid. Finally, the data estimated by the method as haploid have been evaluated as false positive (FP). Mathematical calculation formulas for performance metrics are as follows:

$$Accuracy = \frac{TP + TN}{TP + FP + FN + TN} \quad \textbf{(5)}$$

Celal Bayar University Journal of Science
Volume 16, Issue 3, 2020, p 323-331
Doi: 10.18466/cbayarfbe.742889

$$Precision = \frac{TN}{TN + FP} \quad (6)$$

$$Sensitivity = \frac{TP}{TP + FN} \quad (7)$$

$$F - score = \frac{2TP}{2TP + FP + FN} \quad (8)$$

Feature classification experiment results performed with the SVM classifier are given in Table 2. The values given in the table are; confusion matrix (TP, FP, FN, and TN), accuracy (Acc.), precision (Prec.), sensitivity (Sens.), F-Score, and runtime of the SVM classifier. According to the acquired results, the CNN model with the highest performance of the SVM method is ResNet50 with an accuracy rate of 91.4%. While the network with the second-highest performance is VGG16 with 91% accuracy, this performance has been achieved with the obtained features from the FC6 fully connected layer of the network. While the third-highest accuracy model is VGG16, 89.6% accuracy has been achieved with the features acquired from the FC7 layer of this network. While the highest precision is 0.91 in the ResNet50 model, the highest sensitivity is in the VGG16 model with 0.93. The F1-Score used to eliminate extreme situations that occurred on the ResNet50 model has been determined by about 0.90. When the classification working times of SVM classifier according to the obtained features from the models are examined; in layers where 1000 features are obtained, the elapsed time is less than 1 minute, while in layers where 4096 features are obtained, this time is over 2 minutes.

Table 2 Classifier Results with SVM Method.

CNN Model	TP	FP	FN	TN	Acc.	Pre.	Sen.	F-Score	Time
AlexNet FC6	1120	110	214	1556	89,2%	0,88	0,91	0,87	148,39s
AlexNet FC7	1104	126	230	1540	88,1%	0,87	0,90	0,86	154,82s
AlexNet FC8	1083	147	255	1515	86,6%	0,86	0,88	0,84	38,59s
GoogLeNet	1076	154	254	1516	86,4%	0,86	0,87	0,84	45,64s
ResNet18[3*]	1103	127	209	1561	88,8%	0,88	0,90	0,87	32,04s
ResNet50[1*]	1136	94	165	1605	**91,4%**	0,91	0,92	0,90	27,51s
VGG16 FC6[2*]	1139	91	178	1592	91,0%	0,90	0,93	0,89	139,54s
VGG16 FC7	1116	114	198	1572	89,6%	0,89	0,91	0,88	133,91s
VGG16 FC8	1093	137	198	1572	88,8%	0,89	0,89	0,87	32,60s

*1, 2, 3; top three CNN models and layers with the highest performance

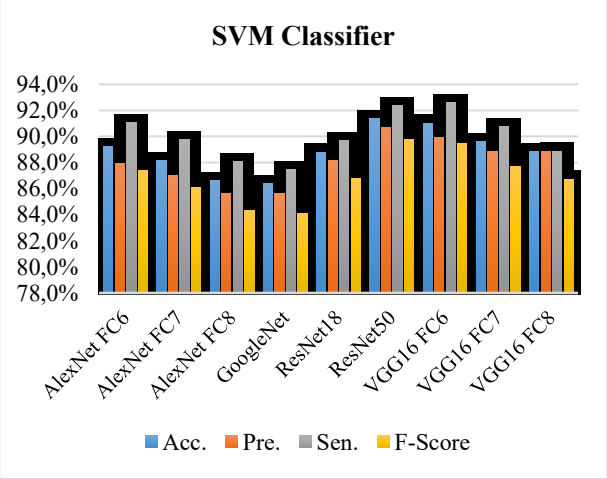

Figure 3. SVM classifier and performance metrics of CNN models.

Accuracy, precision, sensitivity, and F-Score values obtained in the pre-trained CNN models with the SVM classifier are given graphically in Figure 3.

Feature classification experiment results performed with the KNN classifier are given in Table 3. The highest performance has been obtained in the ResNet50 model with 87.5% accuracy in the classification experiments using the KNN classifier. The second-highest performance has been achieved in the VGG16 FC6 layer with an 84.9% accuracy rate, while the third-highest performance has been achieved in the ResNet18 model with 84.3% accuracy. The highest sensitivity value has been realized in the ResNet50 model with 0,84, while the highest sensitivity is in the FC6 layer with 0,94 in the VGG16 model. The highest F-Score value has been obtained in the ResNet50 model with 0.86. The acquired classification times in the KNN classifier are less than 1 minute for layers with 1000 features, and over 1 minute for layers with 4096 features.

Table 3. Classifier Results with KNN Method.

CNN Model	TP	FP	FN	TN	Acc.	Pre.	Sen.	F-Score	Time
AlexNet FC6	1048	182	382	1388	81,2%	0,78	0,85	0,79	92,07s
AlexNet FC7	1001	229	382	1388	79,6%	0,78	0,81	0,77	83,75s
AlexNet FC8	955	275	379	1391	78,2%	0,79	0,78	0,74	51,49s
GoogLeNet	1021	209	360	1410	81,0%	0,80	0,83	0,78	54,00s
ResNet18[3*]	1096	134	337	1433	84,3%	0,81	0,89	0,82	51,99s
ResNet50[1*]	1130	100	276	1494	**87,5%**	0,84	0,92	0,86	51,51s
VGG16 FC6[2*]	1162	68	385	1385	84,9%	0,78	0,94	0,84	93,08s
VGG16 FC7	1106	124	384	1386	83,1%	0,78	0,90	0,81	83,08s
VGG16 FC8	1104	126	371	1399	83,4%	0,79	0,90	0,82	18,26s

*1, 2, 3; top three CNN models and layers with the highest performance

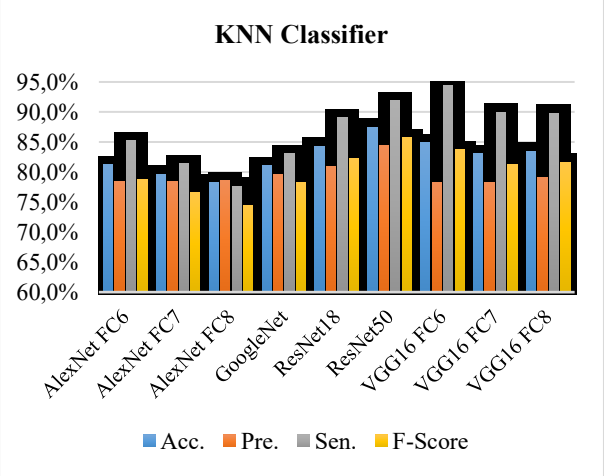

Figure 4. KNN classifier and performance metrics of CNN models.

Accuracy, precision, sensitivity, and F-Score values obtained through KNN classifier and pre-trained CNN models are graphically given in Figure 4.

Feature classification experiment results performed with the DT classifier are given in Table 4. The highest accuracy in the DT classifier is again in the ResNet50 model with a rate of 82.5%. The second and third best accuracy rates have been obtained from ResNet18 and VGG16 FC6 models as 80.5% and 79.8%, respectively. The best sensitivity value is realized in the ResNet50 model as 0.82. The best sensitivity value has been found as 0.84 in the ResNet50 model. In F-Score values, the best value has been obtained as 0.80 with the ResNet50 model. When the obtained values according to the classification times of the DT classifier are examined; it has been observed that classifiers took less than 1 minute in all models. However, in layers containing 1000 features, this time is around 30 seconds at most, while in layers containing 4096 features, it is quite close to the 1-minute.

Table 4. Classifier Results with DT Method.

CNN Model	TP	FP	FN	TN	Acc.	Pre.	Sen.	F-Score	Time
AlexNet FC6	894	336	407	1363	75,2%	0,77	0,73	0,71	59,79s
AlexNet FC7	958	272	429	1341	76,6%	0,76	0,78	0,73	58,79s
AlexNet FC8	920	310	430	1340	75,3%	0,76	0,75	0,71	12,47s
GoogLeNet	962	268	380	1390	78,4%	0,79	0,78	0,75	31,47s
ResNet18[2*]	933	237	335	1435	80,5%	0,81	0,80	0,77	30,97s
ResNet50[1*]	1031	199	326	1444	**82,5%**	0,82	0,84	0,80	30,51s
VGG16 FC6[3*]	984	246	360	1410	79,8%	0,80	0,80	0,76	57,84s
VGG16 FC7	954	276	373	1397	78,4%	0,79	0,78	0,75	56,89s
VGG16 FC8	956	274	345	1425	79,4%	0,81	0,78	0,76	12,57s

*1, 2, 3; top three CNN models and layers with the highest performance

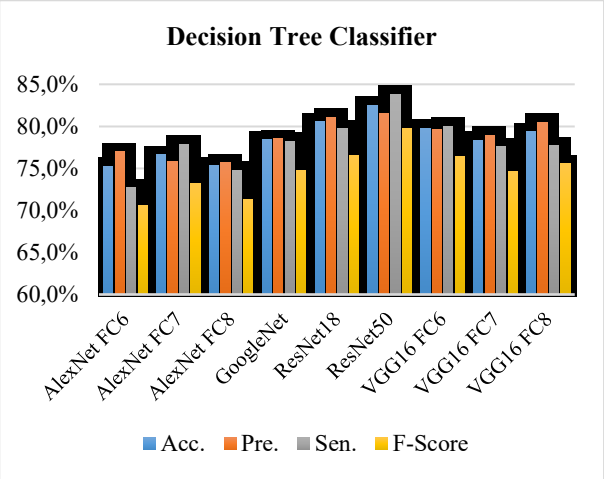

Figure 5. DT classifier and performance metrics of CNN models.

Accuracy, precision, sensitivity, and F-Score values obtained for the decision tree classifier and pre-trained CNN models are graphically given in Figure 5.

5. Discussion and Conclusion

In this study, including haploid and diploid seeds; features of 3000 maize seed images have been obtained from fully connected layers of pre-trained CNN models. Three different classifier methods have been proposed to classify maize seeds using these features. As a result of the experiments carried out, the highest accuracy in CNN models has been obtained in the ResNet50 model. While the best performance in precision (haploid recognition rate) values occurred in the ResNet50 model, the best model in sensitivity (diploid recognition rate) values is VGG16. In the VGG16 model, the layer with the highest value has been observed as the FC6 fully connected layer.

When the results are analyzed in terms of classification performance, the SVM classifier generally demonstrates the best classification performance in all CNN models. When using the SVM classifier, the highest accuracy has occurred in the ResNet50 model with 91.4%, while the lowest performance is in the GoogLeNet model with 86.4%. The second-best performance has been achieved with the KNN classifier. The highest performance with KNN is 87.5% in the ResNet50 model, while the lowest performance is 78.2% in the FC8 layer of the AlexNet model. DT classifier has shown the lowest classification performance. The highest achievement in accuracy with this classifier is again 82.5% in the ResNet50 model and the lowest has been observed in the AlexNet model FC6 layer with 75.2%. This study successfully demonstrates the potential to perform computer-aided maize seed classification based on deep features obtained using pre-trained CNN models. The study will be a source of inspiration for the systems that can be implemented in different types of agricultural products.

In future studies, in order to increase the performance, it is aimed to give embryo areas on the maize seed by segmenting them instead of giving all maize seed images as input directly to the models. On the other hand, based on the knowledge gained from this study, it is aimed to increase the performance to higher levels with the fusion of the features obtained from different CNN models. In other words, deep features from different CNN models will be used together. Fusion approaches will be developed to improve overall performance by readjusting these features.

Author's Contributions

Emrah Dönmez: Drafted and wrote the manuscript, proposed a CNN based classification approach for maize seeds. He has performed the experiment and analyzed the classification results.

Ethics

There are no ethical issues after the publication of this manuscript.

References

1. Altuntaş, Y, Kocamaz, AF, Yeroğlu, C. Identification of Apricot Varieties Using Leaf Characteristics and KNN Classifier. International Conference on Artificial Intelligence and Data Processing Symposium: IDAP-2019, 2019.

2. Dönmez, E, Zadeh, PV. A modified graph based approach for leaf segmentation with GPGPU support. 23rd Signal Processing and Communications Applications Conference: SIU-2015, 2015.

3. Chidzanga, C, Muzawazi, F, Midzi, J, Hove, T. 2017. Production and use of haploids and doubled haploid in maize breeding: A review. *African J. Plant Breed;* 201-213.

4. Prasanna, BM, Chaikam, V, Mahuku, G. 2012. Doubled haploid technology in maize breeding: theory and practice. *CIMMYT.*

5. Röber, FK, Gordillo, GA, Geiger, HH. 2005. In vivo haploid induction in maize - Performance of new inducers and significance of doubled haploid lines in hybrid breeding. *Maydica.*

6. Nanda, DK, Chase, SS. 1966. An Embryo Marker for Detecting Monoploids of Maize (Zea Mays L.1). *Crop Sci;* 6: 213-215.

7. Altuntaş, Y, Kocamaz, AF, Cengiz, R, Esmeray, M. Classification of haploid and diploid maize seeds by using image processing techniques and support vector machines. 26th IEEE Signal Processing and Communications Applications Conference: SIU-2018, 2018.

8. Lecun, Y, Bengio, Y, Hinton, G. 2015. Deep learning. *Nature;* 521: 436-444.

9. Couto, EG de O, Davide, LMC, Bustamante, F de O, Von, Pinho RG, Silva, TN. 2013. Identification of haploid maize by flow cytometry, morphological and molecular markers. *Ciência e Agrotecnologia.*

10. Boote, BW, Freppon, DJ, Fuente, GN de La, Lübberstedt, T, Nikolau, BJ, Smith, EA. 2016. Haploid differentiation in maize kernels based on fluorescence imaging. *Plant Breed.*

11. Yu, L, Liu, W, Li, W, Qin, H, Xu, J, Zuo, M. 2018. Non-destructive identification of maize haploid seeds using nonlinear analysis method based on their near-infrared spectra *Biosyst. Eng.*

12. Lin, J, Yu, L, Li, W, Qin, H. 2018. Method for Identifying Maize Haploid Seeds by Applying Diffuse Transmission Near-Infrared Spectroscopy. *Appl. Spectrosc;* 72: 611–617.

13. Wang, Y. et al. 2018. Identification of maize haploid kernels based on hyperspectral imaging technology. *Comput. Electron. Agric.*

14. Fuente, GN de La, Carstensen, JM, Edberg, MA, Lübberstedt, T. 2017. Discrimination of haploid and diploid maize kernels via multispectral imaging. *Plant Breed.*

15. Wang, XY, Liao, WX, An, D, Wei, Y. 2018. Maize Haploid Identification via LSTM-CNN and Hyperspectral Imaging Technology. *CoRR;* abs/1805.0.

16. Altuntaş, Y, Kocamaz, AF, Cömert, Z, Cengiz, R, Esmeray, M. Identification of Haploid Maize Seeds using Gray Level Co-occurrence Matrix and Machine Learning Techniques. International Conference on Artificial Intelligence and Data Processing, IDAP2018, 2019.

17. Altuntaş, Y, Cömert, Z, Kocamaz, AF. 2019. Identification of haploid and diploid maize seeds using convolutional neural networks and a transfer learning approach. *Comput. Electron. Agric.*

18. Altuntaş, Y, Kocamaz, AF. 2019. Renk Momentleri ve Destek Vektör Makineleri Kullanarak Haploid Mısır Tohumlarının Tanımlanmasında Renk Uzaylarının Sınıflandırma Performansına Etkisinin Karşılaştırılması. *Fırat Üniversitesi Mühendislik Bilim. Derg;* 31: 551–560.

19. Song, P, Zhang, H, Wang, C, Luo, B, Zhang, JX. 2018. Design and Experiment of a Sorting System for Haploid Maize Kernel. *Int. J. Pattern Recognit. Artif. Intell.*

20. Krizhevsky, A, Sutskever, I, Hinton, GE. 2012. ImageNet classification with deep convolutional neural networks. *Advances in Neural Information Processing Systems*.

21. He, K, Sun, J. Deep Residual Learning for Image Recognition, IEEE Conference on Computer Vision and Pattern Recognition (CVPR), 770-778, 2016.

22. Szegedy, C. et al. Going deeper with convolutions, Proceedings of the IEEE Computer Society Conference on Computer Vision and Pattern Recognition, 2015.

23. Simonyan, K. Zisserman, A. Very deep convolutional networks for large-scale image recognition, 3rd International Conference on Learning Representations: ICLR-2015, Conference Track Proceedings, 1–14, 2015.

24. Zanaty, EA. 2012. Support Vector Machines (SVMs) versus Multilayer Perception (MLP) in data classification. *Egypt. Informatics J.*

25. Guo, G., Wang, H, Bell, D, Bi, Y, Greer, K. 2013. KNN model-based approach in classification. *Lect. Notes Comput. Sci.*

26. Kotsiantis, SB. Decision trees: A recent overview. *Artificial Intelligence Review*.

Celal Bayar University Journal of Science

Inferences from Bootstrap Method for Ability Parameters in 2-Parameter Logistic Model

Hülya Olmuş[1], Ezgi Nazman[2]*

[1]Gazi University, Faculty of Science, Statistics, Ankara, Turkey
[2]*Sivas Cumhuriyet University, Faculty of Science, Statistics and Computer Sciences, Sivas, Turkey
*ezgicabuk@cumhuriyet.edu.tr
*Orcid No: 0000-0003-0189-3923

Received: *20 September 2019*
Accepted: *14 September 2020*
DOI: *10.18466/cbayarfbe.622868*

Abstract

The ability parameter of persons/examinees estimates can be obtained using the Joint Maximum Likelihood (JML) estimation in Item Response Theory (IRT). However, JML estimates can be biased in some cases. Although the Bootstrap method has been considered for JML, existing studies remain far from satisfactory concerning the ability parameter estimation. This research evaluates the performances of JML and Bootstrap estimates of the ability parameter in terms of Standard Error Measurement (SEM) in the 2-Parameter Logistic (2-PL) model conducting a detailed Monte Carlo simulation study. According to the results, the average SEM estimates of the Bootstrap method are less than the average SEM estimates of JML in terms of the ability parameter.

Keywords: ability parameter, difficulty parameter, discrimination parameter, joint maximum likelihood estimation, two-parameter logistic model

1. Introduction

Measurement and evaluation methods have gained importance in many fields such as education, psychology, and medicine in past decades [1]. In general, researchers have considered measuring the ability parameter of persons/examinees (latent variable) such as intelligence, mathematical or scholastic abilities. Evaluating results of measurement techniques can be difficult in some fields where the latent variable has an important role. Classical Test Theory (CTT) is unable to assess the true measurement of the ability of examinees and the characteristics of items. The mathematical or verbal ability of students in education, consumer preferences in marketing, political attitude of voters in politics, etc. can be given as an example of the field where the ability parameter of examinees cannot be measured by CTT directly. Thus, Item Response Theory (IRT) has been widely used to estimate both items and examinee parameters in literature [2, 3].

IRT is a mathematical model that indicates the relation among examinee and item parameters and provides parameter estimates of both ability parameter and item parameters [4]. This model is based on the probability of giving the correct answer to a given specific item. This probability is the chance that the *i*-th examinee correctly answers to the *j*-th item and is denoted by $P(Y_{ij}=1|\theta_i)$

IRT models have three basic assumptions: unidimensionality, local independence, and monotonicity. The unidimensionality indicates that all items should measure only one examinee parameter. The local independence states that the probability of the correct response from the examinee is based solely on the ability of the examinee and each individual item, and not the interrelationship of multiple items. The monotonicity describes the functionality between an examinee's ability and performance on each item of the assessment [5].

IRT models are generalized linear models since they involve a transformation of the expected values with the help of a link function to depend on a linear formulation, and they are also mixed because one or more weights in the linear component are random variables [6]. Logit and Probit are widely used link functions in IRT. The logit link function is benefitted from standard logistic distribution and rather preferable function because of the computation easiness. The most widely used models in IRT are one-parameter logistic (1-PL), two-parameter logistic (2-PL) and three

Celal Bayar University Journal of Science
Volume 16, Issue 3, 2020, p 333-338
Doi: 10.18466/cbayarfbe.622868

parameter logistic (3-PL) models. 1-PL model is also known as Rasch model and contains only item discrimination parameter (a_j). 2-PL model, which is known as Birnbaum model, consist of both item discrimination and difficulty parameters [4]. In addition to the item discrimination and difficulty parameters, 3-PL model has a chance parameter (c_j) [7].

Item discrimination (a) and difficulty parameter (b) ranges from $-\infty$ to $+\infty$. However, it is assumed that, in practice, b value ranges from -3 to +3, when the examinee parameter (θ) has the standard normal distribution. The discrimination parameter indicates how well the item differentiates examinees. A higher discrimination parameter differentiates better among examinees. In the same way, a higher difficulty parameter indicates that the item is hard [1, 4]. The chance parameter (c) ranges from 0 to 1 and it is generally $c \leq 0.25$.

Liou and Yu [8] mentioned that the Bootstrap method can be used to determine the statistical accuracy of ability estimates in with given item parameters. Atanasov [9] studies on estimation of IRT parameters of the items with a small sample size using bootstrapping. Heene et al. [10] evaluated the performance of the Bootstrap for the Rasch model under the violations of non-intersecting item response functions. Wolfe and McGill [11] indicated that the Bootstrap critical values allow for greater statistical power in diagnosing item misfit caused by varying item slopes and lower asymptotes for the Rash model. Patton et al. [12] compared the performance of bootstrap standard error with the asymptotic standard error under 20 and 40 items for 500 and 2000 samples. Olmuş and Nazman [13] evaluated parameter estimations of 2-PL model using JML estimation. Liu and Yang [14] proposed a resampling-based method, namely bootstrap calibration, to reduce the impact of the carry over sampling error on the interval estimates of ability parameter. Liu et al [15] reviewed Monte Carlo methods in the literature in recent years. Chen et al. [16] used pseudo-population bootstrap to perform in terms of relative bias and coverage probability. However, there is still need to clear the performance of the Bootstrap method for higher item numbers. Therefore, we considered the 2-PL model in order to evaluate JML and the Bootstrap ability parameter estimation considering Standard Error Measurement (SEM) conducting a detailed Monte Carlo simulation study. The study was organized as follows: The model, item information function, test information function and standard error of measurement were explained in the second section. Parameter estimation of the model, JML estimation and the Bootstrap method were presented in the third section. Monte Carlo simulation study and obtained results were shown in the fourth and fifth sections, respectively.

2. Materials and Methods

2.1. Two-Parameter Logistic (2-PL) Model

The most widely used model in IRT is two-parameter logistic (2-PL) model. Let's consider a testing situation in which n examinees answer to k items. Let i=1, …, n and j=1, …, k be the random variables associated with the response of the i th examinee to the j-th item. These responses can be binary or discrete with a number of categories. Y_{ij} is the response for the i-th examinee to the j-th item and assumed to be identical for each item in the test. Here θ_i denotes the ability parameter for i-th examinee.

$P(Y_{ij}=1|\theta_i)$ denotes for the chance that the i-th examinee correctly answers the j-th item. Logit term of this probability and 2-PL model equation were given below respectively [3, 7].

$$\text{logit}(P(Y_{ij}=1))=ln\left(\frac{P(Y_{ij}=1)}{1-P(Y_{ij}=1)}\,\middle|\,\theta_i\right)=a_j\left(\theta_i-b_j\right) \quad \textbf{(2.1)}$$

$$P(Y_{ij}=1\,|\,\theta_i)=\frac{exp\left[a_j\left(\theta_i-b_j\right)\right]}{1+exp\left[a_j\left(\theta_i-b_j\right)\right]} \quad \textbf{(2.2)}$$

or

$$P(Y_{ij}=1\,|\,\theta_i)=\frac{1}{1+exp\left[-a_j\left(\theta_i-b_j\right)\right]} \quad \textbf{(2.3)}$$

where

a_j : the item discrimination parameter of j th item

b_j : the item difficulty parameter of j th item

2.1.1. Item Information Function (IIF)

An examinee's unknown ability do not depend upon the examinee's responses to the items. On the other hand, an examinee's unknown ability depends only on the parameter values of k items [17]. In 2-PL model, the general interest is mostly the estimated value of ability parameter for an examinee. The amount of information based on an item is able to be computed for any ability level. Item Information Function (IIF) for 2-PL model is shown as in Eq. (2.4):

$$I_i\left(\theta,b_j,a_j\right)=a_j^2\,P_i\left(\theta,b_j\right)Q_i\left(\theta,b_j\right) \quad \textbf{(2.4)}$$

where

$P_i\left(\theta,b_j\right)=\frac{1}{1+exp\left[-a_j\left(\theta_i-b_j\right)\right]}$ and $Q_i\left(\theta,b_j\right)=1-P_i\left(\theta,b_j\right)$.

The value of discrimination parameter is required to compute IIF [3, 15].

2.1.2. Test Information Function (TIF)

A study such as survey or test is a set of items. Thus, the test information gives the ability level is computed from the sum of the item informations at that level. The Test Information Function (TIF) for 2-PL model is defined as in Eq.(2.5):

$$I_i(\theta_i)=\sum_{j=1}^{k} I_{ij}(\theta_i,b_j,a_j) = \sum_{j=1}^{k} a_j^2 P(\theta,b_j,a_j)Q(\theta,b_j,a_j), \quad i=1,2,...,n \tag{2.5}$$

In general, TIF tends to be higher than that for IIF [18].

2.1.3. Standard Error of Measurement (SEM)

The variance of ability estimate in the 2-PL model can be estimated as the reciprocal value of TIF at the ability estimate. This standard error of ability parameter is given as in Eq.(2.6) [18].

$$SEM(\theta)=\sqrt{1/\sum_{j=1}^{k} a_j^2 P_j(\theta,b_j,a_j)Q(\theta,b_j,a_j)} \tag{2.6}$$

2.2. Parameter Estimation of 2-PL Model

Let $y_{i1},y_{i2},...,y_{ik}$ be the dichotomous response variables of the i th examinee to k items, $\boldsymbol{a}=(a_1,a_2,...,a_k)$ and $\boldsymbol{b}=(b_1,b_2,...,b_k)$ be the vectors of discrimination and difficulty parameters. When we assume that an examinee taking the test responses each item independently, the probability of observing a particular response matrix of the i-th examinee is given as in Eq.(2.7):

$$P(Y_{i1}=y_{i1},...,Y_{ik}=y_{ik}/\theta_i,\boldsymbol{a},\boldsymbol{b})=\prod_{j=1}^{k} P(Y_{ij}=y_{ij}/\theta_i,\boldsymbol{a},\boldsymbol{b}) \tag{2.7}$$

Then the likelihood function for all responses of examinees become as in Eq.(2.8):

$$L(\theta,a,b)=\prod_{i=1}^{n} P_j^{y_{ij}}(1-P_j)^{1-y_{ij}} \tag{2.8}$$

This function represents the likelihood of obtaining the observed data as a function of the model parameters. Therefore, it is logical to estimate these model parameters using those values that maximize this likelihood function.

2.2.1. Joint Maximum Likelihood Estimation (JML)

One of the important tasks when a test is examined is to estimate these parameter values because actual values of item parameters in a test are unknown. In IRT, estimation of both item and ability parameters is a crucial process. In the case of the 2-PL model, the log-likelihood for examinees is shown in Eq.(2.9):

$$ln\,L(\theta,a,b)=\prod_{i=1}^{n}\prod_{j=1}^{k}\left[y_{ij}ln(P_{ij})+(1-y_{ij})ln(1-P_{ij})\right] \tag{2.9}$$

Its partial derivations are taken with respect to each parameter and set them to zero. The obtained equations are not linear. Therefore, the Newton-Rapson method is used to obtain item and ability parameter estimations. JML method is used to estimate both item and ability parameters treating the parameters as fixed parameters. In the first stage, the item parameters are estimated assuming known examinee abilities. In the second stage, it is assumed that the item parameter values are known for the estimated examinee's ability parameters. Then, the process yields estimates for both item and ability parameters [18].

2.2.2 Bootstrap Method

The bootstrap resampling method allows researchers to quantify uncertainty by calculating standard errors and confidence intervals and performing significance tests. They require fewer assumptions than traditional methods and generally give more accurate answers [19]. In this study, the bootstrap method steps for 2- PL model as shown [12]:

Step 1: Estimate item and person parameters based on the original sample.
Step 2: Select the values of the item and person parameters randomly from the estimated values.
Step 3: Generate simulated data sets that fit the 2-PL model for each the bootstrap resampling.
Step 4: Compute the statistics of interest (the average estimates of the item and ability parameters) for each of the resamples.
Step 5: Compute averages of the statistics of interest across the bootstrap rasamples.
Step 6: Compare the value of the statistics of interest to the average bootstrap values.

3. Simulation Study

A Monte Carlo simulation study was conducted to compare estimated ability parameter with JML and Bootstrap method using MATLAB R2017b. Item numbers and sample sizes were determined as 60, 90, 180, and 150, 500, 1000, respectively. The ability parameters and the item difficulty parameter values were generated from N(0,1). Item discrimination parameters were randomly selected from the possible values of {0.2, 0.4, 0.6, 0.8, 1.0, 1.2, 1.4, 1.6}. First, the data set of 0's and 1's were generated using n ability examinees and k items each with two parameters. Using $n*k$ data matrix of simulated responses, the JML estimates were obtained for item and ability parameters

[20, 21]. In addition, the estimated values of ability estimation and SEM of ability parameters were obtained using the Bootstrap method when all item and ability parameters were estimated, SEM of the ability parameter estimates of JML were compared with SEM of the ability parameter estimates of the Bootstrap method. With this aim, we run 100 bootstrap resampling for each examinee. For each bootstrap resampling, item and ability parameter values were estimated using JML estimates again.

4. Results and Discussion

Estimation and standard error values (SEM) for the ability parameter of JML and the Bootstrap were given in Table1. The average SEM estimates for the ability and item parameters were estimated by using JML and the Bootstrap was given in Table1.

Table 1. Average estimations for ability parameter and SEM using JML and bootstrap methods.

n	k	a	b	θ	SEM(θ)	a_{boot}	b_{boot}	θ_{boot}	SEM(θ_{boot})
150	60	1.0348	0.0040	-0.0032	0.0227	1.2378	-0.0218	0.0038	0.0199
	90	0.9177	-0.1941	0.0098	0.0205	1.0519	-0.1677	0.0194	0.0184
	180	0.9252	0.0119	-0.0009	0.0144	1.0139	0.0180	-0.0083	0.0133
500	60	0.9408	-0.0093	-0.0018	0.0135	1.0644	-0.0166	-0.0118	0.0124
	90	0.9328	-0.0423	0.0004	0.0109	1.0196	-0.0340	0.0084	0.0103
	180	0.9289	0.0988	-0.0033	0.0078	0.9860	0.0941	-0.0139	0.0074
1000	60	0.9630	-0.1698	0.0043	0.0096	1.0892	-0.1634	0.0066	0.0086
	90	0.9786	-0.1141	0.0022	0.0076	1.0658	-0.1225	0.0030	0.0071
	180	0.9551	0.0470	-0.0042	0.0054	1.0119	0.0544	-0.0044	0.0052

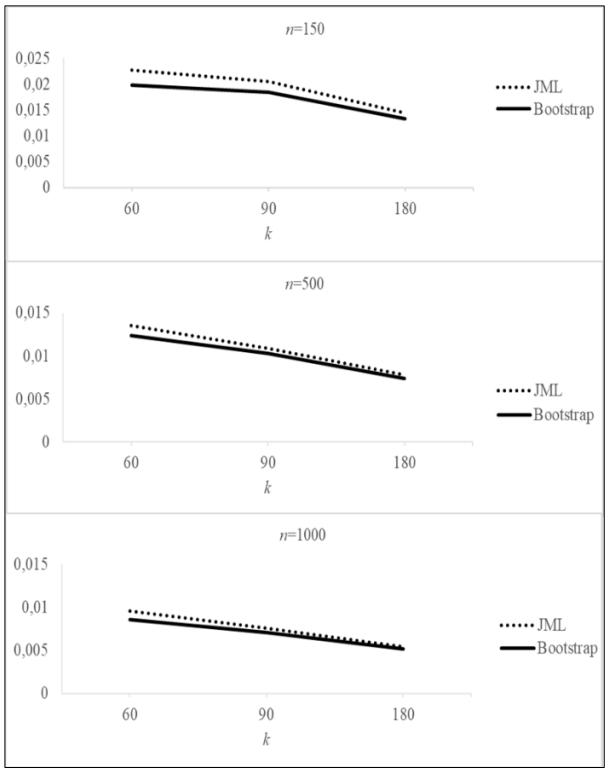

Figure 1. Average JML and Bootstrap estimates of ability parameter.

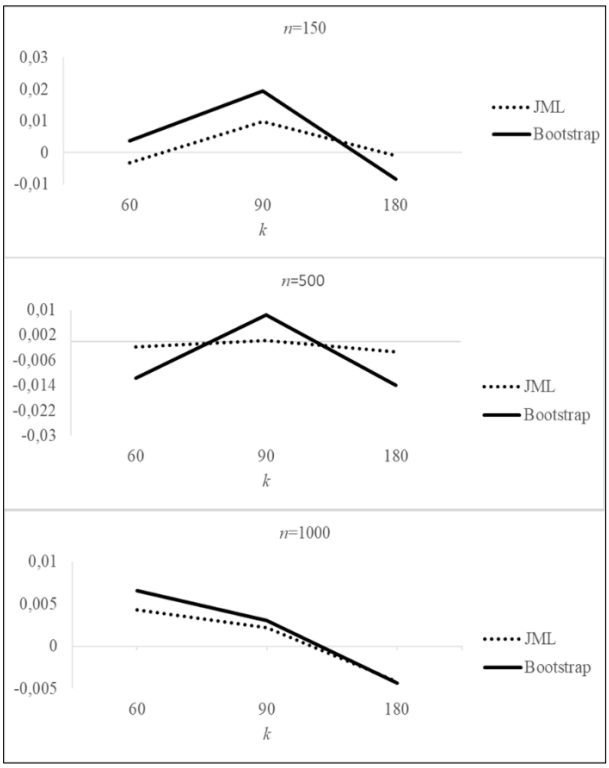

Figure 2. Average JML and bootstrap SEM estimates of ability parameter.

The Figure1 shows the variations of the discrimination parameter for various sample sizes and item numbers in this study.

3.1. Comments on Discrimination Parameter:

As shown in Figure2, when the number of items was low (k=60), for all sample sizes, it was seen that the average JML estimates of item discrimination

Celal Bayar University Journal of Science
Volume 16, Issue 3, 2020, p 333-338
Doi: 10.18466/cbayarfbe.622868

parameters were obtained less than the Bootstrap method. When the sample size is low (n=150), for all item numbers, it was obtained that the average discrimination parameter JML estimates were less than the Bootstrap method of item discrimination parameters. When the sample size increased for all item numbers, the average JML estimates differed from the average Bootstrap estimates in terms of item discrimination parameter. All in all, the Bootstrap method caused an increase in the average estimated value of the discrimination parameter. Figure 2 shows the variations of the difficulty parameter for various sample sizes and item numbers in this study. The major findings of this parameter are as follows:

3.2. Comments on Difficulty Parameter:

The average JML estimates of the item difficulty parameters tended to be so close with the average Bootstrap estimates of the item difficulty parameters when the sample size increased for item number 60, 90, and 180.

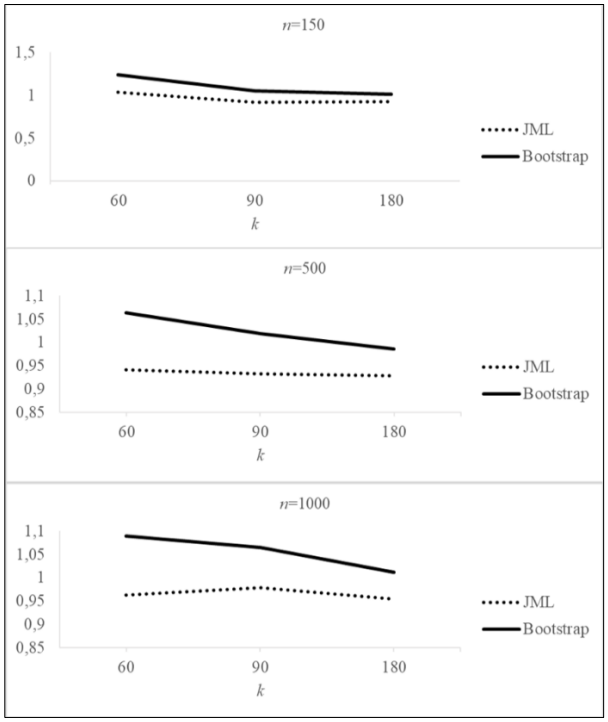

Figure 3. Average JML and Bootstrap estimates of discrimination parameter.

When the item number and sample size increased, an increase was observed in the average estimate values of the item difficulty parameter. The Figure3 shows the variations of the ability parameter for various sample sizes and item numbers.

3.3. Comments on Ability Parameter:

When the item number and sample size increased, the averages JML and Bootstrap estimates of ability parameters tended to be so close. Also, when the sample size and item number increased, the ability level of the examinee is on the decrease. When the sample size was and item number was low (n=150 and k=60), the ability level tended to increase. However, the average Bootstrap estimates were less than the average JML estimates in terms of ability parameters. Figure 4 shows the variations of the average SEM of the ability parameter for various sample sizes and item numbers in this study.

3.4. Comments on Standart Error (SEM) of Ability Parameter:

When the sample size increased for the low item number, the average SEM of JMLs was less than the average SEM of the Bootstrap estimates for the ability parameter. However, the average SEM of JMLs and the Bootstrap estimates were closer when the item number and sample sizes increase.

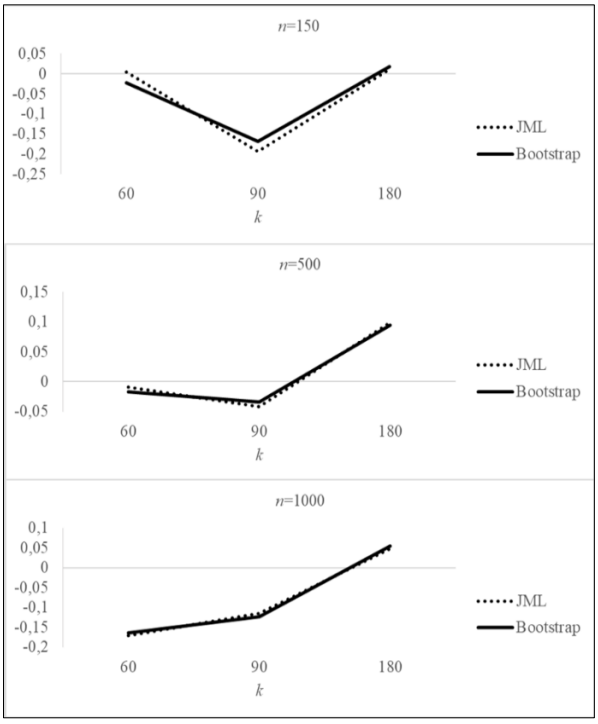

Figure 4. Average JML and Bootstrap estimates of difficulty parameter.

4. Conclusion

The major focus of this study was to compare the performances of Joint Maximum Likelihood and Bootstrap methods concerning the ability parameter and standard error measurement of ability parameter in two-parameter logistic model. It is well known that Joint

Maximum Likelihood estimates can be biased in some cases. According to the study, the Bootstrap is one of the approaches that may reduce the bias of Joint Maximum Likelihood estimates. It is seen that bootstrap method cause decrease on bias of ability parameter estimates in this study.

In general, item number has large impact on the accuracy of ability estimation than sample size. Therefore, Joint Maximum Likelihood and Bootstrap estimates give the same results when item number increase. The results show that in general for two-parameter logistic model, as item number increases, the accuracy of ability estimate measured by standard error measurement increases. However, it is result that bootstrap estimates causes an increase in estimation variability which can be shown in standard error measurement of ability parameter. It is seen that bootstrap method cause decrease on bias of estimated ability parameter.

Acknowledgement

Authors would like to thank the editor and two anonymous referees who kindly reviewed the earlier version of this manuscript and provided valuable suggestions and comments.

Author's Contributions

Hülya Olmuş: Drafted and wrote the manuscript, performed the experiment and result analysis.
Ezgi Nazman: Drafted and wrote the manuscript, performed the experiment and result analysis.

Ethics

There are no ethical issues after the publication of this manuscript.

References

1. Rasch, G. Probabilistic Models for Some Intelligence and Attainment Tests; Chicago: MESA; 1960.

2. Hambleton, RK, Jones, RW. 1993. Comparison of classical test theory and item response theory and their applications to test development. *Educational Measurement: Issues and Practice*; 12(3): 38-47.

3. Baker, FB. The basis of item response theory. ERIC. 2001.

4. Birnbaum, A. Some latent trait models and their use in inferring an examinee's ability, In Lord, FM, Novick, MR (Eds.), Statistical Theories of Mental Test Scores; 1968.

5. Paolino, JP. Penalized joint maximum likelihood estimation applied to two parameters logistic item. Columbia University Graduate School of Arts and Sciences; 2013.

6. McCulloch, CE, Searle, SR. Generalized, linear, and mixed models. John Wiley & Sons, New York; 2001.

7. Harris, D. Comparison of 1-,2- and 3-parameter IRT models, instructional topics in educational measurement, An NCME Instructional Module on; 1989.

8. Liou, M., Yu, L. 1991. Assesing statistical accuracy in ability estimation: bootstrap approach. *Psychometrika;* 56(1): 55-67.

9. Atanasov, D. 2009. Estimation of IRT parameters over a small sample: Bootstrapping of the item responses. *Pliska Studia Mathematica Bulgaria*; 19: 58-68.

10. Heene, M, Draxler, C, Ziegler, M, Bühner, M. 2011. Performance of the bootstrap Rasch model test under violations of non-intersecting item response functions. *Psychological Test and Assessment Modeling*; 53:283–294.

11. Wolfe, EW, McGill, MT. Comparison of asymptotic and bootstrap item fit indices in identifying misfit to the Rasch model. National Conference on Measurement in Education New Orleans; 2011.

12. Patton, JM, Cheng, Y, Yuan, KH, Diao, Q. 2014. Bootstrap standard errors for maximum likelihood ability estimates when item parameters are unknown. *Educational and Psychological Measurement*; 74(4): 697-712.

13. Olmuş, H., Nazman, E. 2017. An evaluation of the two parameter (2-PL) IRT models through a simulation study. *Gazi University Journal of Science*; 30(1): 235-249.

14. Liu, Y, Yang, JS. 2018. Bootstrap-calibrated interval estimates for latent variable scores in item response theory. *Psychometrika*; 83(2): 333-354.

15. Liu, Y., Hu, G., Cao, L.Wang, X., Chen, M.H. 2019. A comparison of Monte Carlo methods for computing marginal likelihoods of item response theory models. *Journal of the Korean Statistical Society*; 48:503-512.

16. Chen, S., Haziza, D., Leger, C., Mashreghi, Z. 2019. Pseudo-population bootstrap methods for imputed survey data. *Biometrica*; 106(2):369-384.

17. Baker, FB, Kim, SH. Item Response Theory: Parameter Estimation Techniques. Marcel Dekker, Inc; 2004.

18. Partchev, I. 2004. A visual guide to item response theory, Friedrich-Schiller-Universitat Jena. https://www.metheval.uni-jena.de/irt/ VisualIRT.pdf.

19. Hesterberg, T, Monaghan, S, Moore, DS, Clipson, A, Epstein, R. Bootstrap method and permutation tests. W.H. Freeman and Company New York; 2003.

20. Baur, T, Lukes, D. 2009. An Evaluation of the IRT models through monte carlo simulation. *Journal of Undergraduate Research XII:1-7*. Clearinghouse on Assessment and Evaluation.

21. Toribio, SG. Bayesian model checking strategies for dichotomous item response theory models. Graduate College of Bowling Green State University; 2006.

Celal Bayar University Journal of Science
Volume 16, Issue 3, 2020, p 339-343
Doi: 10.18466/cbayarfbe.683771

Celal Bayar University Journal of Science

Pointwise Bi-Slant Submersions

Sezin AYKURT SEPET*

Department of Mathematics, Faculty of Science and Arts, Kırşehir Ahi Evran University, Kırşehir, TURKEY
*saykurt@ahievran.edu.tr
*Orcid No: 0000-0003-1521-6798

Received: *03 February 2020*
Accepted: *14 September 2020*
DOI: *10.18466/cbayarfbe.683771*

Abstract

In the present paper we study pointwise bi-slant submersions from almost Hermitian manifolds onto Riemannian manifolds as a generalization of anti-invariant, semi-invariant, slant, bi-slant, pointwise semi-slant, pointwise slant, pointwise hemi-slant submersions. We mainly focus on pointwise bi-slant submersions from Kaehler manifolds onto Riemannian manifolds. We give some characterizations for such maps. We obtain necessary and sufficient conditions for the totally geodesicness of the distributions $D1$ and $D2$ mentioned in the definition of the pointwise bi-slant submersions. Also we investigate the geometry of vertical and horizontal distributions. Then we give necessary and sufficient conditions for pointwise bi-slant submersions to be totally geodesic.
Keywords: Almost Hermitian manifold, Pointwise bi-slant submersion.

1. Introduction

Given M and N C^∞-Riemannian manifold of dimension m and n respectively. A surjective C^∞-map $\pi: M \to N$ is a C^∞-submersion if it has maximal rank at any point of M. According to the conditions on the map π, we have several types the following: Riemannian submersion [9, 13], slant and semi-slant submersions [10, 11, 14, 17], anti-invariant and semi-invariant Riemannian submersions [1, 15, 16], pointwise slant submersions [4, 12], hemi-slant submersions [2, 19], Lagrangian submersions [20], generic submersions [18] etc.

The study of Riemannian submersion between Riemannian manifolds was initiated by O'Neill [13] and Gray [9] in 1960s. Later such submersions were considered by Watson [22] under the name of almost Hermitian submersions between almost Hermitian manifolds. The notions of anti-invariant Riemannian submersions and semi-invariant submersions were introduced by B. Sahin. Also, Sahin investigated slant submersion from almost Hermitian manifold and obtained some characterizations. Pointwise slant submersions which extend slant submersion were studied by J.W. Lee and B. Sahin. They examined the relation between slant submanifolds and pointwise slant submanifolds and found some important results.

On the other hand, as a generalization of CR-submanifolds, slant and semi-slant submanifolds, bi-slant submanifolds in almost contact metric manifolds defined by Cabrerizo et al. [6]. In Carriazo [7] studied bi-slant immersions in almost Hermitian manifolds. Uddin et al. [21] studied warped product bi-slant immersions in Kaehler manifolds and obtained some

results. Also Alqahtani et al. [3] investigate geometric properties warped product bi-slant submanifolds of cosymplectic manifolds and gave an example for warped product pseudo-slant submanifolds.

In purpose of the present paper is to examine pointwise bi-slant submersions from almost Hermitian manifolds onto Riemannian manifolds. In section 2, we review and collect some basic properties about almost Hermitian manifolds and Riemannian submersions. In section 3 we define pointwise bi-slant submersions and investigate the geometry of leaves of distributions and we a need and sufficient condition to be geodesic of such submersions.

2. Preliminaries

In this section we recall some information about almost Hermitian manifolds and Riemannian submersions. A $2n$-dimensional smooth manifold M is called an almost Hermitian manifold with a tensor field J of type (1,1) and a Riemannian metric g such that

$$J^2 = -I \quad \text{and} \quad g(X,Y) = g(JX,JY).$$

An almost Hermitian manifold is said to be Kahler manifold if

$$(\nabla_X J)Y = 0, \quad \forall X, Y \in \Gamma(TM)$$

Celal Bayar University Journal of Science
Volume 16, Issue 3, 2020, p 339-343
Doi: 10.18466/cbayarfbe.683771

where ∇ is the Levi-Civita connection on M.

Let $\pi: M \to N$ be a C^∞-map between (M, g_M) and (N, g_N) C^∞-Riemannian manifolds of dimension m and n respectively. A C^∞-submersion $\pi: M \to N$ is called a Riemannian submersion if at each point p of M, π_{*p} preserves the length of the horizontal vectors [8].
For each $q \in N$, $\pi^{-1}(q)$ is an $(m-n)$-dimensional submanifold of M called fiber. If a vector field on M is always tangent (or orthogonal) to fibers then it is said to be vertical (or horizontal) [13]. A vector field X on M is called basic if it is horizontal and $\pi_* X_p = X_* \pi(p)$ for $X_* \in \Gamma(TN)$ all $p \in M$. We will show the projection morphisms on the distributions $(\ker\pi_*)$ and $(\ker\pi_*)^\perp$ by $\mathcal{V}$ and $\mathcal{H}$, respectively.

A Riemannian submersion $\pi: M \longrightarrow N$ determines two $(1,2)$ tensor fields $\mathcal{T}$ and $\mathcal{A}$ on M. These tensor fields are called the fundamental tensor fields or the invariants of π. For $X, Y \in \Gamma(TM)$, these tensor fields can be given by the formulae

$$\mathcal{T}_X Y = \mathcal{H}\nabla_{\mathcal{V}X}\mathcal{V}Y + \mathcal{V}\nabla_{\mathcal{V}X}\mathcal{H}Y \quad \textbf{(2.1)}$$

$$\mathcal{A}_X Y = \mathcal{V}\nabla_{\mathcal{H}X}\mathcal{H}Y + \mathcal{H}\nabla_{\mathcal{H}X}\mathcal{V}Y \quad \textbf{(2.2)}$$

where ∇ is the Levi-Civita connection of (M, g_M). On the other hand for $U, V \in \Gamma(\ker\pi_*)$ and $\xi, \eta \in \Gamma((\ker\pi_*)^\perp)$ the tensor fields satisfy the following equations

$$\mathcal{T}_U V = \mathcal{T}_V U \quad \textbf{(2.3)}$$

$$\mathcal{A}_\xi \eta = -\mathcal{A}_\eta \xi = \frac{1}{2}\mathcal{V}[\xi, \eta]. \quad \textbf{(2.4)}$$

Note that a Riemannian submersion $\pi: M \longrightarrow N$ has totally geodesic fibers if and only if $\mathcal{T}$ vanishes identically.

We now remember the following lemma.

Lemma 2.1. *([13])* Let $\pi: M \longrightarrow N$ be a Riemannian submersion between Riemannian manifolds and suppose that ξ and η *are* basic vector fields of M π-related to ξ_* and η_* on N. Then

i. $g_M(\xi, \eta) = g_N(\xi_*, \eta_*) \circ \pi$,

ii. $[\xi, \eta]^{\mathcal{H}}$ is a basic vector field,

iii. $[V, \xi]$ is vertical for any vector field V of $(\ker\pi_*)$,

iv. $\left(\nabla^M_\xi \eta\right)^{\mathcal{H}}$ is the basic vector field i.e.

$$\pi_*\left(\left(\nabla^M_\xi \eta\right)^{\mathcal{H}}\right) = \nabla^N_{\xi_*}\eta_*,$$

where ∇^M and ∇^N are the Levi-Civita connection on M and N, respectively.

Furthermore from (2.1) and (2.2) we have

$$\nabla_U V = \mathcal{T}_U V + \overline{\nabla}_U V \quad \textbf{(2.5)}$$

$$\nabla_U \xi = \mathcal{H}\nabla_U \xi + \mathcal{T}_U \boldsymbol{\xi} \quad \textbf{(2.6)}$$

$$\nabla_\xi U = \mathcal{A}_\xi U + \mathcal{V}\nabla_\xi U \quad \textbf{(2.7)}$$

$$\nabla_\xi \eta = \mathcal{H}\nabla_\xi \eta + \mathcal{A}_\xi \eta \quad \textbf{(2.8)}$$

for $\xi, \eta \in \Gamma((\ker\pi_*)^\perp)$ and $U, V \in \Gamma(\ker\pi_*)$, where $\overline{\nabla}_U V = \mathcal{V}\nabla_U V$. Moreover, if ξ is basic then $\mathcal{H}\nabla_U \xi = \mathcal{A}_\xi U$.

Let (M, g_M) and (N, g_N) be Riemannian manifolds and $\psi: M \longrightarrow N$ is a smooth mapping between them. The second fundamental form of ψ is given by

$$\nabla\psi_*(X, Y) = \nabla^\psi_X \psi_*(Y) - \psi_*(\nabla^M_X Y) \quad \textbf{(2.9)}$$

for $X, Y \in \Gamma(TM)$, where ∇^ψ is the pullback connection. The smoooth map ψ is said to be harmonic if $trace\nabla\psi_* = 0$ and ψ is called a totally geodesic map if $(\nabla\psi_*)(X, Y) = 0$ for $X, Y \in \Gamma(TM)$ [5].

3. Pointwise Bi-slant submersions from Almost Hermitian Manifolds

Definition 3.1. Let (M, g_M, J) be an almost Hermitian manifold and (N, g_N) a Riemannian manifold. A Riemannian submersion $\pi: M \longrightarrow N$ is called a pointwise bi-slant submersion if for $i = 1,2$ the angles θ_i between JU_i and a pair of orthogonal distributions D_i, respectively, are independent of the choice of the nonzero vector $U_i \in \Gamma(ker\pi_*)$ such that $ker\pi_* = D_1 \oplus D_2$ and $JD_i \perp D_j$ for $j = 1,2$. Then the angle θ_i, is called the slant function of the pointwise slant submersion.

Let $\pi: (M, g_M, J) \to (N, g_N)$ be a pointwise bi-slant submersion. For $U \in \Gamma(\ker\pi_*)$, we can write

$$U = PU + QU \quad \textbf{(3.1)}$$

where $PU \in \Gamma(D_1)$ and $QU \in \Gamma(D_2)$.

Also, for $U \in \Gamma(\ker\pi_*)$, we obtain

$$JU = \phi U + \omega U \quad \textbf{(3.2)}$$

where $\phi U \in \Gamma(\ker\pi_*)$ and $\omega U \in \Gamma(\ker\pi_*)^\perp$.

For $\xi \in \Gamma(\ker\pi_*)^\perp$, we have

$$J\xi = B\xi + C\xi \quad \textbf{(3.3)}$$

where $B\xi \in \Gamma(\ker\pi_*)$ and $C\xi \in \Gamma(\ker\pi_*)^\perp$.

The horizontal distribution $(\ker\pi_*)^\perp$ is decompesed as

$$(\ker\pi_*)^\perp = \omega D_1 \oplus \omega D_2 \oplus \mu$$

where μ is the complementary distribution to $\omega D_1 \oplus \omega D_2$ in $(\ker\pi_*)^\perp$.Using (3.2) and (3.3) we arrive

$$\phi D_1 = D_1, \phi D_2 = D_2, B\omega D_1 = D_1, B\omega D_2 = \mathrm{D}_2$$

Thus we can give the following result.

Theorem 3.1. Let π be a Riemannian submersion from an almost Hermitian manifold (M, g_M, J) onto a Riemannian manifold (N, g_N). Then π is a pointwise bi-

Celal Bayar University Journal of Science
Volume 16, Issue 3, 2020, p 339-343
Doi: 10.18466/cbayarfbe.683771

slant submersion if and only if there exist bi-slant function θ_i defined on D_i such that

$$\phi^2 = -(\cos^2\theta_i)I,\ i = 1,2.$$

Proof. The proof of this theorem is the same as slant submersions [17].

Theorem 3.2. Let π be a pointwise bi-slant submersion from Kaehlerian manifold (M, g_M, J) onto a Riemannian manifold (N, g_N) with bi-slant functions θ_1, θ_2. Then the distribution D_1 defines a totally geodesic foliation if and only if

$$\sin^2\theta_1 g_M([U,\xi],V) = \sin 2\theta_1 \xi[\theta_1] g_M(U,V) + g_M(\mathcal{A}_\xi \omega\phi U, V) - g_M(\mathcal{A}_\xi \omega U, \phi V) - g_M(\mathcal{H}\nabla_\xi \omega U, \omega V)$$

and $g_M(\mathcal{T}_U \omega V, \phi W) + g_M(\mathcal{H}\nabla_U \omega V, \omega W) = 0$

where $U, V \in D_1$, $W \in D_2$ and $\xi \in \Gamma((\ker\pi_*)^\perp)$.

Proof. For any $U, V \in D_1$ and $\xi \in D_2$ we can write

$$\begin{aligned} g_M(\nabla_U V, \xi) &= -g_M([U,\xi],V) - g_M(\nabla_\xi U, V) \\ &= -g_M([U,\xi],V) - g_M(\nabla_\xi \phi U, JV) \\ &\quad - g_M(\nabla_\xi \omega U, JV) \\ &= -g_M([U,\xi],V) + g_M(\nabla_\xi \phi^2 U, V) \\ &\quad + g_M(\nabla_\xi \omega\phi U, V) - g_M(\nabla_\xi \omega U, JV). \end{aligned}$$

From Theorem 3.1, the above equation takes the form

$$\begin{aligned} \sin^2\theta_1 g_M(\nabla_U V, \xi) &= -\sin^2\theta_1 g_M([U,\xi],V) \\ &\quad + g_M(\nabla_\xi \omega\phi U, V) - g_M(\nabla_\xi \omega U, JV) \\ &\quad + \sin^2\theta_1 X[\theta_1] g_M(U,V). \end{aligned}$$

Thus using (2.8) we have

$$\begin{aligned} \sin^2\theta_1 g_M(\nabla_U V, \xi) &= -\sin^2\theta_1 g_M([U,\xi],V) \\ &\quad + g_M(\mathcal{A}_\xi \omega\phi U, V) - g_M(\mathcal{A}_\xi \omega U, \phi V) \\ &\quad + \sin^2\theta_1 X[\theta_1] g_M(U,V) \\ &\quad - g_M(\mathcal{H}\nabla_\xi \omega U, \omega V). \end{aligned}$$

Furthermore, for $W \in \Gamma(D_2)$

$$\begin{aligned} g_M(\nabla_U V, W) &= g_M(\nabla_U \phi V, JW) + g_M(\nabla_U \omega V, JW) \\ &= -g_M(\nabla_U \phi^2 V, W) + g_M(\nabla_U \omega V, JW) \end{aligned}$$

From the equation (2.6) and Theorem 3.1 we arrive at

$$\begin{aligned} \sin^2\theta_1 g_M(\nabla_U V, W) &= g_M(\mathcal{T}_U \omega V, \phi W) \\ &\quad + g_M(\mathcal{H}\nabla_U \omega V, \omega W). \end{aligned}$$

Theorem 3.3. Let π be a pointwise bi-slant submersion from Kaehlerian manifold (M, g_M, J) onto a Riemannian manifold (N, g_N) with bi-slant functions θ_1, θ_2. Then the distribution D_2 defines a totally geodesic foliation if and only if

$$\sin^2\theta_2 g_M([W,\xi],Z) = \sin 2\theta_2 \xi[\theta_1] g_M(W,Z) + g_M(\mathcal{A}_\xi \omega\phi W, Z) - g_M(\mathcal{A}_\xi \omega W, \phi Z) - g_M(\mathcal{H}\nabla_\xi \omega W, \omega Z)$$

and

$$g_M(\mathcal{T}_W \omega Z, \phi U) + g_M(\mathcal{H}\nabla_W \omega Z, \omega U) = 0$$

where $U \in D_1$, $W, Z \in D_2$ and $\xi \in \Gamma((\ker\pi_*)^\perp)$.

Proof. By using similar method in Theorem 3.2 the proof of this theorem can be easily made.

Theorem 3.4. Let π be a pointwise bi-slant submersion from Kaehlerian manifold (M, g_M, J) onto a Riemannian manifold (N, g_N) with bi-slant functions θ_1, θ_2. Then the distribution $(ker\pi_*)^\perp$ defines a totally geodesic foliation on M if and only if

$$\begin{aligned} g_M(\mathcal{H}\nabla_\xi \eta, \omega\phi U) &= (\cos^2\theta_1 - \cos^2\theta_2) g_M(A_\xi \eta, QU) \\ &\quad + g_M(\omega \mathcal{A}_\xi \eta, \omega U) + g_M(C\mathcal{H}\nabla_\xi \eta, \omega U). \end{aligned}$$

where $\xi, \eta \in \Gamma(\ker\pi_*)^\perp$ and $U \in (\ker\pi_*)$.

Proof. Suppose that $\xi, \eta \in \Gamma(\ker\pi_*)^\perp$ and $U \in (\ker\pi_*)$. So we can write

$$\begin{aligned} g_M(\nabla_\xi \eta, U) &= -g_M(\nabla_\xi \eta, \phi^2 PU) + g_M(J\nabla_\xi \eta, \omega U) \\ &\quad - g_M(\nabla_\xi \eta, \omega\phi U) - g_M(\nabla_\xi \eta, \phi^2 QU). \end{aligned}$$

From Theorem 3.1 we obtain

$$\begin{aligned} g_M(\nabla_\xi \eta, U) &= \cos^2\theta_1 g_M(\nabla_\xi \eta, PU) - g_M(\nabla_\xi \eta, \omega\phi U) \\ &\quad + g_M(J\nabla_\xi \eta, \omega U) + \cos^2\theta_2 g_M(\nabla_\xi \eta, QU). \end{aligned}$$

Using the equations (2.8) and $PU = U - QU$ we have

$$\begin{aligned} \sin^2\theta_1 g_M(\nabla_\xi \eta, U) &= -g_M(\mathcal{H}\nabla_\xi \eta, \omega\phi U) + g_M(\omega \mathcal{A}_\xi \eta, \omega U) + g_M(C\mathcal{H}\nabla_\xi \eta, \omega U) + (\cos^2\theta_2 - \cos^2\theta_1) g_M(A_\xi \eta, QU). \end{aligned}$$

Considering above equation we have the desired equation.

Theorem 3.5. Let π be a pointwise bi-slant submersion from Kaehler manifold (M, g_M, J) onto a Riemannian manifold (N, g_N) with bi-slant functions θ_1, θ_2. Then the distribution $(ker\pi_*)$ defines a totally geodesic foliation on M if and only if

$$\begin{aligned} g_M(\mathcal{A}_\xi \omega U, \phi V) &= -\sin^2\theta_1 g_M([U,\xi],V) + \sin 2\theta_1 \xi[\theta_1] g_M(PU, PV) - g_M(\mathcal{H}\nabla_\xi \omega U, \omega V) + \sin 2\theta_2 \xi[\theta_2] g_M(QU, QV) - g_M(\mathcal{A}\nabla_\xi \omega\phi U, V) \\ &\quad + (\cos^2\theta_1 - \cos^2\theta_2) g_M(\mathcal{V}\nabla_\xi U, V) \end{aligned}$$

where $\xi \in \Gamma(\ker\pi_*)^\perp$ and $U, V \in (\ker\pi_*)$.

Proof. Given $\xi \in \Gamma(\ker\pi_*)^\perp$ and $U, V \in (\ker\pi_*)$. Then we derive

$$\begin{aligned} g_M(\nabla_U V, \xi) &= -g_M([U,\xi],V) - g_M(J\nabla_\xi U, JV) \\ &= -g_M([U,\xi],V) - g_M(\nabla_\xi \phi^2 PU, V) \\ &\quad - g_M(\nabla_\xi \phi^2 QU, V) + g_M(\nabla_\xi \omega\phi U, V) \\ &\quad - g_M(\nabla_\xi \omega U, JV). \end{aligned}$$

By using Theorem 3.1 we have

$$g_M(\nabla_U V, \xi) = \sin 2\theta_1 \xi[\theta_1] g_M(PU, PV)$$

$$-g_M([U,\xi],V) - \cos^2\theta_2 g_M(\nabla_U QV,\xi)$$
$$+g_M(\nabla_\xi \omega\phi U,V) - \cos^2\theta_1 g_M(\nabla_\xi PV,\xi)$$
$$+\sin 2\theta_2 \xi[\theta_2] g_M(QU,QV)$$
$$-g_M(\nabla_\xi \omega U, JV)$$

Making use of equations (2,7), (2.8) and $PU = U - QU$ we arrive

$$\sin^2\theta_1 g_M(\nabla_U V,\xi) = (\cos^2\theta_1 - \cos^2\theta_2) g(\mathcal{V}\nabla_\xi QU,V) - \sin^2\theta_1 g_M([U,\xi],V) - g_M(\mathcal{A}_\xi \omega U,\phi V) + g_M(\mathcal{A}_\xi \omega\phi U,V) - g_M(\mathcal{H}\nabla_\xi \omega U,\omega V) + (\sin 2\theta_1)\xi[\theta_1] g_M(PU,PV) + (\sin 2\theta_2)\xi[\theta_2] g_M(QU,QV)$$

Using above equation we obtain the desired equation.

Theorem 3.6. Let π be a pointwise bi-slant submersion from Kaehler manifold (M, g_M, J) onto a Riemannian manifold (N, g_N) with bi-slant functions θ_1, θ_2. Then π is totally geodesic if and only if

$$\cos^2\theta_1 \mathcal{T}_U PV + \cos^2\theta_2 \mathcal{T}_U QV = C\mathcal{H}\nabla_U \omega V + \omega \mathcal{T}_U \omega V$$

and

$$\cos^2\theta_1 \mathcal{A}_\xi PU + \cos^2\theta_2 \mathcal{A}_\xi QU = -C\mathcal{H}\nabla_\xi \omega V - \omega \mathcal{A}_\xi \omega V$$

where $\xi \in \Gamma(\ker\pi_*)^\perp$ and $U, V \in (\ker\pi_*)$.

Proof. Firstly since π is a Riemannian submersion for $\xi, \eta \in \Gamma(\ker\pi_*)^\perp$ we have

$$(\nabla\pi_*)(\xi,\eta) = 0.$$

Therefore for $\xi, \eta \in \Gamma(\ker\pi_*)^\perp$ and $U, V \in (\ker\pi_*)$ it is enough to show that $(\nabla\pi_*)(U,V) = 0$ and $(\nabla\pi_*)(\xi,U) = 0$. So we can write

$$(\nabla\pi_*)(U,V) = -\pi_*(\nabla_U V).$$

Then using the equation (2.6) and (2.7), we obtain

$$(\nabla\pi_*)(U,V) = -\pi_*(\nabla_U V) = -\pi_*(J\nabla_U \phi V + J\nabla_U \omega V) = -\pi_*(\nabla_U \phi^2 PV + \nabla_U \phi^2 QV + J\nabla_U \omega V).$$

From Theorem 3.1 we find

$$(\nabla\pi_*)(U,V) = -\pi_*(-\cos^2\theta_1 \nabla_U PV - \cos^2\theta_2 \nabla_U QV + J\nabla_U \omega V) = \pi_*(\cos^2\theta_1(\mathcal{T}_U PV + \overline{\nabla}_U PV) + \cos^2\theta_2(\mathcal{T}_U QV + \overline{\nabla}_U QV) - J\mathcal{T}_U \omega V - J\mathcal{H}\nabla_U \omega V).$$

Therefore we arrive at the first equation of Theorem 3.6.

On the other hand, we have

$$(\nabla\pi_*)(\xi,U) = -\pi_*(\nabla_\xi U).$$

Then using the equation (2.7) and (2.8), we arrive

$$(\nabla\pi_*)(\xi,U) = \pi_*(\cos^2\theta_1(\mathcal{A}_\xi PU + \mathcal{V}\nabla_\xi PU) + \cos^2\theta_2(\mathcal{A}_\xi QU + \mathcal{V}\nabla_\xi QU) - J\mathcal{A}_\xi \omega U - J\mathcal{H}\nabla_\xi \omega U).$$

This concludes the proof.

Author's Contributions

S. Aykurt Sepet: Drafted and wrote the manuscript, performed the experiment and result analysis.

Ethics

There are no ethical issues after the publication of this manuscript.

References

1. Akyol, MA, Sahin, B. 2016. Conformal anti-invariant submersions from almost Hermitian manifolds. *Turkish Journal of Mathematics.*; 40: 43-70.

2. Akyol, MA, Gündüzalp, Y. 2016. Hemi-slant submersions from almost product Riemannian manifolds. *Gulf Journal of Mathematics*; 4(3): 15-27.

3. Alqahtani, LS, Stankovic, MS, Uddin, S. 2017. Warped Product Bi-slant Submanifolds of Cosymplectic Manifolds. *Filomat*; 31(16): 5065-5071.

4. Aykurt Sepet, S, Ergüt, M. 2016. Pointwise slant submersions from cosymplectic manifolds. *Turkish Journal of Mathematics;* 40: 582-593.

5. Baird, P, Wood, JC. Harmonic morphisms between Riemannian manifolds. London Mathematical Society Monographs, Oxford University Press, Oxford 2003.

6. Cabrerizo, JL, Carriazo, A, Fernandez, LM, Fernandez, M. 1999. Slant Submanifolds in Sasakian Manifolds. *Geometriae Dedicata*; 183-199.

7. Carriazo, A. "Bi-slant Immersions," In Proceeding of the ICRAMS, 2000, 88-97.

8. Falcitelly, M, Ianus, S, Pastore, AM. Riemannian Submersions and Related Topics, World Scientific, River Edge, NJ, 2004.

9. Gray, A. 1967. Pseudo-Riemannian almost product manifolds and submersions. *Journal of Mathematics and Mechanics.*; 16: 715-737.

10. Gündüzalp, Y. 2013. Slant submersions from almost product Riemannian manifolds. *Turkish Journal of Mathematics.*; 37: 863-873.

11. Gündüzalp, Y. 2016. Semi-slant submersions from almost product Riemannian manifolds. *Demonstratio Mathematica*; 49(3): 345-356.

12. Lee, JW, Sahin, B. 2014. Pointwise slant submersions. *Bulletin of the Korean Mathematical Society*; 51(4): 1115-1126.

13. O'Neill, B. 1966. The fundamental equations of a submersion. *Michigan Mathematical Journal.*; 13: 458-469.

14. Park, KS, Prasad, R. 2013. Semi-slant submersions. *Bulletin of the Korean Mathematical Society*; 50(3): 951-962.

15. Şahin, B. 2010. Anti-invariant Riemannian submersions from almost Hermitian manifolds. *Central European Journal of Mathematics*; 8(3): 437-447.

16. Şahin, B. 2011. Semi-invariant Riemannian submersions from almost Hermitian manifolds. *Canadian Mathematical Bulletin*; 56: 173-183.

17. Şahin, B. 2011. Slant submersions from almost Hermitian manifolds. *Bulletin Mathématique de la Société des Sciences Mathématiques de Roumanie*; 54(102): 93-105.

18. Sayar, C, Taştan, HM, Özdemir, F, Tripathi, MM. 2020. Generic submersions from Kaehlerian Manifolds. *Bulletin of the Malaysian Mathematical Sciences Society;* 43: 809-831.

19. Taştan HM, Şahin B, Yanan, Ş. 2016. Hemi-slant submersions. *Mediterranean Journal of Mathematics*; 13: 2171-2184.

20. Tastan, HM. 2017. Lagrangian submersions from normal almost contact manifolds. *Filomat*; 31(12): 3885-3895.

21. Uddin, S, Chen, BY, Al-Solamy, FR. 2017. Warped Product Bi-slant Immersions in Kaehler Manifolds. *Mediterranean Journal of Mathematics*; 14 (95).

22. Watson, B. Almost Hermitian submersions. 1976. *Journal of Differential Geometry;* 11(1): 147-165.

Celal Bayar University Journal of Science

Optimization of Base Energy Resolution in Hemispherical Deflector Analyzer by using Genetic Algorithm

Murat İnce[1]*, Nimet Işık[2]

[1] Vocational School of Technical Sciences, Isparta University of Applied Sciences, Isparta, Turkey
[2] Mathematics and Science Education Department, Burdur Mehmet Akif Ersoy University, Turkey
*muratince@isparta.edu.tr
*Orcid No: 0000-0001-5566-5008

Received: *29 January 2020*
Accepted: *14 September 2020*
DOI: *10.18466/cbayarfbe.681519*

Abstract

The aim of this study is to demonstrate the Genetic Algorithm (GA) optimization results for energy resolutions of the Hemispherical Deflector Analyzer (HDA). The HDAs are designed specifically to distinguish electrons according to their energies. In this context, high energy resolutions are important for the prevention of experimental data loss. Thus, the energy resolution values can be obtained in a short time with the aid of the genetic algorithm implemented in the proposed software. Genetic algorithm (GA) is an effective method developed with artificial intelligence technology. For the first time, analyzer resolution values in the widest range in the literature were calculated by genetic algorithm software. Optimum solutions not only for centric entry HDA but also for paracentric entry Hemispherical Deflector Analyzer (HDA) were obtained by the genetic algorithm.

Keywords: Artificial intelligence, electron optics, electrostatic energy analyzer, genetic algorithm, optimization.

1. Introduction

Energy resolution studies are investigations aimed at increasing the resolution of energy analyzers used in a wide range of fields, from atomic and molecular physics to medical physics [1]. An ideal energy analyzer with high resolution means that the detector located at the analyzer output can better represent, solve, and distinguish different energetic charged particles. The numerically calculations to determine the energy resolution of hemispherical deflector analyzer dates back to the results by Kuyatt and Simpson [2] in the late 1960s, but novel methods of producing fast and effective solutions remain important today. Energy profiles of transmitted particles and variation of the observed energy resolution of an HDA with mean kinetic energy are given by Imhof et al. [3]. It has been proposed to improve the energy resolution of charged particles analyzed by slowing down in subsequent studies [4-7]. Benis and Zouros [8] first showed that the energy resolution of an HDA can be improved by displacing the HDA input to a new position from the conventional position of R (mean radius). With this method, called with paracentric entry HDA, high energy resolution has been achieved [9,10]. The computational results of base energy resolution as a the function of beam entry diameter are given by Sise et al. [11]. These calculations are carried out by the electron ray-tracing program SIMION which uses the finite difference method [12]. The basic parameters used to determine the energy resolution are dispersion, magnification M and deviation coefficients. For this reason, the calculation values obtained for the different configurations of these parameters are also given by Sise et al. [13]. In these studies, the energy resolution is calculated for some values of parameters. Although these studies in the literature are successful, they need an appropriate dataset to predict an unknown data with high accuracy. Moreover, some of these studies require a training dataset. In this study, the energy resolution is calculated for a wide range of parameter values to get a dataset for future studies without any previously known data.

The aim of this study is the investigation of optimum base energy resolution of the centric and paracentric entry HDA using the genetic algorithm. GA is an artificial search algorithm based on the mechanics of biological evolution [14]. The GA is used widely for many search and optimization problems such as science, business, engineering and education areas [15,16]. In physics, GAs is used for irreversible radiative-type heat engine optimization [17] and lithium-ion battery model optimization [18]. Similarly, in this study, the GA is

used effectively to optimize the base energy resolution of the hemispherical deflector energy analyzers over a wide range of parameters. The energy resolution equation has many parameters in a wide range of values. Thus, the GA is useful for these types of equations to get optimum values in a fast and simple way.

This study consists of three basic parts: In Section 2, the energy resolution of the HDA and the genetic algorithm explained. Section 3 gives the results of the proposed method. The last section concludes the study.

2. Material and Methods

2.1. Base Energy Resolution of Hemispherical Deflector Analyzer

The HDA base energy resolution is related to the maximal beamwidth of electrons. It is defined as the full width of the energy transmission function. The base energy resolution of HDA is given by

$$\frac{\Delta E}{E} = \frac{\Delta r_\pi - M\Delta r_0}{D} - \frac{P_1}{D}\alpha - \frac{P_2}{D}\alpha^2 \qquad (2.1)$$

Here, M and D represent the analyzer magnification, and energy dispersion, respectively. P_1 and P_2 stand for the angular aberration coefficients. Δr_0 stands for the beamwidth of the analyzer entry and Δr_π represent the exit beam width for the hemispherical deflector analyzer. Boundaries of these parameters are as follow; $0 < \alpha < 5$, $0 < \Delta r_\pi < 2$, $0 < \Delta r_0 < 2$, $-2 < M < 4$, $100 < D < 500$, $-250 < P_1 < 250$ and $-250 < P_2 < 250$.

2.2. Basic Principles of the Genetic Algorithm Method

A genetic algorithm is a heuristic optimization and search method to find the best solutions for many problems [19]. As an evolutionary algorithm, the GA is inspired by evolutionary genetics in biology. Inheritance, mutation, selection, and crossover are fundamental components of the GA [20]. The basic steps of the GA are shown in Figure 1. Firstly, the population is initialized with random chromosomes. Then, according to the fitness function, each individual chromosome is evaluated. Best fitted chromosomes are selected to the new population. Selected chromosomes are reproduced by crossing over and mutated [21]. Thereafter, the new population is exposed to the new iteration. When the maximum number of generation count or termination conditions is reached, the GA is stopped [22]. The GA is used for many optimizations, search, and selection problems. The best parameters of components, arrangement, pinch, and approach point are obtained by optimization of a heat recovery steam generator [23]. In Askarzadeh's study [24], power generation in a Microgrid is optimized for minimization of the energy production cost in the smart grid framework. In another study, optimal sensor placement is obtained for the construction of accurate strain maps for large-scale structural components [25]. Armaghani et. al. [26] make airblast prediction to minimize or reduce the environmental effects of overpressure. In another study, the electrical power load is forecasted to balance the electricity supply and demand [27].

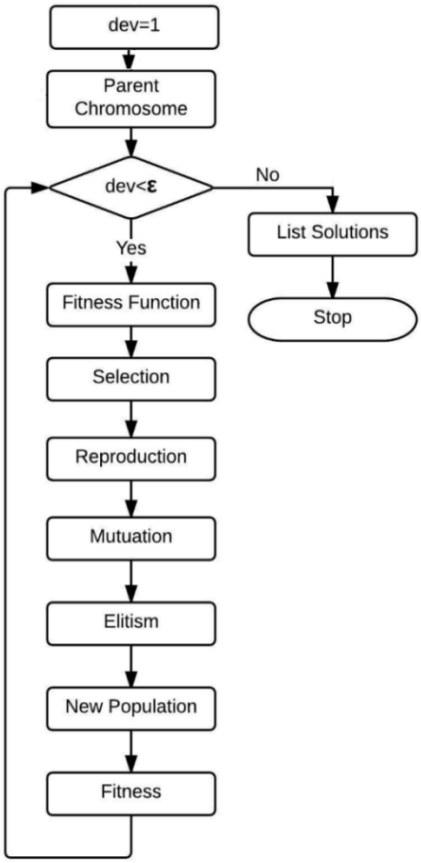

Figure 1. Flow chart of genetic algorithm.

3. Results and Discussion

The proposed GA is used to find a base energy resolution of HDA using Equation (2.1).

1. The initial population is generated. α, Δr_π, Δr_0, M, D, P_1 and P_2 that are variables in base energy resolution equation which are encoded as a chromosome with real numbers according to the boundaries (Figure 2). In this encoding, each chromosome is regarded as a candidate solution CS_1 to CS_n where n is population size. CS_1G_1 to CS_nG_1 are genes that represent α, CS_1G_2 to CS_nG_2 are genes that represent, Δr_π, CS_1G_3 to CS_nG_3 are genes that represent Δr_0, CS_1G_4 to CS_nG_4 are genes that represent M, CS_1G_5 to CS_nG_5 are genes that represent D, CS_1G_6 to CS_nG_6 are genes that represent P_1, CS_1G_7 to CS_nG_7 are genes that represent P_2.
2. In Equation (2.1), $\frac{\Delta E}{E}$ is expected to be have a maximum value. Therefore, the fitness function which is to be minimized is founded as:

$$F(x) = 1/\left(\frac{\Delta r_\pi - M\Delta r_0}{D} - \frac{P_1}{D}\alpha - \frac{P_2}{D}\alpha^2\right) \qquad (3.1)$$

Celal Bayar University Journal of Science
Volume 16, Issue 3, 2020, p 345-349
Doi: 10.18466/cbayarfbe.681519

3. Calculate the initial chromosome population according to the F(x) fitness function. Then, using the election rate, the best chromosomes that minimize the F(x) are selected to the new population (Figure 3). After, new chromosomes are regenerated and mutated by the mutation rate. The population size was 100, the mutation rate was 0.25, the election rate was 0.15, and the maximum generation count (ε) was 1000.
4. When the maximum generation count (ε) is reached, GA is finished. The best chromosome in the last population is shown as the base energy resolution of the HDA (Figure 4). In Fig. 5, the genetic algorithm solutions for the M versus P_1 and P_2 values for α=0˚, Δr_π=0, Δr_0 =1.97, D=100 mm are given. Although the variation of energy resolution parameters has been examined using different methods in the literature [10,11], for the first time in the literature, the variation of these parameters in Fig. 5 is given in detail, to the best of our knowledge.

		$0<\alpha<5$	$0<\Delta r_\pi<2$	$0<\Delta r_0<2$	$-2<M<4$	$100<D<500$	$-250<P_1<250$	$-250<P_2<250$
CS_1	→	CS_1G_1	CS_1G_2	CS_1G_3	CS_1G_4	CS_1G_5	CS_1G_6	CS_1G_7
CS_2	→	CS_2G_1	CS_2G_2	CS_2G_3	CS_2G_4	CS_2G_5	CS_2G_6	CS_2G_7
•	→	•	•	•	•	•	•	•
•	→	•	•	•	•	•	•	•
•	→	•	•	•	•	•	•	•
•	→	•	•	•	•	•	•	•
•	→	•	•	•	•	•	•	•
CS_n	→	CS_nG_1	CS_nG_2	CS_nG_3	CS_nG_4	CS_nG_5	CS_nG_6	CS_nG_7

Figure 2. Encoded chromosomes and their boundaries for base energy resolution optimization.

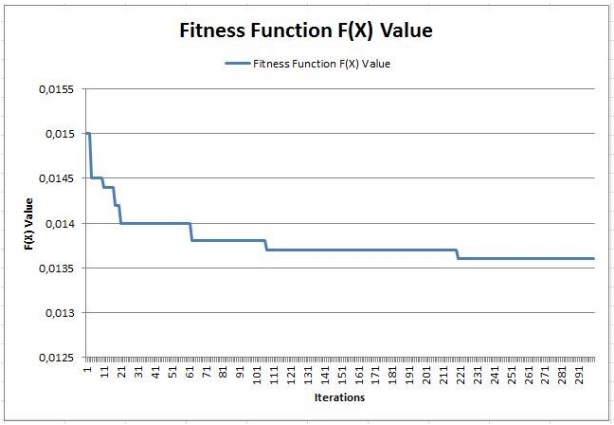

Figure 3. Fitness function values that is to be minimized.

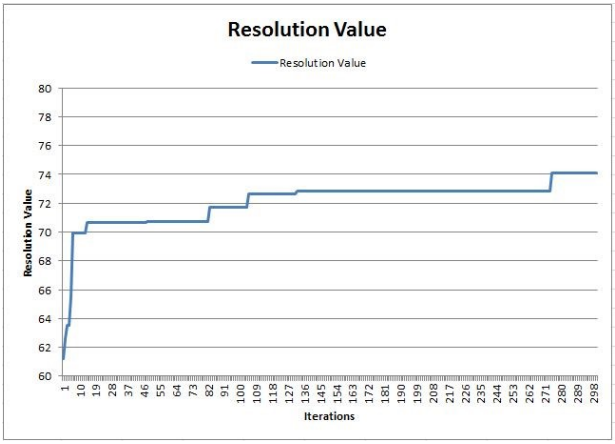

Figure 4. Base energy resolution values that is to be maximized.

The computation results are obtained with the genetic algorithm for the HDA. The calculations are performed using Equation (1) according to $0 < \alpha < 5$, $0 < \Delta r_\pi < 2$, $0 < \Delta r_0 < 2$, $-2 < M < 4$, $100 < D < 500$, $-250 < P_1 < 250$ and $-250 < P_2 < 250$. For this context, comparison of M versus P_1 and P_2 values for α=0˚, Δr_π=0, Δr_0 =1.97, D=100 mm are given in Figure 5. Moreover comparison of M versus P_1 and P_2 values for α=0˚, Δr_π=0, Δr_0 =1.97, D=100 mm are given in Figure 6. Considering the results, the GA gives the analyzer parameter values over a wide range of the operation.

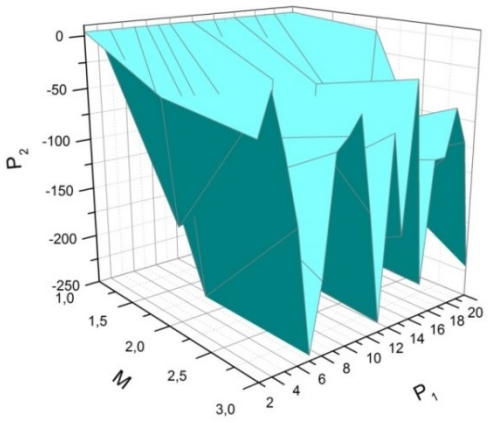

Figure 5. The genetic algorithm solutions for the M versus P_1 and P_2 values for α=0˚, Δr_π=0, Δr_0 =1.97, D=100 mm.

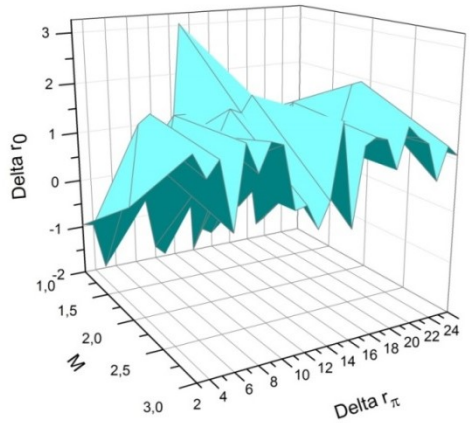

Figure 6. The genetic algorithm solutions for the M versus Δr_π and Δr_0 values for α=1˚, D=100 mm, P_1=P_2=-250.

4. Conclusion

In this study, the base energy resolution of the 180˚ hemispherical deflector energy analyzers are calculated for optimization over a wide range of parameters. An artificial intelligence method, GA, is used for these calculations. The results have been presented in graphical form to show the effectiveness of the algorithm. The evolutionary computing based GA is useful for experimental studies in terms of giving solutions for many problems with a large number of parameters. While searching for solutions for the base energy resolutions, the fact that being trapped within the local minimums can be prevented by running the GA several times. The results show that the GAs prove to be an efficient tool to provide usable optimal solutions in a short amount of time. The proposed algorithm for HDA base energy resolution equations provides a list of good solutions and not just a single solution. Therefore, the GA method is very useful when the search space is very large and there are a large number of parameters involved. Without using any training dataset like ANN, Regression, etc., the GAs are very simple to apply for many problems and also fast for other methods. This article can guide for experimentalists to acquire optimum parameter values for the HDA having high energy resolution.

Author's Contributions

Murat İnce: Drafted and wrote the manuscript, performed the experiment and result analysis.
Nimet Işık: Assisted in analytical analysis on the structure, supervised the experiment's progress, result interpretation and helped in manuscript preparation.

Ethics

There are no ethical issues after the publication of this manuscript.

References

1. Harting E., Read F.H. Electrostatic Lenses; Elsevier: Newyork, 1976
2. Kuyatt, C.E., Simpson, J.A. 1967. Electron monochromator design. *Review of Scientific Instruments;* 38: 103-111.
3. Imhof, R.E., Adams, A. King, G.C. 1976. Energy and time resolution of the 180 degrees hemispherical electrostatic analyzer. *Journal of Physics E: Scientific Instruments*; 9: 138-142.
4. Ballu, Y. 1968. Source d'électrons lents monocinétiques. *Revue de Physique Appliquée;* 3: 46-52.
5. Polaschegg, H.D. 1974. Spherical analyzer with pre-retardation. *Applied physics;* 4: 63-68
6. Wannberg, B., Sköllermo, A. 1977. Computer optimization of retarding lens systems for ESCA spectrometers. *Journal of Electron Spectroscopy and Related Phenomena;* 10(1): 45-78.
7. Dubé, D., Roy, D., Ballu, Y. 1981. New approach to improve performances of electron spectrometers. *Review of Scientific Instruments;* 52: 1497-1500.
8. Benis, E.P., Zouros, T.J.M. 2000. Improving the energy resolution of a hemispherical spectrograph using a paracentric entry at a non-zero potential. *Nuclear Instruments and Methods in Physics Research Section A: Accelerators, Spectrometers, Detectors and Associated Equipment;* 440: 462-465.
9. Zouros, T.J.M. 2006. Theoretical investigation of the energy resolution of an ideal hemispherical deflector analyzer and its dependence on the distance from the focal plane. *Journal of Electron Spectroscopy and Related Phenomena;* 152(1-2): 67-77.
10. Zouros, T. J. M., Sise, O., Ulu, M., Dogan, M. 2006. Using the fringing fields of a hemispherical spectrograph to improve its energy resolution. *Measurement Science and Technology;* 17(12): N81.
11. Sise, O., Zouros, T.J.M., Ulu, M., Dogan, M. 2007. Novel and traditional fringing field correction schemes for the hemispherical analyzer: comparison of first-order focusing and energy resolution. *Measurement Science and Technology;* 18(7): 1853.
12. Dahl, D.A. 1996. SIMION 3D v7.0 (Idaho Falls: Idaho National Engineering Laboratory)
13. Sise O., Ulu M., Dogan M., Martinez G., Zouros T.J. 2010. Fringing field optimization of hemispherical deflector analyzers using BEM and FDM. *Journal of Electron Spectroscopy and Related Phenomena;* 177: 42-51.
14. Goldberg, D.E., Holland, J.H. 1988. Genetic algorithms and machine learning. *Machine learning;* 3: 95-99.
15. Bashir, L.Z., Mahdi, N. 2015. Use Genetic Algorithm in Optimization Function for Solving Queens Problem. *World Scientific News;* 11: 138-150.
16. İnce, M., Yiğit, T., Işık, A.H. 2019. A hybrid AHP-GA method for metadata-based learning object evaluation. *Neural Computing and Applications;* 31(1): 671-681.
17. Ahmadi, M.H., Ahmadi, M.A. 2016. Thermodynamic analysis and optimisation of an irreversible radiative-type heat engine by using non-dominated sorting genetic algorithm. *International Journal of Ambient Energy;* 37: 403-408.
18. Zhang, L., Wang, L., Hinds, G., Lyu, C., Zheng, J., Li, J. 2014. Multi-objective optimization of lithium-ion battery model using genetic algorithm approach. *Journal of Power Sources;* 270: 367-378.
19. Goldberg, D.E., 1989. Genetic algorithms in search optimization and machine learning. Addison Wesley, Reading Menlo Park.
20. Abkenar, S.M.S., Stanley, S.D., Miller, C.J., Chase, D.V., McElmurry, S.P. 2015. Evaluation of genetic algorithms using discrete and continuous methods for pump optimization of water distribution systems. *Sustainable Computing: Informatics and Systems;* 8: 18-23.
21. Davis, L. Handbook of genetic algorithms, 1991.
22. Srinivas, M., Patnaik, L.M. 1994. Genetic algorithms: A survey. *Computer;* 27(6): 17-26.
23. Rezaie, A., Tsatsaronis, G., Hellwig, U. 2019. Thermal design and optimization of a heat recovery steam generator in a combined-cycle power plant by applying a genetic algorithm. *Energy;* 168: 346-357.

24. Askarzadeh, A., 2018. A memory-based genetic algorithm for optimization of power generation in a microgrid. *IEEE Transactions on Sustainable Energy;* 9: 1081-1089.
25. Downey, A., Hu, C., Laflamme, S. 2018. Optimal sensor placement within a hybrid dense sensor network using an adaptive genetic algorithm with learning gene pool. *Structural Health Monitoring;* 17: 450-460.
26. Armaghani, D.J., Hasanipanah, M., Mahdiyar, A., Majid, M. Z. A., Amnieh, H. B., Tahir, M. M. 2018. Airblast prediction through a hybrid genetic algorithm-ANN model. *Neural Computing and Applications;* 29: 619-629.
27. Ray, P., Panda, S.K., Mishra, D.P. Short-term load forecasting using genetic algorithm. Computational Intelligence in Data Mining; Springer: Singapore, 2019; pp 863.

Celal Bayar University Journal of Science
Volume 16, Issue 3, 2020, p 351-354
Doi: 10.18466/cbayarfbe.685759

Celal Bayar University Journal of Science

Coefficient Estimates for Certain Subclasses of Analytic Functions Defined by New Differential Operator

Sibel Yalçın[1], Hasan Bayram[2]*

[1,2] Department of Mathematics, Faculty of Arts and Science, Bursa Uludag University, Bursa, Turkey
*hbayram@uludag.edu.tr
*Orcid No: 0000-0001-8106-6834

Received: *6 January 2020*
Accepted: *14 September 2020*
DOI: *10.18466/cbayarfbe.685759*

Abstract

The study of operators plays an essential role in Mathematics, especially in Geometric Function Theory in Complex Analysis and its related fields. Many derivative and integral operators can be written in terms of convolution of certain analytic functions. The class of analytic functions, which has an essential place in the theory of geometric functions, has been studied by many researchers before. This topic still maintains its popularity today. In this paper, we investigate certain subclasses of analytic functions defined by generalized differential operators involving binomial series. Also, we obtain coefficient estimates involving of the nonhomogeneous Cauchy-Euler differential equation of order r.

Keywords: Analytic functions, coefficient bounds, differential operator, subordination.

1. Introduction

Let A denote the class of all analytic functions in the open unit disc

$$\mathbb{D} = \{z \in \mathbb{C} : |z| < 1\}$$

and having the form for $z \in \mathbb{D}$,

$$f(z) = z + \sum_{n=2}^{\infty} a_n z^n. \qquad (\mathbf{1})$$

A function $f \in A$ is said to belong to the class $S^*(\alpha)$ of starlike functions of order α if and only if

$$\mathrm{Re}\left(1 + \frac{zf'(z)}{f(z)}\right) > \alpha \qquad (\mathbf{2})$$

for $z \in \mathbb{D}$ and $0 \leq \alpha < 1$.

Also, a function $f \in A$ is said to belong to the class $K(\alpha)$ of convex functions of order α if and only if

$$\mathrm{Re}\left(1 + \frac{zf''(z)}{f'(z)}\right) > \alpha \qquad (\mathbf{3})$$

for $z \in \mathbb{D}$ and $0 \leq \alpha < 1$.

The classes $S^*(\alpha)$ and $K(\alpha)$ considered by Silverman [9]. We consider that $S^*(0)$ and $K(0)$ are respectively, the classes of starlike functions and convex functions.

Let the functions $f, g \in A$ be analytic in $\mathbb{D}$. Then f is said to be subordinate g if there exists a Schwarz function $w(z)$ on $\mathbb{D}$ with $w(0) = 0$, $|w(z)| < 1$, such that $f(z) = g(w(z))$ for $z \in \mathbb{D}$. We denote this subordination by $f(z) \prec g(z)$ for $z \in \mathbb{D}$. In particular, if the function g is univalent in $\mathbb{D}$, then we get

$$f(z) \prec g(z) \Leftrightarrow f(0) = g(0) \text{ and } f(\mathbb{D}) \subset g(\mathbb{D}).$$

Making use of the binomial series for $k \in \mathbb{N} := \{1,2,3,\cdots\}$, $m \in \mathbb{N}_0 = \mathbb{N} \cup \{0\}$

$$(1-\lambda)^k = \sum_{m=0}^{k} \binom{k}{m} (-1)^m \lambda^m$$

and for $f \in A$, $\lambda \in \mathbb{R}$, $\mu \geq 0$ with $\lambda + \mu > 0$ and $\delta \in \mathbb{N}_0$, Wanas [11] introduced the differential operator $W_{\lambda,\mu}^{k,\delta} f(z)$ which is defined as follows:

$$W_{\lambda,\mu}^{k,0} f(z) = f(z)$$

$$W_{\lambda,\mu}^{k,1} f(z) = \frac{[1-(1-\lambda)^k] f(z) + [1-(1-\mu)^k] z f'(z)}{2-(1-\lambda)^k - (1-\mu)^k}$$

$$\vdots$$

$$W_{\lambda,\mu}^{k,\delta} f(z) = W_{\lambda,\mu}^{k,1}\left(W_{\lambda,\mu}^{k,\delta-1} f(z)\right). \qquad (\mathbf{4})$$

If f is given by (**1**), then from (**4**) we see that

$$W_{\lambda,\mu}^{k,\delta} f(z) = z + \sum_{n=2}^{\infty}\left[\sum_{m=1}^{k} \binom{k}{m} (-1)^{m+1} \left(\frac{\lambda^m + n\mu^m}{\lambda^m + \mu^m}\right)\right]^{\delta} a_n z^n. \qquad (\mathbf{5})$$

If we choose the parameters λ, μ, k and δ special, we obtain operators which studied by various authors;

Celal Bayar University Journal of Science
Volume 16, Issue 3, 2020, p 351-354
Doi: 10.18466/cbayarfbe.685759

(i) $W_{\lambda,\mu}^{k,1} = I_{\lambda,\mu}^{\delta}$ ([10]),
(ii) $W_{\lambda,1}^{1,\delta} = I_{\lambda}^{\delta}$; $\alpha > -1$ ([3,4]),
(iii) $W_{1-\mu,\mu}^{1,\delta} = D_{\mu}^{\delta}$; $\mu \geq 0$ ([2]),
(iv) $W_{0,1}^{1,\delta} = S^{\delta}$ ([8]).

In references ([12-20]) can be found similar studies on analytical functions in recent years.

Herefrom we introduce the following subclasses of analytic functions with using $W_{\lambda,\mu}^{k,\delta}$.

1.1 Definition

Let $p: \mathbb{D} \to \mathbb{C}$ be a convex function such that $p(0) = 1$ and $Re\{p(z)\} > 0$, $z \in \mathbb{D}$. We denote by $S_g^{*,\delta}(\lambda, \mu, k; \alpha)$ the subclass of A given by

$$S_g^{*,\delta}(\lambda, \mu, k; \alpha) =$$

$$\left\{ f: f \in A \text{ and } \frac{1}{1-\alpha}\left(\frac{z\left(W_{\lambda,\mu}^{k,\delta} f(z)\right)'}{W_{\lambda,\mu}^{k,\delta} f(z)} - \alpha \right) \in g(\mathbb{D}) \right\} \tag{6}$$

where $z \in \mathbb{D}$, $\lambda \in \mathbb{R}$, $\mu \geq 0$ with $\lambda + \mu > 0$ and $\delta \in \mathbb{N}_0$, $k \in \mathbb{N}$, and $\alpha \in [0,1)$.

1.2 Definition

A function $f \in A$ in the class $C_g^{\delta}(\lambda, \mu, k, t; r)$ if it satisfies the following non-homogeneous Cauchy-Euler differential equation of order t;

$$z^t \frac{d^t w}{dz^t} + \binom{t}{1}(r + t - 1)z^{t-1}\frac{d^{t-1}w}{dz^{t-1}} + \cdots + \binom{t}{t} w \prod_{i=0}^{t-1}(r+i) = g(z)\prod_{i=0}^{t-1}(r+i+1), \tag{7}$$

where $w = f(z)$, $f \in A$, $g(z) \in S_g^{*,\delta}(\lambda, \mu, k; \alpha)$, $r \in \mathbb{R}\backslash(-\infty, -1]$ and $t \in \mathbb{N}_2 = \mathbb{N} - \{1\} = \{2,3,\cdots\}$.

Clearly, by suitably specializing parameters for

$$g(z) = \frac{1 + Az}{1 + Bz} \quad (-1 \leq B \leq A \leq 1, z \in \mathbb{D})$$

and

$$g(z) = \frac{1 + (1-2\alpha)z}{1 - z} \quad (0 \leq \alpha < 1, z \in \mathbb{D}),$$

$S_g^{*,\delta}(\lambda, \mu, k; \alpha)$ reduces to the various subclasses of analytic functions (see [9]). Motivated from the recent work of Al-Hawary [1] (see also, for example [5,6,7]) the main object of our investigation is to obtain some coefficient bounds for functions in the subclasses $S_g^{*,\delta}(\lambda, \mu, k; \alpha)$ and $C_g^{\delta}(\lambda, \mu, k, t; r)$ of analytic functions of order α by using the subordination principle between analytic functions.

To prove our main results, we recall 1.3 Lemma.

1.3 Lemma

Let

$$g(z) = \sum_{n=1}^{\infty} b_n z^n.$$

This function where $z \in \mathbb{D}$ be convex in $\mathbb{D}$.

Let

$$f(z) = \sum_{n=1}^{\infty} a_n z^n.$$

This function where $z \in \mathbb{D}$ be analytic in $\mathbb{D}$. If $f(z) \prec g(z)$ where $z \in \mathbb{D}$ then

$$|a_n| \leq |b_n|$$

for $n \in \mathbb{N}$.

2. Coefficient Bounds for the Classes $S_g^{*,\delta}(\lambda, \mu, k; \alpha)$ and $C_g^{\delta}(\lambda, \mu, k, t; r)$

We start by acquiring coefficient bounds for functions in the class $S_g^{*,\delta}(\lambda, \mu, k; \alpha)$.

2.1. Theorem

Let the function $f \in A$ be given by (**1**). If $f \in S_g^{*,\delta}(\lambda, \mu, k; \alpha)$, then

$$|a_n| \leq \frac{\prod_{j=0}^{n-2}(j + (1-\alpha)|g'(0)|)}{(n-1)!\left|\sum_{m=1}^{k}\binom{k}{m}(-1)^{m+1}\left(\frac{\lambda^m + n\mu^m}{\lambda^m + \mu^m}\right)\right|^{\delta}} \tag{8}$$

for $n \in \mathbb{N}_2$.

Proof.

By the equation (**5**), the function $W_{\lambda,\mu}^{k,\delta} f(z)$ has the Taylor-Maclaurin series expansion

$$W_{\lambda,\mu}^{k,\delta} f(z) = z + \sum_{n=2}^{\infty} A_n z^n$$

for $z \in \mathbb{D}$ where

$$A_n = \left[\sum_{m=1}^{k}\binom{k}{m}(-1)^{m+1}\left(\frac{\lambda^m + n\mu^m}{\lambda^m + \mu^m}\right)\right]^{\delta} \tag{9}$$

for $n \in \mathbb{N}_2$.

We see that $W_{\lambda,\mu}^{k,\delta} f(z)$ is analytic in $\mathbb{D}$ with

$$W_{\lambda,\mu}^{k,\delta} f(0) = \left(W_{\lambda,\mu}^{k,\delta} f\right)'(0) - 1 = 0.$$

Now, from Definition 1.1 we have

$$\frac{1}{1-\alpha}\left(\frac{z\left(W_{\lambda,\mu}^{k,\delta} f(z)\right)'}{W_{\lambda,\mu}^{k,\delta} f(z)} - \alpha \right) \in g(\mathbb{D}).$$

Let us define the function $p(z)$ by

Celal Bayar University Journal of Science
Volume 16, Issue 3, 2020, p 351-354
Doi: 10.18466/cbayarfbe.685759

$$p(z)=\frac{1}{1-\alpha}\left(\frac{z\left(W_{\lambda,\mu}^{k,\delta}f(z)\right)'}{W_{\lambda,\mu}^{k,\delta}f(z)}-\alpha\right). \qquad (10)$$

We deduce that $p(0)=g(0)=1$ and $p(z)\in g(\mathbb{D})$ $(z\in\mathbb{D})$. Therefore, we have $p(z)\prec g(z)$, $(z\in\mathbb{D})$. Thus according to Lemma 1.3, we obtain

$$\left|\frac{p^{(n)}(0)}{n!}\right|\leq|g'(0)| \quad n\in\mathbb{N} \qquad (11)$$

where $p(z)=1+p_1(z)+p_2(z)+\cdots$ is analytic in $\mathbb{D}$. From (**10**), we easily get

$$z\left(W_{\lambda,\mu}^{k,\delta}f(z)\right)'-\alpha W_{\lambda,\mu}^{k,\delta}f(z)=(1-\alpha)p(z)W_{\lambda,\mu}^{k,\delta}f(z) \qquad (12)$$

for $z\in\mathbb{D}$.
Since $A_1=1$, from (**12**), it follows that $(n-\alpha)A_n=(1-\alpha)(p_{n-1}+p_{n-2}A_2+\cdots+p_1A_{n-1})$. Especially, for $n=2,3,4,\cdots$, we have

$$|A_2|\leq(1-\alpha)|g'(0)|,$$

$$|A_3|\leq\frac{(1-\alpha)|g'(0)|(1+(1-\alpha)|g'(0)|)}{2!}$$

and

$$|A_4|\leq\frac{(1-\alpha)|g'(0)|(1+(1-\alpha)|g'(0)|)(2+(1-\alpha)|g'(0)|)}{3!}$$

respectively.
Thus, by appealing to the principle of mathematical induction, we obtain

$$|A_n|\leq\frac{\prod_{j=0}^{n-2}(j+(1-\alpha)|g'(0)|)}{(n-1)!} \qquad (13)$$

for $n\in\mathbb{N}_2$.
We now immediately find from (**9**) that

$$|a_n|\leq\frac{\prod_{j=0}^{n-2}(j+(1-\alpha)|g'(0)|)}{(n-1)!\left|\sum_{m=1}^{k}\binom{k}{m}(-1)^{m+1}\left(\frac{\lambda^m+n\mu^m}{\lambda^m+\mu^m}\right)\right|^{\delta}}.$$

This completes the proof.
Next, we give coefficient bounds for functions In the $C_g^{\delta}(\lambda,\mu,k,t;r)$.

2.2. Theorem

Let the function $f\in A$ be given by (**1**). If $f\in C_g^{\delta}(\lambda,\mu,k,t;r)$, then

$$|a_n|\leq\frac{\prod_{j=0}^{n-2}(j+(1-\alpha)|g'(0)|)\prod_{i=0}^{t-1}(r+i+1)}{(n-1)!\left|\sum_{m=1}^{k}\binom{k}{m}(-1)^{m+1}\left(\frac{\lambda^m+n\mu^m}{\lambda^m+\mu^m}\right)\right|^{\delta}\prod_{i=0}^{t-1}(r+i+n)} \qquad (14)$$

for $t,n\in\mathbb{N}_2$ where $r\in\mathbb{R}\backslash(-\infty,-1]$.

Proof.
Let the function $f\in A$ be given by (**1**) and

$$g(z)=\sum_{n=1}^{\infty}b_nz^n\in S_g^{*,\delta}(\lambda,\mu,k;\alpha).$$

Then from (**7**), we get

$$a_n=\frac{\prod_{i=0}^{t-1}(r+i+1)}{\prod_{i=0}^{t-1}(r+i+n)}b_n$$

for $n\in\mathbb{N}_2$, $r\in\mathbb{R}\backslash(-\infty,-1]$. Hence from Theorem 2.1 we obtain inequality (**14**). This completes the proof.

Author's Contributions

All authors contributed equally to this manuscript and all authors reviewed the final manuscript.

Ethics

There are no ethical issues after the publication of this manuscript.

References

1. Al-Hawary, T., Frasin, B. A., Yousef, F. 2018. Coefficients estimates for certain classes of analytic functions, *Afrika Mathematika*, 29, 1265-1271.
2. Al-Oboudi, F. M. 2004. On univalent functions defined by a generalized Salagean operator, *Int. J. Math. Math. Sci*. 27, 1429-1436.
3. Cho, N. M., Kim, T. H. 2003. Multiplier transformations and strongly close to convex functions, *Bull. Korean Math. Soc*. 40-3, 399-410.
4. Cho, N. M., Srivastava, H. M. 2003. Argument estimates of certain analytic functions defined by a class of multiplier transformations, *Math. Comput. Modelling* 37-1-2, 39-49.
5. Miller, S. S., Mocanu, P. T., Differential subordination, Monographs and Textbooks in Pure and Applied Mathematics,. Marcel Dekker Inc. New York, 2000; pp 225.
6. Robertson, M. S. 1936. On the theory of univalent functions, *Annals of Mathematics* 37, 374-408.
7. Rogosinski, W. 1943. On the coefficients of subordinate functions, *Proc. Lond. Math. Soc*. (Ser 2) 48, 48-82.
8. Salagean, G. 1983. Subclasses of univalent functions, *Lecture Notes in Math., Springer Verlag, Berlin* 1013, 362-372.
9. Silverman, H. 1978. Subclasses of starlike functions, *Rev. Roum. Math. Pures et Appl*. 23, 1093-1099.
10. Swamy, S. R. 2012. Inclusion properties of certain subclasses of analytic functions, *Int. Math. Forum* 7-36, 1751-1760.
11. Wanas, A. K. 2019. New differential operator for holomorphic functions, *Earthline Journal of Mathematical Sciences* 2-2, 527-537.

12. Galib Atshan, W., Ibrahim Badawi, E., 2019. On Sandwich Theorems for Certain Univalent Functions Defined by a New operator. *Journal of Al-Qadisiyah for Computer Science and Mathematics*, *11*(2), math 72-80.

13. Atshan, W. G., Abbas, I. A., Yalcin, S., 2020. New Concept on Fourth-Order Differential Subordination and Superordination with Some Results for Multivalent Analytic Functions. *Journal of Al-Qadisiyah for Computer Science and Mathematics*, *12*(1), Math Page 96-107.

14. Frasin, B., & Murugusundaramoorthy, G., 2020. A subordination results for a class of analytic functions defined by q-differential operator, *Annales Universitatis Paedagogicae Cracoviensis. Studia Mathematica* (published online ahead of print 2020).

15. Çakmak, S., Yalçın, S., & Altınkaya, Ş., 2019. An application of the power series distribution for certain analytic univalent function classes. *Lıbertas Mathematıca (new series)*, *39*(1), 95-102.

16. Srivastava, H. M., & El-Deeb, S. M., 2020. A certain class of analytic functions of complex order connected with a q-analogue of integral operators. *Miskolc Mathematical Notes*, *21*(1), 417-433.

17. Khan, B., Srivastava, H. M., Khan, N., Darus, M., Tahir, M., & Ahmad, Q. Z., 2020. Coefficient estimates for a subclass of analytic functions associated with a certain leaf-like domain. *Mathematics*, 8(8), 1334.

18. Liu, G., Liu, Z., & Ponnusamy, S., 2020. Refined Bohr inequality for bounded analytic functions. *arXiv preprint arXiv:2006.08930*.

19. Porwal, S. 2020. Mapping Properties Of Certain Subclasses Of Analytic Functions Associated With Generalized Distribution Series. *Applied Mathematics E-Notes*, *20*, 39-45.

20. Atshan, W. G., Abbas, I. A., & Yalcin, S., 2020. New Concept on Fourth-Order Differential Subordination and Superordination with Some Results for Multivalent Analytic Functions. *Journal of Al-Qadisiyah for Computer Science and Mathematics*, *12*(1), Math Page 96-107.